N64-28052

ION ROCKET ENGINE SYSTEM RESEARCH AND DEVELOPMENT

by

R. C. Speiser, R. M. Worlock, F. A. Barcatta,
G. C. Reid, and G. Sohl

prepared for

NATIONAL AERONAUTICS AND SPACE ADMINISTRATION

CONTRACT NAS3-2516

E●S ELECTRO-OPTICAL SYSTEMS, INC., PASADENA, CALIFORNIA

Requests for copies of this report should be referred to

National Aeronautics and Space Administration
Office of Scientific and Technical Information
Attention: AFSS-A
Washington, D.C. 20546

/96952

FINAL REPORT

ION ROCKET ENGINE SYSTEM RESEARCH AND DEVELOPMENT

by

R. C. Speiser, R. M. Worlock, F. A. Barcatta,
G. C. Reid, and G. Sohl

prepared for

NATIONAL AERONAUTICS AND SPACE ADMINISTRATION

28 June 1964

CONTRACT NAS3-2516

ELECTRO-OPTICAL SYSTEMS, INC.

300 No. Halstead Street

Pasadena, California

ABSTRACT

An applied research and development program on an electron bombardment cesium ion engine system is reported. The engine system includes a zero-gravity feed system and an automatic control system. The 3 kilowatt engine system produces a thrust of 0.04 to 0.05 newtons at a specific impulse between 4,000 and 7,000 seconds. Component development, system integration, and system tests are described in detail.

CONTENTS

CONTENTS (Cont)

CONTENTS (Cont)

ILLUSTRATIONS

ILLUSTRATIONS (Cont)

ILLUSTRATIONS (Cont)

ILLUSTRATIONS (Cont)

ILLUSTRATIONS (Cont)

TABLES

LIST OF SYMBOLS

A   Anode radius

A_P Aperture area of Faraday probe

a   Diameter of capillary or pore

α Angle between walls of a tapered tube

B   Magnetic field flux density

B_Z Axial magnetic flux density

b   Radius of corner-trapped cesium surface

c^2 Cross sectional area of corner-trapped cesium

D   Radial diffusion coefficient of electrons

e   Electronic charge

F   Force

f_M Maxwellian distribution function

g   gravitational field

γ Force on liquid in earth g's

h   Height of liquid in a tube

η Coefficient of viscosity

η_E Overall engine efficiency

η_m Mass utilization efficiency

η_P Power efficiency

θ Angle between solid surface and surface of wetting liquid

I_A Arc current

I_B Beam Current

I_C Collector current

I_F Front magnet current

I_M Maximum beam current

I_N Neutral efflux in equivalent ion current

I_n Neutralizer emission current

I_{ND} Neutral detector current

I_{NE} Engine mounted neutral detector current

I_{NT} Tank mounted neutral detector current

I_o Mass flowrate in equivalent ion current

I_P Faraday probe current

I_R Rear magnet current

I_{sp} Specific impulse

I_- Accelerator drain current

g_B Beam current density

j_e Electron current density

j_+ Ion current density

k Boltzmann's constant

ℓ Length

M_{Cs} Mass of trapped cesium

M_R Mass of porous rod

m Atomic mass

n_e Electron density

n_o Neutral density

n_p Primary electron density

n_+ Ion density

υ_p Reciprocal of equilibration time for primary electrons

P_A Arc power

P_B Beam power

P_D Drain power

P_K Cathode heater power

P_M Magnet power

P_N Neutralizer heater power

P_T Total engine power

P/T Power-to-thrust ratio

r Radial coordinate

ρ Density of liquid

ρ_{Cs} Density of cesium

ρ_R Density of basic porous rod material

Se Ionization efficiency (ion pairs/cm-mm Hg)

σ Energy per unit area where $\sigma_o = -\sigma_1$

σ_o Energy per unit area of free liquid surface

σ_1 Energy per unit area of wetted surface

σ_{01} Ionization cross section

σ_I Inelastic collision cross section for electrons and atoms

$\overline{\sigma v}$ Ionization coefficient

T	Thrust
T_e	Electron temperature
T_+	Ion temperature
t	Time
τ	Volume of a given quantity of liquid
τ_E	Mean equilibration time for primary electrons
τ_I	Mean time for inelastic collisions
U	Energy
V	Electron energy
V_A	Arc voltage
V_C	Collector voltage
V_{Cs}	Volume of cesium
V_I	Ionization potential
V_R	Volume of porous rod
V_r	Open volume in porous rod
V_+	Engine source potential
V_-	Accelerator potential
v	Electron velocity
v_f	Flow velocity
v_+	Mean ion velocity
ω	Angular frequency
x	Cartesian coordinate

SUMMARY

$\sqrt{}$

This summary report for the period 27 December 1962 to 29 February 1964 describes the work performed under Contract NAS3-2516, "Ion Rocket Engine System Research and Development". The objective of the program was to develop a 3 kilowatt electron bombardment cesium ion engine system. The engine system was defined to include the engine, the propellant feed and storage systems, and the engine control system including power supplies.

The engine was to operate at a thrust in excess of 0.04 newtons (9 mlb) at a specific impulse between 4,000 and 7,000 seconds. The feed system was to be designed to operate in a zero-gravity environment. The control system was to be a rack mounted package operating with laboratory-type power supplies. It was to be capable of automatically starting and stopping the engine and handling transients.

The engine developed under the program produces thrusts in excess of 9 mlb at specific impulses over 5,000 seconds. Overall engine efficiency ranges from 63 percent at 4,500 seconds to 76 percent at 6,900 seconds. The engine uses a cesiated cathode heated by ion bombardment from the discharge plasma and has a high perveance, muliple aperture accelerator electrode system design.

The feed system utilizes surface tension forces with no mechanical moving parts. Capillary action delivers cesium liquid to the surface of a porous rod which is locally heated to produce the desired cesium vapor flow rate. This system has excellent control characteristics.

The control system automatically programs the startup procedure for the engine and feed system and brings the engine system up to preset performance levels where the beam current, arc power, and feed

system power are regulated. The complete engine system was put through ten consecutive start-stop tests and a 77-hour regulated operation test at the specified performance level. Two complete engine systems were delivered to NASA-LRC at the completion of the program.

1. INTRODUCTION

The work described in this report was performed under Contract NAS3-2516 administered by the National Aeronautics and Space Administration's Lewis Research Center (NASA-LRC). The program resulted in the delivery to NASA-LRC of two complete engine systems including zero-g feed systems, laboratory control systems, and power supplies. This report delineates the development program undertaken to produce the system components and describes the design, operation, and performance of the delivered engine system.

1.1 Previous Work

The general requirements of an ion source for electrostatic propulsion applications are high power efficiency, high mass utilization (percentage ionization), and long lifetime. In addition, size and weight considerations favor high current and thrust densities which require the use of ionic species with a low charge to mass ratio. The first demonstration that these requirements might be met with sources in which ions were extracted from a low density plasma generated by electron bombardment was made by H. Kaufman of NASA-LRC in 1960.

The Kaufman source, using mercury as propellant, consisted of a thermionic cathode placed inside a cylindrical anode with a magnetic field parallel to the axis of the system. A plasma is generated within the cylinder, and those ions which drift to one end are extracted through apertures in a screen by an accelerating electrode. This source differed from the Finkelstein oscillating electron source primarily in the use of the gridded anticathode or screen electrode through which ions are withdrawn. The mercury ion engine has since been brought to a very high state of development by Kaufman and Reader at NASA-LRC.

In 1961, following the Kaufman source, Forrester and Speiser of EOS proposed the use of cesium in an electron bombardment ion engine to take advantage of several unique properties of such a system. The source differs from the mercury source in that cesium is introduced through the cathode which is a cesiated thermionic emitter. In addition, the cathode is heated by ion bombardment from the plasma. This is feasible in the cesium source because the bombarding energy is below the sputtering threshold. Other advantages accruing from the use of cesium are lower arc voltage, lower magnetic field, the absence of doubly charged ions, and a very high percentage ionization.

The cesium ion source was investigated at EOS under Contract NAS8-2511, "Study of a Gas Discharge Cesium Ion Source". The engine system developed under the present program (NAS3-2516) was based on the results of that study.

1.2 Program Objectives

The objective of the program was to develop a 3 kw electron bombardment cesium ion engine system. The engine system was defined to include the engine, the propellant feed and storage systems, and the engine control system including power supplies. The 3 kw was considered to be input power to flight type power conditioning equipment and, therefore, not completely available to the engine.

The engine was to operate at a thrust in excess of 0.04 newtons (9 mlb) at a specific impulse between 4,000 and 7,000 seconds. It was also to be of flight prototype construction and to be fabricated of materials likely to be capable of long operation in a partially shielded reactor radiation environment.

The feed system was to be designed to operate in a zero-gravity (zero-g) environment and capable of running the engine at least 50 hours. A large feed system with a cesium capacity equivalent to 750 hours engine operation was an additional goal added late in the program.

The control system was to be a rack-mounted package. It was to operate with laboratory-type power supplies and be capable of automatically starting and stopping engine operation and handling momentary breakdowns and transients.

The engine system was to be capable of being completely shut down and started up at least ten times without servicing or other adjustment. At the end of the program, two of the developed engine systems were to be delivered to NASA-LRC.

1.3 Organization of Report

In order to provide continuity of subject matter together with some degree of chronological development, the engine system is discussed in terms of its major subsystems. Section 2 covers engine development and related applied research areas. Section 3 describes the feed system development program and details of design and operation of the zero-g feed systems of the surface tension type. Section 4 discusses the development of the control system and presents a detailed description of the final version which was delivered to NASA-LRC. Section 5 gives performance data for the final version of the engine system and describes the tests which were performed and their results.

Appendix A describes the quality assurance plan used throughout the program. It also lists the special processing specifications and inspection and test procedures generated under the plan. Action taken on DE system failure reports is also included.

Reference 1 presents some design considerations for a 10,000-hour 30-kilowatt flight system based on an assembly of 3 kw engine system modules. It includes a description of engine electrical requirements and a discussion of radiation hardened components.

The authors thank Dr. A. T. Forrester for his interest in the program and for several illuminating discussions of technical problems. The authors also wish to thank Mr. G. E. Trump who played a significant role in feed system development, Mr. S. Lyons who designed circuits and supervised construction of the control system, and Mr. D. West who worked with Mr. Reid on engine design. Special thanks are due Mr. S. Zafran, our Quality Assurance Engineer, for a splendid job in setting up and administering the quality assurance program which was executed very smoothly.

2. ENGINE RESEARCH AND DEVELOPMENT

The configuration of an electron bombardment cesium ion engine is depicted in Fig. 2-1. There is a cylindrical arc chamber with a cylindrical anode supported within it. The anode is operated at a potential positive with respect to the end plates which are at cathode potential. One of the end plates is the anticathode or screen electrode and has apertures in it. Magnet coils set up a magnetic field parallel to the axis of the chamber. The whole chamber is run at a high positive potential V_+ and an accelerating electrode is run at a negative potential V_-, with apertures that match the apertures in the screen electrode. Ions diffusing to the plasma sheath at the screen electrode can be accelerated by fields across the accelerating gap through the apertures and into beams. These beams are then neutralized by the injection of electrons from an emitter at, or close to, ground potential. Under these conditions the exhaust becomes a plasma at a potential close to ground.

The negative potential on the accelerating electrode provides the barrier necessary to prevent the neutralizing electrons from going back into the source. Ions are accelerated through a voltage drop of $V_+ + |V_-|$ and decelerated through a potential $|V_-|$ to a velocity corresponding to the energy eV_+.

The unique cathode in the cesium engine operates in the following manner. Cesium from the feed system diffuses around a baffle and must go past and between the turns of a heated helix of refractory metal to get into the arc chamber. The surface of the helix thereby gets coated with cesium and provides a good electron emitter. As will be discussed in Subsection 2.1.2, in the autocathode mode of operation, the refractory metal helix is heated by ion bombardment from the plasma.
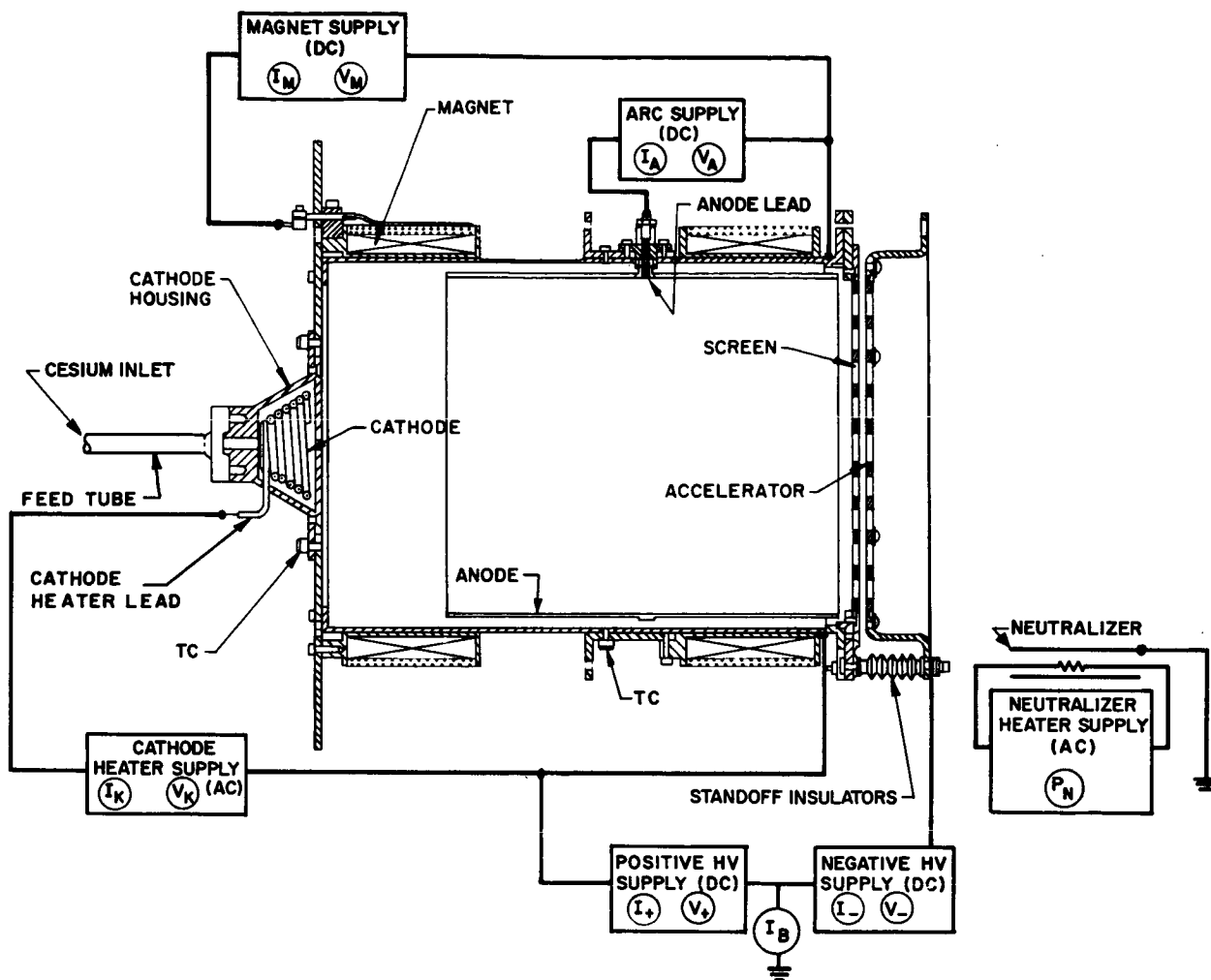
FIG. 2-1   SCHEMATIC OF ELECTRON BOMBARDMENT CESIUM
ION SOURCE

2.1 Technical Background

This section describes some of the significant features of the cesium discharge and reviews some of the earlier work with cesium engines. A complete description of early work on cesium gas discharge ion sources is available in Ref. 2.

2.1.1 Cesium Discharge

Table 2-I presents some atomic properties of interest for electron impact ionization of cesium. It can readily be seen that the low value of the first ionization potential allows operation of a cesium discharge at low arc voltages. The much higher value of the second ionization potential, higher than the optimum electron energy for single ionization, indicates a minimum of second ionization at discharge parameters leading to efficient single ionization of cesium. In correlation of beam and thrust measurements (Ref. 2) no double ionization in the beam was found.

TABLE 2-I

IMPACT IONIZATION PARAMETERS FOR CESIUM

1st ionization potential (ev)	3.9
2nd ionization potential (ev)	23.4
Optimum electron energy (ev) for ionization by single electron impact	~ 18
S_e (ion pairs/cm-mm Hg) at or below 2nd ionization threshold	9.8
Initial slope of ionization curve, Δ (for $S_e = \Delta(V-V_I)$)	2.8

Typical arc voltages of 7 to 8 volts are used in the cesium ion source. The cesium discharge in the engine can be further understood by evaluating what happens to electrons accelerated into the plasma across the cathode sheath. The inelastic cross section for a 7 volt electron

in cesium vapor is approximately

$$\sigma_I \sim 6 \times 10^{-16} \ cm^2 \ .$$

The mean time for an inelastic collision is therefore

$$\tau_I \sim 10^{-4} \ sec \ for \ 10^{11} \ atoms/cm^3$$

where $\tau_I = \dfrac{1}{n_o \sigma v}$; n_o is the atom density and v the electron velocity.

Langmuir probing of the cesium discharge (Ref. 2) disclosed Maxwellian electron distributions of about 10^{12} electrons/cm^3 with 1 to 2 ev mean electron temperatures and the virtual absence of electrons of primary (arc voltage) energy. The mean equilibration or thermalization time, that is, the time required for a 7 ev electron to join the Maxwellian distribution due to coulomb collisions with the Maxwell electrons is

$$\tau_E \sim 6 \times 10^{-7} \ sec$$

for a Maxwellian distribution of 10^{12} electrons/cm^3 with 1.8 ev mean energy. The ratio of the two times is

$$\frac{\tau_E}{\tau_I} \sim 0.006$$

Thus it is clear that the first thing that happens to an electron entering the plasma from the cathode is that it equilibrates with the Maxwellian electron distribution due to elastic collisions.

Ionization Due to Maxwell Electrons

The volume ionization rate due to electrons of velocity v is given by

$$\frac{dn_+}{dt} = n_o \ n_e \ \sigma_{oi} v \tag{1}$$

where n_o is the neutral atom density, n_e the electron density, σ_{oi} the ionization cross section (a function of velocity) and v the electron velocity. If we define an electron distribution $f(v)$ such that the mean velocity is $\bar{v} = \int_o^\infty v\, f(v)\, dv$, for the Maxwellian distribution $f_M(v)$ we have

$$\frac{dn_+}{dt} = n_o\, n_e \int_o^\infty \sigma_{oi} v\, f_M(v)\, dv = n_o\, n_e\, \overline{\sigma v} \quad . \tag{2}$$

Figure 2-2 shows the ionization coefficient $\overline{\sigma v}$ for cesium as a function of electron temperature for Maxwellian electron distributions. The ionization is due to the high energy tail of the electron energy distribution. The shape of the curve and the steep rise at 2 ev indicates the expected electron temperatures of between 1 and 2 ev for the cesium discharge.

The most important effect of the magnetic field is now clear; it prevents primary electrons from reaching the anode before they have become equilibrated with the Maxwellian electron distribution. The magnetic field also governs the diffusion of Maxwell electrons to the anode, thereby giving rise to a nonuniform radial plasma distribution in the source.

Plasma Density Distribution

The radial diffusion equation for the Maxwell electrons is found to be

$$D \left[\frac{1}{r} \frac{d}{dr}\ \frac{r\, dn_e}{dr} \right] + n_o\, n_e\, \overline{\sigma v} + \nu_p\, n_p = 0 \tag{3}$$

where D is the diffusion coefficient for the electrons across the magnetic field, $n_o\, n_e\, \overline{\sigma v}$ is the rate at which additional electrons are produced due to ionization and $\nu_p n_p$ is the rate at which primary electrons join the Maxwellian electron distribution; ν_p is the reciprocal of the mean thermalization time and n_p is the primary electron density.

The various approximations to the solution of this equation, based on taking average values of densities or temperatures in evaluating the diffusivity and electron production rates, all give rise to solutions in which the electron or plasma density decreases from the center of the source to the anode. This is observed experimentally and will be discussed in more detail in Section 2.3.2.

2.1.2 Autocathode

The cesium engine could be operated with conventional thermionic cathodes. One of the advantages, however, of using cesium in the discharge is the low work function obtained from a layer of cesium on various metals. As an example, consider the Langmuir-type S-curves of Fig. 2-3. Electron emission from cesiated tantalum is plotted against the reciprocal of the tantalum temperature. The parameters on each curve refer to the temperature at which the vapor pressure at which the curves were taken is in equilibrium with liquid cesium. As indicated, emissions of amperes per square centimeter are obtainable at very reasonable cesium densities and at fairly low cathode temperatures.

By a configuration where the cesium is introduced through the cathode in such a way as to maintain a cesium coating on the surface, an efficient cathode of long lifetime is achieved. Such a configuration is shown in Fig. 2-3. Poisoning does not occur; in fact, ion bombardment brings more cesium to the cathode surface. The low voltage of the cesium discharge is below the sputtering threshold of most materials so no lifetime limitation is apparent except for heater failure. The auto-cathode, however, requires no heater.

Autocathode Operation

At normal operation in the main discharge chamber, the cesium ion current delivered to the cathode by ions accelerated from the plasma across the sheath is

$$j_+ = \frac{1}{4} e \, n_+ v_+ \qquad (4)$$
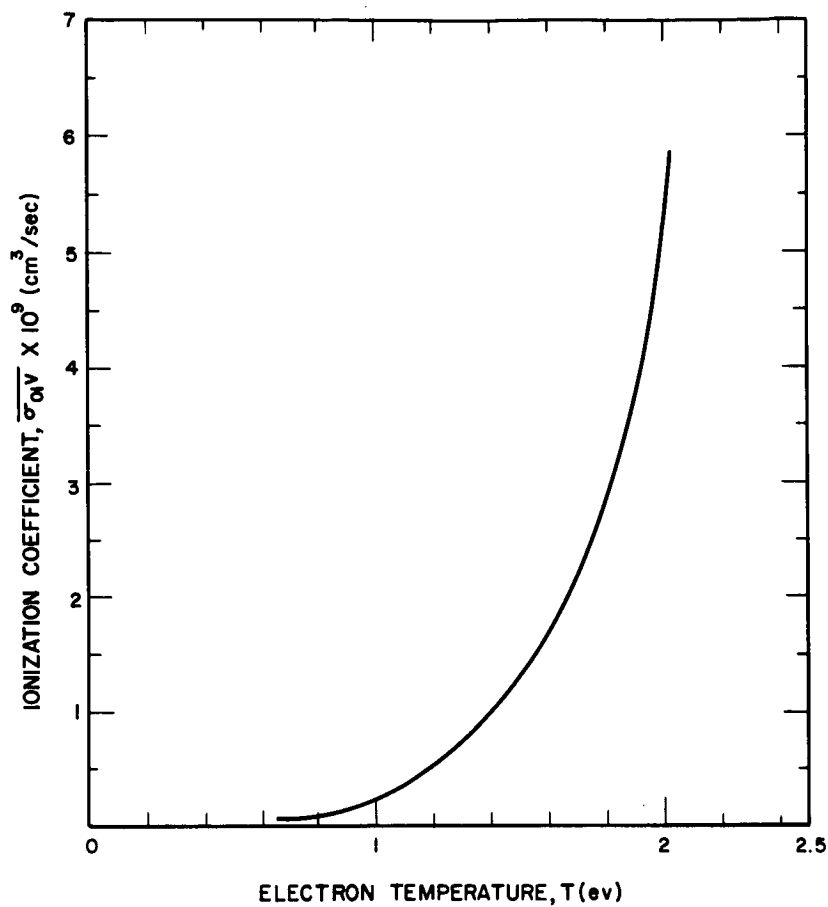
FIG. 2-2

ION PRODUCTION COEFFICIENT VS ELECTRON TEMPERATURE FOR CESIUM
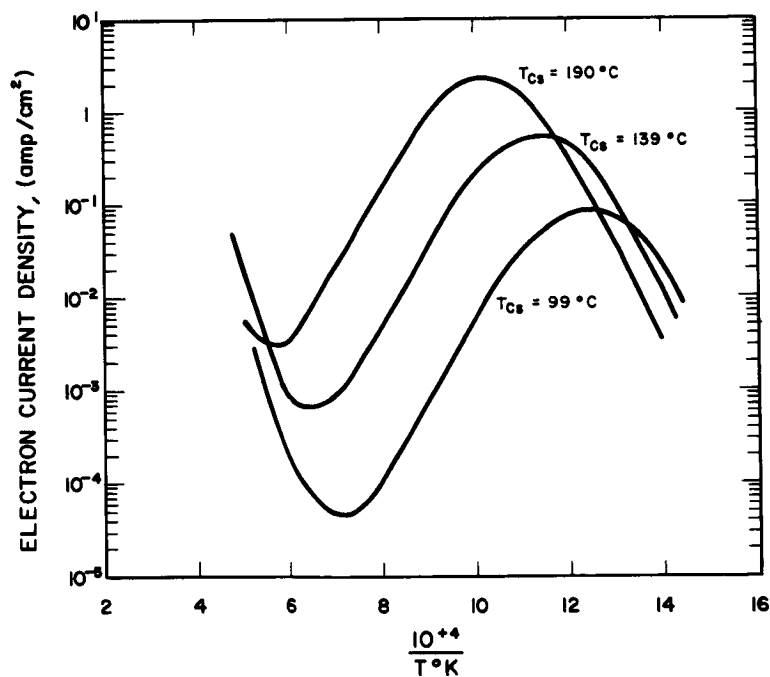
FIG. 2-3

THERMIONIC ELECTRON EMISSION OF CESIUM ON TANTALUM

where n_+ is the ion density, e the electronic charge, and v_+ the mean ion velocity corresponding to an ion temperature T_+, i.e.,

$$v_+ = \left[\frac{kT_+}{2\pi m_{Cs}}\right]^{1/2} \qquad (5)$$

For an ion temperature of 10^4 °K and an ion density of 2×10^{11} ions/cm^3 the ion current density would be 1 ma/cm^2. For a 10 volt cathode sheath potential in the low voltage cesium discharge, the power delivered to the cathode surface would only be 10^{-2} watts/cm^2. The temperature necessary for an emission of 5 amperes per cm^2 from a cesiated surface is about 1100°K at which temperature the power radiated would be about 3 watts/cm^2 for an emissivity of 0.4. This power can be provided by increasing the ion density and current density in the vicinity of the cathode by a large factor. This is accomplished in the autocathode configuration depicted in Fig. 2-4.

Typically, the cathode orifice in the autocathode is about 1/400 the total area of all the beam extraction apertures. Accordingly, the densities in the autocathode are about 400 times larger than in the discharge chamber and the power delivered to the autocathode surface by ion bombardment is about 4 watts/cm^2 with an ion current density approaching 0.5 amp/cm^2. The autocathode surfaces are supported so as to minimize heat loss by conduction. The autocathode sustains the cesium discharge with no additional heater power. Due to cesium condensation, it is difficult to initiate the discharge with a cold cathode. In the present engines the cathode is heated until the arc starts.

Source Characteristics

Typical arc characteristics with an autocathode are shown in Fig. 2-5. This figure was reproduced from an oscilloscope photograph. As can be seen, except at very low arc voltage (and very high voltages), the arc current varies linearly with the arc voltage.
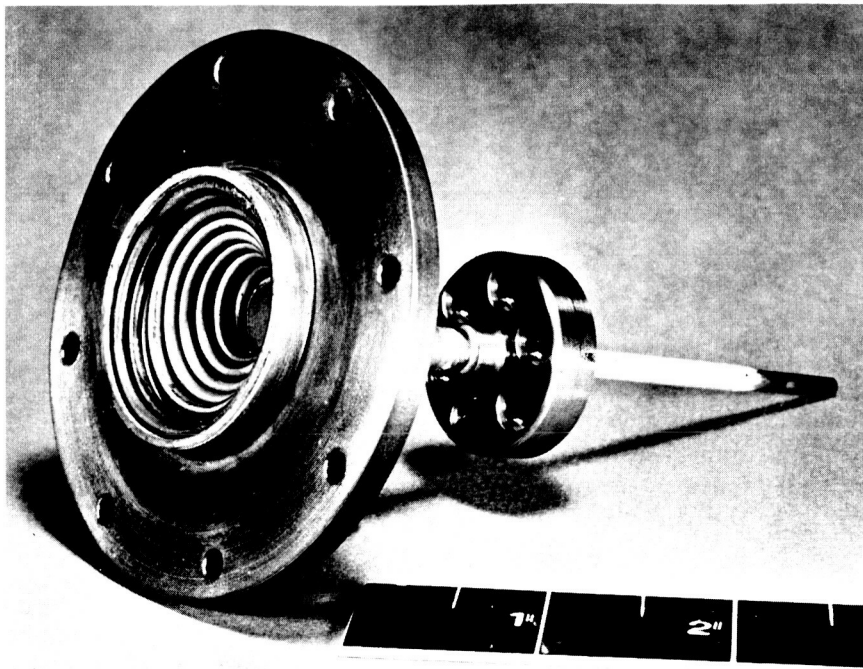
FIG. 2-4   CATHODE K5
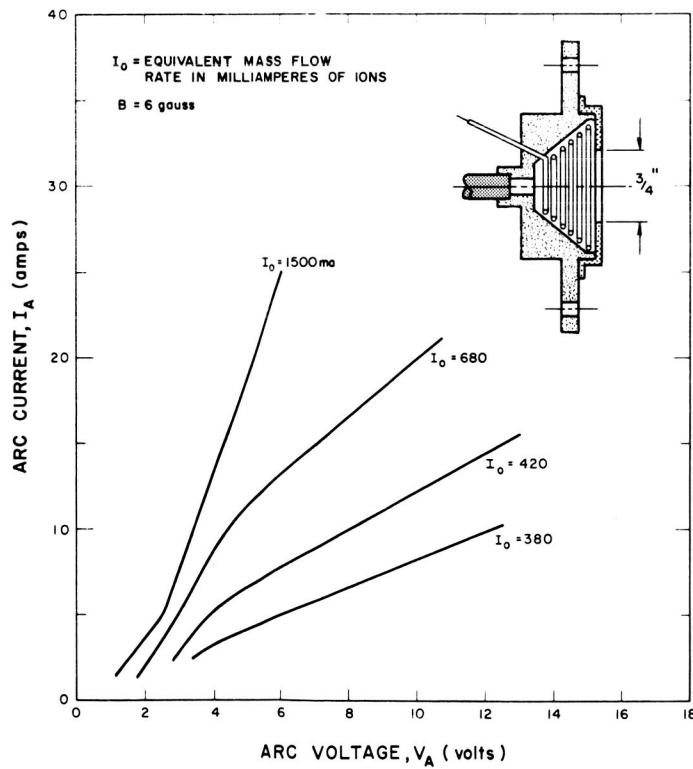
FIG. 2-5

ARC CHARACTERISTIC FOR CATHODE
K5A (10 cm Ion Source)

Higher feedrates give higher arc currents as expected for autocathode operation.

The best cathode configuration found in testing with large engines was cathode K5B, which was depicted in the schematic of Fig. 2-1. Figure 2-6a shows some arc current versus arc voltage data taken with this cathode with a 10 cm diameter ion source. The data show the usual linearity in the range in which they were taken. Figure 2-6b shows the beam current versus the arc current for the same six data points. At low mass utilization efficiency the beam current is usually proportional to the arc current. However, at high mass utilization the beam current is limited to the feedrate and increases very little with arc current (or voltage).

2.1.3   Early Engines

The ideas involved in the operation of a cesium gas discharge engine with the low voltage arc mode were first investigated with a small device of the general configuration as has been discussed. A 40 ma ion beam was produced at an arc voltage of 6 volts and an arc current of 3 to 4 amperes. The magnet current was a few amps giving that configuration about a 10 gauss field in the center of the arc chamber. These results, together with the considerations of the theory and operation of the device, led to the design of a small engine.

6.5 CM Engine

An engine of an improved configuration was designed based on the initial data. This source was a 6.5 cm diameter configuration, the size being determined by the diameter of the anode cylinder since all of the beam apertures lay within this dimension. The discharge chamber itself was a tantalum cylinder 3 inches in diameter and 4 inches long. The cathode was mounted at the rear of the chamber. The anode was copper and ran nearly the full length of the chamber. The magnetic field coils were mounted on the tantalum cylinder. At the center of the discharge chamber these coils provided about 10 gauss per ampere of coil current. The discharge chamber was rigidly mounted to the screen electrode.
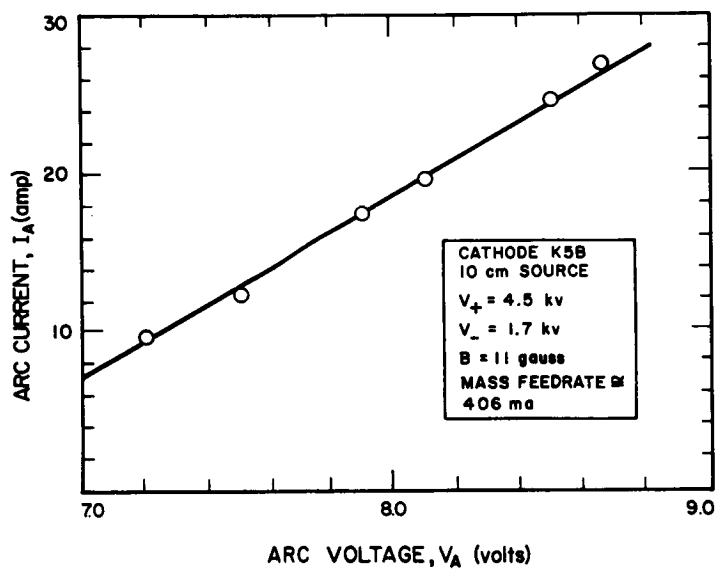
FIG. 2-6a

I_A VS V_A FOR 10 cm SOURCE
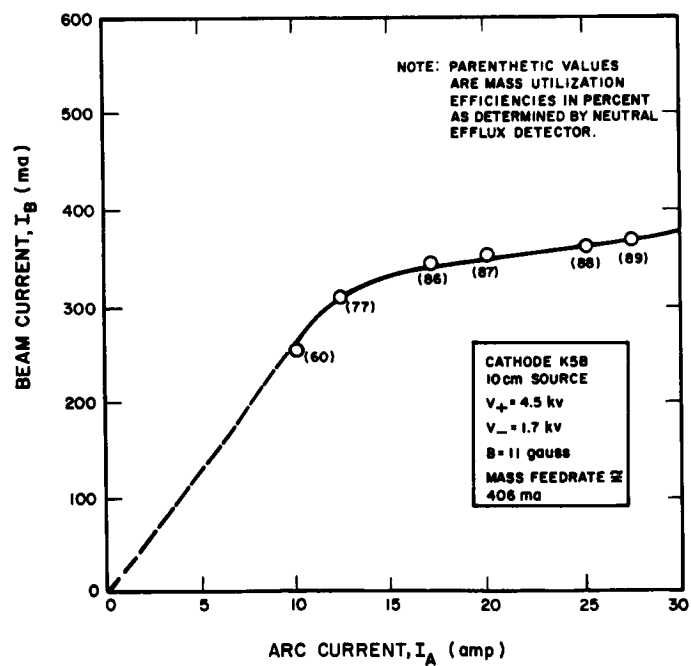
FIG. 2-6b

I_B VS I_A FOR 10 cm SOURCE

Each of the electrodes was supported on three insulating posts to which it was attached by assemblies which allowed free radial expansion. In addition, the use of eccentrics allowed adjustments for accurate alignment of the apertures.

The various electrode configurations used are tabulated below. The screen electrodes were molybdenum and the accel electrodes of copper or molybdenum.

TABLE 2-II

ELECTRODE GEOMETRIES

Number of Apertures	Aperture Diameter (Screen Electrode)	Aperture Diameter (Accel Electrode)	Distance Between Centers
37	3/16 inch	0.16 inch	1/4 inch
61	3/16 inch	0.16 inch	1/4 inch
91	3/16 inch	0.16 inch	1/4 inch
109	3/16 inch	0.16 inch	7/32 inch
301	1/8 inch	1/8 inch	9/64 inch

Decel electrodes were sometimes used, with apertures 12 percent larger than those of the screen electrode. Accelerating gaps were about equal to the screen electrode aperture diameter or slightly smaller.

This source operated with beam currents up to 150 ma and thrusts to 4 mlb. It also demonstrated mass utilization efficiencies as high as 95 percent.

10 CM Engine

A larger source, with a 10 cm diameter anode, was then designed and tested. The source is shown in Figs. 2-7a and 2-7b. The discharge chamber was of stainless steel (nonmagnetic 300 series) and the magnet coils were mounted directly onto the shell. The coil resistances were about 1 ohm, providing 5.5 gauss per ampere coil current.
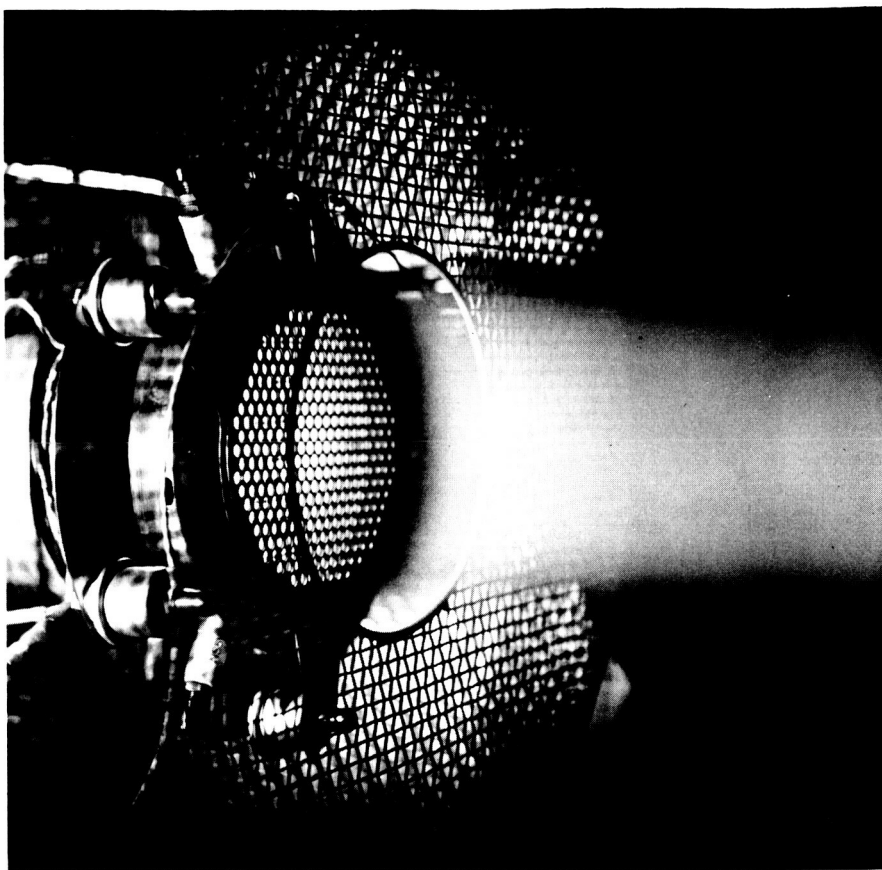
FIG. 2-7a   10 cm SOURCE IN OPERATION
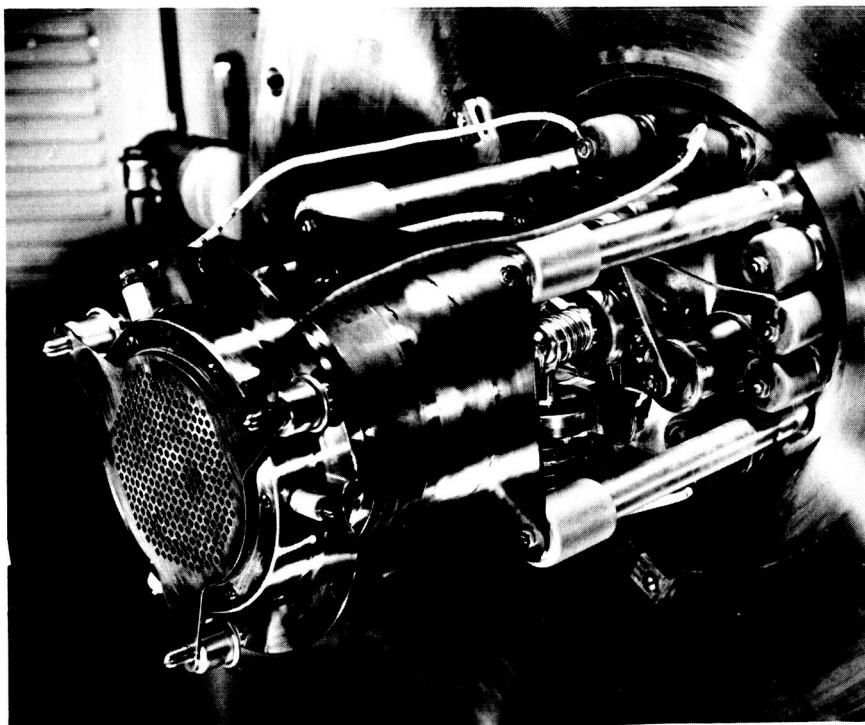
FIG. 2-7b   10 cm ENGINE

The chamber was 6 inches long with a 4 inch diameter copper anode ring of 4 inches length mounted with one end close to the screen electrode. The only electrode system used had 313 apertures of 3/16 inch diameter spaced 7/32 inch between centers for both the screen electrode and accelerator electrode. Both electrodes were of molybdenum. The accelerator electrode was mounted to the chamber on insulators. The accelerating gap was set at 3/16 inch or slightly less.

The 10 cm engine produced beams up to 430 ma and thrusts to 10 mlb.

Engine Performance

Mass utilization data were taken with a hot filament neutral cesium detector such as described in Ref. 2. Total flow rate calibrations were checked by consistency of the sum of the ions and neutrals for arc parameters producing different beam current levels at the same feed system settings. Data for the two different size sources with high performance cathodes are presented in Fig. 2-8. The mass utilization efficiency η_m is plotted against arc energy per ion. Since there is no cathode heater power and, since the magnet power is negligible, this is the total source energy per ion. The 10 cm source data were taken at ion beam levels to over 350 ma. The 6.5 cm source operated with cathode K1A and the 10 cm engine with K5B. Tests with a movable neutral detector gave the same beam on-beam off neutral efflux measurements over a range of 10° to 50° off the beam axis and indicated the reliability of the stationary detector measurements.

In general, both sources achieved the same high performance with the cathodes found most favorable for each. In Fig. 2-9 the overall engine efficiency η_E (the product of the power efficiency and the mass utilization efficiency) is plotted against the specific impulse (corrected for less than 100 percent ionization) for the 6.5 cm source. The data would be changed little by inclusion of neutralizer filament power and the feed system power is excluded in accordance with practice.
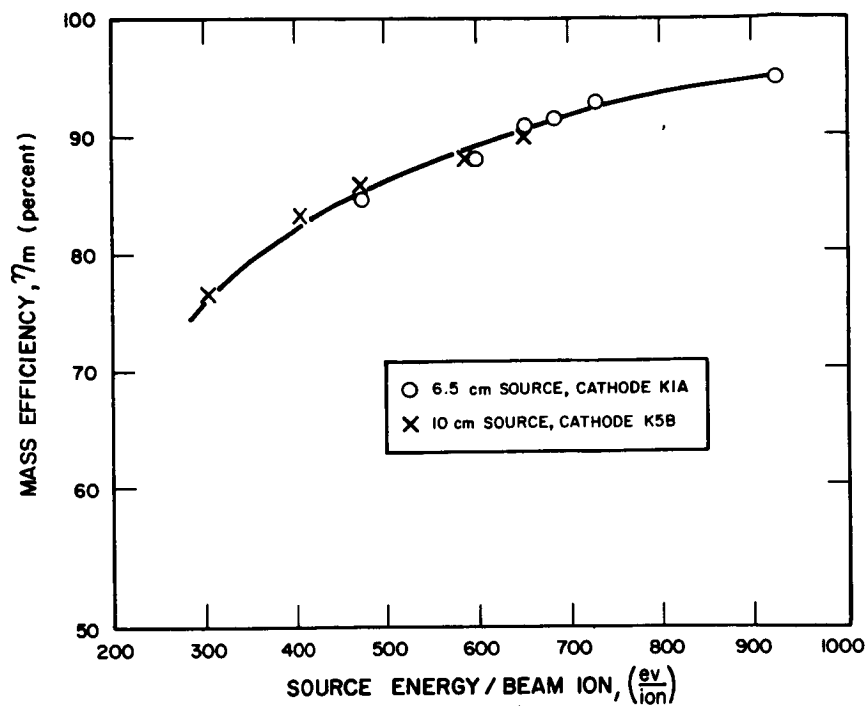
FIG. 2-8   MASS UTILIZATION DATA FOR 6.5 cm AND
            10 cm ENGINES
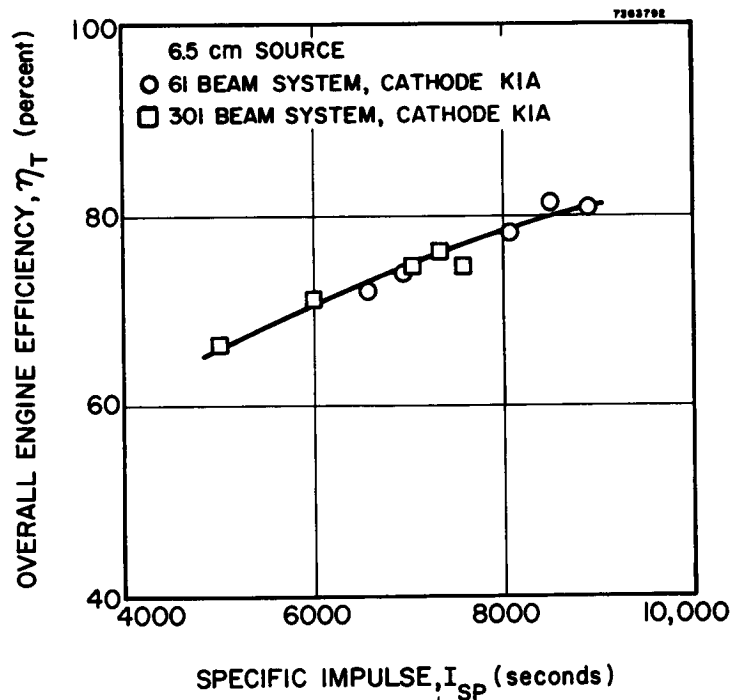
FIG. 2-9   OVERALL ENGINE EFFICIENCY
            VS SPECIFIC IMPULSE FOR
            6.5 cm SOURCE

2.2 DD Engine

The first engines built were designed to meet the performance
goals of the program but no restrictions were imposed on size, weight,
or construction.

2.2.1 DD Engine Design

A layout of the DD engine is shown in Fig. 2-10. The
SN-1 feed system, discussed in Section 3 is also shown in the figure.
The engine is mounted within a ground cylinder which also supports the
neutralizer and a neutral cesium detector. Figures 2-11a and 2-11b are
views of the assembled engine. The magnet coils are mounted on the dis-
charge chamber cylinder and operate at the chamber potential. They are
positionable but are located at a spacing slightly greater than that for
a Helmholtz configuration. The coils are each made of 70 turns of 18
gauge copper wire with refrasil (woven silica fiber) insulation. The
coil forms are aluminum. The impedance of each coil is 0.67 ohms at
room temperature and the field produced at the center of the chamber
is about 5 gauss per ampere of coil current.

The accelerating electrode, shown in Fig. 2-12, is an
0.080-inch thick molybdenum plate containing 421 apertures each of
0.156-inch diameter with 0.219 inch between centers. On the side facing
the source, the edges of the apertures are radiused and polished. The
screen electrode, through which beams are extracted from the plasma in
the discharge chamber, was 0.080-inch thick molybdenum plate with
0.171-inch diameter apertures. To facilitate testing of electrode
geometries, the electrodes and associated supports were designed as
a separate assembly as shown in Fig. 2-13. This feature allowed assembly
and alignment of the electrode system as a unit which then attached to
the discharge chamber. The electrode system was aligned to within
0.001 inch on a special jig.

The basic cathode configuration originally designed
for the DD engine was a larger version of the K5 cathode (Ref. 2).
Early in the engine testing program, however, the K5B design,
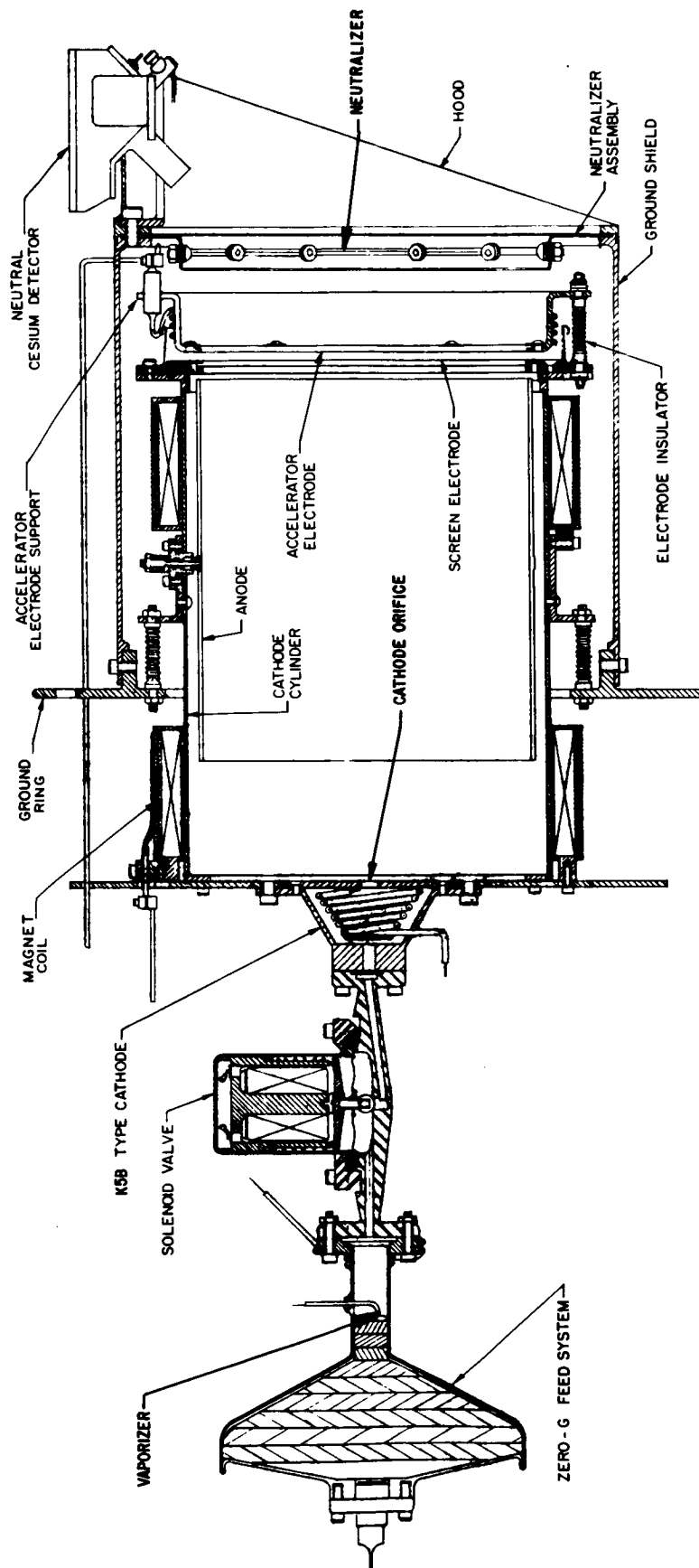
FIG. 2-10 MODEL DD GAS DISCHARGE ENGINE SYSTEM
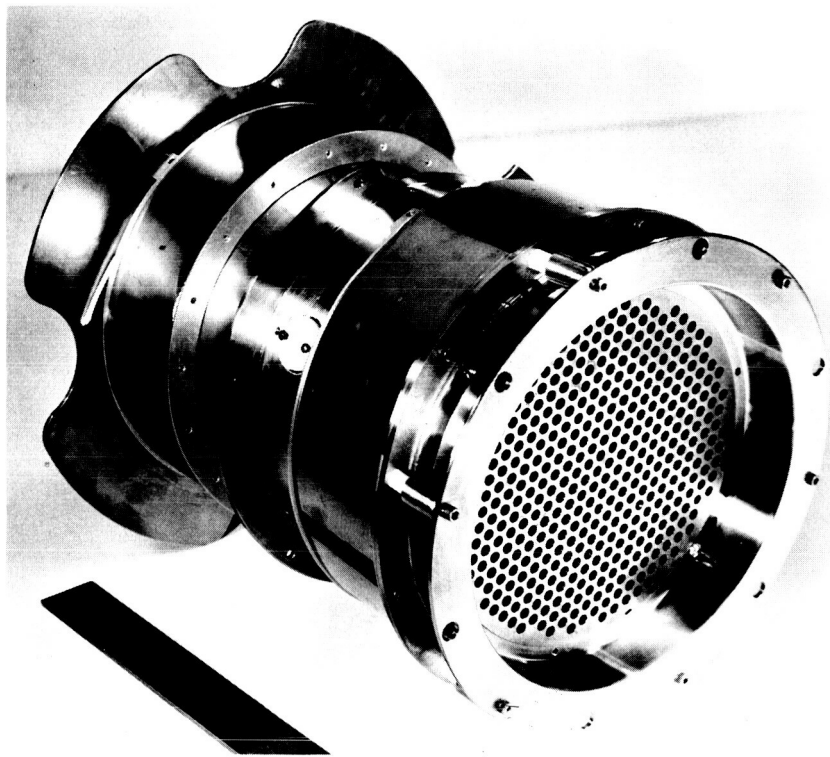
FIG. 2-11 a   MODEL DD ENGINE
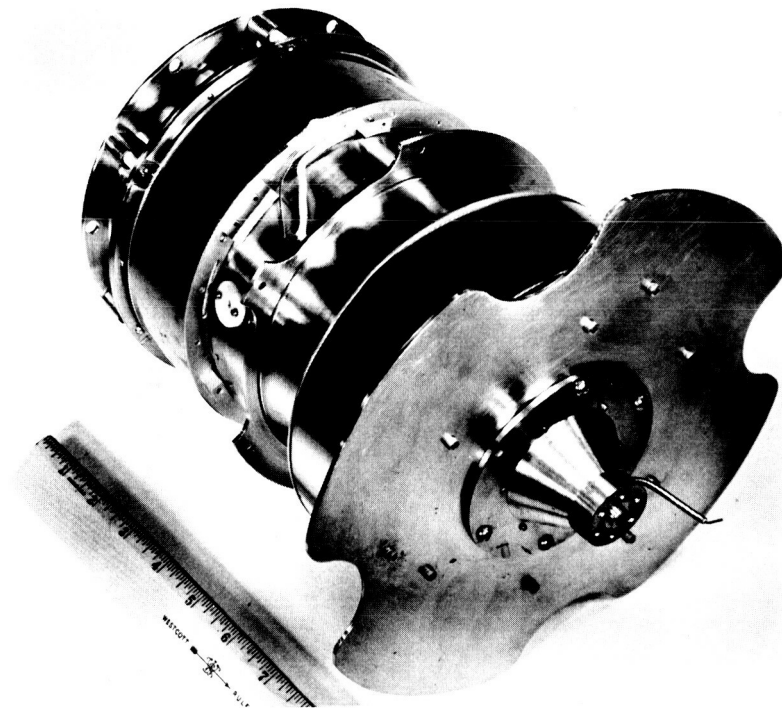
FIG. 2-11 b   MODEL DD ENGINE
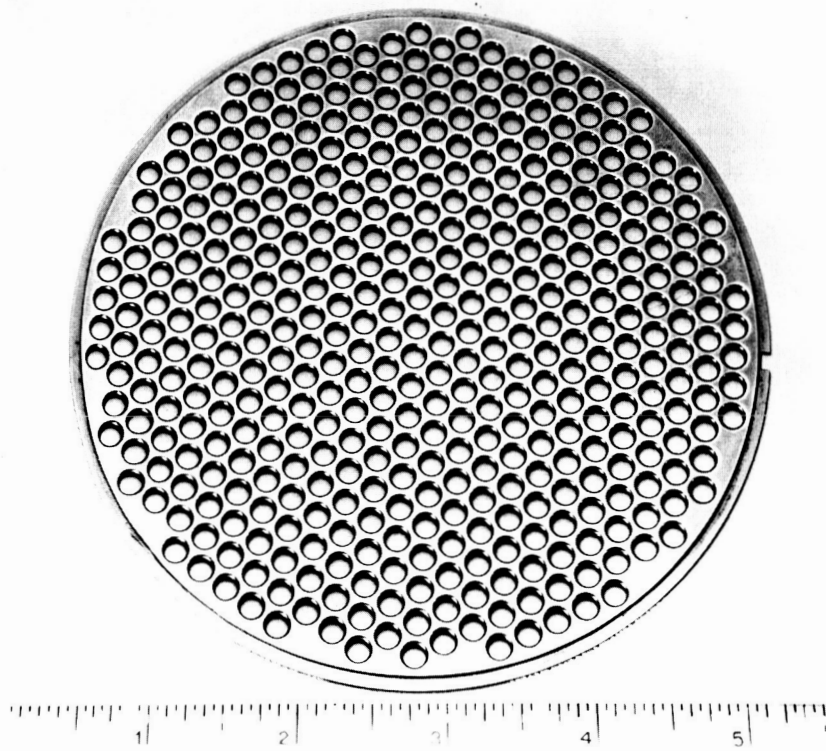
FIG. 2-12   ACCELERATOR ELECTRODE
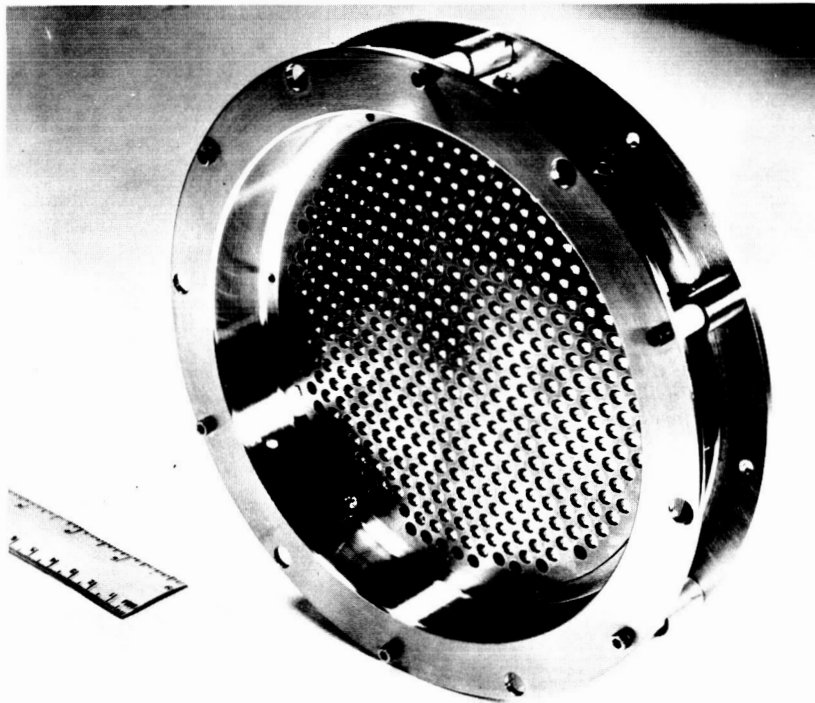
FIG. 2-13   ELECTRODE ASSEMBLY

shown in Fig. 2-10, was found to give the best performance and was adopted for the DD engine. A completely assembled DD engine is shown in Fig. 2-14.

2.2.2 DD Engine Performance

DD engine performance was mapped over a wide range of operating parameters. For these tests a laboratory feed system was used. The electrodes were those shown in Fig. 2-13 with a 0.100 inch gap. Cathode K5B was used for all the tests and the neutral efflux detector was independently calibrated for each feedrate. Detailed data are presented in Table 2-III. At operating temperature the magnet coils have about 1.2 to 1.3 ohms impedance and magnet currents of 1.0 to 1.2 amperes were used. However, for data reduction, a magnet power of 3 watts was used throughout to allow for contact impedances and other extraneous factors.

Figure 2-15a presents mass utilization data in graphic form. It can be seen that the DD engine runs more efficiently at design thrust levels (9 to 12 mlbs) than at lower thrusts. This is also demonstrated in Figs. 2-15b and 2-15c which present the overall engine efficiency and the power-to-thrust ratio as a function of specific impulse. The performance necessary to meet program goals was achieved. At 6550 seconds, 9.12 mlbs thrust was obtained with 1.79 kw power and with 93.5 percent mass utilization. At 7040 seconds, 11.52 mlbs thrust was achieved with 2.31 kw power and with 93.5 percent mass utilization. At a slightly lower mass utilization, 91.5 percent, the design thrust of 0.05 newtons (11.27 mlbs) was obtained at 6890 seconds and a total power of 2.22 kw with a power-to-thrust ratio of 197 kw/lb. Performance of the engine design was therefore considered to be satisfactory.

It is of interest to compare the best operating points obtained with the DD engine with the best performance of the smaller engines. Figures 2-16a, b, and c show the data for a 6.5 cm diameter anode source, a 10 cm source, and the DD engine. There is sufficient
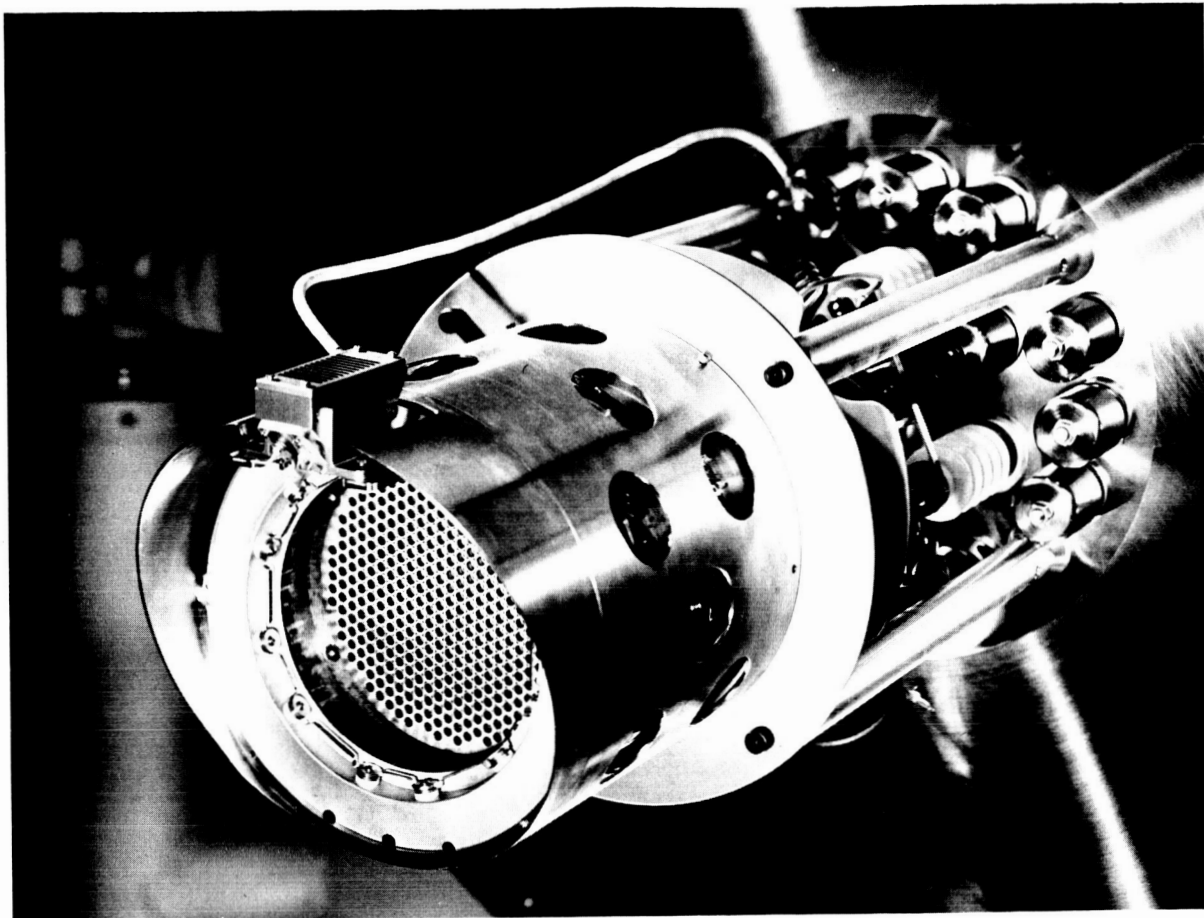
FIG. 2-14   DD ENGINE

TABLE 2-III

ENGINE PERFORMANCE

Positive High Voltage, V_+ (kv)	2.0	2.0	2.0	2.75	2.75
Negative High Voltage, V_- (kv)	1.0	1.0	1.0	1.5	1.5
Negative HV Current, I_- (amp)	0.0035	0.0035	0.0035	0.006	0.006
Beam Current, I_B (amp)	0.200	0.213	0.223	0.325	0.334
Arc Voltage, V_A (volt)	5.9	6.1	6.5	6.3	6.65
Arc Current, I_A (amp)	21.5	25	29.5	40	45
Beam Power, P_B (kw)	0.400	0.426	0.446	0.894	0.919
Drain Power, P_D (kw)	0.011	0.011	0.011	0.026	0.026
Magnet Power, P_M (kw)	0.003	0.003	0.003	0.003	0.003
Arc Power, P_A (kw)	0.127	0.153	0.192	0.252	0.299
Total Power, P_T (kw)	0.541	0.593	0.652	1.175	1.247
Thrust, T (mlb)	3.37	3.58	3.75	6.41	6.59
Power to Thrust, P/T (kw/lb)	161	165	174	183	189
Power Efficiency, η_p (percent)	74 %	72 %	68.5 %	76 %	73.5 %
Mass Efficiency, η_M (percent)	82.5 %	88 %	92 %	89 %	92 %
Overall Engine Efficiency, η_E (percent)	61 %	63 %	63 %	67.5 %	67.5 %
Specific Impulse, I_{sp} (sec)	4540	4840	5060	5740	5930
Ratio of Drain Current to Beam Current, I_-/I_B (percent)	1.75%	1.65%	1.6%	1.8%	1.8%
Source Energy per Ion, P_A/I_B (kev/ion)	0.635	0.720	0.860	0.775	0.895

TABLE 2-III (Continued)

ENGINE PERFORMANCE

V_+ (kw)	3.25	3.25	3.25	3.25	3.25	3.25	3.5
V_- (kw)	1.2	1.2	1.2	1.2	1.2	1.2	0.65
I_- (amp)	0.009	0.009	0.009	0.009	0.009	0.009	0.006
I_B (amp)	0.397	0.412	0.415	0.420	0.425	0.429	0.299
V_A (volt)	5.8	6.2	6.2	6.8	6.7	7.2	6.8
I_A (amp)	45	50	50	55	55	60	32
P_B (kw)	1.290	1.339	1.349	1.365	1.381	1.394	1.042
P_D (kw)	0.040	0.040	0.040	0.040	0.040	0.040	0.025
P_M (kw)	0.003	0.003	0.003	0.003	0.003	0.003	0.003
P_A (kw)	0.261	0.310	0.310	0.374	0369	0.432	0.218
P_T (kw)	1.594	1.692	1.702	1.782	1.793	1.869	1.288
T (mlb)	8.52	8.84	8.90	9.01	9.12	9.20	6.65
P/T (kw/lb)	187	191	191	198	197	203	193
η_p (percent)	81 %	79 %	79.4%	76.4 %	77 %	74.5%	81 %
η_M (percent)	87.5%	90.5 %	91.5 %	92.5 %	93.5 %	94.5%	93 %
η_E (percent)	71 %	71.4 %	72.5 %	71 %	72 %	70.5 %	75 %
I_{sp} (sec)	6130	6340	6410	6480	6550	6620	6720
I_-/I_B (percent)	2.3 %	2.2 %	2.2 %	2.1 %	2.1 %	2.0 %	2 %
P_A/I_B (kev/ion)	0.660	0.750	0.745	0.890	0.870	1.010	0.730

TABLE 2-III (Continued)

ENGINE PERFORMANCE

V_+ (kw)	3.75	3.75	3.75	3.75	3.75	3.75	4.5
V_- (kw)	1.0	1.0	0.87	0.87	0.87	0.87	0.48
I_- (amp)	0.0135	0.0135	0.010	0.010	0.010	0.010	0.009
I_B (amp)	0.503	0.5145	0.438	0.470	0.489	0.500	0.391
V_A (volt)	6.0	6.4	5.5	5.75	6.15	6.4	7.15
I_A (amp)	58	64.5	45	50	55	60	37
P_B (kw)	1.886	1.929	1.643	1.763	1.834	1.875	1.760
P_D (kw)	0.064	0.064	0.046	0.046	0.046	0.046	0.045
P_M (kw)	0.003	0.003	0.003	0.003	0.003	0.003	0.003
P_A (kw)	0.348	0.413	0.248	0.288	0.338	0.384	0.265
P_T (kw)	2.301	2.409	1.940	2.100	2.221	2.308	2.073
T (mlb)	11.59	11.86	10.09	10.83	11.27	11.52	9.85
P/T (kw/lb)	199	203	192	194	197	200	210
η_n (percent)	82 %	80 %	84.5 %	84 %	82.5 %	81 %	85 %
η_M (percent)	90.5 %	92.5 %	85 %	88 %	91.5 %	93.5 %	91.5 %
η_E (percent)	74 %	74 %	69 %	74 %	75.5 %	75.5 %	78 %
I_{sp} (sec)	6800	6950	6175	6625	6890	7040	7550
I_-/I_B (percent)	1.8 %	1.75 %	2.3 %	2.1 %	2.0 %	2.0 %	2.3 %
P_A/I_B (kev/ion)	0.690	0.805	0.565	0.615	0.690	0.770	0.680
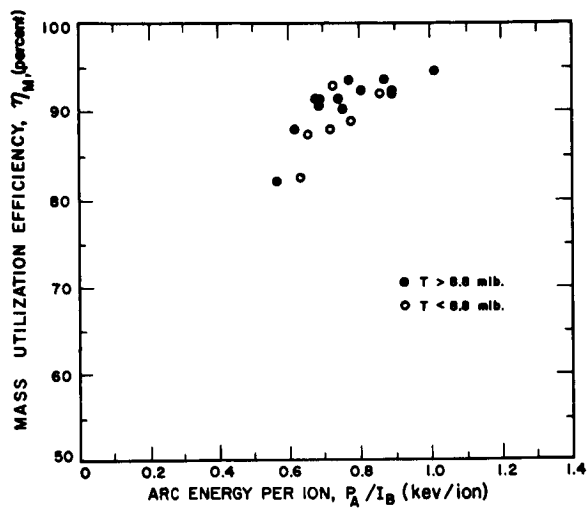
a

MASS UTILIZATION VS SOURCE
ENERGY PER ION
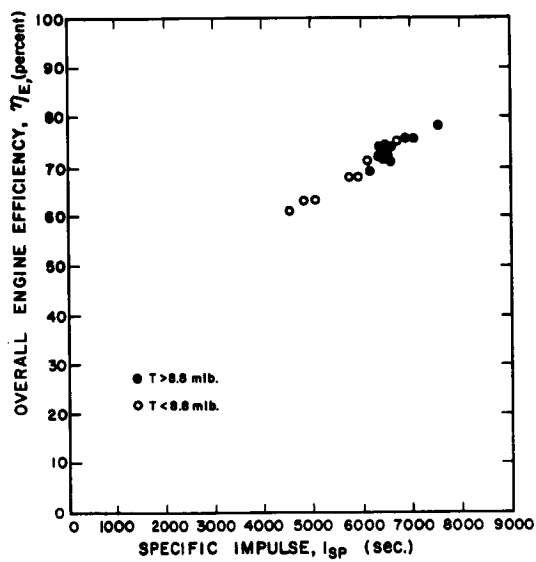
b

OVERALL ENGINE EFFICIENCY
VS SPECIFIC IMPULSE

c
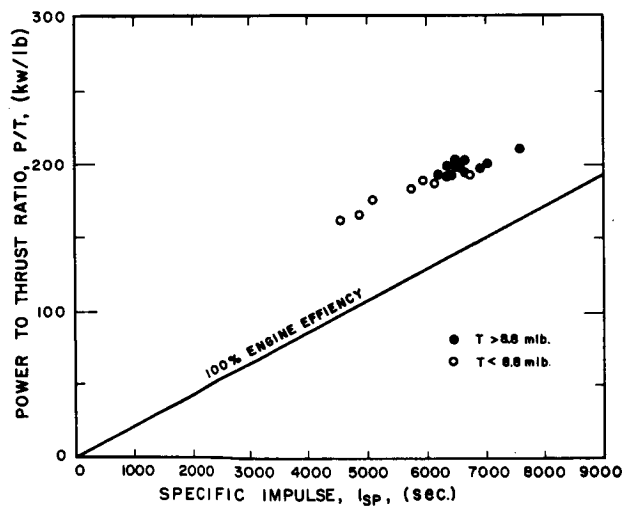
POWER TO THRUST RATIO VS
SPECIFIC IMPULSE

FIG. 2-15   DD ENGINE PERFORMANCE
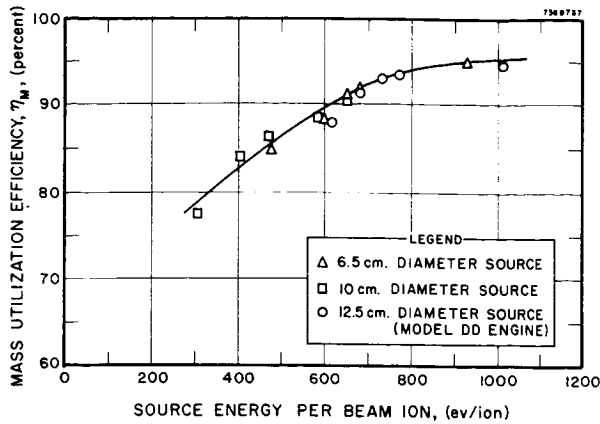
a

MASS UTILIZATION VS SOURCE ENERGY
PER ION
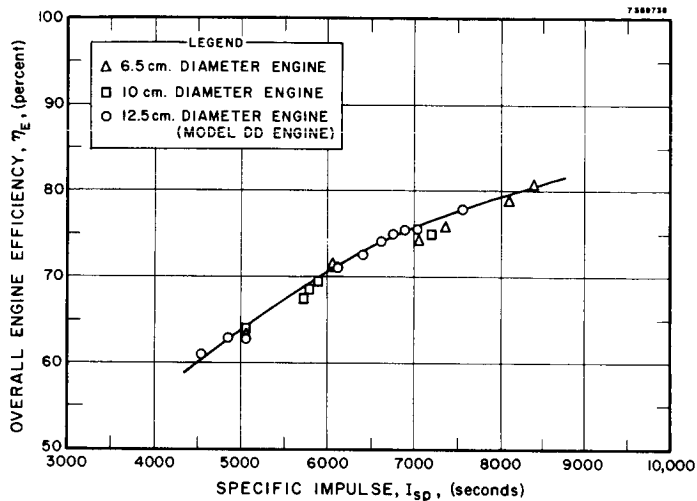
b

OVERALL ENGINE EFFICIENCY VS
SPECIFIC IMPULSE

c
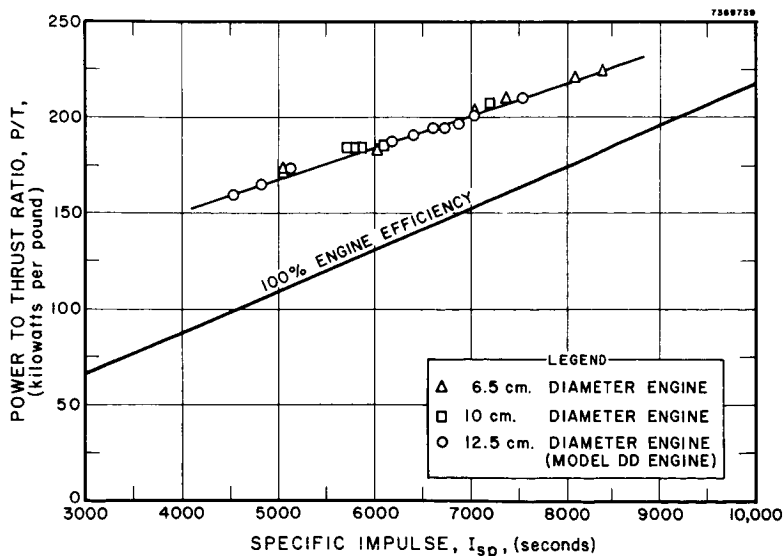
POWER TO THRUST RATIO VS
SPECIFIC IMPULSE

FIG. 2-16   COMPARISON OF DD ENGINE PERFORMANCE WITH SMALLER SOURCES

overlap of the operating ranges to demonstrate the identical performance of the various sources although in each case the cathode and electrode configurations found to be most suitable for the individual sources were used.

2.3 Applied Research

The DD engines were used in conjunction with an applied research program to determine and develop engine design parameters.

2.3.1 Chamber Configuration

A movable cathode plate modification of the DD engine was tested to determine the effect of arc chamber length on engine performance. The system was operated at the design length of 7-1/2 inches and with the chamber shortened to 4-1/2 inches by moving the cathode plate forward. Arc characteristics, beam probe, traces, extrusion limits, and some neutral efflux measurements were taken at different mass flow rates and magnetic fields.

While arc power was lower at low mass utilization with the short chamber, it was very difficult to achieve high values of mass utilization efficiency. At high mass utilization (>80 percent) the shortened system required 20 to 50 percent more arc power, other parameters being equal for the two cases. The extrusion limit was much more sensitive to the magnetic field for the short chamber. While high mass and power efficiencies could be obtained at high magnetic fields, the beam current was limited to about 85 percent of that obtainable for the same accelerating voltages with the 7-1/2 inch chamber.

As would be expected, for a given density and magnetic field, the arc impedance was found to be higher for the shorter chamber. However, the mass utilization efficiency was lower as might be predicted since a neutral spends less time in the chamber before exiting. The effect of the high magnetic fields in limiting the beam current and the desire for high values of mass utilization leads to the choice of the longer chamber configuration.

The extrusion limit mentioned above is determined by the shape of the plasma sheath at the screen apertures. When the arrival

rate of ions at the screen aperture exceeds the rate at which ions can be extracted in a focused beam the plasma protrudes into the accelerating gap and high drain currents are encountered. The use of higher accelerating voltages raises the extrusion limit. In uniform geometry electrode systems, extrusion always occurs at the center of the electrodes since the plasma is most dense at that region.

The reason that increasing the magnetic field lowers the extrusion limit is simply that higher magnetic fields make the plasma density distribution more peaked in the center of the electrode system.

DD Engine Operating Temperatures

A DD engine was instrumented with thermocouples and temperatures during operation were observed. Typical results are presented in Fig. 2-17. These data were taken with 250 to 300 watts arc power being dissipated in the chamber. As can be seen, the temperatures are moderate and present no material problems. Resistive heating of the anode lead is responsible for the higher anode temperature measured near that point.

2.3.2 Magnetic Field

The effect of the magnetic field configuration was investigated. The axial component of the magnetic field in the discharge chamber of the DD engine was mapped as a function of axial position in the source. This was done for positions on the axis (Fig. 2-18a) and near the anode (Fig. 2-18b). The field intensity for one ampere current in the rear coil is presented with the ratio of current in the front coil to that in the rear coil as a parameter.

There was little change in engine characteristics or performance as the ratio of the coil currents was varied for an operating engine. The field at the rear of the engine limits the current emission of the autocathode and, as can be seen in Fig. 2-18a, is almost independent of the current in the front coil. Increasing the field at the rear of the engine reduced the arc current. Varying the current in the front coil had much less effect on the arc current and appeared to change beam extraction only slightly with a small reduction for divergent fields.
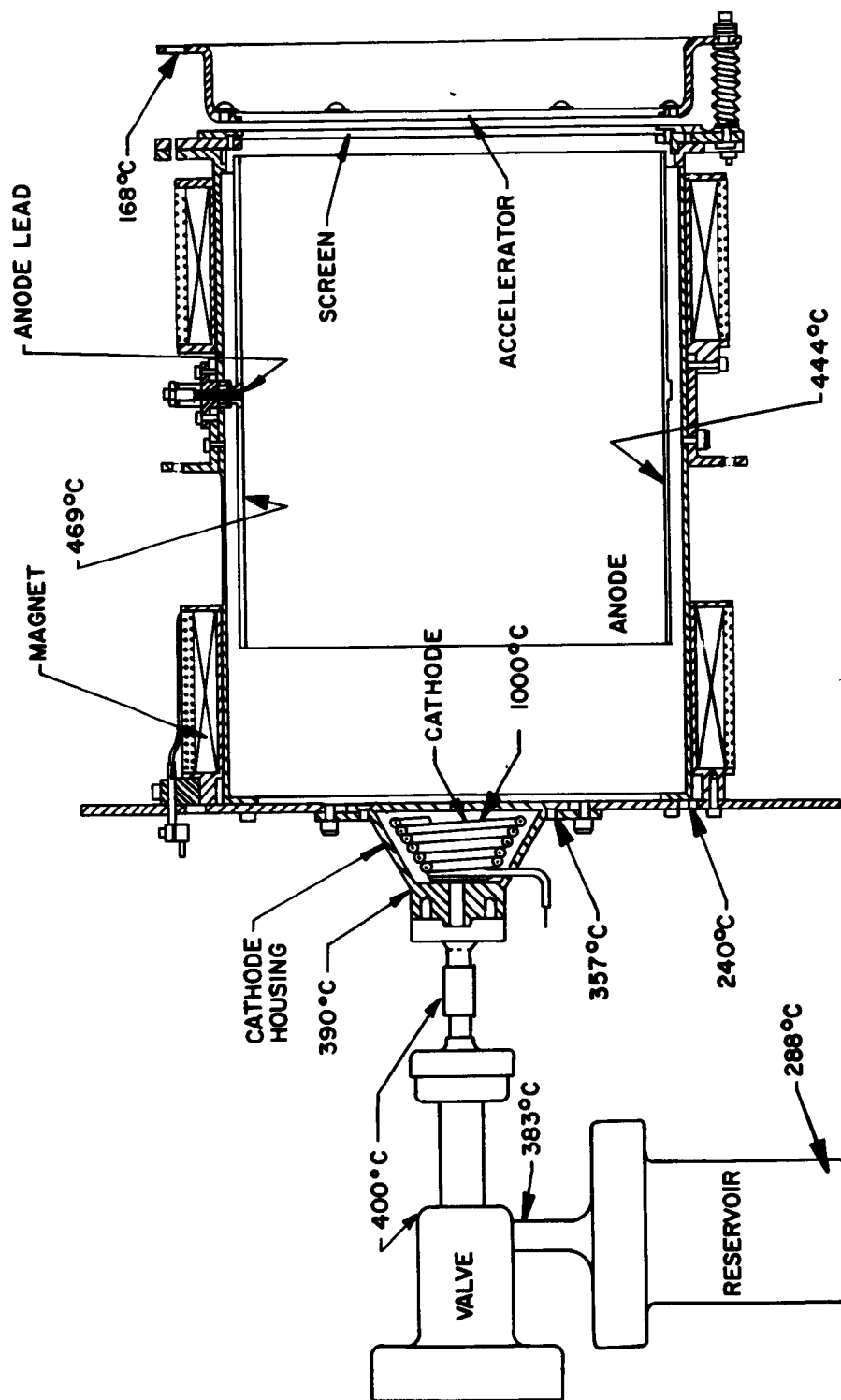
FIG. 2-17 DD ENGINE OPERATING TEMPERATURES
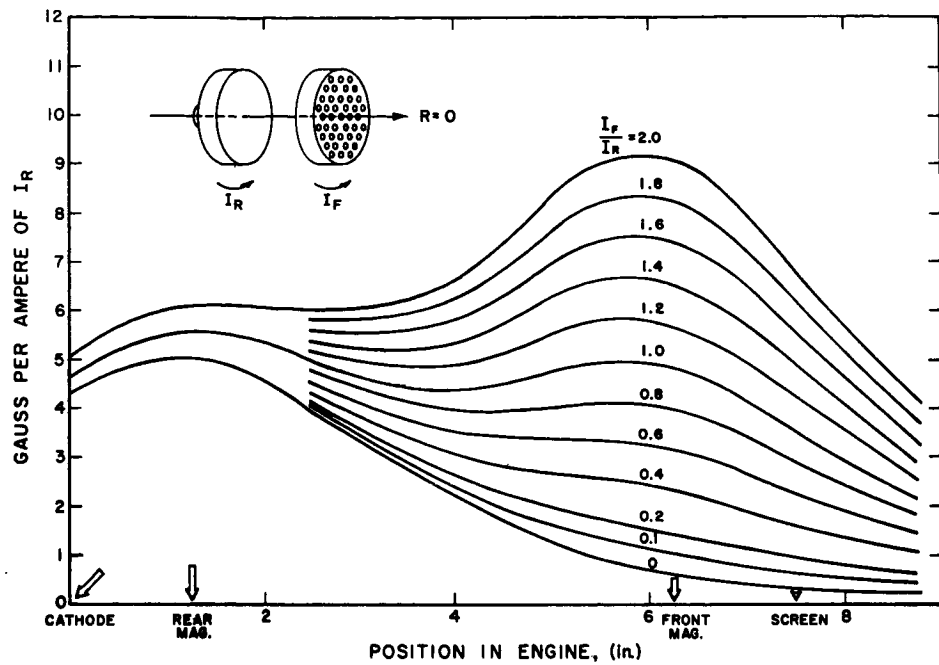
FIG. 2-18a   AXIAL MAGNETIC FIELD COMPONENT ON AXIS
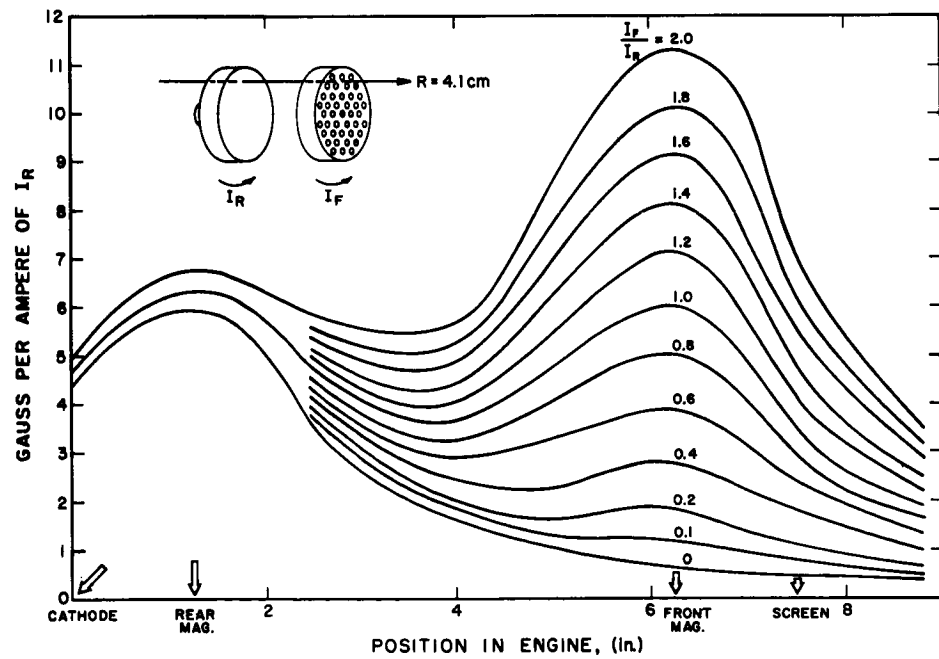
FIG. 2-18b   AXIAL MAGNETIC FIELD COMPONENT NEAR ANODE

The indications are that the arc current, as established by diffusion of electrons out of the autocathode, is limited by the magnetic field in that region, as well as by thermionic emission limitations due to the autocathode temperature and degree of cesium coverage.

As indicated in Section 2.1, the magnetic field must be sufficient to prevent primary electrons, entering the plasma from the cathode, from reaching the anode. At higher fields the plasma density distribution becomes more peaked. It has been observed that with some cathode configurations, the arc current decreases with increasing magnetic fields (Ref. 2). This is apparently due to autocathode effects, since, as will be shown, the effect on the diffusion of plasma electrons to the anode should be small.

The radial electron current density, as regulated by diffusion across the magnetic field, is

$$j_e = -e \, D \, \frac{dn_e}{dr}$$

where D is the diffusion coefficient. The density gradient varies with the magnetic field in an inverse manner to that by which the diffusion coefficient depends on the magnetic field. This can be understood by considering the diffusion equation

$$D \, \frac{1}{r} \, \frac{d}{dr} \, (r \, \frac{dn_e}{dr}) \, + \, \nu_p n_p \, = \, 0 \tag{6}$$

where the quantities are as identified in Section 2.1.1 and the term $n_e n_o \overline{\sigma v}$ is neglected since it is small compared to $\nu_p n_p$.

If we assume $D = D_o f(B)$ where $f(B)$ is dependent only on the magnetic field and D_o is independent of the magnetic field, we have, by rearrangement and integration,

$$\frac{dn_e}{dr}\bigg|_{r=A} = -\frac{1}{Af(B)}\int_0^A \frac{r\nu_p n_p\, dr}{D_o} \tag{7}$$

so that

$$j_e(A) = -eD_o f(B)\left(-\frac{1}{Af(B)}\int_0^A \frac{r\nu_p n_p\, dr}{D_o}\right) \tag{8}$$

$$= \frac{eD_o}{A}\int_0^A \frac{r\nu_p n_p\, dr}{D_o} \tag{9}$$

In the above treatment the magnetic field is assumed to be independent of radius and the rate at which primary electrons join the plasma electron distribution is assumed to be independent of the magnetic field. The derivation indicates that the dependence of the arc current on the magnetic field should be small unless the autocathode operation is affected by the magnetic field.

In the DD engine configuration, it has been observed that at low magnetic fields the beam current varies more than the arc current as the magnetic field is changed. At zero field the beam current is very low, about 10 percent of the feedrate. As the field is increased, the beam current increases to about 90 percent of the feedrate and thereafter has very little dependence on the magnetic field. This is interpreted as the increased containment of primary electrons in the chamber (prevention of their reaching the anode) so that they join the plasma electron distribution. This maintains the electron temperature and increases the plasma density and ionization rate. Since increasing the plasma density raises the power delivered to the autocathode, the arc current can also increase as the magnetic field is raised.

The radial plasma distribution arises from the fact that as the magnetic field is increased, the plasma density gradient becomes larger and the distribution is more peaked in the center.

2.3.3 Electrode Geometry

One of the problems of electrode design is that of providing thermal-mechanical stability of a large diameter electrode and preventing warping or bowing due to differential thermal expansion. Relatively thick accelerating electrodes are found to be suitable for the extraction of beams with low interception but the screen electrode presents a problem. At the current densities for which the DD engine is operated, a thin screen electrode has been found to be most suitable with respect to minimizing direct ion interception and transient breakdowns.

Figure 2-19 presents some extraction geometries which have been studied. The thin electrode configuration is shown in Fig. 2-19a. If mechanical stability is achieved by making the screen electrode thicker, the situation shown in Fig. 2-19b obtains and the interception due to the defocusing parts of the sheath provide large drains.

The divergent design of Fig. 2-19c is indeed strongly focusing at low current densities but it has been found that at high current densities the situation as shown in the figure provides large drain currents. Figure 2-19d shows a design which provides plasma sheath conditions similar to that of the thin screen electrode and the desired mechanical stability.

Of the other factors that may play a large role in the experimental comparisons of these geometries, the effective, accelerating gap length is certainly significant. From a transient breakdown viewpoint for operation with cesium, the closest approach of the two electrodes is a significant parameter. For all other factors taken equal, the highest perveance should be obtained with the geometry of Fig. 2-19d. To date this has been found to be the case. The drains approached 10 percent at total beams of 1/4 amp for the geometries of Figs. 2-19b and 2-19c. Five percent drains at 1/2 amp were obtained with the geometry of Fig. 2-19d. Accordingly, the geometry of Fig. 2-19d was adopted for most engine tests as it provides operation comparable to that of a thin

A
PLASMA
SCREEN ACCEL
THIN SCREEN ELECTRODE
Cs⁺
SHEATH

B
PLASMA
SCREEN ACCEL
THICK SCREEN ELECTRODE
Cs⁺
SHEATH

C
PLASMA
SCREEN ACCEL
DIVERGENT SCREEN ELECTRODE
Cs⁺
SHEATH

D
PLASMA
SCREEN ACCEL
CONVERGENT SCREEN ELECTRODE
Cs⁺
SHEATH
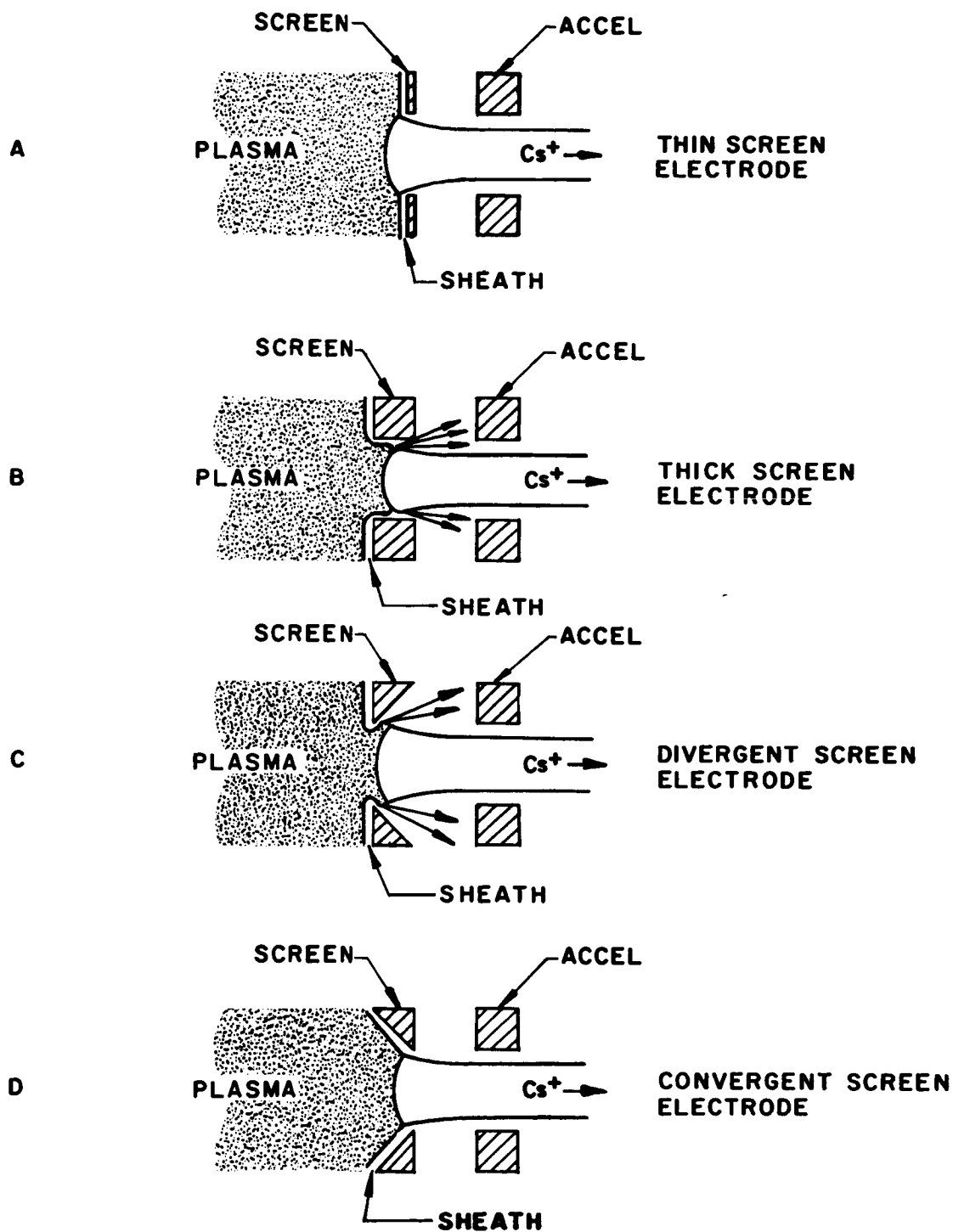
FIG. 2-19   ION EXTRACTION GEOMETRIES

screen electrode with thermal mechanical stability.

Ion Optics and Plasma Density Distribution

The nonuniformity of the plasma density across the diameter of a source creates major ion optics problems. If the electrode potentials are adjusted for good focusing from apertures near the center of the source, the arrival rate of ions at the plasma sheaths of the apertures near the periphery of the source will be too low and sheath shapes leading to poor focusing will result.

There are several approaches to this problem. The sheath shapes might be controlled somewhat by forcing them to follow a fine mesh screen of the desired shape mounted in the screen electrode apertures. However, even with a high transparency, such a screen would provide surfaces for ion adsorption and neutral emission. While such an approach would involve fabrication problems which might compromise the basic simplicity of construction of a gas discharge engine, it remains a possibility.

A more sophisticated electrode geometry provides a most interesting approach to the problem. Given the radial plasma density distribution of a source, the ion optics could be improved by varying the size of the apertures and gaps of the electrode geometry to provide a perveance per unit area which varies radially in the same way as the ion density in the source. The perveance per aperture would be the same for central or peripheral apertures and so would the relative shapes of the plasma sheaths. The total geometry, however, would be scaled to match the ion density distribution.

This method of improving optics over the entire source was investigated experimentally. Preliminary investigations with the 10 cm engine were made, using a Faraday probe to map the ion beam current density. The probe had an 0.002 cm^2 aperture and was located six centimeters downstream from the accelerator electrode.

The probe was driven through a nonlinear linkage by a drive which held its speed constant within 10 percent. The probe

current was measured on a strip-chart recorder which ran at a constant speed of 2 inches per minute. Typical strip-chart traces are presented in Fig. 2-20.

The objectives of the preliminary tests were to investigate the effect of varied cathode orifice plate geometry on the plasma density distribution at the screen electrode and to determine the requirements for design of a better probe system.

The 10 cm engine was run at 4 kv net accelerating potential using two different cathode orifice plates on a basic K5 cathode assembly. The two orifice plates used are shown in Fig. 2-21. Cathode K5B had a single 3/16-inch center hole and K5C had six 1/8-inch holes evenly spaced on a 1.32-inch diameter. The expected effect of cathode K5C was to increase the peripheral beam density thus flattening out the beam profile as observed with the Faraday cup. The raw data for these two runs is shown in Fig. 2-20. Total beam currents were about 120 ma. The copper probe heated excessively at higher beam currents.

The data were first converted from a time base to a distance base since a non-linear drive between the near-constant-speed source and the probe resulted in the skewing of the curves recorded on the strip-chart recorder. The corrected data were then numerically integrated over the area of the beam to check the total of this integral against the measured beam current I_B. Ideally the relation

$$I_B = \frac{1}{A_p} \int_o^a I_p 2\pi r \, dr \qquad (10)$$

should hold true, where I_p is the current to the probe, r is the radius, and A_p is the probe aperture area. Agreement was found within about 10 percent, some error being due to a change in the recorder gain between runs and lack of knowledge of the exact aperture area (the probe used had an aperture with a sharp edge which had sputtered open somewhat during use). To allow comparison of the data from the two runs, the
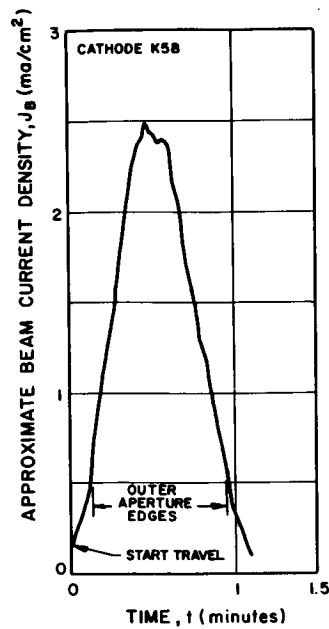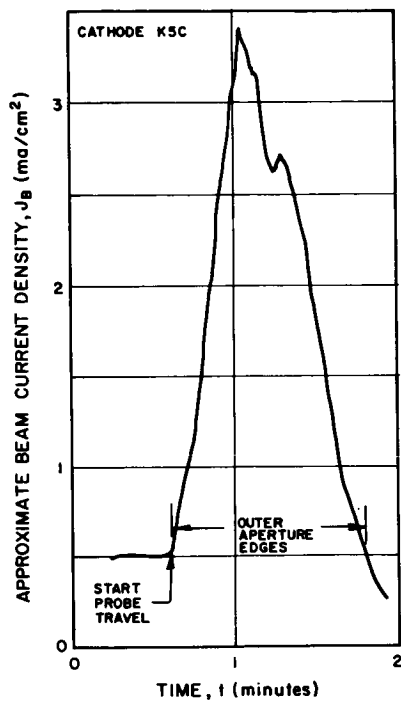
FIG. 2-20   FARADAY CUP BEAM PROBE DATA
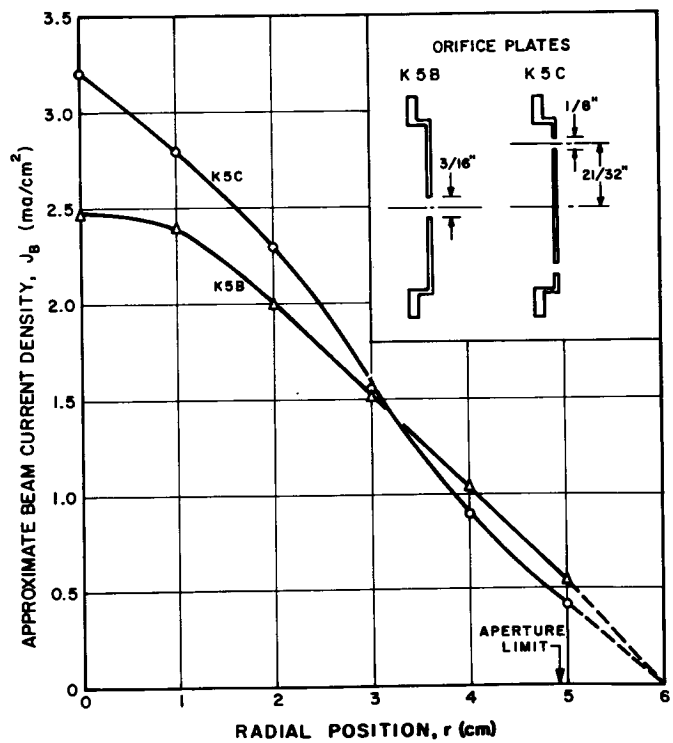
FIG. 2-21   BEAM DENSITY PROFILES

data for cathode K5C were reduced to make their current-area integral equal to that of the data for cathode K5B. The data corrected in this fashion are shown in Fig. 2-21.

These curves indicate that the effect of the six-hole orifice plate was to sharpen the beam profile rather than to flatten it as anticipated. In view of the corrections required and the skewed curve shape, these results were not considered conclusive.

It is of interest to note that the variation of the beam density is so close to being inverse with the radius that the contributions to the total beam of each annular region of area $\Delta A = 2\pi R\ \Delta R$ are about equal. This means that even with this very peaked distribution, the peripheral apertures contribute significantly to the total beam. The relatively large distance of the probe from the engine does allow an individual beam spreading factor to become significant in peaking the total beam profile. Probe measurements made closer to the exit plane would be expected to show a less steep profile.

The experiment yielded good design requirements for an improved probe system which was fabricated and used in further tests.

The profile shown in Fig. 2-22 is typical of measurements with the improved probe. The individual peaks correspond to electrode apertures but symmetry is reduced since the probe motion was at a slight angle to the line of apertures. Also, the probe did not scan a row of close-spaced apertures but instead alternately scanned an aperture and then scanned between two apertures, reading the overlapping beams in the latter case.

Using data from probe traces such as those of Fig. 2-22, the varied geometry concept was pursued and an electrode system designed on that basis. The concept is based on scaling the electrode geometry so that the perveance per unit area at any radial position is proportional to the plasma density. The objective is to provide the same focusing conditions at the periphery of the engine as at the center for the radially decreasing plasma densities encountered in this type of source.
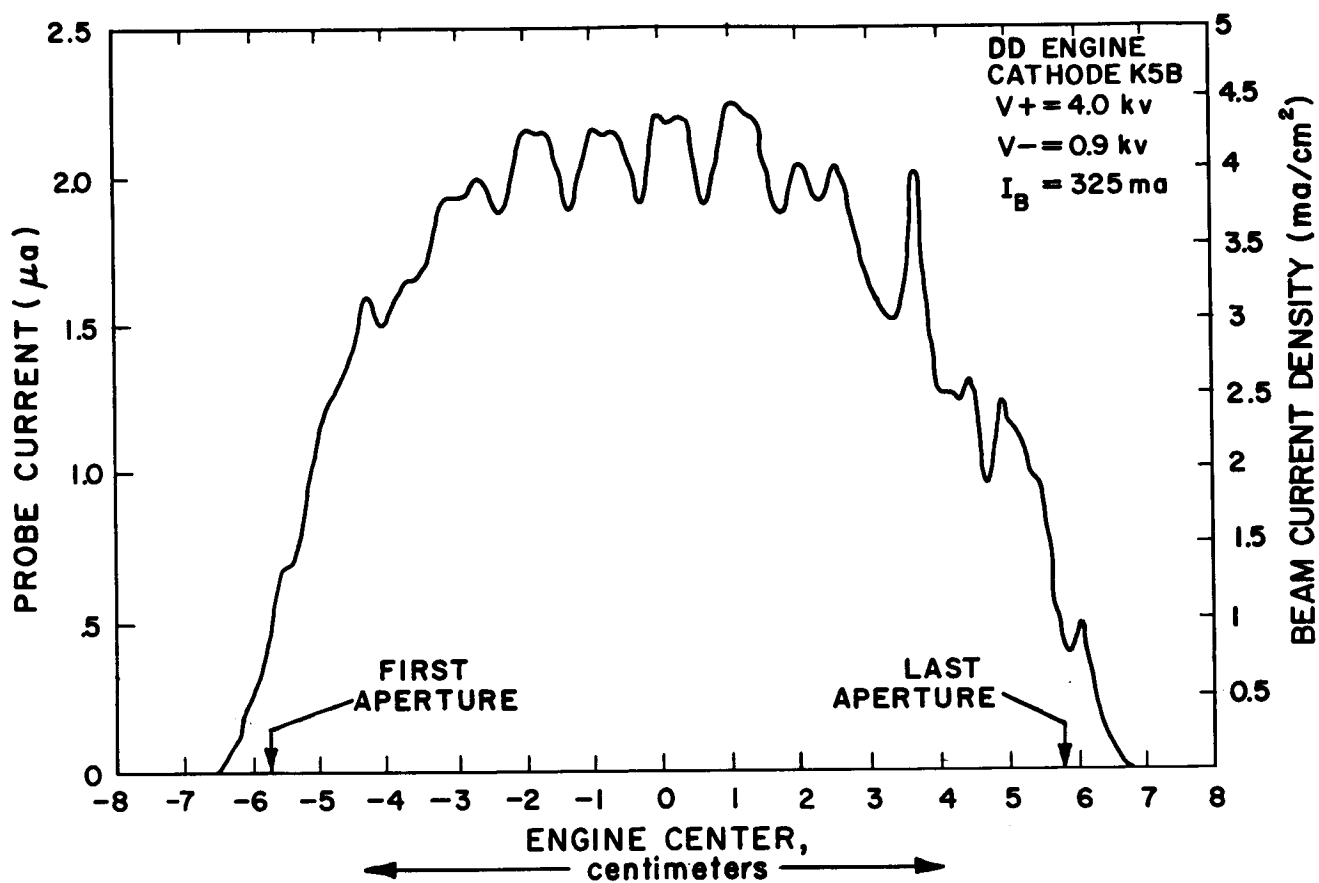
FIG. 2-22   BEAM DENSITY DISTRIBUTION

A design curve is shown in Fig. 2-23a. A simple ion density distribution in the source has been assumed but this approximates the results of beam mapping with a Faraday probe. The derived design curve is a scale factor pertaining to both the aperture diameter and the accelerating gap as a function of radius, both referenced to the geometry of the central apertures. This design curve can itself be approximated with straight segments. The resulting electrode design for the DD engine is shown in Fig. 2-23b. This electrode system was fabricated and is shown in Figs. 2-24a and 2-24b.

The distributed geometry electrodes were operated with the DD1 engine. With no masking the electrodes operated with an accel drain current of about 2 percent of the beam current, comparable to the regular electrode system. It did appear, however, that when plasma extrusion occurred, it was fairly uniform over the entire source rather than at the center as with the regular electrodes.

When the outer two rows of apertures were masked off, the drain current dropped to about 1 percent of the beam current. This is believed to be due to the reduction of interception of the periphery of the beam by the accelerating electrode support structure of the DD system and is consistent with results with the regular electrodes.

Masking of the outer two rows reduced the number of apertures by 22 percent (from 361 to 281) and appeared to reduce the total perveance of the system by the same amount. Figure 2-25 shows some plots of beam current versus total voltage across the accelerating gap. At the design spacing it appears that the geometry is well matched to the plasma distribution and an unambiguous dependence of the current on the 3/2 power of the voltage is observed. For these measurements the current level just prior to plasma extrusion is used. When the spacing is reduced, the perveance of the central apertures is increased more than that of the outer apertures and the electrode system no longer matches the plasma density distribution. In this case a clear-cut value of the "perveance" does not exist as indicated in the uppermost curve of Fig. 2-25.
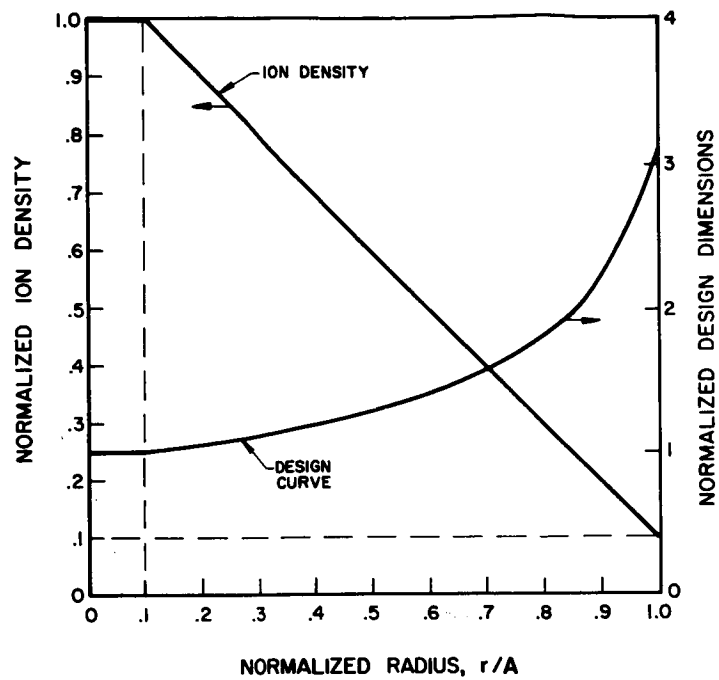
FIG. 2-23a

DESIGN CURVE FOR VARIED
GEOMETRY ELECTRODES

FIG. 2-23b

VARIED GEOMETRY
ELECTRODE DESIGN
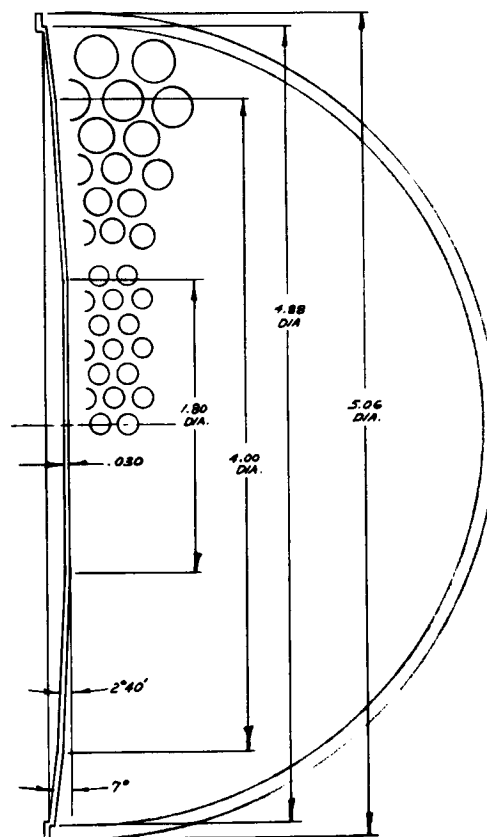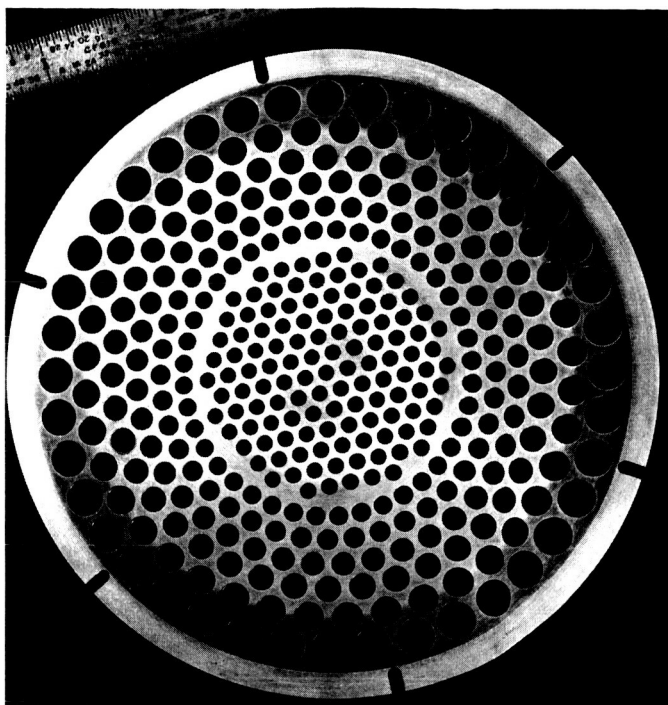
a
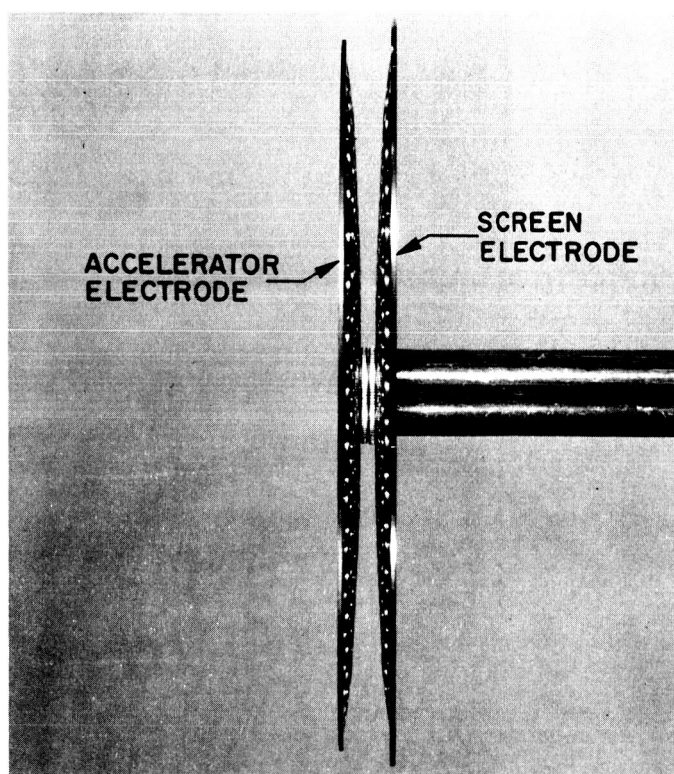
b

FIG. 2-24   DISTRIBUTED GEOMETRY ELECTRODE SYSTEM

The lowest curve on Fig. 2-25 gives the current per aperture for data taken at the design spacing with and without the mask. The perveance per aperture of 1.8×10^{-9} amp/volt$^{3/2}$ calculated from this curve is in good agreement with simple design calculations.

Tests of the distributed geometry electrode system were continued with a modification to permit the attainment of higher perveance. The curved accel electrode was replaced with a flat electrode with apertures machined to match those in the curved screen electrode. The use of the flat accel plate with the distributed geometry screen electrode allowed the reduction of the design gap. This new geometry had a perveance per unit area which varied radially in fair approximation to the plasma density. The results are shown as curve B of Fig. 2-26. In this figure the extent of the curves show the ranges over which measurements were made.

Curve E of Fig. 2-26 is included to show that at an arbitrary gap setting the dished-flat electrode system does not exhibit an unambiguous value of the perveance. Curves A, B, C, and D follow the $I \propto V^{3/2}$ relation very closely. As in Fig. 2-25, the data for Fig. 2-26 were taken by determining the beam current level just prior to plasma extrusion.

The apertures in the central portion of the distributed geometry screen electrode were then tapered to provide plasma sheath conditions approximating those of a thin electrode and the data of curves C and D were taken. Table 2-IV summarizes the results of the investigations. The most significant result is that the dished-flat electrode system with its smaller design gap exhibits about twice the perveance of the system with both electrodes dished.

While it is clear that this approach to electrode design successfully solves the plasma density distribution problem, the distributed electrode system was not superior to the regular electrodes with respect to drain currents. The total beam handling capacity of the
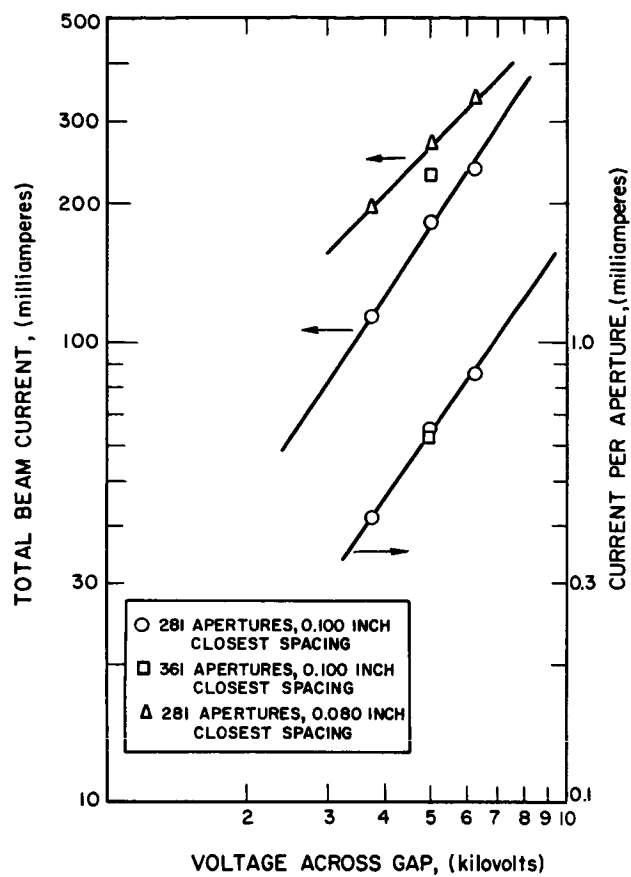
FIG. 2-25

BEAM CURRENT NEAR EXTRUSION VS
TOTAL ACCELERATING VOLTAGE
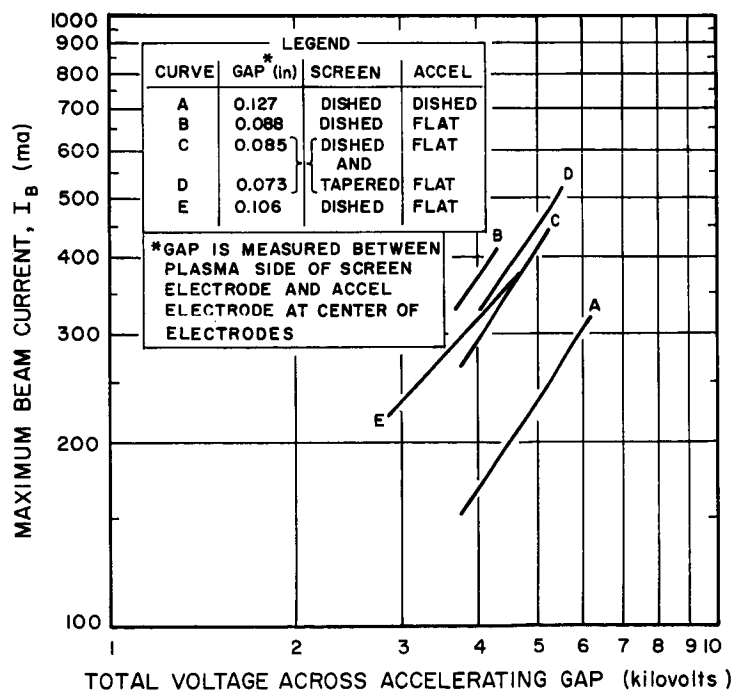
FIG. 2-26

DISTRIBUTED GEOMETRY ELECTRODE
SYSTEM EXTRUSION DATA

TABLE 2-IV

DISTRIBUTED GEOMETRY ELECTRODE PERVEANCE DATA

	CONFIGURATION			
	A	B	C	D
Accelerating Gap (inches)	0.127	0.088	0.085	0.073
Screen Electrode	dished	dished	dished and tapered	dished and tapered
Accelerating Electrode	dished	flat	flat	flat
Total Perveance (361 apertures)(10^{-6}amp/volt$^{3/2}$)	0.66	1.47	1.17	1.28
Perveance per Aperture (10^{-9}amp/volt$^{3/2}$)	1.8	4	3.2	3.5
Current per Aperture at 5 kv across gap (ma) (V_+ = 3.75 kv, V_- = 1.25 kv)	0.64	1.4	1.14	1.25
Total Current at 5 kv across gap (ma)	230	507	410	450
Current Density through Central Apertures of Screen Electrode (ma/cm^2)	8.0	17.6	14.3	15.7

distributed geometry electrode system was at best comparable to that of the uniform geometry flat electrodes. For example, with operating voltages of 3.75 kv for V_+ and -1.0 kv for V_-, the uniform geometry electrodes (421 apertures of 0.172-inch diameter each) can handle a total beam of over 500 ma with a gap spacing of 0.100 inch. However, the space factor or ratio of aperture area to total area is somewhat higher for the uniform geometry electrodes and the perveance of the central apertures is enhanced somewhat by the smaller apertures of the accel electrode (0.157-inch diameter).

It appeared feasible to take advantage of the bowed screen electrodes enhanced thermal-mechanical stability and a very moderate version of the distributed geometry electrode concept was adopted for the DE engine (Section 2.4).

2.3.4 Neutralizers

The first neutralizer system designed for the DD engine was made of oxide-coated nitung ribbon coated with RCA C-131. This combination had been found to have a particularly low activation temperature and high stability of the oxide layer. A difficulty with the oxide-coated nitung ribbon-type neutralizer, however, is the structural distortion caused by the high thermal expansion of the material. The neutralizer must be in close proximity to the beam edge but if it distorts into the beam the neutralizer is sputtered away. A small local reduction in cross section is sufficient to provide a hot spot which leads to the loss of the neutralizer.

For the above reason, and in order to obtain more efficient neutralizers, a study of various thermionic emitters was undertaken. The four cathodes studied were a vane loaded cavity cathode, a sponge nickel button cathode, a nitung sleeve cathode, and a sintered nickel matrix cathode purchased from EIMAC of San Carlos, California. The results obtained with each of these are discussed below.

Vane Loaded Cavity Cathode

This cathode consisted of a cylindrical cavity, approximately 1/2-inch in diameter by 1/2-inch deep, into which radial vanes of nickel were inserted. A tantalum-clad tantalum heater wire was wound about the cavity. Heat shielding and a mounting bracket were attached to the cavity cylinder as shown in Fig. 2-27a. The surfaces within the cavity were coated with Baker Chemical R-500, a barium and strontium carbonate suspension. The cavity cathode was activated at a temperature of $1000^\circ C$ to $1100^\circ C$.

In the tests a planar anode was placed 0.080 inch from the cathode and the data presented in Fig. 2-27a were taken. The best performance as shown was at approximately 2.5 milliamperes per watt with 100 milliamperes per square centimeter at 200 volts plate voltage. Plate heating and insufficient plate supply power prevented operation at higher currents and voltages in this test--consequently the emission limited portion of the characteristic was not achieved.

Sponge Nickel Button Cathode

This cathode consisted of a 1/2-inch diameter sponge nickel button soaked in Baker-500 and pressed by a pressure of approximately 1000 pounds per square inch into a 1/2-inch diameter nickel tube. A pancake heater, consisting of a tightly wound spiral of 0.076-inch tantalum-clad tantalum heater wire, was employed behind the button to activate and heat the cathode. In the tests no heat shielding was attached to the cathode and its performance at approximately 1.5 milliamperes per watt with 100 milliamperes per square centimeter at 200 volts plate voltage does not represent the best possible performance. The data taken in the operation of the cathode are shown in Fig. 2-27b.

Nitung Sleeve Cathode

The nitung sleeve cathode consisted of a 0.002-inch wall nitung sleeve, coated with Baker-500, over a 0.31-inch tantalum

wire. A cylindrical diode configuration as shown in Fig. 2-27c was chosen for evaluation of this cathode.

Its performance was superior to the other cathodes tested. The data of the test are given in Fig. 2-27c. At 862°C the emission current density was approximately 300 milliamperes per square centimeter.

EIMAC Sintered Nickel Matrix Cathode

Six sintered nickel cathodes were purchased from Eitel-McCullough, Inc. of San Carlos, California. The purchased cathodes were stock klystron cathodes, 1.625 inches in diameter and concave with about a 15-centimeter radius of curvature. A spiral pancake heater was mounted behind the cathode and without heat shielding the data of Fig. 2-27d were taken. At 900°C - 965°C efficiencies as high as 5 milliamperes per watt were achieved at space-charge-limited current densities of less than 100 milliamperes per square centimeter.

Of the neutralizer cathodes studied the most promising for use with the DE engine appeared to be the nitung sleeve cathode. Accordingly, further tests of this type cathode were undertaken.

A cathode consisting of 0.074-inch OD tantalum-clad tantalum heater wire externally wrapped with a 0.005-inch thick layer of nitung and coated with Baker Chemical R-500 was evaluated in terms of total current and emission efficiency (ma/watt). A cylindrical diode geometry was employed, with a 1/2-inch diameter anode. The cathode had a diameter of 0.085 inch with an emitter length of 1.25 inches, giving an emitting area of 2.18 cm^2. The curves of Fig. 2-28 were taken.

The anode power supply was capable of 1000 ma at 300 volts. A maximum total current of 1000 ma at 250 volts was observed at 50 watts input to the cathode heater and an emitter temperature of 1115°C as measured with an optical pyrometer. This observed current corresponds to a space-charge-limited current density of 500 ma per square centimeter at the cathode. Above 885°C emission temperature
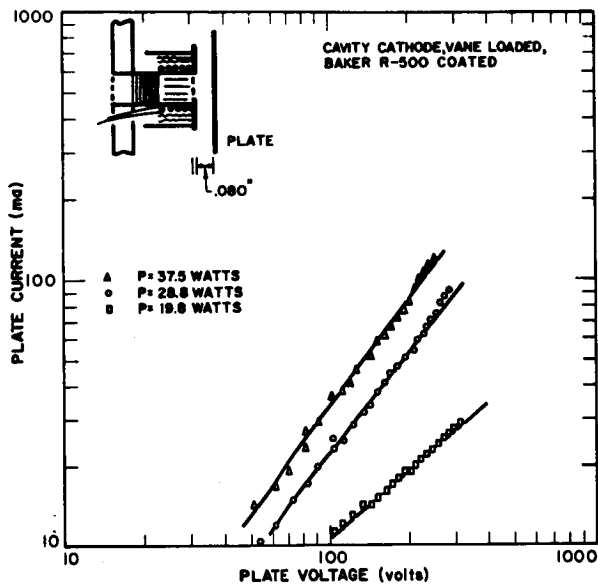
FIG. 2-27(a)   CAVITY CATHODE TEST
DATA
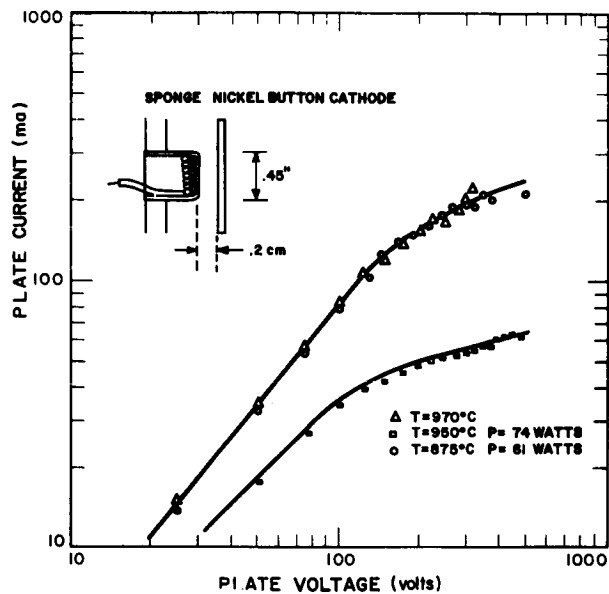
FIG. 2-27(b)   SPONGE NICKEL BUTTON
CATHODE TEST DATA
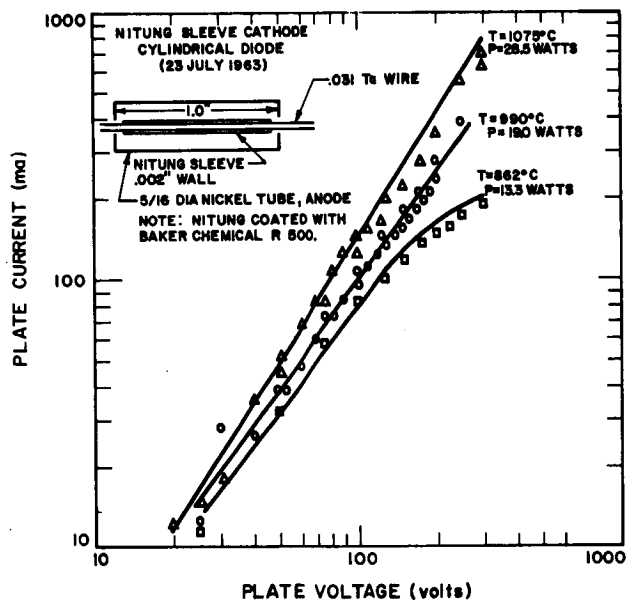
FIG. 2-27(c)   NITUNG SLEEVE CATHODE
TEST DATA
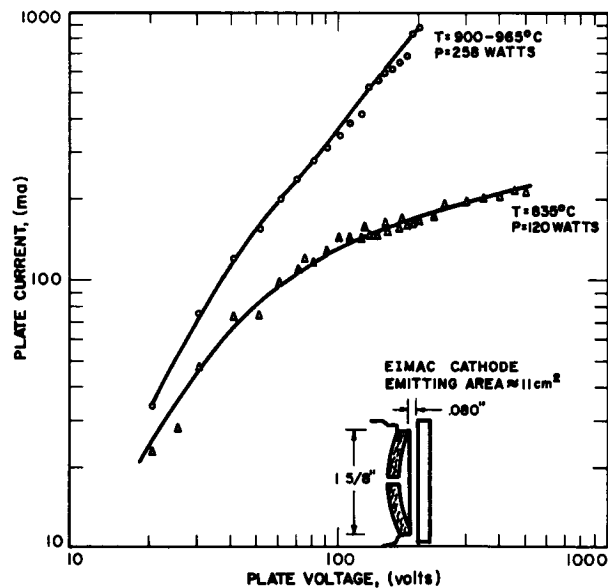
FIG. 2-27(d)   EIMAC CATHODE TEST
DATA

FIG. 2-27   NEUTRALIZER CATHODE TEST DATA
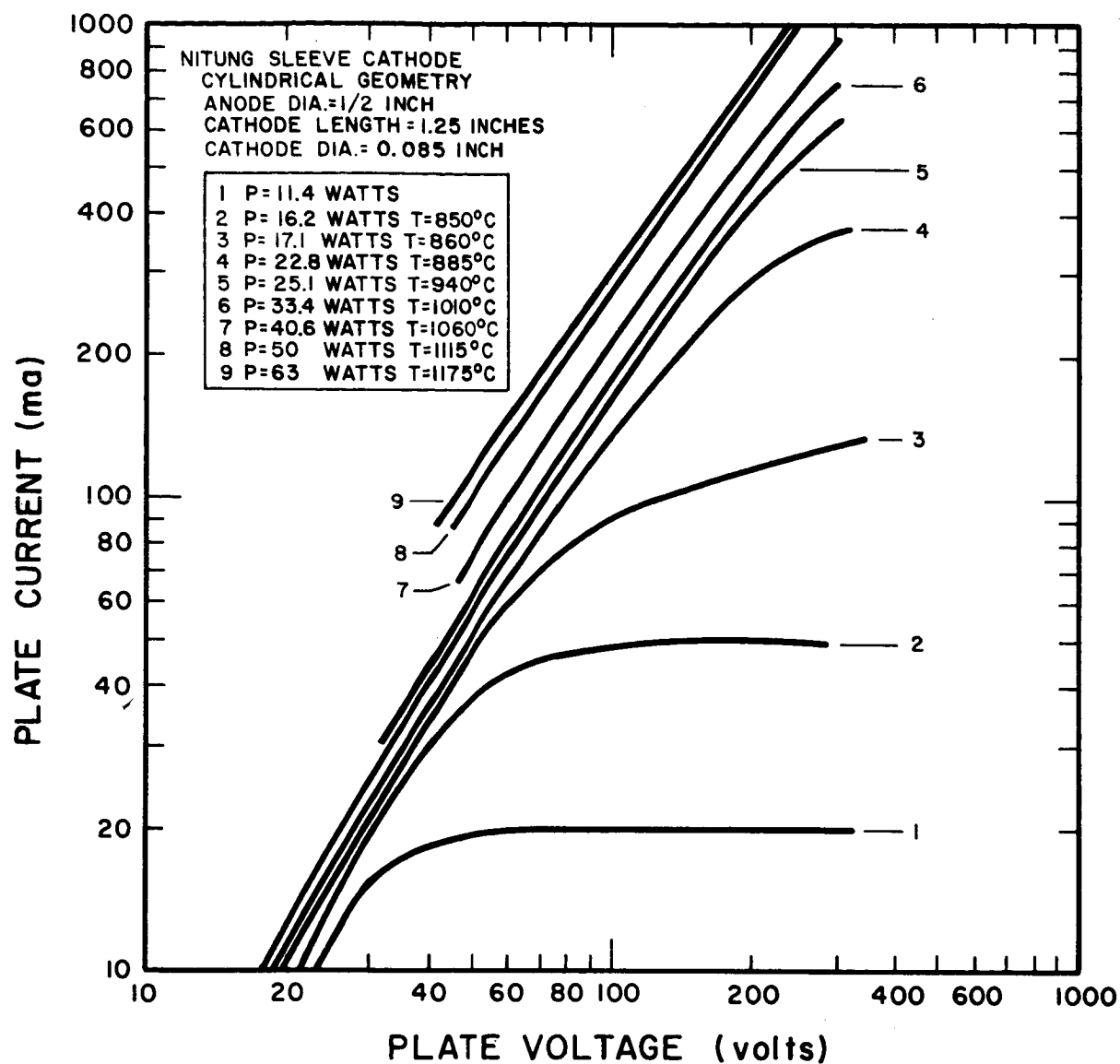
FIG. 2-28 NITUNG SLEEVE CATHODE TEST DATA

it was not possible to achieve the emission limited portion of the characteristic due to plate voltage power supply limitations. Emission limited currents were observed at 11.4 watts input; 16.2 watts, corresponding to 850°C; and 17.1 watts, corresponding to 860°C. The temperature at 11.4 watts was below the useable range of the optical pyrometer. Emission limited current densities at the above three power inputs were 25, 75, and approximately 250 ma/cm^2, respectively. Emission currents of several amperes per square centimeter are apparently achievable with this cathode.

For neutralization of the ion beam of an engine to occur, there must be a potential difference between the beam and the neutralizer. In addition, to achieve long neutralizer lifetime the neutralizer must be sufficiently far from the beam edge to prevent sputtering. For these reasons, a combination of thermionic emission and space charge limitations determine neutralizer efficiency which cannot be ascertained from the emission efficiency of the cathode by itself. While the test geometry does not resemble a neutralizer beam configuration, some idea of performance may be derived. For a 50 mil gap between the neutralizer and an ion beam with a 50 volt potential difference the space charge free field for an extensive neutralizer would be about 1000 volts/inch. For the cathode geometry tested, data at 100 volts diode voltage, which gives a space charge free field of 880 volts/inch at the cathode surface, should allow a rough idea of how the cathode would operate as a neutralizer.

Calculations of the efficiency expressed in terms of milliamperes per watt indicate that the most efficient operation occurs at an emitter temperature of 940°C. The observed operation at temperatures in excess of or less than this temperature was less efficient. For example, at an anode voltage of 100 volts the efficiency at 940°C is 6.38 ma/watt, while it is 6.14 ma/watt at 885°C, 5.26 ma/watt at 860°C, 5.24 ma/watt at 1010°C, and 5.18 ma/watt at 1060°C. At the other anode voltages the same decrease in efficiency either side of 940°C is observed.

At an anode voltage of 300 volts, 24.3 milliamperes per watt was achieved. This point, as inspection of the data reveals, is still on the space charge limited region of the characteristic, and represents the highest achieved efficiency.

A second cathode consisting of a 0.074-inch tantalum-clad tantalum heater wire directly coated with the barium-strontium carbonate suspension (Baker Chemical, R-500) was tested in the same cylindrical geometry. Both total current and efficiency were less for the bariated tantalum than for the nitung. For example, at an emission temperature of $970^\circ C$, requiring 32 watts of power, and at 300 volts the efficiency was 14.4 milliamperes per watt, while at 100 volts the efficiency was 2.81 milliamperes per watt, much less than for the nitung system.

The nitung sleeve cathode was chosen for the DE engine design and testing of this type of neutralizer with the DD engine was begun. The neutralizers tested with the DD engine consisted of two segments each approximately 5 cm long of 0.25-inch diameter oxide-coated nitung. One segment of this neutralizer was just touching the beam edge and the second was 0.25 cm further from the center of the beam. (After operation, both sections of the neutralizer showed effects of sputtering.) The neutralizer section closest to the beam was used primarily for these tests.

Prior to operating the engine, both sections of the neutralizer were heated to convert the carbonates to oxides. By making the neutralizer sheath negative with respect to ground, it was possible to measure a current of about 20 ma at a potential of ten volts with respect to the surrounding shield. After determining that both sections of the neutralizer were operating, the first (closest to the beam) section was heated to approximately $1000^\circ C$ and the engine was started. The tests were carried out at a beam level of 200 ma.

The curves of Fig. 2-29 were then taken with the first neutralizer. The entire beam is not collected by the metered collector so the collector current is always less than the beam current. The

impedance between this collector and ground may be varied and the collector thus floated to a potential, corresponding to the beam potential, determined by the net difference between the ion and electron current. Even with no neutralizer the collector does not rise to very high potentials because of the supply of secondary electrons formed by the ion beam interacting with walls and residual gas in the vacuum chamber. Following this, the second neutralizer section was used and the point shown by the asterisk was obtained at a neutralizer temperature of about 900°C. It appeared that there was little difference between the neutralizers in the two positions relative to the beam.

Figure 2-30 shows the measured electron flow to the neutralizer for data shown in Fig. 2-29. Here the neutralizer current is shown as a function of the collector potential. The curves shown are very typical diode emission characteristics. The curve for 950°C is still space charge limited at 105 ma. This curve would probably pass through a point at 140 ma and 100 volts. It appears that a few more sections of neutralizer would be sufficient to neutralize the engine at 500 ma beam and at a neutralizer temperature of 1000°C or less.

The sum of the collector and neutralizer currents (Figs. 2-29 and 2-30) for a given collector potential appears to be independent of the neutralizer temperature. In addition, the sum diminishes as the collector potential increases, as is expected. This is represented by the curve for the cold neutralizer of Fig. 2-29. Part of this effect may be due to enhanced spreading of the beam due to the potential on the collector.

The nitung sleeve-type neutralizer was later operated with a DE engine. The nitung sleeve was wrapped around a tantalum-clad tantalum sheathed heater wire and was coated with Baker R-500. The cathode was activated by heating it to over 1050°C (150 watts). The temperature was then reduced to 930°C and the engine was operated.
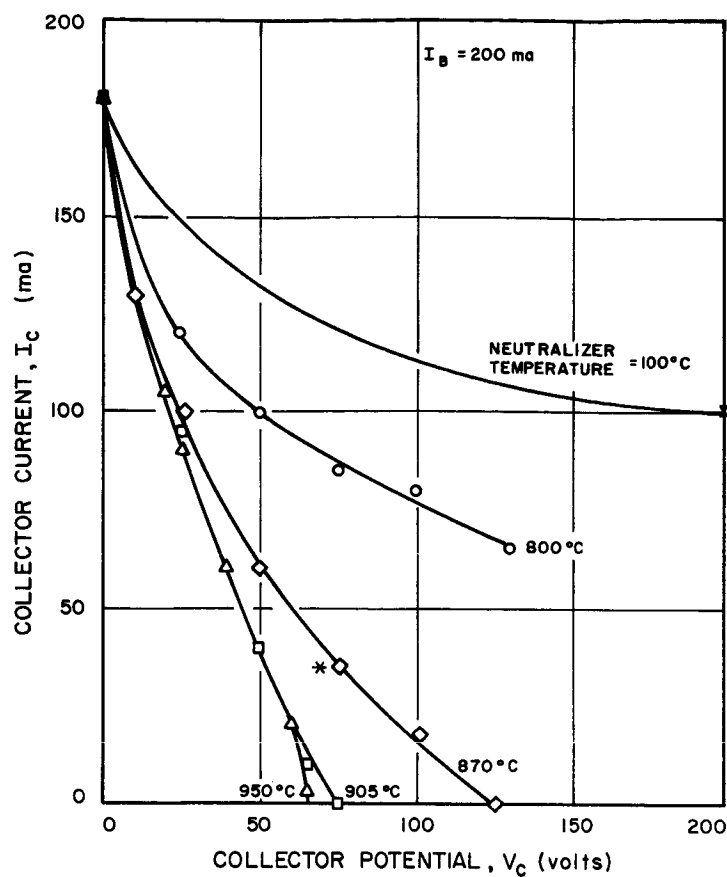
FIG. 2-29
BEAM NEUTRALIZER CHARACTERISTICS

FIG. 2-30
NEUTRALIZER CHARACTERISTICS
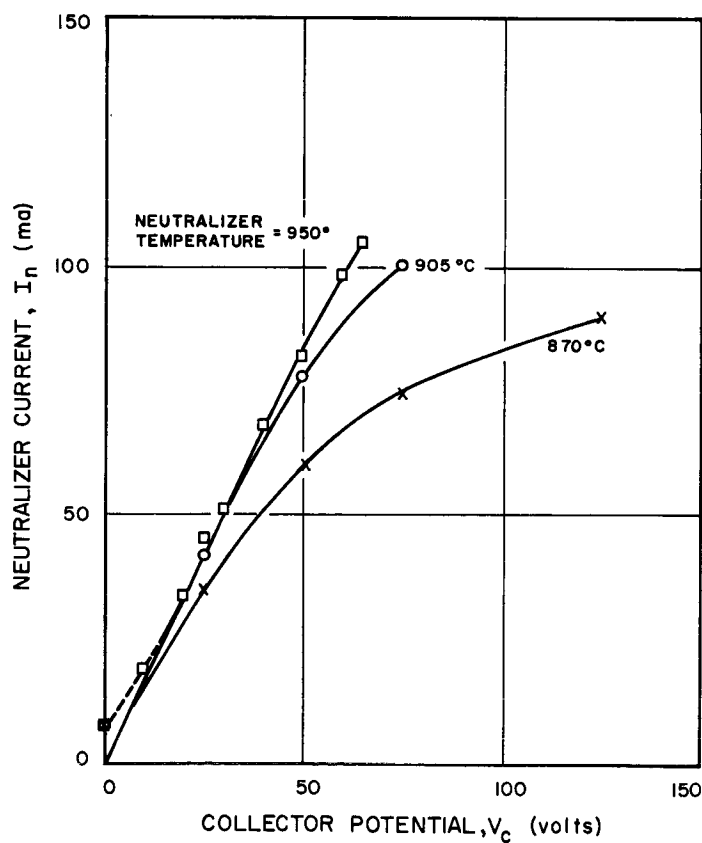
Data from the neutralizer tests are shown in Table 2-V. The beam current is the net positive ion current leaving the engine. The collector current is that measured by shorting the collector to ground through a current meter. It may be noted that about 96 percent of the beam was collected. The collector potential was measured by floating the collector with a high impedance voltmeter between it and ground.

From the data of Table 2-V it can be seen that neutralization was satisfactory but high neutralizer temperatures (970°C) were required for beam currents over 400 ma. Once cooled, a neutralizer cannot be reused in our facility since it gets covered with copper sputtered back from the liner and collector.

2.4 DE Engine

The DD engine test data were used to design the DE engine. The DE engine is similar in size to the DD configuration and matches the performance of the latter. The engine was designed to provide a high strength-to-weight ratio and weighs approximately 5 lbs. including the neutralizer and neutral cesium detector. More significant, perhaps, than the lower weight is the lower thermal mass of the DE engine. The importance of this is discussed in Section 4, Control System Development.

The DE engine and feed system are shown in Fig. 2-31. The system is complete except for the neutralizer which had not been mounted. An M-2 neutral cesium detector is mounted on the hood. The engine and feed system are units which were qualified and delivered. Figure 2-32 shows the cathode assembly and orifice plate. This cathode differs from the K5B cathode only in that the housing and orifice plate are of titanium instead of molybdenum. This cathode has been operated with the DD engine and no differences in performance were observed. Figure 2-33 presents a view of the arc chamber assembly with the anode installed.

Figures 2-34a and 2-34b are views of the electrode assembly. As can be seen, there are two sizes of apertures in this modified version of the distributed geometry electrode configuration. Figure 2-34b is a

TABLE 2-V

NEUTRALIZER OPERATION

TEST	BEAM CURRENT I_B, (ma)	GROUNDED COLLECTOR CURRENT I_c, (ma)	FLOATING COLLECTOR POTENTIAL V_c, (volt)	NEUTRALIZER TEMPERATURE T_N (°C)	NEUTRALIZER POWER P_N (watts)
1)	146	140	< 40	930	110
2)	187	180	40	930	110
3)	239	230	48	930	110
4)	354	340	58	930	110
5)	460	442	>180	930	110
6)	530	510	65	970	135
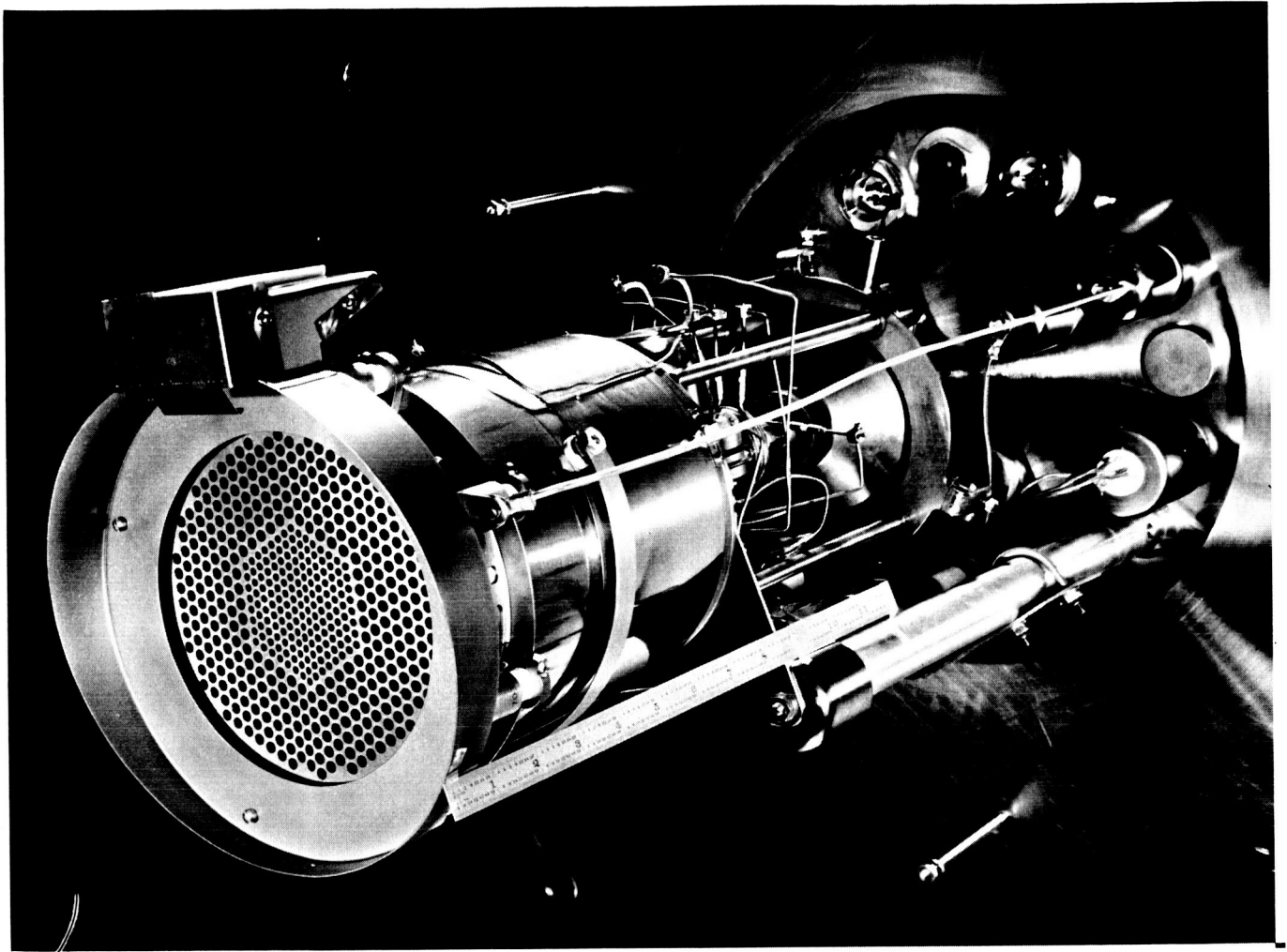
FIG. 2-31   DE ENGINE AND FEED SYSTEM
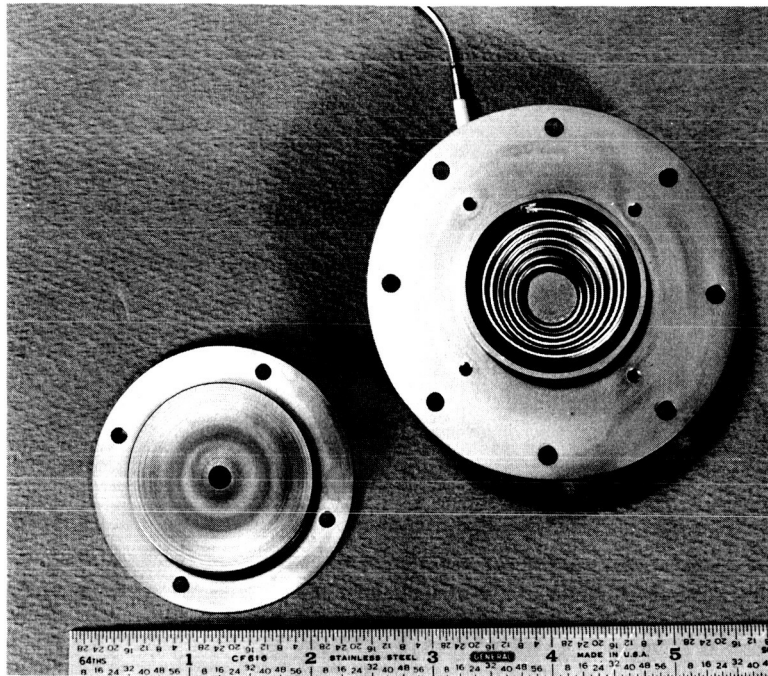
FIG. 2-32

DE ENGINE CATHODE

ANODE

FIG. 2-33

DE ENGINE DISCHARGE
CHAMBER ASSEMBLY

view from the plasma side of the screen electrode and shows the tapering of the individual apertures to provide plasma sheath conditions approaching those of a thin electrode. Figures 2-35a and 2-35b are photographs of the assembled components. The outer shell or cathode cylinder is machined from titanium tubing and has three support rings, one at each end and one in the middle. The nominal wall thickness of this housing is 0.030 inch. All other major components affix to the three rings machined into the cathode cylinder. The one layer magnet coils are covered with 3 mil sheet to provide a smooth shell exterior. The copper strap in the middle of the engine shell joins three terminals which are both insulated feedthroughs and supports for the anode.

As shown in Fig. 2-36, the magnetic field configuration for the DE engine is more solenoidal than that of the DD engine. The total impedance of the DE coils is 1.3 ohms cold and about 2.2 ohms at engine operating temperature. About 2 amperes coil current is required for an adequate magnetic field intensity. For a typical operating field of 7 gauss, the coils dissipate about 10 watts.

DE engine performance data are presented in Section 5, Engine System Performance and Evaluation.
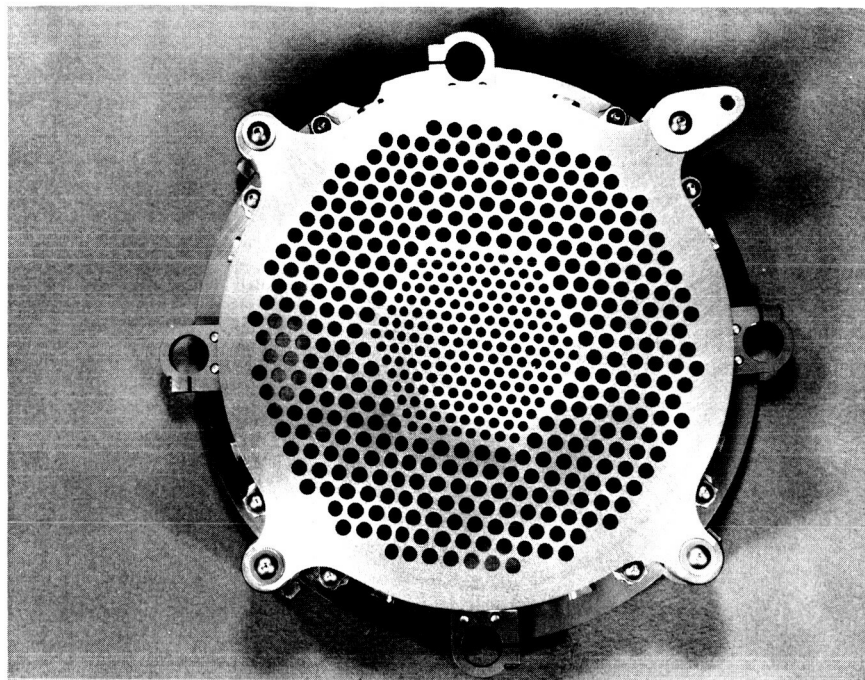
a   EXIT SIDE OF ACCELERATOR ELECTRODE
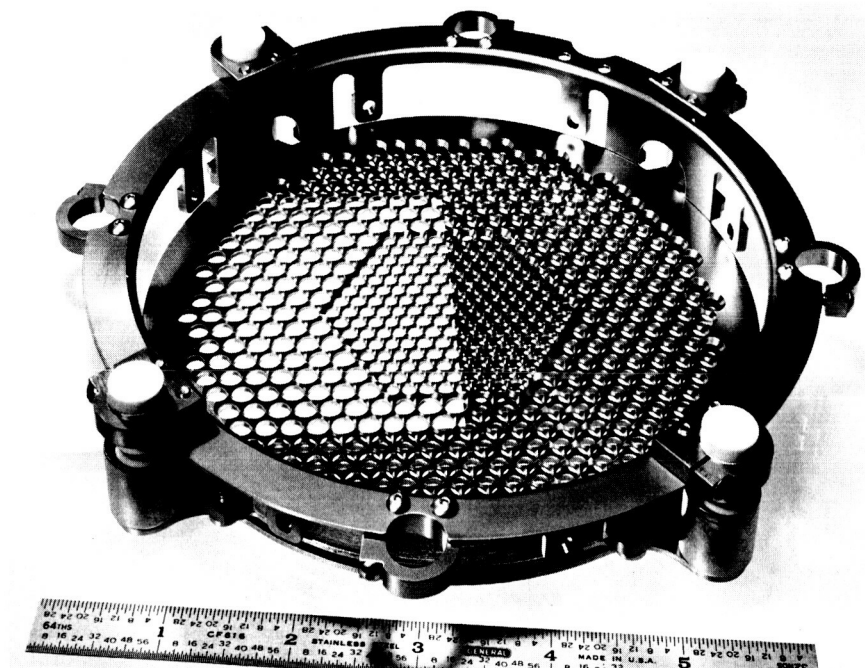
b   PLASMA OR ANODE SIDE OF SCREEN ELECTRODE

FIG. 2-34   DE ENGINE ACCELERATOR ASSEMBLY
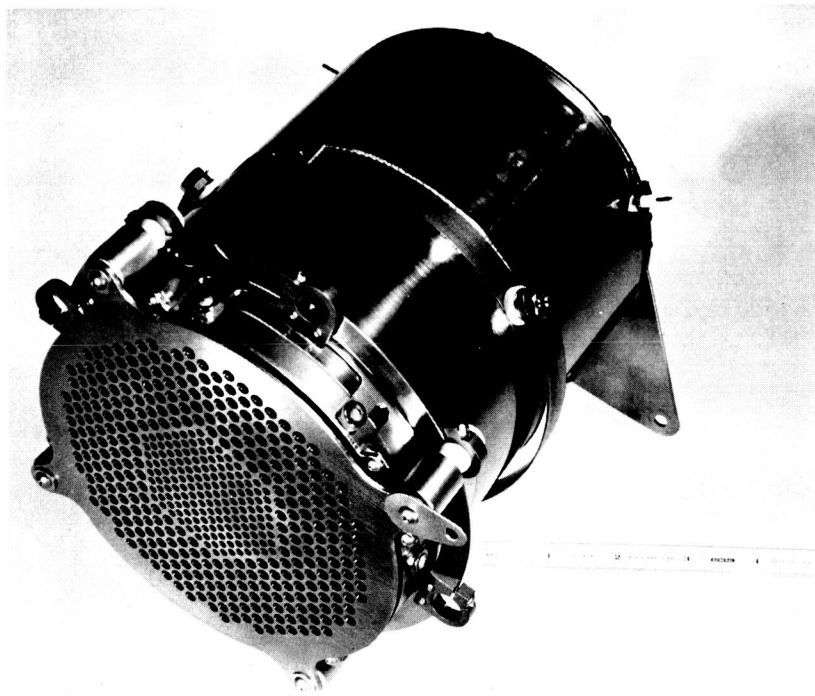
a
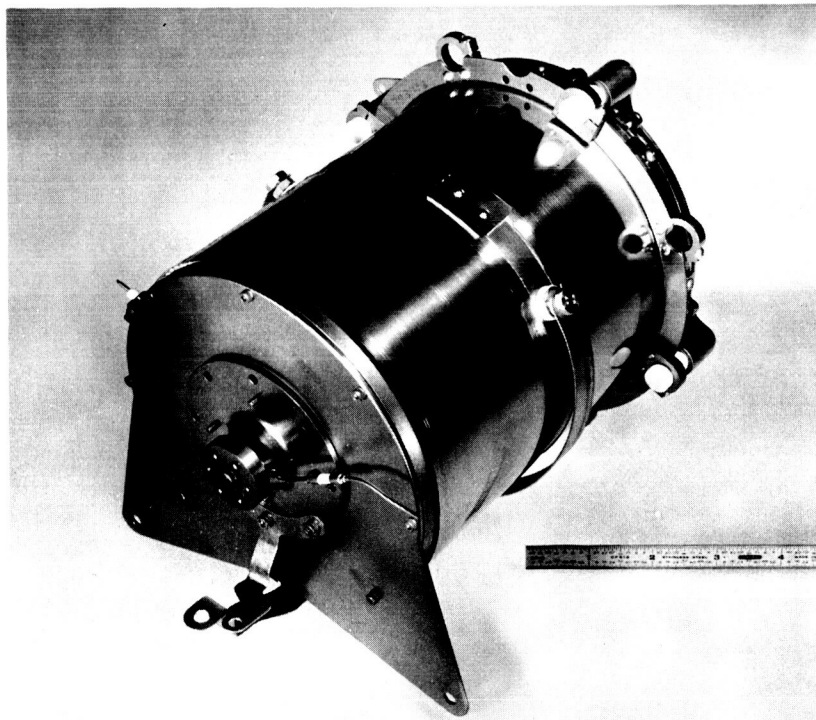
b

FIG. 2-35   DE ENGINE
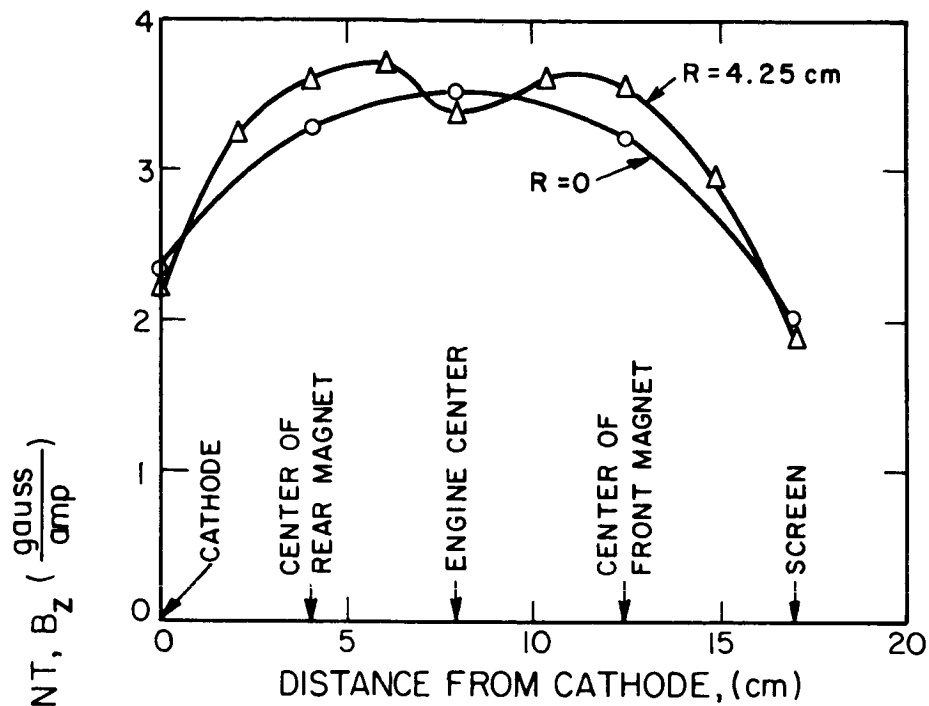
a   DE Engine Magnetic Field
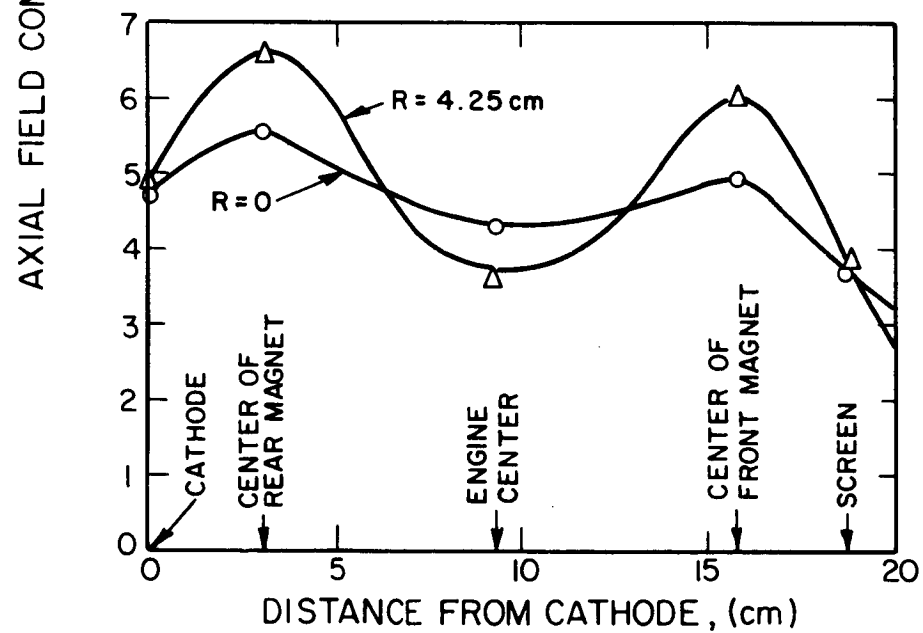
b   DD Engine Magnetic Field

FIG. 2-36   MAGNETIC FIELD CONFIGURATIONS

3670-Final

3. FEED SYSTEM RESEARCH AND DEVELOPMENT

   3.1 Propellant Feed and Storage Using Surface Tension Forces

During the contract period EOS designed, built, tested, and delivered feed systems using surface tension forces for the storage and transport of liquid cesium. This new concept has shown to be entirely reliable and has met all feed system and engine performance goals. A detailed analysis of propellant feed mechanisms using the surface tension concept follows.

   3.1.1 Tapered Tube Feed System

In its simplest form the system consists of a hollow tube of a diameter decreasing in the direction of flow.

It will be shown that in the situation shown in Fig. 3-1a there is a force on the liquid in the direction indicated. This force will move the liquid to the right until the configuration shown in Fig. 3-1b is achieved. In the latter case the shape of the meniscus at the small end of the tube is changed until the net force on the column is zero. Delivery of vapor can be achieved by heating the small end of the tube and utilizing surface tension forces to deliver the liquid to the narrow end of the tube as it is vaporized.

   Surface Energies

To make the calculations which demonstrate the requisite properties of this feed system it is advantageous to utilize the surface energy concept. Energy is required to form a free liquid surface and the energy per unit area of this surface is the usual surface term which we call σ_o. This is always a positive quantity. There is also an energy per unit area associated with a free solid surface and another with the liquid solid interface. In using energy one is concerned only with the variations with changes in configuration rather than with the absolute magnitude of the energy. Since the

decrease in free solid surface is always exactly equal to the increase in liquid solid interface (until vaporization is considered) it is adequate to use an energy per unit area which is the difference between these two surface energy terms. This will be either an energy proportional to the free solid surface or an energy proportional to the contacting surface. These two terms will have the same magnitude but opposite signs. It appears more convenient to use a term σ_1 proportional to the contact area between the liquid and tube. Consider the situation shown in Fig. 3-2. A relationship between the surface energies σ_1 and σ_0 is established in terms of the contact angle θ for a vertical column of liquid of height h in a tube of radius r.

$$h = \frac{2\sigma_0}{\rho_{gr}} \cos \theta \tag{1}$$

The energy associated with the column of liquid is

$$U = \sigma_1 \, 2 \, \pi r h + \frac{\pi r^2 h^2 \rho g}{2} \tag{2}$$

where the first term on the right is the energy associated with the interface and the second term is the gravitational potential energy term. The free surface term is not included since it does not include a variation with h. The height of the column is obtained by setting dU/dh = 0 which gives:

$$h = \frac{-2\sigma_1}{\rho g r} \tag{3}$$

A comparison between the two expressions for h gives immediately*

$$\sigma_1 = -\sigma_0 \cos \theta \tag{4}$$

In the wetting case ($0 < \theta < \frac{\pi}{2}$), σ_1 is always negative. For the nonwetting case ($\frac{\pi}{2} < \theta < \pi$), σ_1 is positive.

Let us now examine a liquid-solid combination in which $\cos \theta \approx 1$, ($\theta \lesssim 20°$). This is a good approximation for cesium and most compatible solids. In this case σ_1 reduces to $-\sigma_0$ and the

*Equation (4) can also be found derived in textbooks. See for example, "Physical Chemistry" by F.H. MacDougall, Macmillan Co., New York, (1947) p 92. MacDougall's ($\gamma_{12} - \gamma_{13}$) is the same as σ_1.
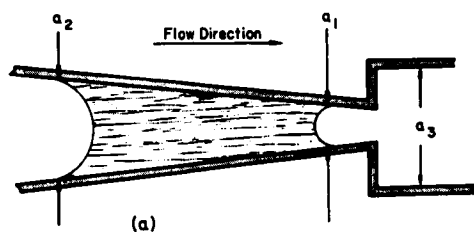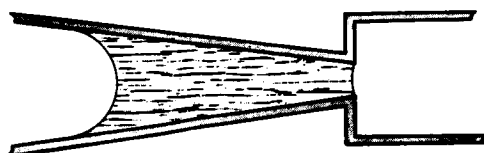
FIG. 3-1

ELEMENTARY FORM OF TAPERED
TUBE FEED SYSTEM

FIG. 3-2

DROP OF WETTING LIQUID IN
A CAPILLARY TUBE
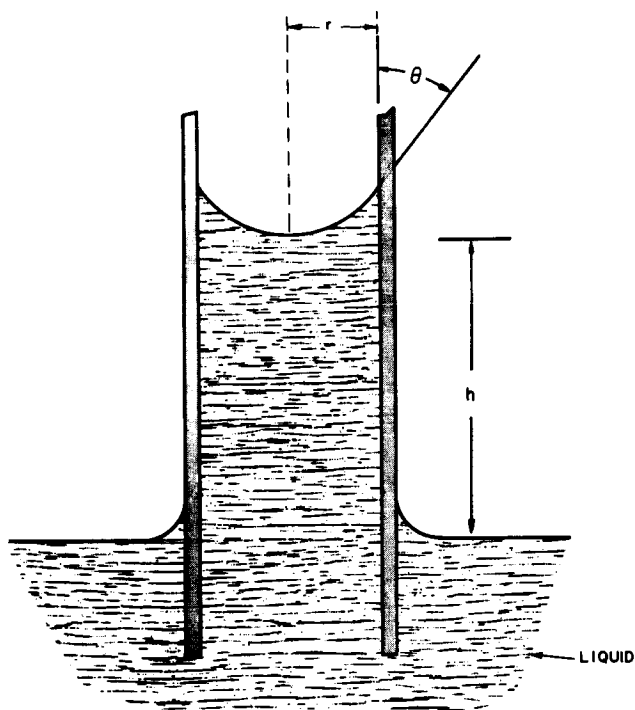
notation is considerably simplified by the use of a single term $\sigma = \sigma_o = -\sigma_1$.

Drop of Liquid In a Tapered Capillary

Consider a drop of liquid in a conical tube as shown in Fig. 3-3. Assume that the drop is small enough, or the taper gentle enough that the radius varies very little over the length of the liquid column. Let τ = volume of the drop, then the length of the drop is $4\tau/\pi a^2$ where a is the diameter of the tube. Assume the ends of the liquid column to be hemispheres; the energy can then be written as

$$U \;=\; \pi a^2 \sigma - \pi a \,\frac{4\tau}{\pi a^2}\, \sigma \tag{5}$$

$$=\; \sigma\left(\pi a^2 - \frac{4\tau}{a}\right).$$

The force on the column is

$$F = -\frac{dU}{dx} \;=\; -\sigma\left(2\pi a + \frac{4\tau}{a^2}\right)\frac{da}{dx}, \tag{6}$$

showing a force oppositely directed to da/dx, i.e., always in the direction of convergence.

If $\tau \gg a^3$ (long droplets) we can neglect the first term in parentheses, obtaining

$$F \;=\; \frac{-4\sigma\tau\alpha}{a^2} \tag{7}$$

where α = da/dx is the angle of the cone. Since $4\tau/\pi a^2 = \ell$ (the drop length) and $\alpha \ell = (\triangle a)$ equation (7) becomes

$$F = -\pi\sigma\,(\triangle a) \tag{8}$$

It is useful to put this force in terms of the weight of the liquid, especially in the case of a system capable of operating both in space and in the laboratory in all configurations. Introduce a proportionality constant $\gamma = F/mg = F/\tau\rho g$, where ρ is the liquid density and g the acceleration of gravity. The quantity γ is the

3670-Final

force in g's on the liquid. Reduction of the equations gives

$$\gamma = \frac{-4\sigma\alpha}{a^2\rho g} \tag{9}$$

Long Column of Liquid

If the following assumptions can be made: a) that drop diameter varies very little over the length of the liquid column; and b) that if the drops were long enough, the first term in Equation (6) could be neglected, then a solution for a long column can be realized.

Equation (8) is valid for liquid columns as long as the diameter does not show large variations and equation (9) is satisfied everywhere. For Equation (9) to have meaning for a long tube of liquid it is necessary that the tube geometry be such that α/a^2 be constant along the length of the tube.

Tube Shapes for Constant γ

Equation (9) makes it possible to design a tube for any desired γ. Three such tubes are shown in Fig. 3-4. For a feed system to be used in the laboratory in various orientations, the tube size required gets so small that the graded porous sponge system discussed in Subsection 3.1.2 is used. For systems to be used exclusively in space, very large diameter, shallow-tapered tubing can readily be used. The value of the surface tension used in these calculations is 64 dynes per centimeter.

Flow Velocity in Tapered Tubes

In addition to information on the force available to keep the liquid moving toward the surface from which vaporization is occurring, it is necessary to consider the velocity of this flow, as limited by viscosity, to determine whether propellant can be delivered fast enough. This is readily accomplished for flow in tubes. For

angle of cone
$da/dx = \alpha$

a

ℓ

F
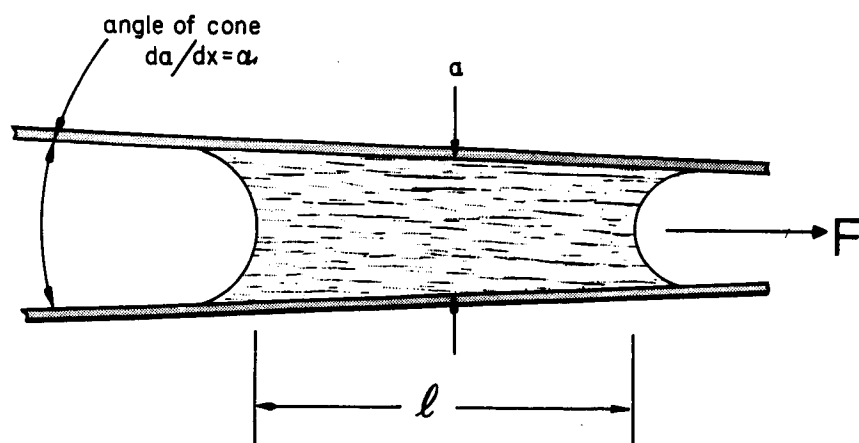
FIG. 3-3

DROP OF WETTING LIQUID IN A
CAPILLARY TUBE

F ——→(FORCE ON LIQUID)

(a)   F = .01g

(b)   F = 0.1g

(c)   F = g
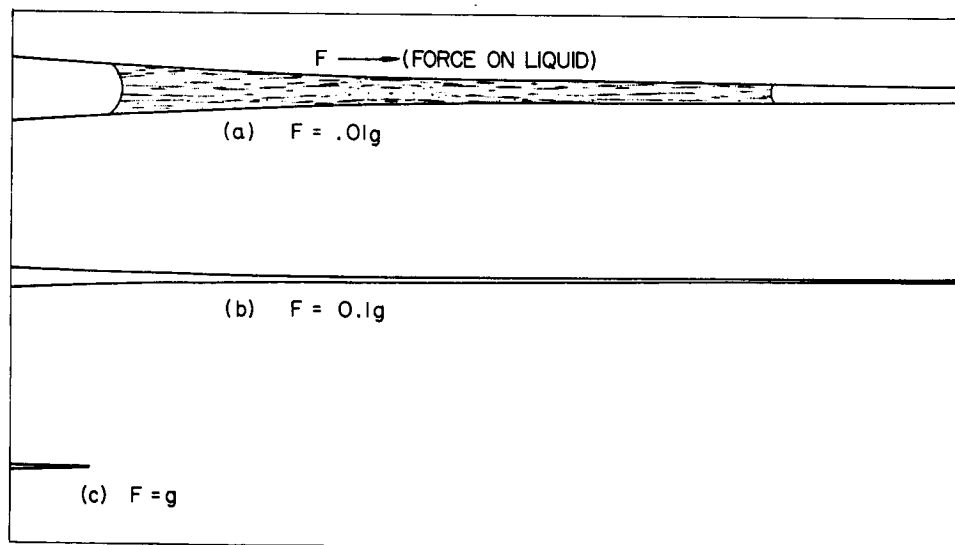
FIG. 3-4

VARIOUS TUBE SIZES AND SHAPES
(Full scale) FOR FORCE EQUIV-
ALENT TO THAT OF A GRAVITA-
TIONAL FIELD OF (a) .01g, (b)
0.1g, and (c) 1g

example, for droplets whose length is large compared to the tube diameter a, the velocity of flow toward the narrow end of the tube can be shown to be

$$v_f = \frac{\sigma}{8\eta} \frac{da}{d_\ell} ,$$ (10)

where η is the coefficient of viscosity, approximately 5×10^{-3} poise for liquid cesium. This can also be written as

$$v_f = \frac{\gamma \rho g}{32\eta} a^2$$ (11)

If 0.03 cm is chosen as the smallest feasible size of the tapered tube, a velocity of 0.1 cm/sec is obtained for the 10^{-2}g taper. This is the velocity of an isolated drop. The velocity of the liquid at the small diameter end of a long column is much greater than the velocity of an isolated drop, since the relatively large mass of liquid in the large diameter portion of the tube, where viscous drag is slight, pushes on the column at the small end. Indeed, if $a_2 \gg a_1$ then the velocity of the liquid at the small end can be shown to be

$$v_f = \frac{1}{8} \frac{\sigma}{\eta} \frac{a_2^2}{a_1^2} \frac{da}{d_\ell}$$ (12)

This may change the velocity of liquid approaching the small end by a factor of 100. All of these velocities are very large compared to the liquid flow velocities required for even very high thrust ion engines.

The actual flow velocities needed may be judged by taking an example. Assume a tube with an area of 0.05 cm^2 feeding a 100 ma engine. An area of 0.05 cm^2 is not large. Even if tapered tubes of smaller area were used they would be in a bundle with that total cross section. The assumed area and current readily lead to a velocity of 1.5×10^{-3} cm/sec in the liquid. This is so small compared to obtainable velocities that there does not appear to be any difficulty in maintaining the liquid vapor interface at the narrow end of the tube.

3.1.2 Porous Sponge Feed System

To simplify construction and to make possible much finer pore sizes a storage and feed system utilizing a graded porous sponge may be used. As in the tapered tube feed, surface tension is responsible for the storage and feed properties of the system.

Approximation Concerning the Porous Material

Extremely low density, high porosity sponges in nickel, stainless steel, and other materials are readily available. For the purpose of this calculation it is necessary that the sponge be characterized by a surface area per unit volume of enclosed liquid. The free surface area of a given volume of liquid can readily be shown to be independent of metal thickness, depending only on the open size of the cells. Accordingly, we will neglect metal thickness completely.

Lacking any experimental data based, say, on adsorption studies which would give a known value of surface area per unit volume for porous sponges, we assume that the volume is made up of communicating cubes of dimension a on an edge.

Force on a Drop in a Graded Sponge

Assume that a very large number of cells is occupied by a drop of liquid. In this case the free surface area of the liquid may be neglected in comparison with the contact area between the liquid and the sponge material. For reasons discussed in Section 3.1.1 of the tapered tube feed system we take an energy $-\sigma$ per unit area of contact where σ is the surface tension of the liquid.

The number of occupied cells is τ/a^3, and the area per cell is $6a^2$, so that the energy may be written

$$U = \frac{-6\tau\sigma}{a}$$

(13)

The force is

$$F_x = - \frac{dU}{dx}$$

or

$$F_x = - \frac{6\tau\sigma}{a^2} \frac{da}{dx} \tag{14}$$

The minus sign indicates a force in the direction of decreasing pore size as anticipated. Eq. (14) has exactly the same form as Eq. (7) if the tube diameter is replaced by the cell size and the force increased by 50 percent. However, sizes which appear completely unfeasible for tapered tubes are completely realistic for a porous sponge. The latter material can be obtained with pore sizes down to about 10 microns with densities of 5 to 10 percent the density of the solid material.

If, as in Section 3.1.1, $\gamma = F/\tau\rho g$ is introduced, the equations reduce to

$$\gamma = \frac{-6\sigma}{\rho g} \frac{1}{a^2} \frac{da}{dx} \tag{15}$$

Large Liquid Volumes

Since free surfaces never entered the calculation for the force on a drop, Eqs. (14) and (15) are also true for large volumes of liquids except that if the quantity $\frac{1}{a^2} \frac{da}{dx}$ is not constant an integral of Eq. (14) must be performed to obtain the total force and, therefore, Eq. (12) is no longer meaningful.

Pore Sizes and Size Gradients

In the graded sponge very high containment and driving forces are readily obtained. This is illustrated in Fig. 3-5 in which the pore size as a function of distance along the sponge is plotted for a 30-cm long sponge with 100 micron (10^{-2} cm) pores at the coarse end. The entire range of pore sizes is an extremely convenient one. Indeed it would be easy to design feed systems based on a graduated porous sponge for much higher accelerations than 2 g.
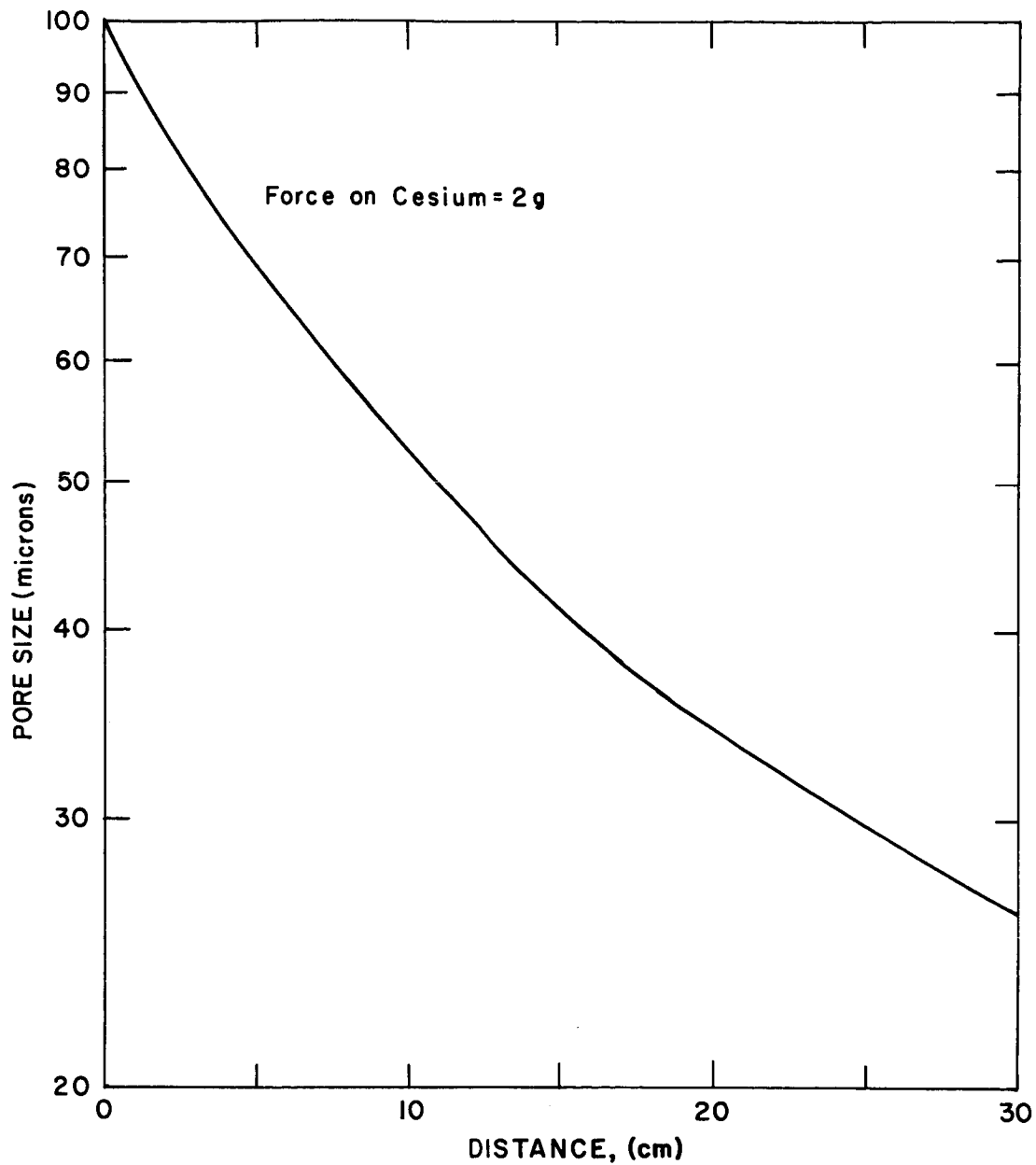
FIG. 3-5   PORE SIZE AS A FUNCTION OF DISTANCE FOR A
2g SPONGE

Flow Velocities in Porous Sponges

It was relatively easy to assume a relationship between surface area/unit volume and pore size which must be a good approximation to the actual values.

It is virtually impossible to make a similarly reliable assumption concerning viscous drag. For a material of a given pore size the pressure drop required to force liquid through at a given rate per unit area can vary from the value required for an array of straight tubes to infinity, depending on the nature of the manner in which pores interconnect.

However, the very low density foamed metals are extremely permeable and microscopic examination of such material shows an appearance which suggests that the flow permeability will not be very much poorer than that of straight tubes. If this is the case the available flow velocities remain extremely large compared to those needed.

Effects of Discontinuous Gradation

Since sponges cannot be made with pore size varying with distance according to a prescribed formula, it is necessary to use an array of slabs. This works equally well. The only requirement necessary to achieve the desired force on the liquid is that the rear portion of the liquid be in a region where the pore size relative to the vaporization section has the correct value.

3.1.3 Effects of Back Pressure

There is still a further consideration to be made concerning these feed systems. It is necessary that the pressure produced by vaporization at the small capillary or small pore size end of the feed system be inadequate to force the liquid away from the vaporizing surface.

For gas discharge engines the desired pressure is about 1 mm Hg which is equivalent to the pressure produced by a column of cesium 0.72 cm long under 1 g conditions. The consequence of this

is that a 1 g system operating in space would operate until the column was 0.72 cm long at which point the liquid column would be pushed away from the vaporization end. The pressure would then further increase (for the same mass flowrate) because of the viscous drop in the flowing vapor. Therefore, this point is a true instability. However, it appears quite simple to make this effect inconsequential. For example, for the 2 g sponge for which data are plotted in Fig. 3-5, only the last 0.36 cm of 30 cm total would be lost. This last 0.36 cm would be in a small diameter section of the reservoir so that the unconsumed material would be completely negligible.

Consider another example, that of a reservoir 10 cm long. In this case a sponge involving pores sizes varying from 100 microns at one end to 17.3 microns at the other would give a 10 g field. Feed would proceed as desired (for a 1 mm Hg back pressure) until the last 0.07 cm. This also would be in a narrow portion of the reservoir and involve a negligible loss in propellant.

3.1.4   750-Hour Feed System Concept

The 750-hour feed system (Fig. 3-6) consists of a combination of two capillary systems, one sized for operation in the laboratory and the other sized for space operation. The combination of these two produces a versatile and low weight system.

To understand the operation, it is best to consider the two modes of operation separately. In the first mode, the laboratory mode, two main forces act upon the liquid cesium. Gravity pulls the cesium down and away from the vaporizing area. Surface tension forces draw the cesium into the porous rod and up to the vaporizing area. The sizing of the fin structure is such that it has negligible effect at 1 g; thus, it need not be considered during laboratory operation, it is only necessary that the pore size of the porous material be of sufficient fineness to draw the cesium by capillary action up to the vaporizer.
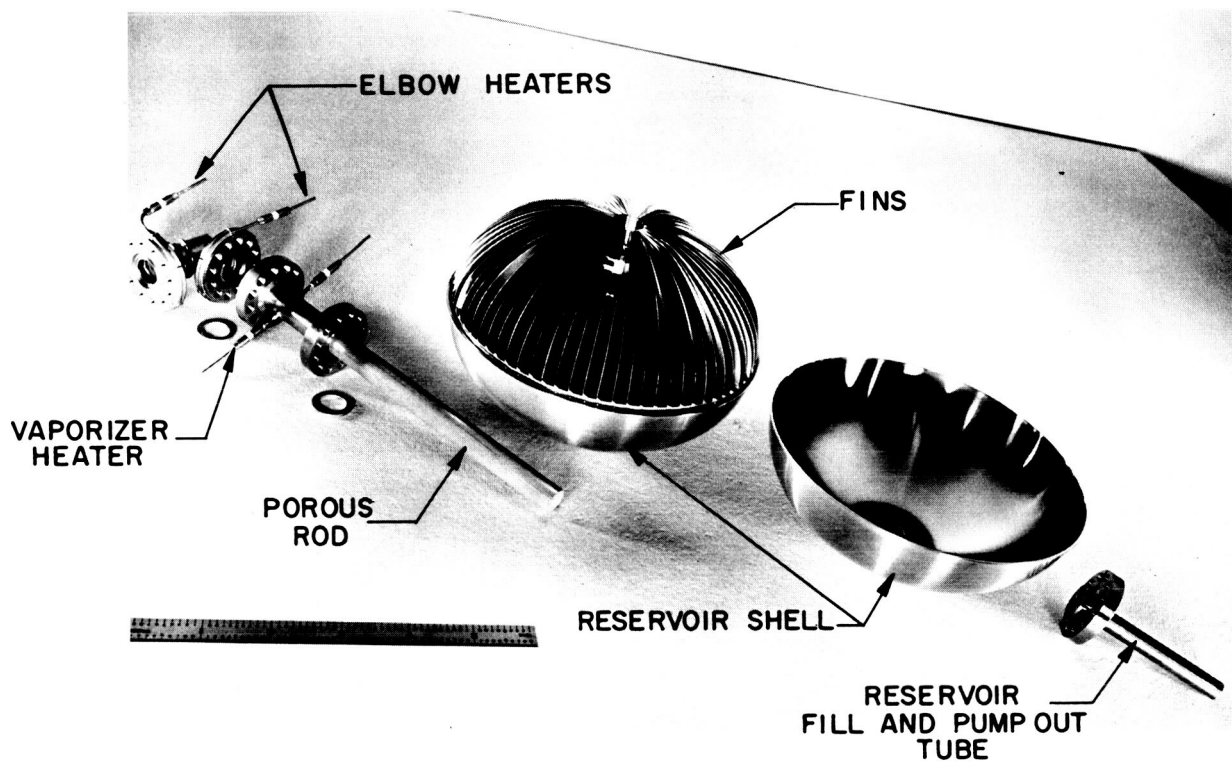
FIG. 3-6   750-HOUR FEED SYSTEM COMPONENTS

In the space mode of operation, surface tension forces become predominant. This is the case even for the relatively large capillaries existing in the fin structure. The capillary channels formed between the radial fins have a tapered configuration and consequently a force is exerted on any propellant toward the central porous rod. After arriving at the rod, the cesium is transported to the vaporizing surface in the same manner as described for the first mode.

3.1.5 Cesium Trapping in the 750-Hour Feed System

One of the advantages offered by the finned feed system configuration is that significant quantities of cesium cannot be trapped in the reservoir during operation. In previous feed systems the amount of trapping could only be determined experimentally; here a simple analytical treatment provides assurance that only small amounts of cesium will remain unused in the system.

The feed system consists basically of a porous rod with many fins extending radially outward. The entire assembly is enclosed in a container. The only liquid that can be trapped in such a configuration is that which remains in the corners between the fins and the container wall and any that remains in the porous rod.

The amount of cesium remaining in the porous rod can be easily calculated. If we assume a uniform pore size throughout the material, no forces will exist to transport the cesium when the supply in the main reservoir has been depleted. Therefore, the amount of unavailable cesium is just the amount necessary to fill the voids of the porous rod.

The mass of cesium remaining in the rod is

$$M_{cs} = \rho_{cs} V \left(1 - \frac{M_R}{V_R \rho_R}\right) \text{ grams} \tag{16}$$

where ρ_{cs} is the density of cesium, ρ_R is the density of the rod

material, M_R is the mass of the rod, and V_R is the total volume of the rod. The term $\frac{M_R}{V_R \rho_R}$ is just the fractional density of the porous rod.

This is usually given in percent. The rod used in the 750-hour feed system has a density of from twenty percent to fifty percent of that of solid nickel and is 0.5 inch in diameter. Choosing the twenty percent dense material as the most unfavorable gives a mass of 27.6 grams trapped cesium. Converting this value to a percentage of the total capacity gives 1.22 percent. The amount of propellant trapped in the rod is small and becomes even less significant as the size of the feed system is increased.

The quantity of cesium trapped in corners of the feed system is also insignificant. Figure 3-7 shows the idealized relationship between the fin, container wall and porous rod. Cesium trapping occurs at the intersection of the fin and the container wall. Intuitively, one would expect that the amount of cesium trapped here would be small and that it would have cross section dimensions comparable to the dimensions of the cavities in the porous rod. To simplify the calculations which show this, it is necessary to make the following assumptions 1) the contact angle between the cesium and any contacting surface is zero; 2) the porous rod is characterized as being made up of many small cubical cells communicating with one another; 3) the radius of curvature of the liquid surface formed is constant and is equal to b as shown in Fig. 3-8.

Liquid continues to enter the porous rod until the sum of the surface forces becomes zero. In this condition the energy of the system is at a minimum. The total energy is the sum of the energy of the free liquid surface in the corner, the energy of the liquid-solid surface in the corner, and the energy of the liquid-solid surface in the porous rod. The free liquid surface in the rod is very small in comparison to the liquid-solid surface, and consequently the energy associated with this surface can be ignored in the calculation.
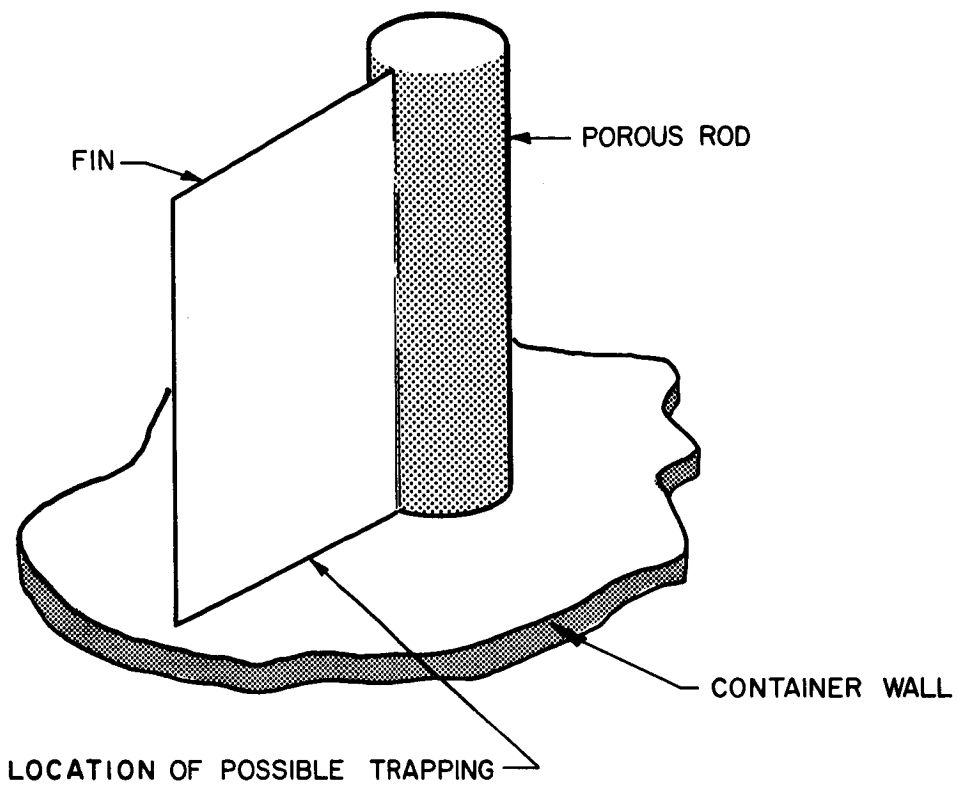
FIG. 3-7 RELATIONSHIP OF FEED SYSTEM ELEMENTS
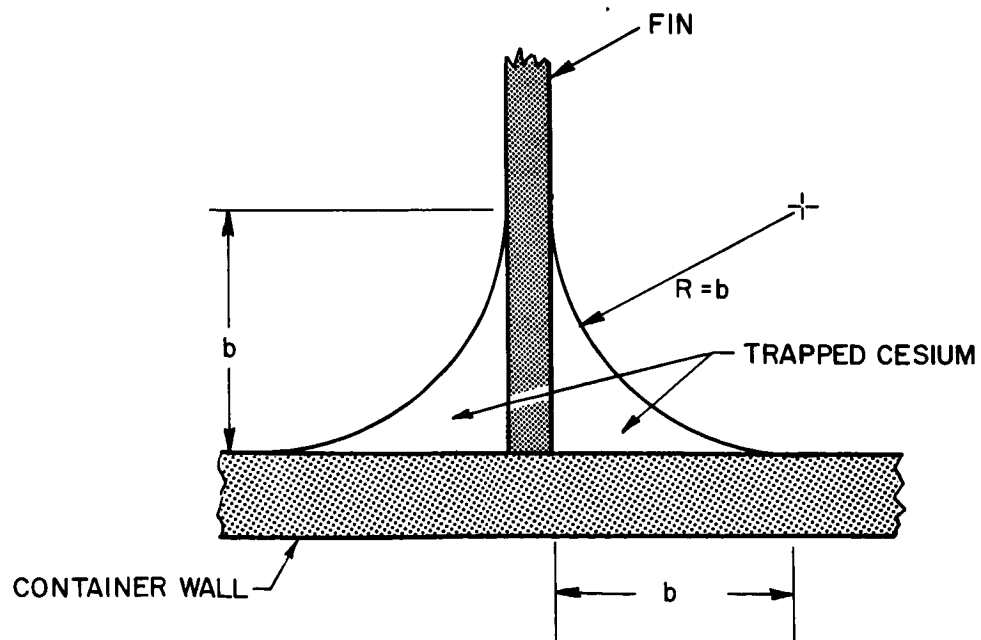
FIG. 3-8 INTERSECTION OF FIN AND CONTAINER WALL
SHOWING TRAPPED CESIUM

The energy of the free liquid surface in the corner, U_1, and the energy of the liquid-solid surface in the corner, U_2, are

$$U_1 = \frac{\pi}{2} b\ell\sigma_o$$
$$U_2 = 2b\ell\sigma_1$$

(17)

where ℓ is the length of the channel formed in the corner, σ_o is the energy per unit area associated with the free surface and σ_1 is the energy per unit area associated with the wetted surface.

In order to determine the energy of the liquid-solid surface in the porous rod it is necessary to approximate the total wetted surface area in the rod. If we assume that the rod is comprised of cubical cells whose sides have length a, then the surface area per unit volume becomes $\frac{6}{a}$. Also, for a constant total cesium volume, V, the volume of cesium in the rod, V_R, is

$$V_r = V_{cs} - b^2\ell \left(1 - \frac{\pi}{4}\right)$$

(18)

The second term of the above equation is the volume trapped in the corner. The total wetted surface area is then the product of the cesium volume in the rod and the surface area per unit volume. The energy associated with this surface, U_3, becomes

$$U_3 = \frac{6}{a}\left[V_{cs} - b^2\ell \left(1 - \frac{\pi}{4}\right)\right]\sigma_1.$$

(19)

Neglecting the energy associated with the free liquid surface in the rod, we obtain the total energy

(20)

$$U = \frac{\pi}{2} b\ell\sigma_o + 2b\ell\sigma_1 + \frac{6}{a} V - b^2\ell \left(1 - \frac{\pi}{4}\right)\sigma_1$$

which can be simplified by substituting $-\sigma_o$ for σ_1. This substitution is valid since

$$\sigma_1 = -\sigma_o \cos \theta$$

and for our case the cosine of the contact angle θ is unity.

The force, F, is

$$F = -\frac{dU}{db} = \sigma_o \left(\frac{4-\pi}{2}\right) - \frac{6b}{a} \ell \sigma_o \left(\frac{4-\pi}{2}\right) \quad (21)$$

and for the case when F = 0, or when the energy is a minimum we obtain

$$b = \frac{a}{6}$$

It is convenient to introduce a new parameter, C, where C^2 is the cross sectional area of the cesium remaining in the corner. It has a magnitude

$$C = \frac{a}{6} \left(1 - \frac{\pi}{4}\right)^{1/2} \approx \frac{a}{12} \quad (22)$$

With this equation, the total amount of propellant that will be trapped in corners of the 750 hour system can now be calculated. It is anticipated that the porous rod used in the above mentioned feed system will have an average pore diameter of about 50 microns. Using this value for a and assuming that a corner exists around the entire perimeter of each fin, a value of 8.7×10^{-4} grams is obtained as the amount of propellant trapped.

A comparison with the amount trapped in the porous rod shows that the amount trapped in the corners is insignificant; therefore, the total amount trapped in the feed system can be considered to be only the amount remaining in the porous rod.

3.2 Preliminary Feed Systems

During the early portion of this contract two preliminary feed systems were designed and fabricated. These systems (Fig. 3-9) are stainless steel shells filled with porous nickel inserts. The inserts are graded with the largest pore size insert at the rear and the smallest in front near the vaporizer heater. Each system has a cesium capacity of 360 grams and a dry weight of 400 grams. Both
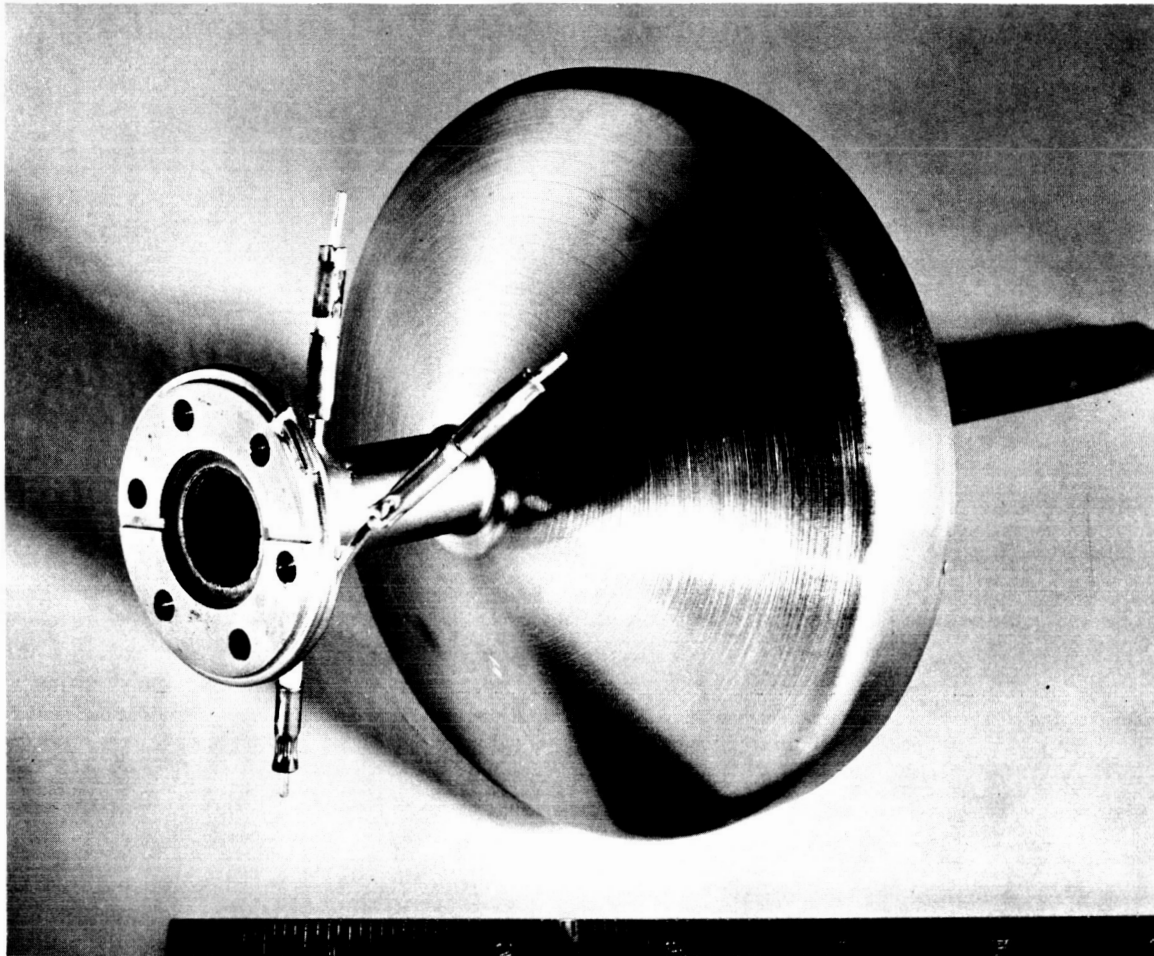
FIG. 3-9   PRELIMINARY FEED SYSTEM - DD ENGINE

were designed for filling by distillation (see Section 3.3).

3.2.1 SN-1 Feed System

The first feed system, SN1, was designed with an internal vaporizer heater. This heater was a close-wound spiral of stainless steel heater wire pressed against the surface of the front nickel insert.

Long duration tests of the preliminary feed system, SN-1, were conducted in a 5 foot x 12 foot vacuum chamber. A neutral detector was used to monitor the cesium vapor flow. Current and voltage measurements were made on all feed system heaters and the temperatures at various positions on the system were continuously recorded.

The test was conducted in two parts. During the first part, the feed system was run while attached to a cesium vapor valve. The valve was used to facilitate loading and was not used as a flow control element. A photograph of the loaded feed system attached to the pneumatic cesium vapor valve is shown in Fig. 3-10. The system was run in a vacuum tank with the flow rate monitored by a neutral detector. Total run time was 8.7 hours. During this time the system was operated up to flow rates equivalent to 100 ma.

A 5-1/2-hour test of the stability of the feed system was conducted during this run. The flow rate during this time was 0.013 mg/sec which is equivalent to about 10 ma of ion current. Stability of the system was excellent and no deterioration of performance was observed. The system was also operated for one hour at an equivalent flow of ~ 40 ma.

The system was not pushed up to the design flow rate during this run because of the high impedance to vapor flow presented by the pneumatic valve. This valve has small flow passages and has a relatively high impedance to vapor flow. It was used during this run because of the unavailability, at the time, of any other suitable valve. The S-1 solenoid valve, to be discussed, is designed to have a much lower impedance. The temperature at the vaporizer during the
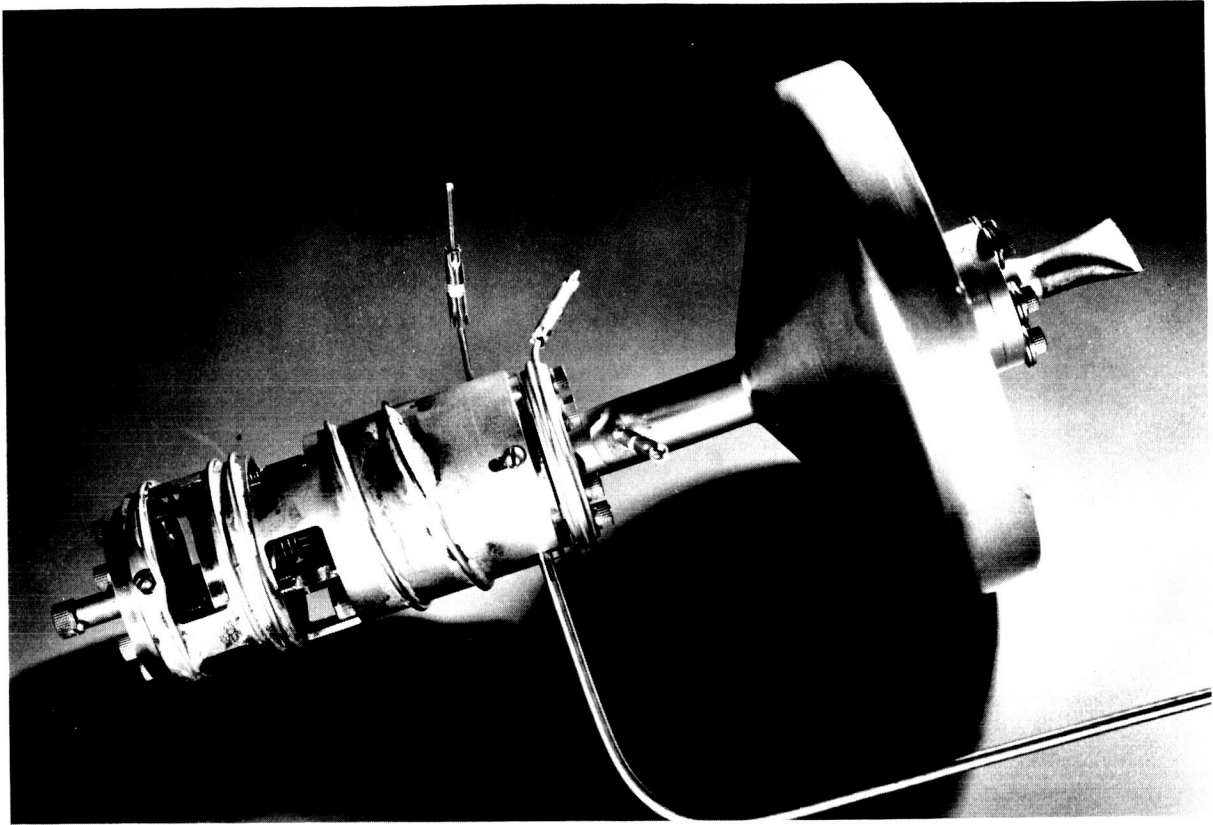
FIG. 3-10   PRELIMINARY FEED SYSTEM AND VALVE

5-1/2-hour test was 240°C. Data from a previous run with a feed system of the same basic design but having no valve show a mass flow of 2 mg/sec at this temperature. This is equivalent to an ion current of about 1.5 amperes, well above the operating level of the DD engine.

The first short run was terminated due to low flow rates and failure of the internal vaporizer heater. The latter may have been due partially to the high temperatures necessary to provide flow through the large valve impedance. The valve was then removed from the feed system and the run continued for 46 hours. During this time, the system was operated continuously for 14 hours at a flow rate of 90 ma. and then at a flow in excess of 0.5 amperes for 29.5 hours. Feed system power at this time was only 31.8 watts.

The maximum flow rate obtained was 1.5×10^{-3} grams/sec. 130.23 grams of cesium were expelled, giving an average flow of 8×10^{-4} grams/sec, equivalent to 0.6 amperes of ion current.

In all, a total of 54.5 hours of run time were accumulated with no noticeable deterioration in performance. The flow characteristics of the system are shown in Fig. 3-11, where the flow rate is plotted as a function of vaporizer temperature. Figure 3-12 shows the equilibrium temperature profile obtained during the 29.5 hour duration run.

Post-run examination of the feed system included an x-ray examination to determine the location of any residual cesium. The system was then dismantled and carefully inspected to determine if any clogging of the porous metal inserts had occurred. No clogging or contamination was observed. A weight measurement of the system after careful cleaning showed that 23 grams of cesium had remained unused.

Failure of the internal heater during the first part of the feed system run described above prompted the initiation of a program to determine the cause of the failure and to apply corrective measures to future feed systems.
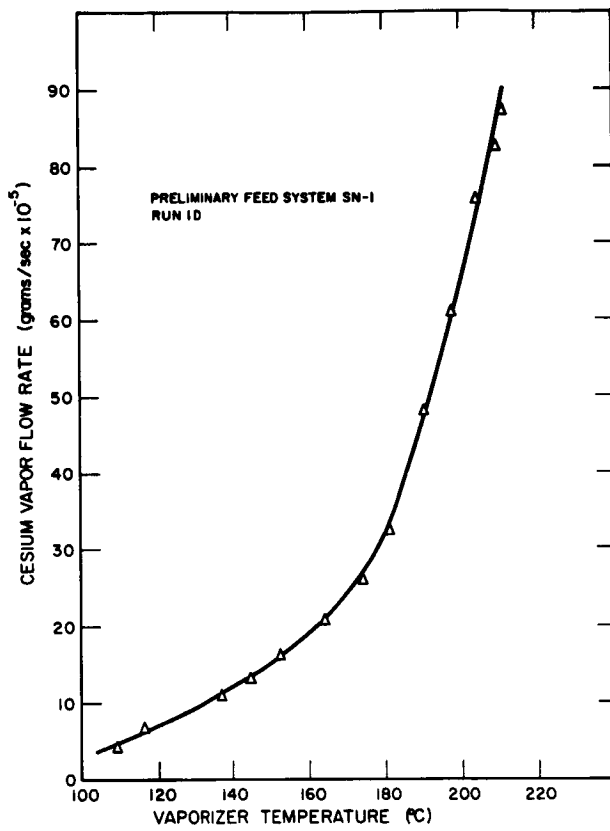
FIG. 3-11

FLOW RATE VS VAPORIZER TEMPERATURE
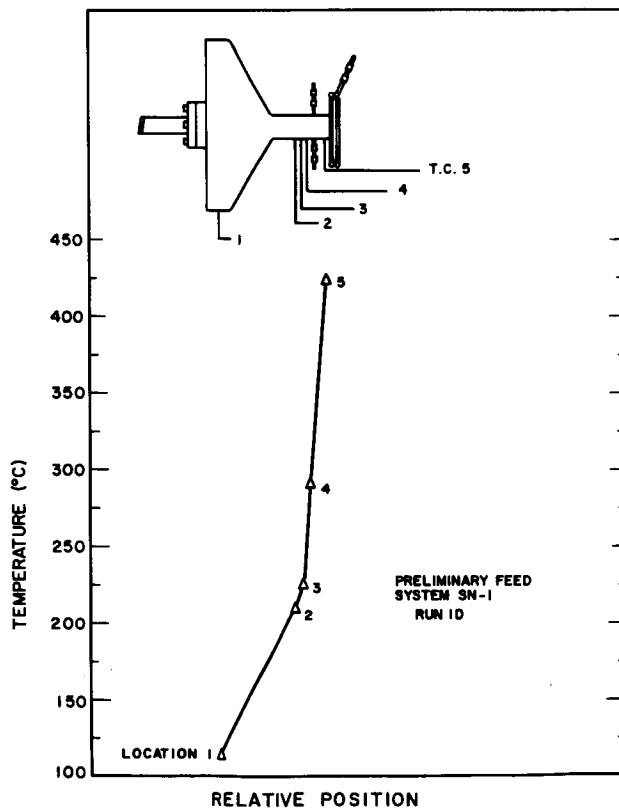
FIG. 3-12

RESERVOIR TEMPERATURE PROFILE

As a first step in this program, a heater test assembly was mated to the feed system and tested during the second part of the run described above. The heater test assembly replaced the pneumatic vapor valve used in the first part of the run.

The test heater performed satisfactorily throughout the run. It was held at a temperature in excess of 500°C for 43 hours in the cesium vapor stream. Post-run examination showed evidence of cesium attack. Figures 3-13a, 3-13b and 3-13c show, respectively, the feed system internal heater, the test heater and, for comparison a new heater. The mechanism of attack is believed to be due to the fact that the heater was in contact with liquid cesium which may contain oxides and hence accelerate corrosion. The heater is also in contact with the first porous nickel insert. This also may be a contributing factor. The relatively unaffected surface of the test heater indicates that the corrosion is probably not due to cesium vapor.

3.2.2 SN-2 Feed System

A second preliminary feed system, SN-2, was then assembled. This system is identical with SN-1 except for the location of the internal heater. The heater is moved away from the first porous insert and is less efficient in heating the front face of the insert.

In preparation for the tests, x-ray photographs were taken of the feed system before and after loading with approximately 100 grams of cesium. The x-ray negatives are shown in Fig. 3-14a. In these photographs the axis of the feed system was kept horizontal. It is interesting to note that in Fig. 3-14b the liquid cesium level assumes approximately a 45° angle, which was predicted by the theory upon which the design of the feed system was based.

In the flow tests of the SN-2 feed system, a total of 33.3 hours of running was accumulated. The feed system performed satisfactorily throughout the test. A total of 61.89 grams of cesium were exhausted giving an average flow rate of 5.16×10^{-4} grams/sec.

a   FEED SYSTEM
     INTERNAL HEATER

b   TEST HEATER

c   NEW HEATER
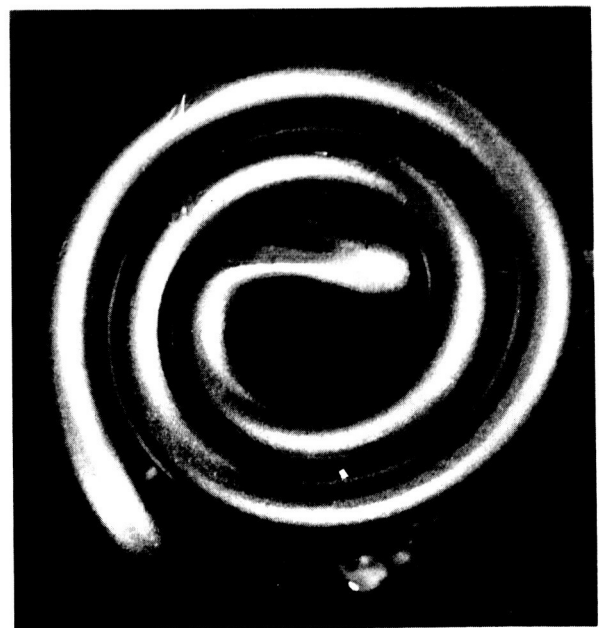
FIG. 3-13   VAPORIZER HEATERS
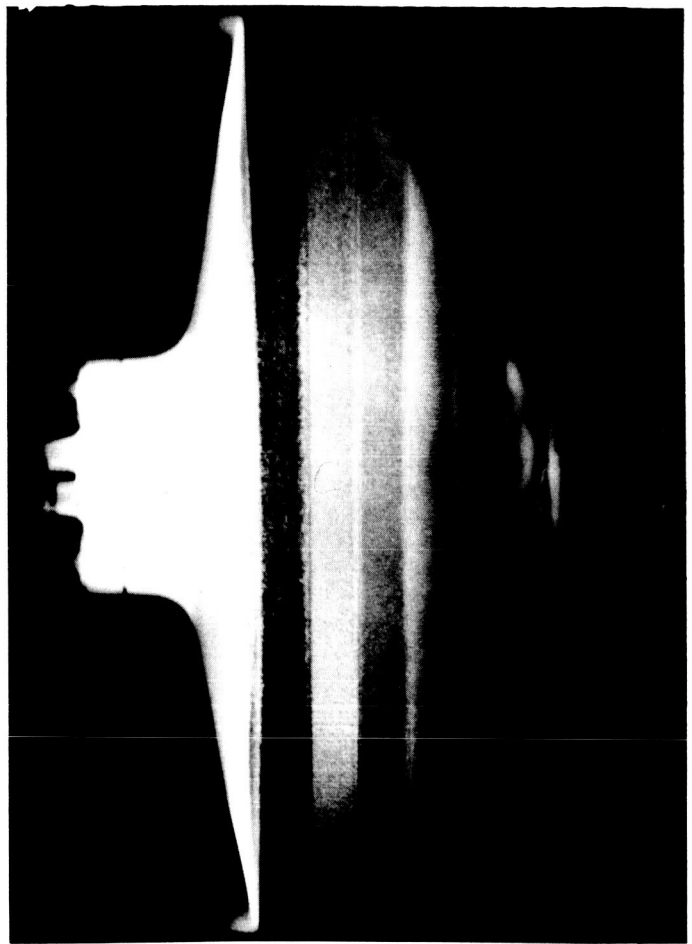
FIG. 3-14a   X-RAY OF FEED SYSTEM SN-2,
EMPTY
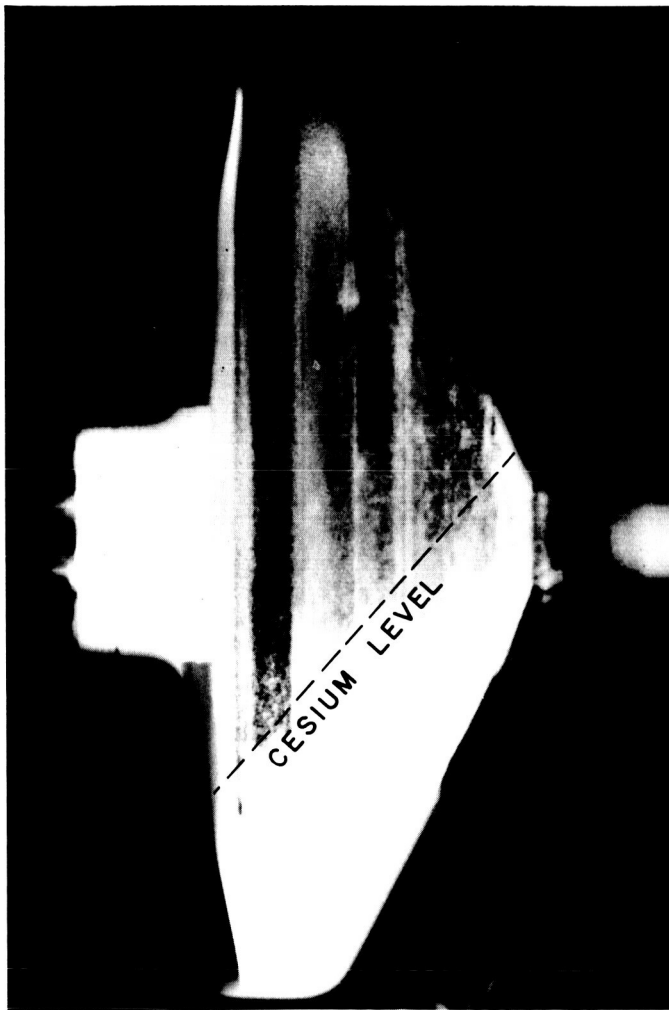
FIG. 3-14b)   X-RAY OF FEED SYSTEM SN-2
LOADED WITH 100 gm CESIUM

As has been discussed, this feed system uses an internal heater which is not in contact with the vaporizer surface. It showed no signs of deterioration during the run and performed satisfactorily during a subsequent run with the engine. However, moving the heater away from the face of the vaporizer affects the response of the system and complicates somewhat the control circuitry.

Approximately 30 grams of cesium remained in the reservoir after flow testing.

Operation With Engine

The SN-2 feed system was operated with the engine, using a laboratory valve. The axis of the feed system was horizontal to ensure that gravitational force played no role in stabilization of the liquid vapor interface. Performance was identical to that obtained during testing of the feed systems by themselves with temperature profiles almost identical to that of Fig. 3-11 and flow characteristics similar to those of Fig. 3-12. Typically, about 25 watts was required for a beam current of about 350 ma.

3.3 Cesium Valves

3.3.1 Solenoid Valve

The necessity of loading and storing the zero-g feed system under vacuum led to the need for an on-off valve to facilitate laboratory use of the system. The S-1 solenoid valve (Figs. 3-15 and 3-16) was developed for this purpose.

During the first part of the contract period, testing and minor modifications of the valve resulted in the lowering of leak rates across the valve seat to less than $10^{-5} \frac{\text{std cc He}}{\text{sec}}$. No major difficulties appeared to prevent the attainment of the design leak rate of $10^{-9} \frac{\text{std cc He}}{\text{sec}}$. It was decided to begin vapor flow testing of the valve since operation at high temperatures with cesium vapor might affect the finish or dimensions of the poppet and seat to such an extent that the careful finishing required to get low leak rates would be wasted effort.

SOLENOID ASSEMBLY

VALVE SPRING

BALL SEAL

COPPER SEAL

VAPOR INLET CHANNEL

VAPOR OUTLET CHANNEL

BODY

FLEXIBLE DIAPHRAGM
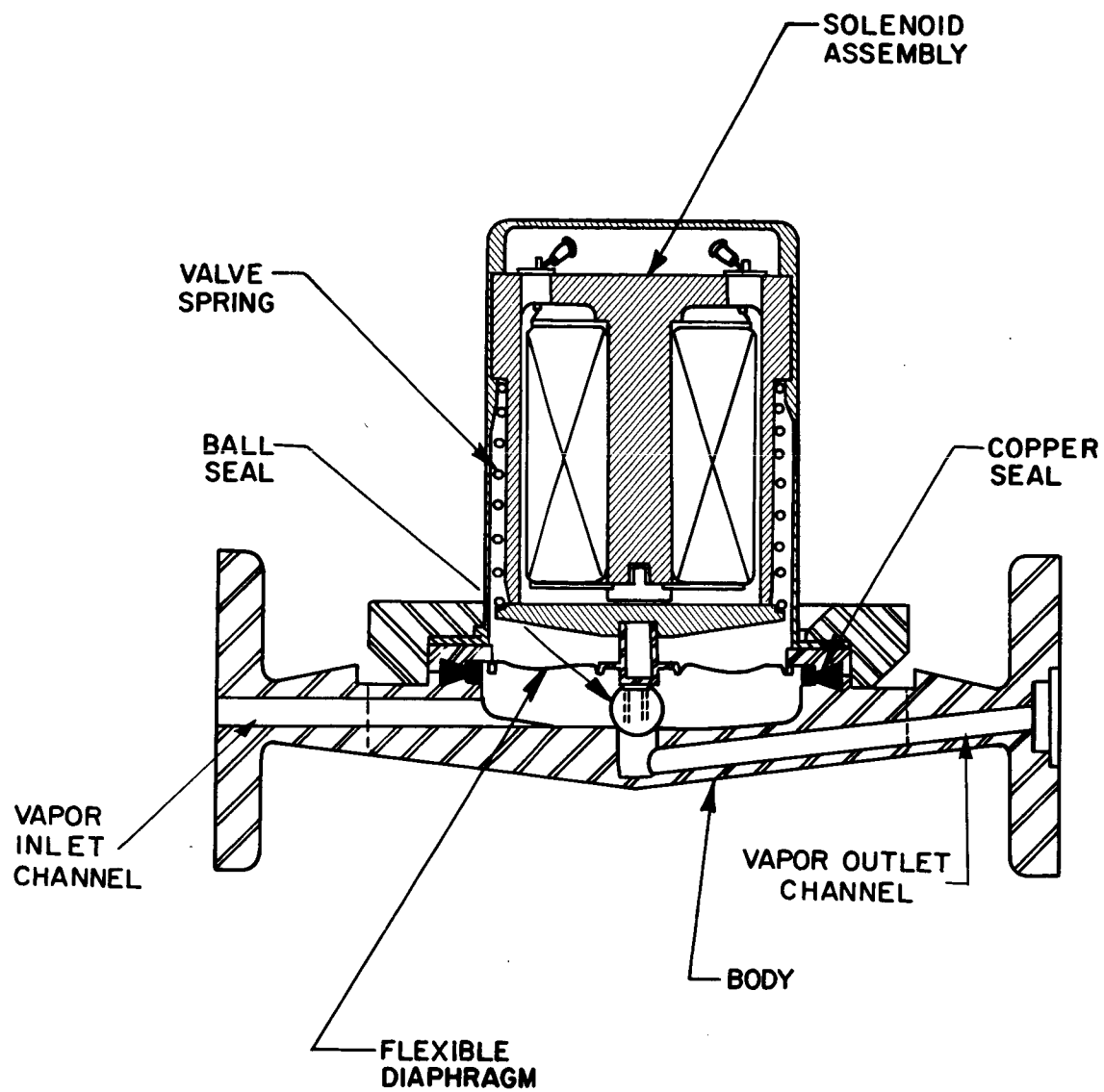
FIG. 3-15   S-1 SOLENOID VALVE
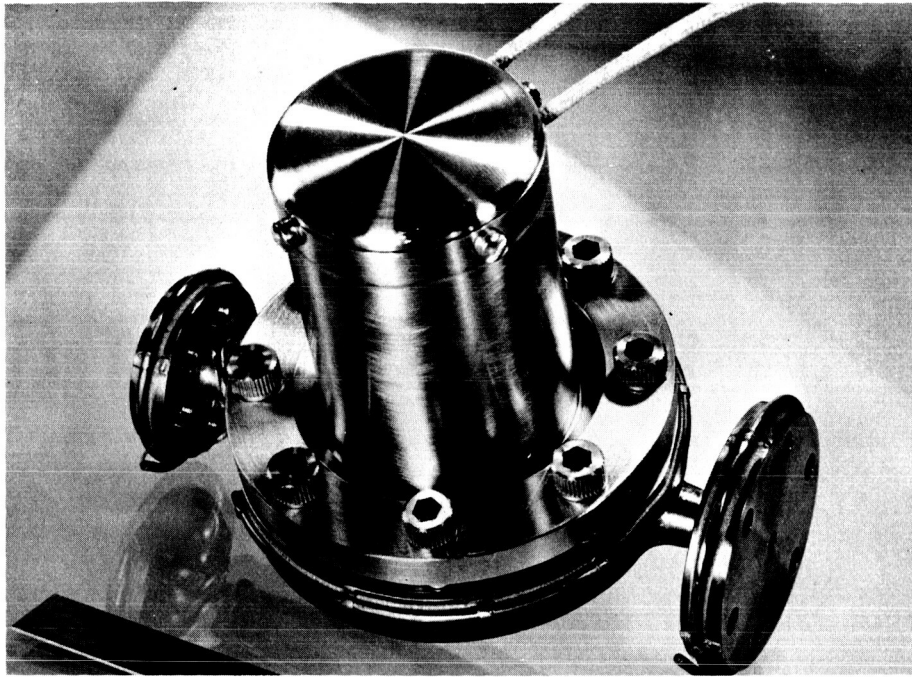
FIG. 3-16a   SOLENOID VALVE
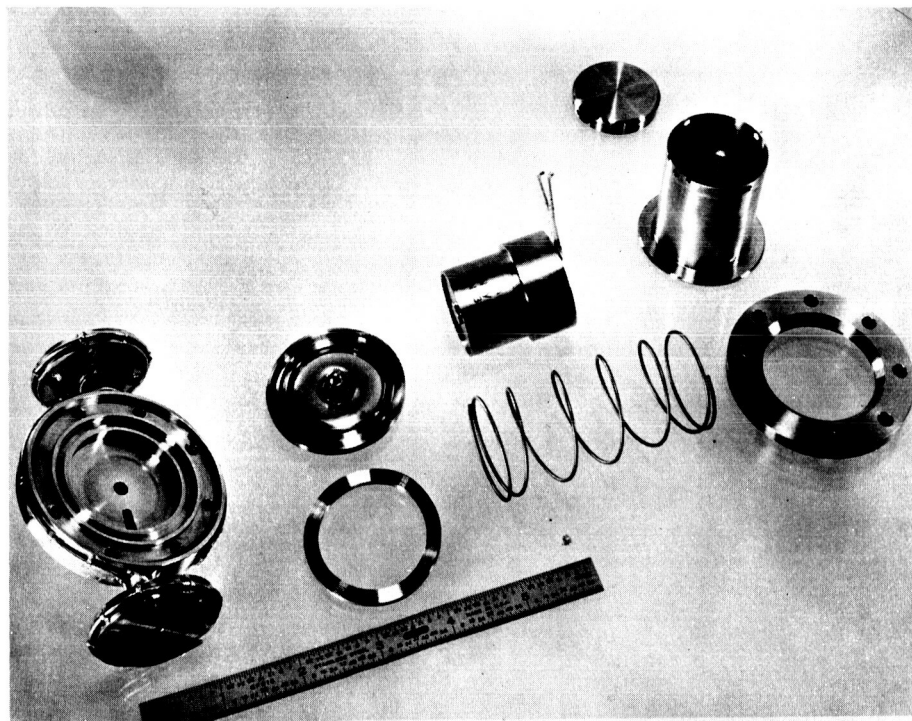
FIG. 3-16b   SOLENOID VALVE PARTS

The valve was mated to a laboratory reservoir and tested with a neutral detector to monitor the vapor flow. Several iron-constantan thermocouples indicated the temperature at various positions on the reservoir and valve. The valve appeared to work quite well. At room temperature, the solenoid current required to open the valve was 250 ma dc but only 30 ma was required to hold it open. The solenoid impedance, 12 ohms at room temperature, increased to 23 ohms at 250°C so that higher energizing voltages were required with the valve hot. A valve energizing circuit was made which uses an RC circuit in conjunction with the solenoid inductance to provide a large energizing current pulse which drops to a steady state dc current sufficient to hold the valve open. This worked well, using 0.3 to 0.6 watts to hold the valve open.

During operation, the highest temperature reached was 460°C at the valve body, at which time the solenoid was at 290°C. The valve body was maintained at about 300°C with a valve heater power of 39.6 watts, and about 400°C at 61 watts. Since no heat shielding was used, the power could be reduced considerably by the addition of radiation shields.

After the test, the valve was leak checked and found to have a leak rate less than $10^{-9} \frac{\text{std cc He}}{\text{sec}}$. Disassembly showed that a thin film of cesium hydroxide had formed on the seat, filling in minute imperfections. After thorough cleaning the leak rate returned to its original value of $10^{-5} \frac{\text{std cc He}}{\text{sec}}$.

The solenoid valve was then used during testing of engines. Further efforts to reduce the leak rate across the seat were continued. One method investigated was the use of a soft metal seat or ball. Copper, for example, is readily deformed even under the low forces exerted by the valve spring. A copper ball was fabricated and tested. However, due to a rocking motion of the diaphragm assembly it was found that the ball was initially seating off center. In order

to eliminate undesirable effects of the rocking motion, a modified diaphragm assembly was designed which allows only motion about the ball center. The ball can, therefore, never rotate out of position. New diaphragm assemblies were then fabricated and testes. Unfortunately, these did not perform as expected and had to be discarded.

Some modifications which were included in the final valves are the incorporation of new seal configurations at the flange surfaces and minor redesign of the solenoid housing to allow the use of stronger valve springs. Springs capable of exerting several pounds of force can be used, and one of 7 pounds was chosen for the final valve.

These changes resulted in increased opening and holding current requirements. The valves now require 1.5 amp opening and 100 milliamps holding current, These modifications resulted in a valve which upon initial assembly had a measured leak rate of less than $10^{-9} \frac{std\ cc\ He}{sec}$. However, after operation with an engine and feed system, which included several temperature cycles, the leak rate had increased to $10^{-4} \frac{std\ cc\ He}{sec}$. At this point it was decided that it was not feasible to attempt to store the cesium under vacuum in the DE feed system. Another solenoid valve was added so that the system could be stored with an inert gas within it and evacuated through the rear. The complete system, with both valves, is shown in Fig. 3-17.

The additional valve replaces the pinch-off tube formerly used to seal the back of the reservoir. Since the temperature remains relatively low in the rear of the reservoir, this valve can use nonmetallic seals (Buna-N rubber) and presents no leakage problems.

When loaded in the dry box (under argon) the feed system is no longer pumped out but maintained with inert gas under atmospheric pressure. After assembly to the engine and check out, the system is heated to insure that the cesium is liquid. After installation in the vacuum facility and immediately after "roughing" is started, the rear valve is opened by energizing its solenoid and
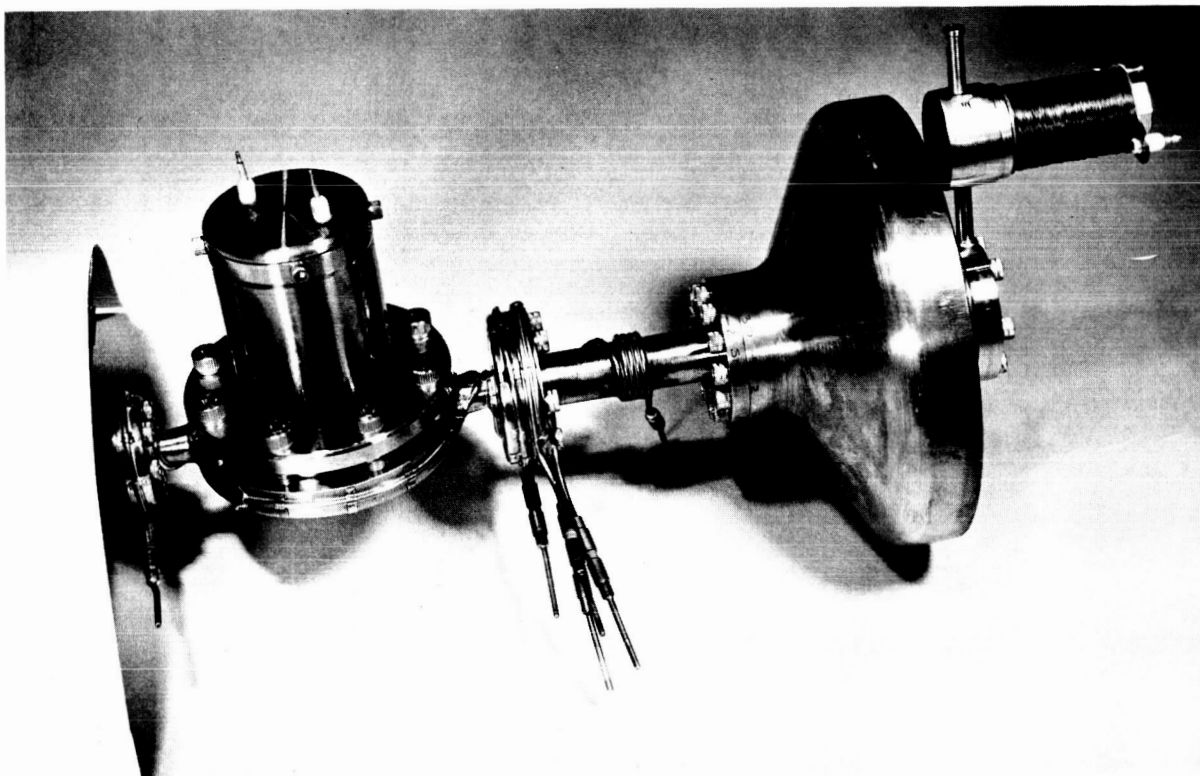
FIG. 3-17   DE FEED SYSTEM

kept open until high vacuum is obtained in the facility. The valve is then closed and the feed system has been evacuated in such a way as to insure that trapped gas pressure does not force cesium through the vaporizer and into the feedline or front valve.

3.3.2 Diaphragm Piercing Valve

Both valves on the present feed system are necessary only for laboratory operations. They are used so that the system may be removed from the vacuum environment for periods of time without necessitating the clean-up and reloading of the feed system. For a space system they would not be necessary if the cesium were stored under vacuum. In this case a pinch-off seal would be used to seal the rear of the system after evacuation. The feed line would be sealed with a diaphragm. A piercing device would rupture the diaphragm when the feed system is to be activated. A diaphragm piercing valve design is shown in Fig. 3-18.

The valve consists of the diaphragm assembly which seals the feed system and the piercing mechanism which breaks the diaphragm upon actuation. The valve is actuated by melting the wire link which holds the plunger. The spring then forces the plunger through the diaphragm and opens the valve. One of the features incorporated into the design is that the diaphragm assembly can be separated from the valve proper. This simplifies the handling of the feed system during loading while maintaining a vacuum tight seal. Another interesting feature is the novel method of sealing the valve after actuation which eliminates the need for any bellows. Upon actuation the conical sealing surface on the plunger mates with the conical sealing surface on the valve body. Several tests with a test assembly have shown the feasibility of this approach. The valve is small and relatively light-weight and for space applications both the weight and size could be reduced considerably.

FUSIBLE LINK

HOUSING

SPRING

PLUNGER

CONICAL SEAL
SURFACES

VAPOR
OUTLET
CHANNEL

VAPOR
INLET
CHANNEL
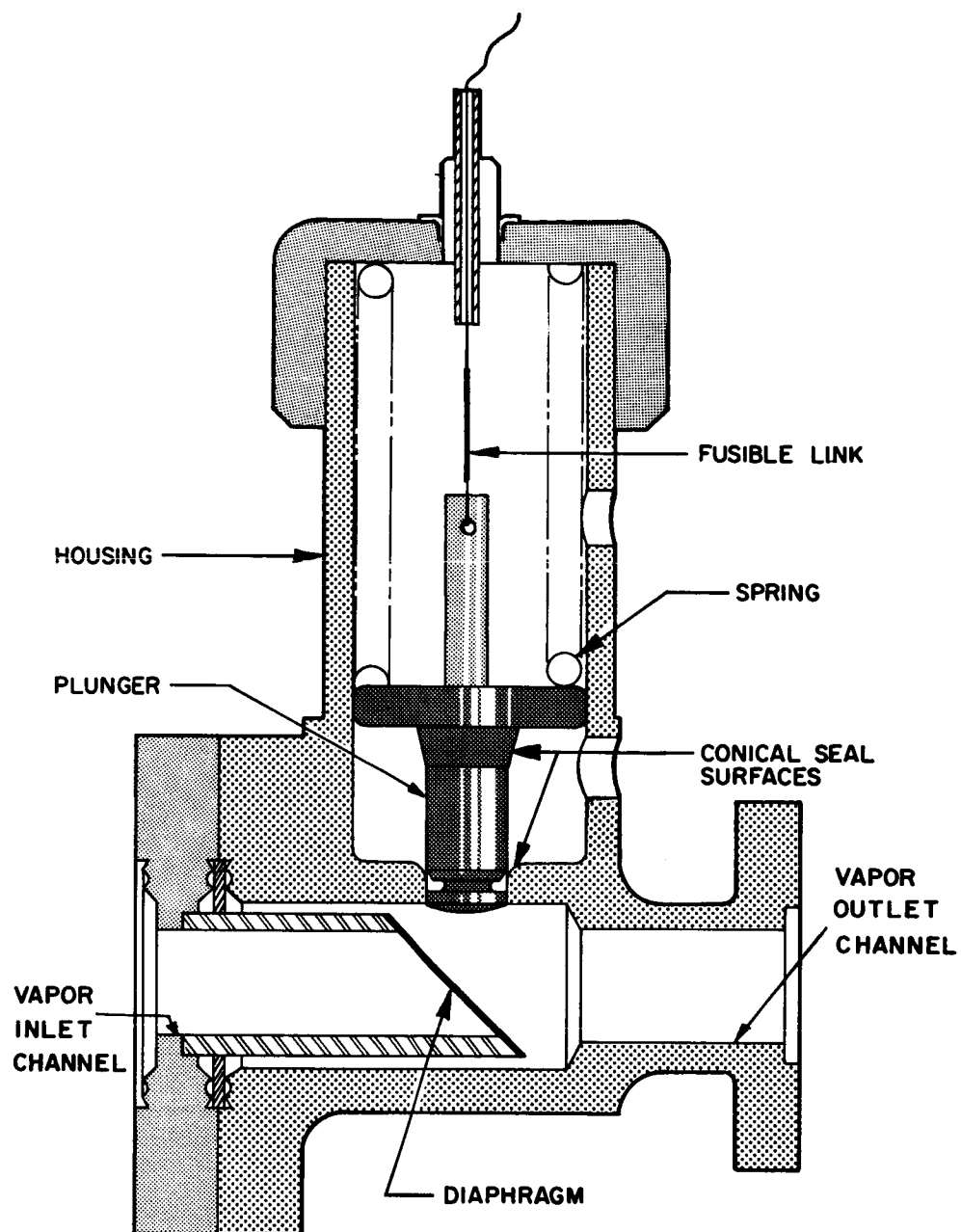
DIAPHRAGM

FIG. 3-18   DIAPHRAGM PUNCTURING VALVE

3.4 DE Feed System

The DE engine feed system, (Fig. 3-17) although similar to the preliminary system, incorporates some important advancements. Among these are a new flange seal design which has been found to be superior to the preliminary design. It was expected that problems arising due to vacuum leaks at joints in the feed system would be greatly reduced. A second area where vacuum leaks have been present is in the feed system housing. For the preliminary feed systems the housings were formed by spinning; however, the spinning operation was found to be too severe and many cracks developed. Housings for the DE engine system are machined to avoid this problem.

A third innovation was a removable vaporizer heater section. (Fig. 3-19) This serves two purposes. It considerably simplifies inspection of the porous inserts and it facilitates changes of heater and porous insert configurations.

3.4.1 DE Feed System Tests

At the beginning of the fourth quarter, a DE feed system was operated with the DD engine. When the first attempt to start the engine was made, the temperature on the wall of the vaporizer tube rose very rapidly to the order of 500°C. No flow rate was observed through the valve, indicating that the cesium had not wet the porous inserts in the vaporizer section of the feed system. The body of the reservoir had been wetted and filled separately from the vaporizer section prior to completing the assembly. The vaporizer was then held at a temperature of about 400°C for the purpose of heating the neck of the reservoir to the wetting temperature of the nickel inserts. After heating for an hour the cesium wet the nickel and feed was suddenly established.

Engine operation was established and the response of the feed system was checked to ascertain that the new system response
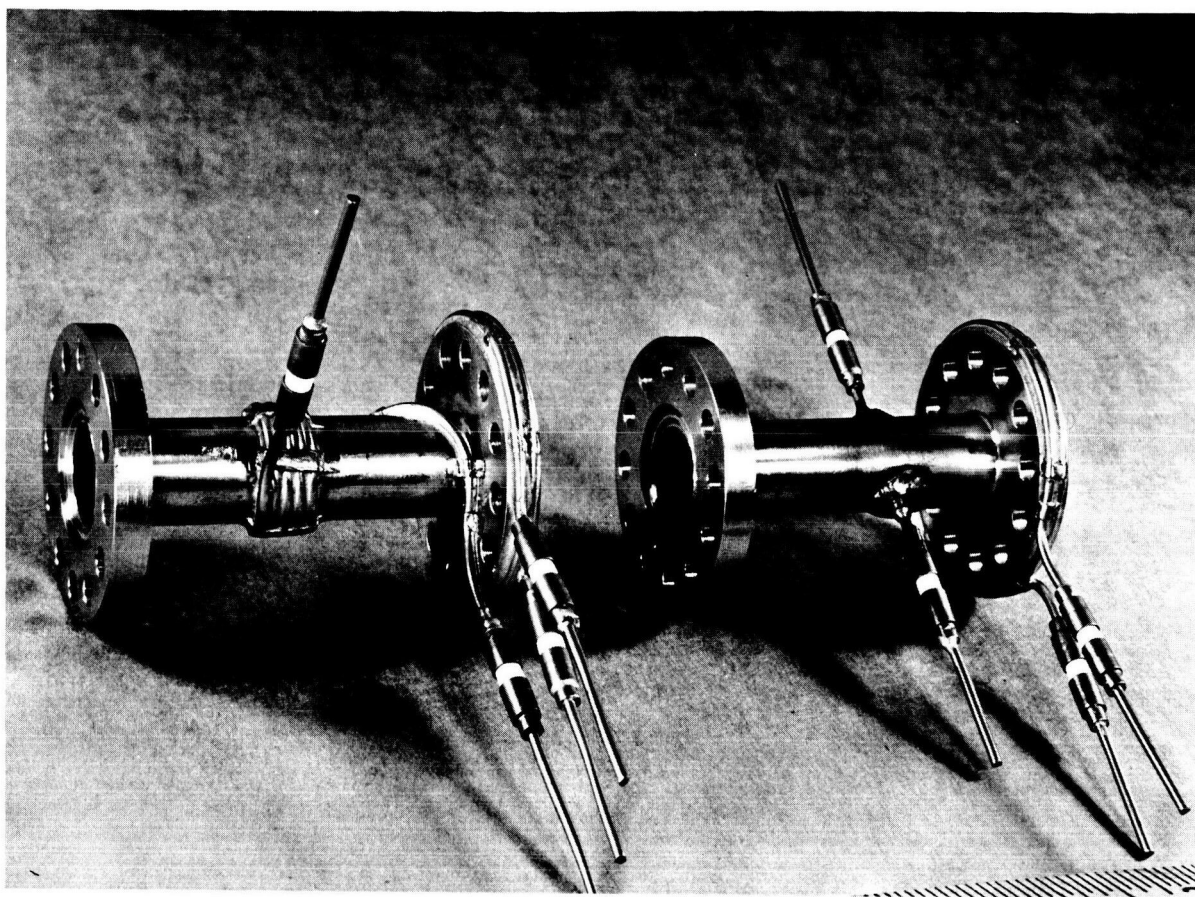
(a)   Internal Heater   (b)   External Heater

FIG. 3-19   VAPORIZER HEATER ASSEMBLIES

was similar to the preliminary. Figure 3-20 shows the response of the preliminary feed system. Figure 3-20 shows the response obtained from the DE prototype feed system using the same electrical lead-log network for feedback compensation as was used with the prototype. These responses are due to step changes in the beam demand. As can be seen, the response is similar although the DE feed system appears to have less delay and somewhat greater stability.

With the engine operating near 400 milliamperes of beam current, the vaporizer temperature was 330°C. This is considerably above the temperature of 250°C where the prototype feed system vaporizer operated. After operating at a beam level of about 400 milliamperes for 20 minutes, the feed began to drop and the control system heated the vaporizer to 500°C at which time the control loop was opened and the vaporizer was allowed to cool. Feed could not be reestablished until the vaporizer had cooled for 10 minutes to 220°C. This occurrence has been observed during feed system flow tests where the vaporizer temperature was raised to the point where the force of the cesium vapor pressure overcame the surface tension force in the porous nickel. When this occurs the liquid cesium is forced away from the interface toward the rear of the reservoir. Subsequent increase in interface temperature aggravates this condition and reduced the feedrate to negligible levels. Once the cesium is forced back from the front insert, the larger pores toward the rear of the reservoir provide less force. Thus, once begun, this breakaway continues.

In an attempt to determine the flow rate or vaporizer temperature where the breakaway occurred, the engine was operated at successively higher beam levels until breakaway occurred. The engine beam current and vaporizer temperature are shown versus time in Fig. 3-20. The changes in beam level were made by increasing the beam reference level in the feed control loop; the "demand" parameter is a dial setting.

At point A in Fig. 3-21, a rise in vaporizer temperature was observed. The feed loop was opened at point B when the vaporizer
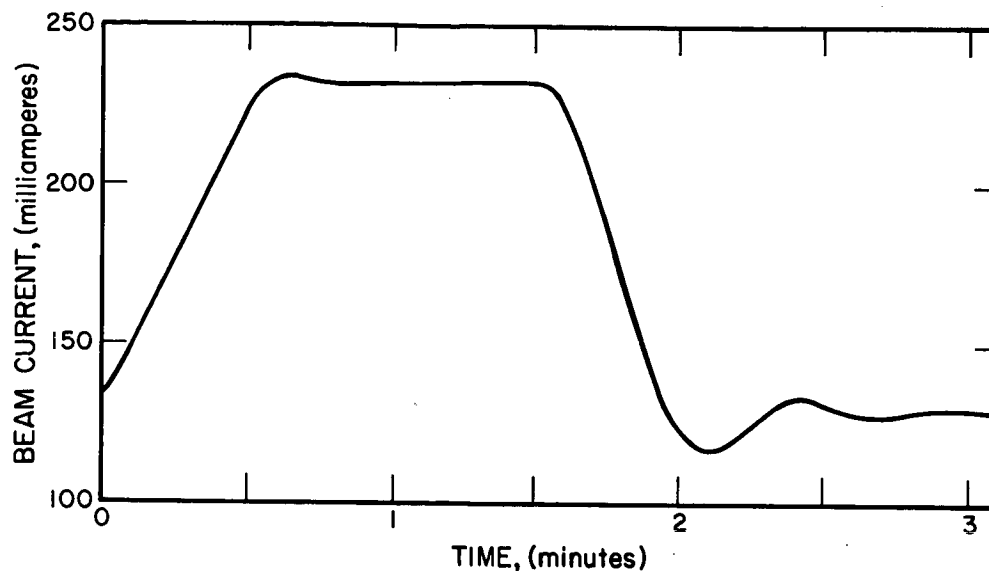
a   DD (Preliminary) FEED SYSTEM RESPONSE (Compensated)
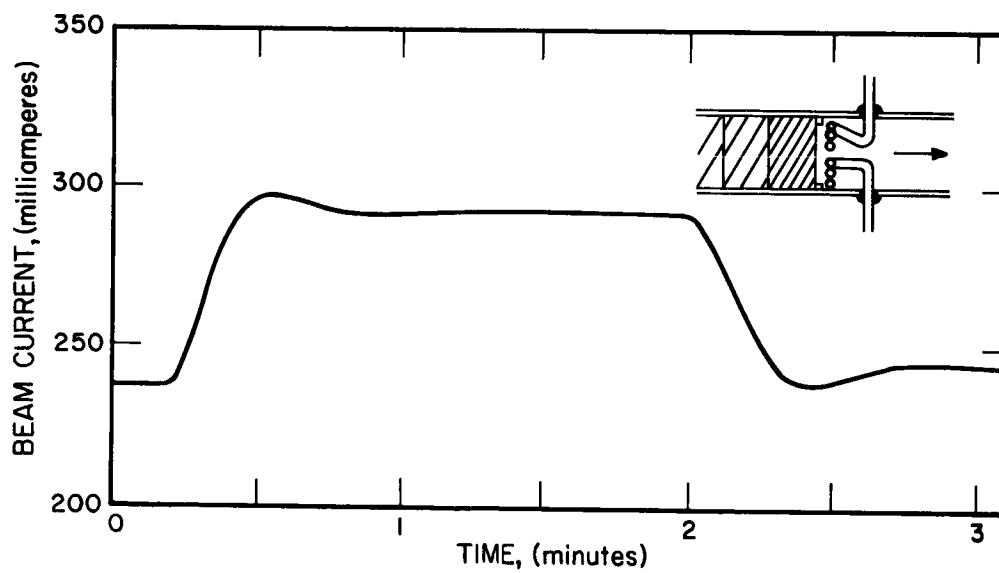
b   DE (Prototype) FEED SYSTEM RESPONSE (Compensated)

FIG. 3-20   DD AND DE FEED SYSTEM RESPONSE

temperature had reached 400°C. Operation was subsequently restored by cooling the vaporizer.

The reason for the susceptibility of this feed system to break away appears to be due to a loose fit between the porous nickel inserts and the outer wall of the vaporizer tube. This would reduce the surface tension feed force, dependent upon the largest pores in the system, to a level incapable of supporting normal operating vapor pressure. This would also account for the excessive temperatures at which the system operated.

The presence of a significant delay in the response of the system indicated that the heat reached the vaporizer interface by conduction along the wall of the assembly. At a vaporizer filament temperature of 400°C, only about one watt could be transmitted to the interface by radiation whereas conduction to the wall of the tube from the outer turn of the internal heater could conduct several watts to the vaporizer, with a temperature differential of only 10 to 20°C. In view of this a vaporizer with an external heater was designed and built for testing with the DE feed system.

The detail of the construction of the external-heater vaporizer is shown in Fig. 3-22a along with a plot of the feed system response using no compensation. (The inside diameter of the vaporizer tube is one-half inch for reference.) The delay characteristics of the internal heater vaporizer is considerably reduced and the feed system is no longer oscillatory when uncompensated. The rise time of the system is about one-third that of the internal heater system. This vaporizer operated at a wall temperature of 260°C with an input power of 9 watts. Minor electrical feedback compensation was used to obtain the response shown in Fig. 3-22b.

The external-heater feed system replaced the internal heater system originally designed for the DE engine. In addition to the improved response, this type of heater is far more reliable since it requires less flexing during fabrication and is not subject to cesium attack. The elimination of the hermetically sealed feedthroughs is also an advantage.

3670-Final

104
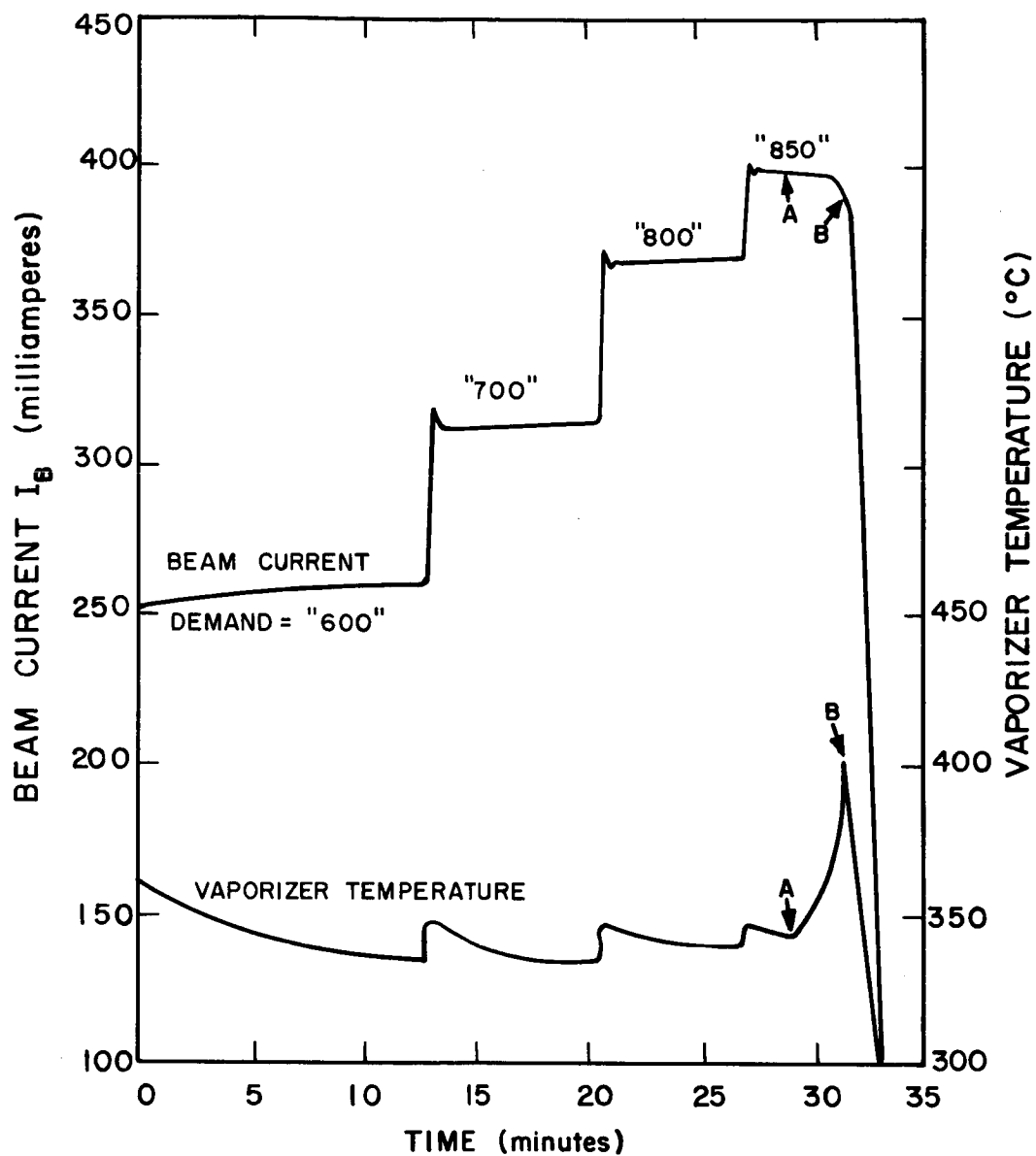
FIG. 3-21   BEAM CURRENT AND VAPORIZER TEMPERATURE
RESPONSE CHARACTERISTICS
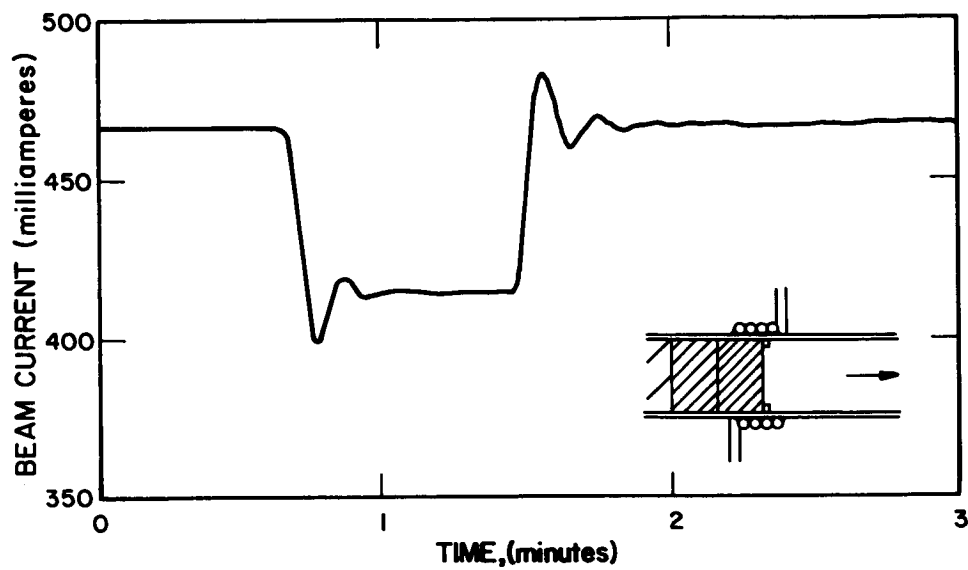
FIG. 3-22a FEED SYSTEM RESPONSE WITH EXTERNAL VAPORIZER
HEATER (Uncompensated)
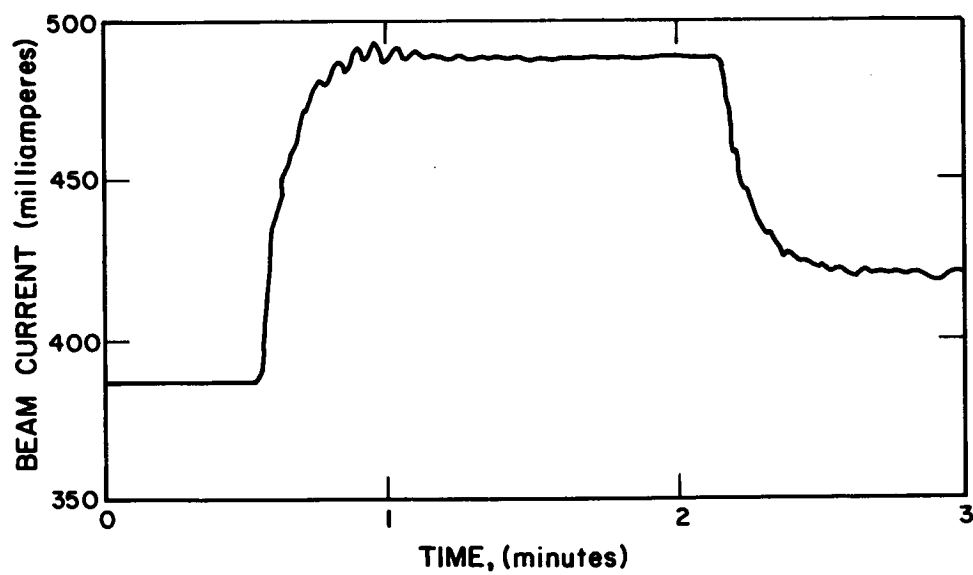
FIG. 3-22b FEED SYSTEM RESPONSE WITH EXTERNAL VAPORIZER
HEATER (Compensated)

3.4.2 Qualification Tests

The DE feed system underwent qualification testing with the engine and control system. These tests consisted of ten automatic start-stop operations and a 77-hour run. The tests are described in detail in Section 5 but certain aspects of the 77-hour run, pertaining to the feed system, will be discussed here.

For the first 56 hours of the long run both the vaporizer temperature and power remained relatively constant. They showed a slight increase with time as is usually encountered under normal operation. This increase is not fully understood but is considered to be the result of three factors:

1. Change in emissivity: As the run progresses the area around the vaporizer heater darkens. This increase in emissivity would lead to more radiation loss and would require an increase in power to maintain a constant flow rate and temperature.

2. Partial clogging of vaporizer surface: As cesium is vaporized from the front insert surface, low vapor pressure impurities are left behind. These can decrease the vaporizer surface area and may lower the vapor pressure. To maintain a constant flow rate the power and temperature would increase.

3. Deposits in valve: After an engine run, a partial buildup of contaminants is observed in the valve. The restriction caused by these deposits on the valve ball would increase the valve impedance and lower the flow rate. The power would then increase to maintain a constant flow rate and the temperature would rise.

At 56 hours and again at 72 hours as indicated in Fig. 3-23, large and rapid changes in power and temperature occurred. These were associated with feed instabilities or "breakaways" but after smooth engine operation was resumed the vaporizer temperature and power necessary to maintain the feedrate was significantly higher. Again, the occurrences are not understood but some possible explanations are presented:
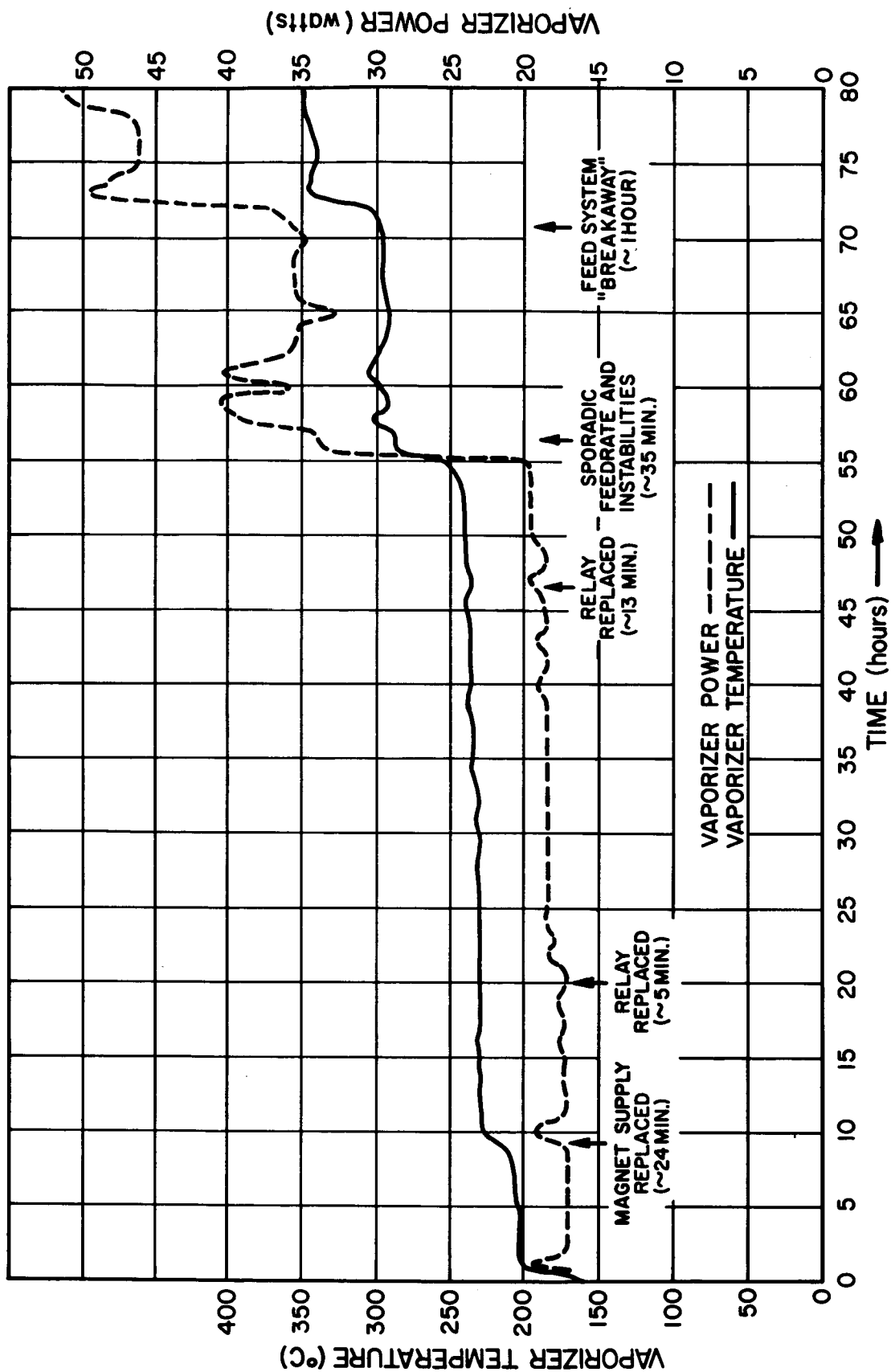
FIG. 3-23   VAPORIZER TEMPERATURE AND POWER DURING 77-HOUR RUN

1. Changes in surface contact: Due to the difference in the coefficients of expansion between nickel and stainless steel a gap may develop between the heater and the porous inserts. This gap would lower the conduction to the inserts and would require increased heater temperature and power for a constant flow rate.

2. Partial breakaway: If the cesium is forced from the vaporizer surface, the conduction decreases and higher temperature and power are required to maintain a constant flow rate.

3. Gap development: Should a gap develop between inserts, cesium would no longer be fed to the vaporizer surface. The heat must then be conducted for a greater distance and the vaporizer temperature and power would increase. The power and temperature must also be increased due to the vapor flow impedance of the now empty insert or inserts.

The only conclusion that can be drawn at this time is that these changes occur after considerable operating time and are either due to clogging effects related to the amount of cesium delivered by the system or depletion of the amount of cesium remaining in the reservoir. Inspection of the system upon disassembly disclosed no significant contamination of feed system components.

3.5 750-Hour Feed System

An addition to the present contract was made which called for the fabrication and test with an engine of a feed system having a capacity (about five pounds of cesium) which would fuel the present engines for 750 hours. The design of such a system was in existence and a development effort was already being undertaken (Ref. 2).

Many advantages over previous surface tension feed systems are offered by the new configuration. It is lighter in weight since a majority of the porous material has been replaced by thin fins. Further, the reservoir body approaches a more spherical shape and can therefore utilize a much thinner wall thickness and still be structurally

strong. Other advantages are that the possibility of trapping significant quantities of propellant is eliminated, the porous metal rod is easily removable, thus making it possible to inspect the rod for clogging or allowing replacement with rods of other materials or other pore sizes, and the loading and cleaning operations are considerably simplified.

When assembled, the feed system shown in Fig. 3-24 has a diameter of 6 inches and an overall length of approximately 8 inches. It contains 72 radial fins of 0.005-inch thick stainless steel. These feed the cesium to the central porous rod which is 0.5 inch in diameter and about 5-1/2 inches long. A vaporizer heater near the end of the rod provides the energy required for vaporization of the propellant. The heater is a sheathed heater having an inner conductor of stainless steel 0.020 inch in diameter. The inner conductor is surrounded by a magnesium oxide insulator which in turn is covered with a stainless steel sheath. The last item is a right angle elbow which directs the cesium vapor stream to the engine. It is heated with a sheathed heater similar to the vaporizer heater just described. During operation, the elbow is maintained at a temperature above the cesium dew point so that no condensation can occur.

3.5.1 750-Hour Feed System Test

Typical test data obtained during a test of a similar feed system appear in Fig. 3-25 (Ref. 2). The data were accumulated at several different times during the course of a 65-hour run which consumed a total of 694 grams of cesium. A detector reading of 1 micro-ampere here is equivalent to a flow rate of 0.278 amperes of cesium ions.

3.5.2 Operation With Engine

The 750-hour feed system was mated to a DE engine and run for approximately 90 minutes. The feed system worked well with response times generally shorter than those of the DE feed system.

FIG. 3-24   750-HOUR FEED SYSTEM

RUN 5B-3 11/4/63 TO 11/8/63
DATA OBTAINED AT SIX DIFFERENT
TIMES DURING THE RUN WHICH
LASTED 65 HOURS
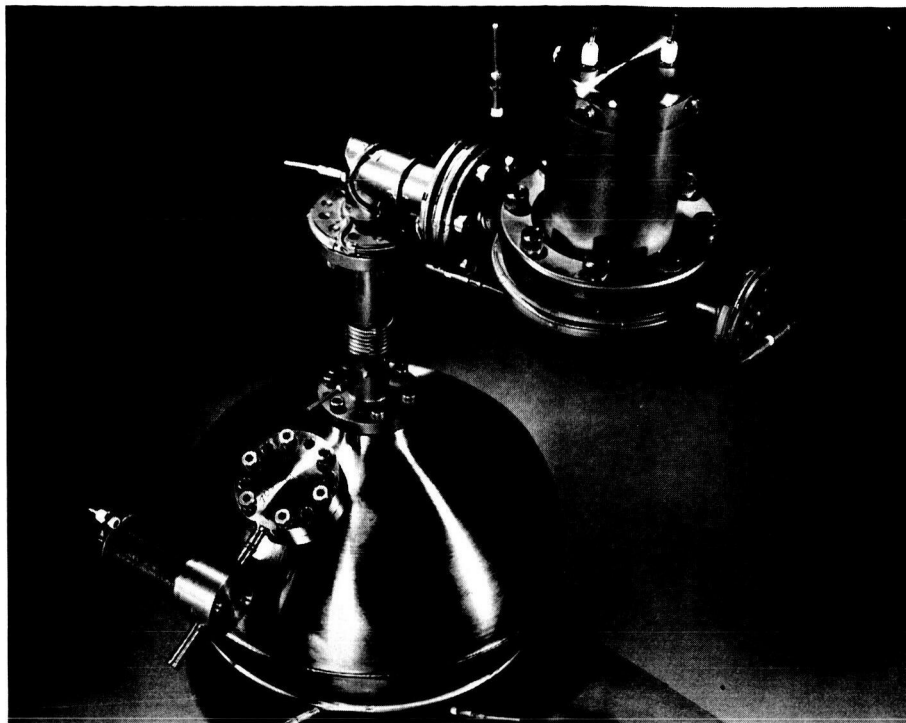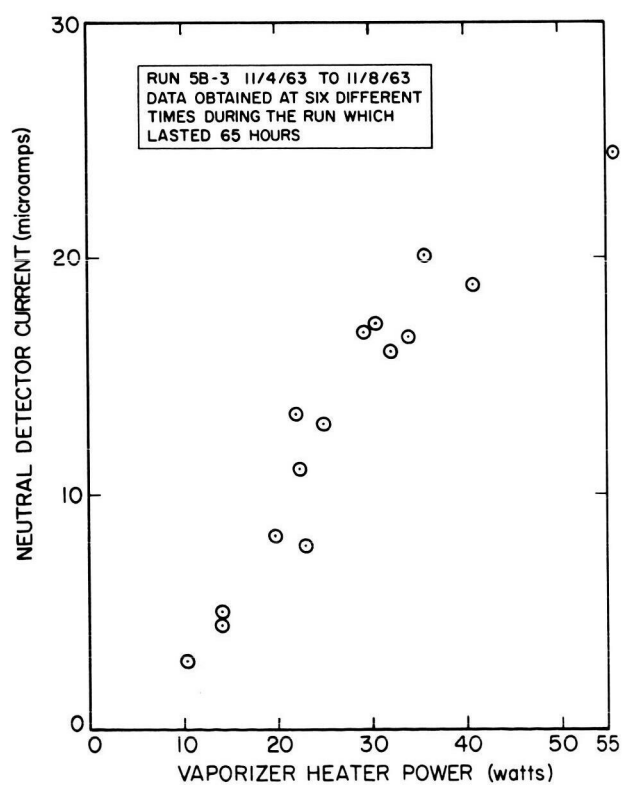
FIG. 3-25

750-HOUR FEED SYSTEM TEST
DATA

4. CONTROL SYSTEM DEVELOPMENT

A substantial amount of work has been done at EOS on development of ion engine control systems, both in the area of analytical and experimental investigations of engine control schemes and in the area of development of flight hardware versions of previously conceived and tested control systems. A large part of this already existing technology was immediately applicable to the electron-bombardment engine control system.

The process of achieving a satisfactory engine control system was, however, an experimental one since it was not possible to predict in detail the response to various control situations. The development program thus proceeded by conceiving several control systems, designing and building the necessary experimental equipment, trying the systems in the laboratory, and, on the basis of the data taken, adopting a satisfactory system and including any necessary modifications or refinements.

4.1 Preliminary Control Schemes

Some control systems and subsystems initially considered for experimental evaluations are shown in Figs. 4-1 to 4-4. In Control System I, there are three feedback loops controlling cesium feed rate, arc voltage, and magnet current. In loop 1, a beam current signal and an "equivalent neutral current" signal are added to give a signal proportional to feed rate which is used to stabilize feed rate at the desired level. The second loop adjusts the arc voltage to produce the required beam current, while the third loop uses a modulator and phase sensitive demodulator to adjust the magnet current for maximum beam current. This appeared to be a good system.
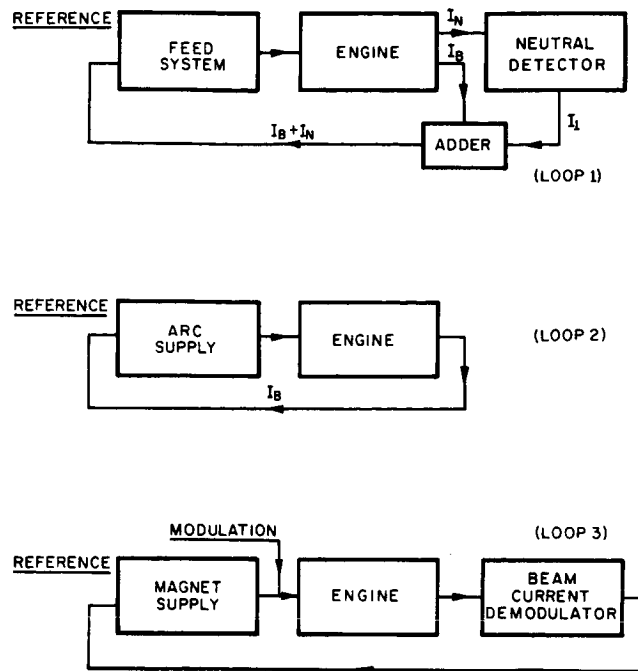
FIG. 4-1   CONTROL SYSTEM I
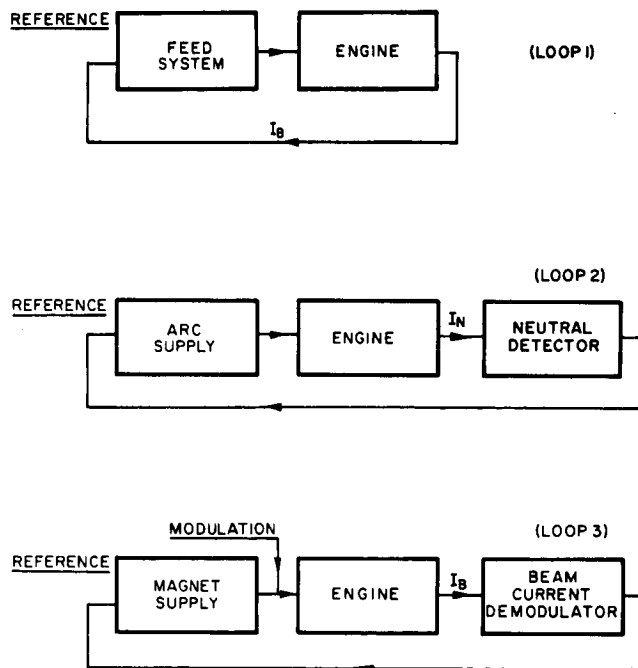
FIG. 4-2   CONTROL SYSTEM II

The second and third loops are strongly coupled since they both have beam current as the controlling variable. The first loop, however, is independent of the others since only the cesium feed rate is involved. This feature simplifies the system by decreasing the number of loop interactions and by decreasing the complexity of the action taken in case of engine sparking. The principal disadvantage of this control system is the requirement for a neutral cesium detector with no calibration change or zero drift. The effect of this system is to produce engine operation at specified thrust level and specific mass efficiency with little restraint on arc power or power efficiency.

Control System II also has three loops as shown in Fig. 4-2 and represents a variation on the first scheme. In loop 1 the beam current is used to control feed rate, in loop 2 the neutral detector signal controls arc voltage, and in loop 3 the magnet current is adjusted as before for maximum beam current. As in System I, operation is stabilized at specified thrust level and mass efficiency.

If, at a given beam current, the variation of neutral efflux with arc voltage is stable and reproducible, the scheme shown in Fig. 4-3 might be substituted for loop 2 in Control System II. The arc voltage is modulated and the appropriate frequency component of the neutral signal used to control the arc supply. This amounts to stabilizing at a specified value of the derivative of equivalent neutral current with respect to arc voltage. If satisfactory, the need for a calibrated, no-drift neutral detector is eliminated; the background subtraction from the detector, now used as a differential detector would be automatic and require no mechanical shutter.

There was some experimental evidence that loop 3 involving the magnet current would not be necessary. In one series of tests it was found possible to cycle an engine from shutdown to full thrust and back without having to make any adjustment of magnet current. If this was found to be possible for the DD and DE engines a substantial simplification in the system could be made.
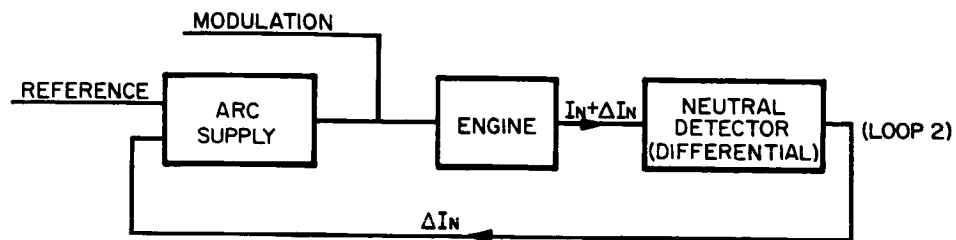
FIG. 4-3   ALTERNATE ARC CONTROL LOOP FOR CONTROL SYSTEM II
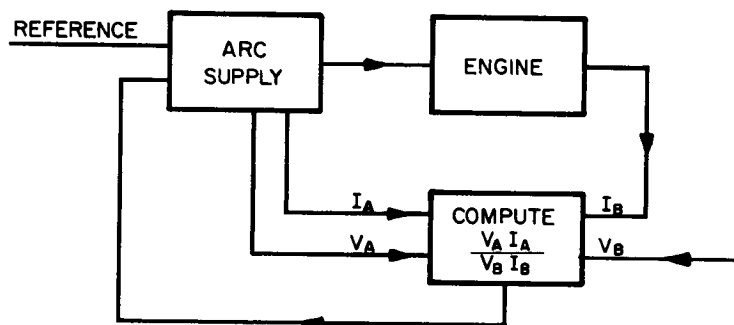
FIG. 4-4   ARC CONTROL LOOP FOR CONSTANT POWER
            EFFICIENCY CONTROL SYSTEM

Several other systems were also considered; one of these involved stabilizing the engine at a preset power efficiency instead of a preset propellant utilization efficiency; part of this system is shown in Fig. 4-4. As before, the feed system is controlled to produce the required beam current or thrust. The beam voltage, beam current, arc voltage, and arc current are fed into a computing element which generates $V_A I_A / V_B I_B$, a quantity related to the power efficiency of the engine. This system is relatively complicated but presented an alternative to controlling the mass utilization efficiency.

4.2 Initial Feed Loop Tests

Prior to designing any hardware for the control system or subsystems, a test was made to check the performance of an automatic feed system control. The system used is shown in Fig. 4-5. The main element is the linear power controller, a commercial component using magnetic amplifier gating and silicon controlled rectifiers. The rms output voltage is controlled in an approximately linear fashion by the algebraic sum of the currents in the control windings. In operation, the controller responds to the difference between a bias signal and the beam current to be regulated. Since the gain of the system is large, an operating point is reached where the bias signal and beam current are very nearly equal.

This feed rate control system was used with the 10 cm engine (Ref. 1), and a laboratory cesium reservoir. Figure 4-6 is a condensed reproduction of a strip chart recorder running at 2 inches per minute. The only controlled parameters were cathode heater power and control system bias current setting. The cathode heater supply was turned on when the arc current was below 10 amperes and off whenever the arc current exceeded 10 amperes.

In Fig. 4-6, prior to point (1), the engine had been operated to see if it was in serviceable condition. It was then turned off and restarted with the reservoir being heated by the control system. Operation was run through points (2) to (10) by changing the bias signal to the
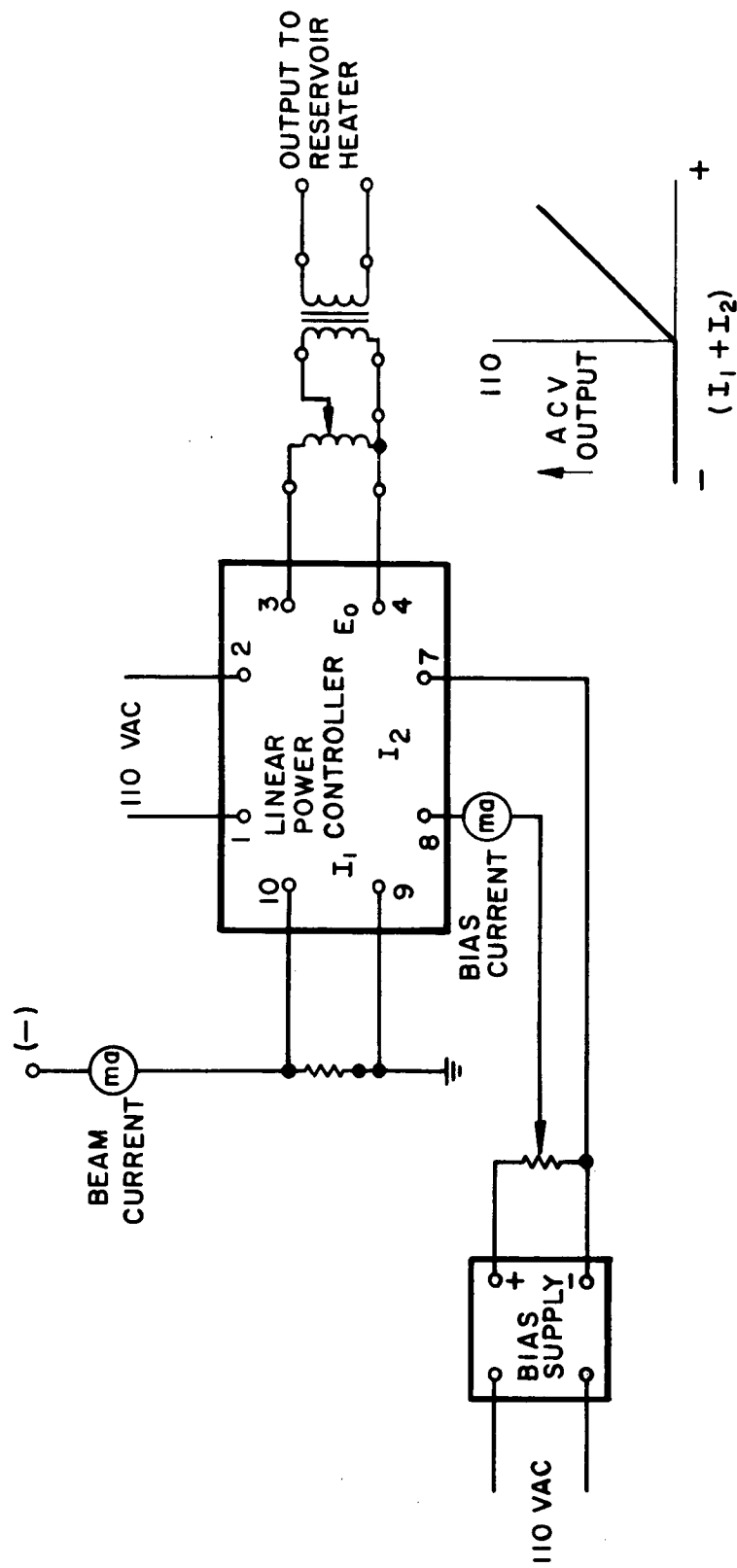
FIG. 4-5   FEEDRATE CONTROL SUBSYSTEM
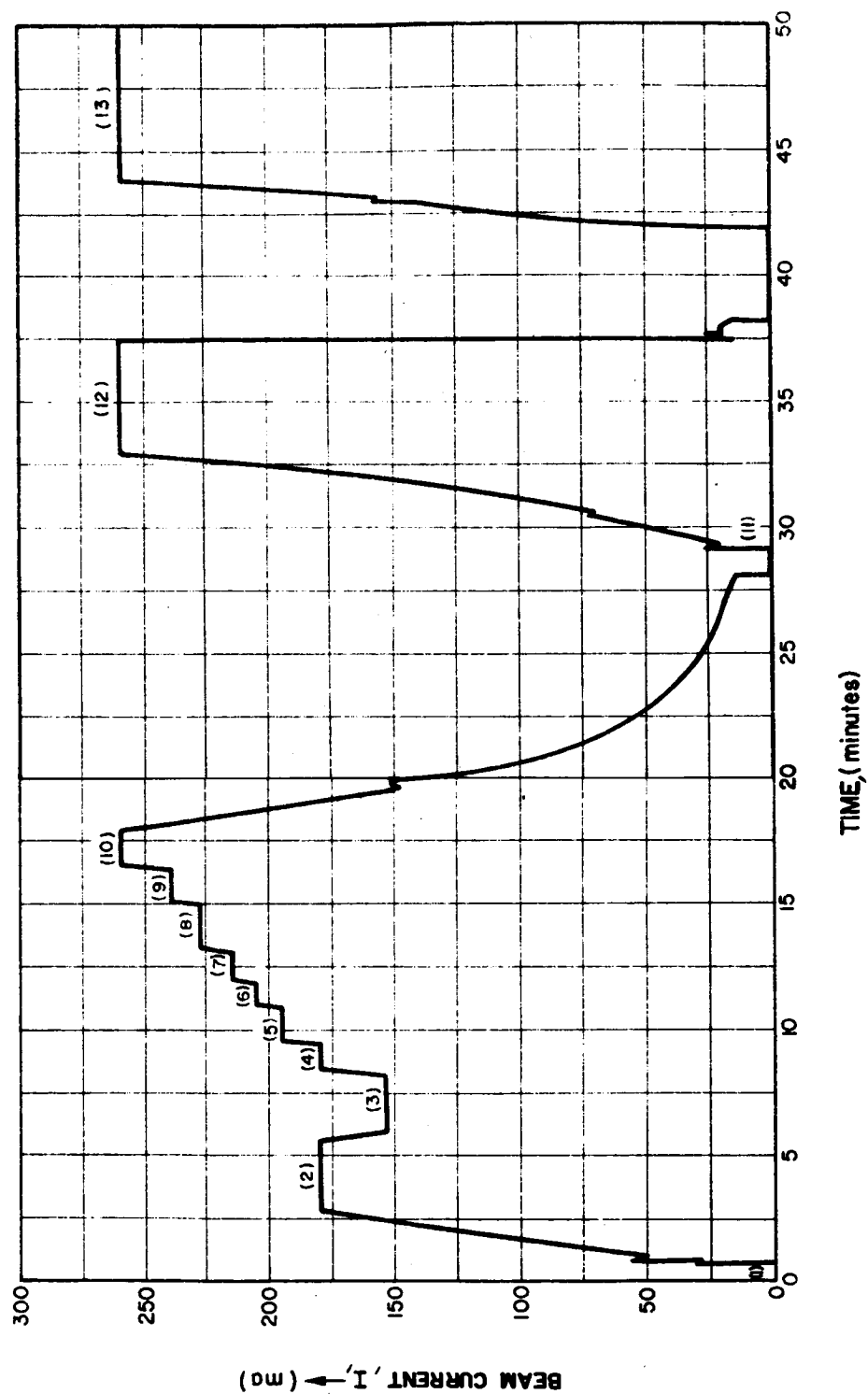
FIG. 4-6   FEEDRATE CONTROL SYSTEM TEST – CESIUM ION CURRENT VS TIME

controller. At the end of (10) the bias signal was dropped to zero. At point (11) in Fig. 4-6, the bias setting of the controller was reset to its value at point (10). The resultant operation at (12) was identical to that at (10). At the end of (12), the engine was turned off by closing the valve. The reservoir was allowed to cool to 200°C and the valve opened and the controller was turned on. Point (13) is the operation established and is identical to that of (10) and (12).

While these tests were made with a laboratory feed system and the 10 cm engine, the results were promising. The zero-g feed system was expected to have faster response characteristics and work as well or better with a control system. At any rate, these tests seemed to indicate non-critical start up characteristics and stability for this type of engine system.

4.3 Initial Neutral Detector Tests

When the DD engine was assembled, a neutral detector was mounted in the vacuum tank, and the problem of reliability of neutral efflux measurements on the gas discharge engine was investigated.

Some data taken are presented in Figs. 4-7a, 4-7b, and 4-7c for different operating conditions. For a given feed rate, the accelerating voltages and magnetic field were left unchanged and the arc power was reduced from that giving the maximum beam current, I_M, shown on the figures. With the beam current plotted against the neutral efflux detector signal, the curves can be seen to be extremely linear. From the intersection of the line with the beam current axis (vertical axis), the mass flow rate, I_o, is obtained. Together with the maximum extracted beam current, I_M, this gives a mass utilization factor

$$\eta_M = \frac{I_M}{I_o}$$

Alternatively, if i_1 is the neutral detector signal when I_M is extracted and i_2 is the intersection with the neutral detector signal axis
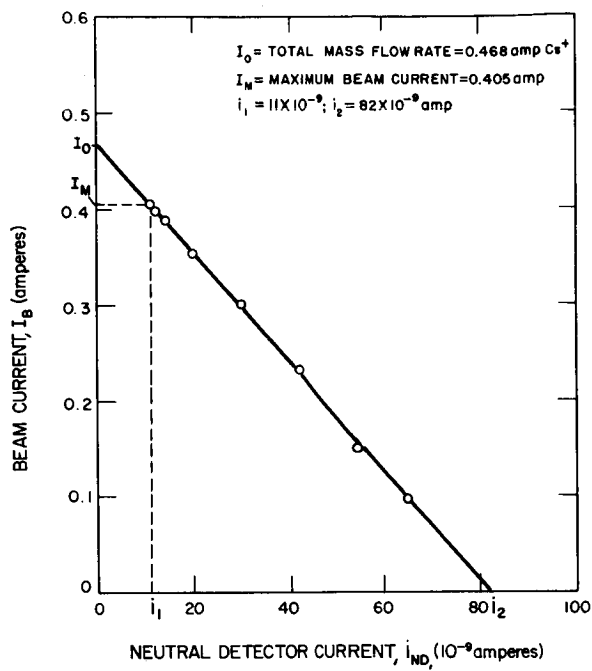
a
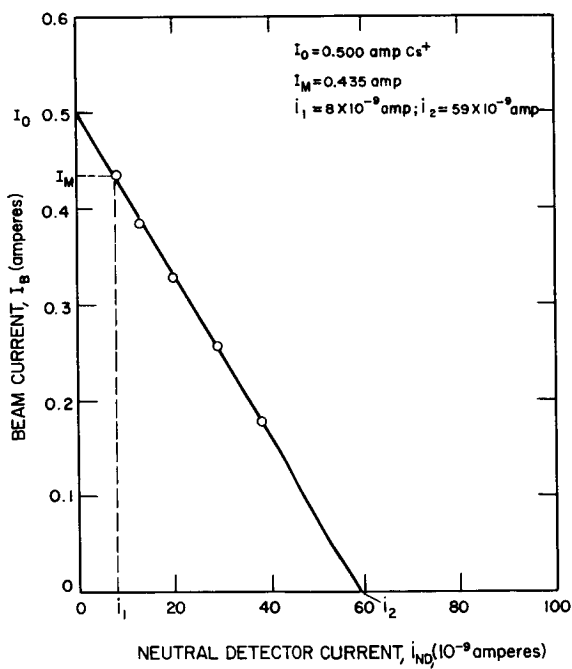
b
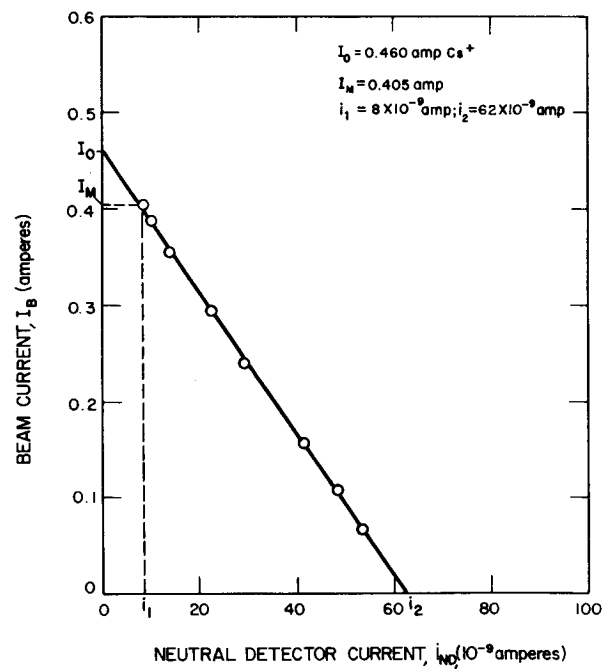
c

FIG. 4-7   BEAM CURRENT VS NEUTRAL DETECTOR SIGNAL

(horizontal axis), the mass utilization factor is given by

$$\eta_M = \frac{i_2 - i_1}{i_2}$$

since i_2 corresponds to the neutral efflux when no beam is being extracted.

The slopes shown in Figs. 4-7a and 4-7c differed considerably although in the two cases most of the operating parameters were alike except for the magnetic field.

Further investigation disclosed that the main factor involved in the slope of the calibration curves was the temperature of the discharge chamber walls. Figure 4-8 shows three curves taken at the same feed rate and for various magnetic fields. In each of the curves the magnet coil currents were varied with little or no effect on the calibration (slope). As can be seen, until thermal equilibrium is reached, the total mass flow out of the engine is not necessarily equal to that introduced by the feed system.

It appeared that the mass utilization measurements, as calibrated by the method discussed, were accurate and reliable. The noise level and drift of the neutral detector was about 0.2×10^{-9} amperes. Since at typical engine operating parameters the detector signal is greater than 5×10^{-9} ampere, the use of the detector in a control loop seemed feasible.

4.4 Subsystem Development

It was possible to construct certain control subsystems before arriving at the final configuration of the total system. It was clear that in any system it would be necessary to control cesium feed rate and arc power. Accordingly, subsystems for providing for these controls were designed and constructed.

The first feed rate control system used consisted of a differential relay comparison system which operated a motor driven variable transformer to adjust reservoir power. The equipment for the first arc control loop was similar but included a three phase rectifier to

FIG. 4-8 BEAM CURRENT VS NEUTRAL DETECTOR SIGNAL

The figure shows a plot of BEAM CURRENT, I_B (amperes) on the vertical axis versus NEUTRAL DETECTOR CURRENT, I_{ND} (10^{-9} amperes) on the horizontal axis.

DD ENGINE
CATHODE K5B
$V_+ = 4$ kv
$V_- = .75$
$B = 2$ TO 5 GAUSS

○ DISCHARGE CHAMBER AT 240°C

□ CHAMBER AT 245 TO 250°C

▽ CHAMBER AT EQUILIBRIUM TEMPERATURE (258 TO 260°C)
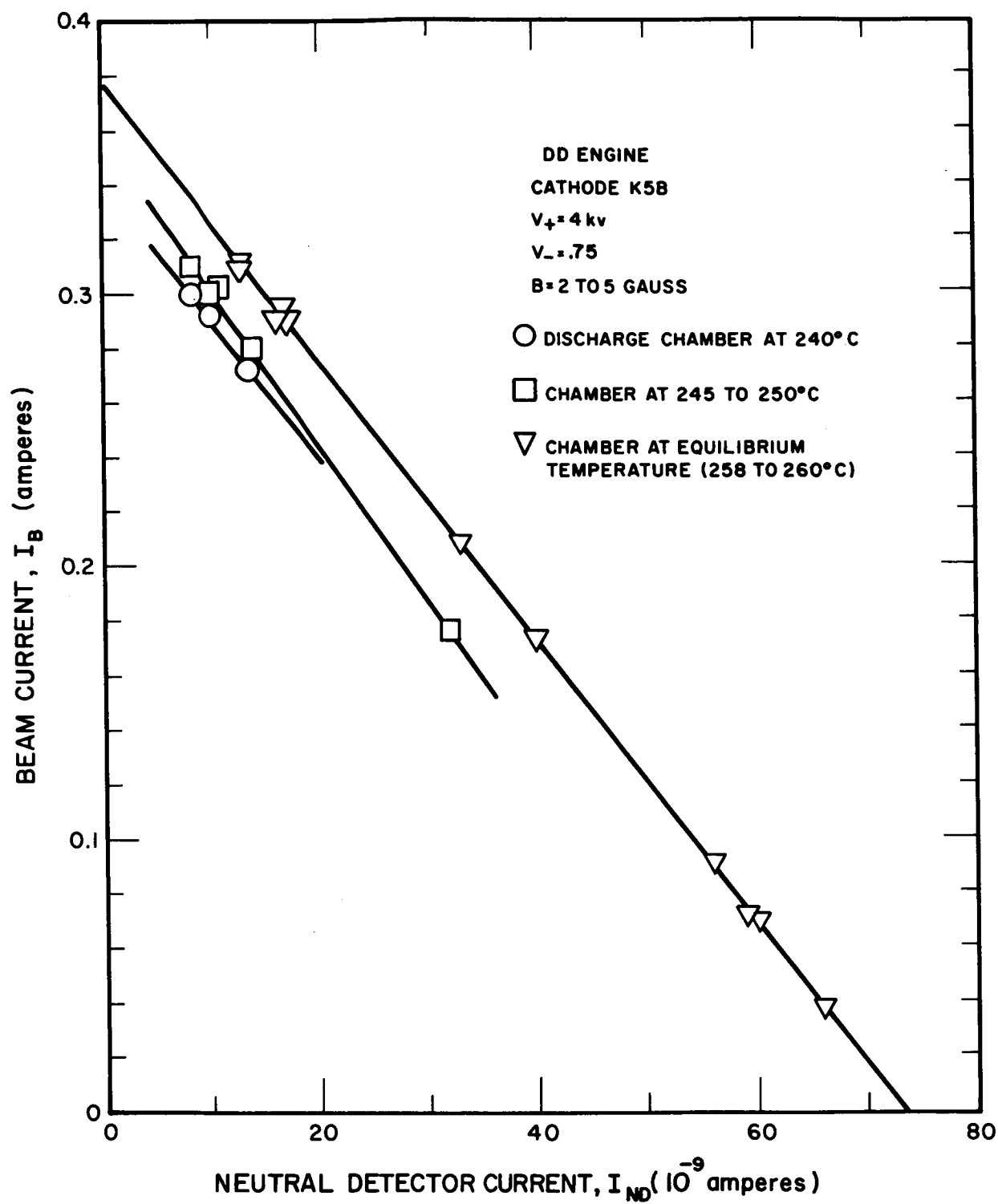
provide direct current for the arc. Figure 4-9 shows the first feed rate and arc power subsystems mounted in their console.

4.4.1 Arc Control Loop Tests

The arc control loop shown in Fig. 4-10 was connected for experimental operation with the DD engine. The first trial of this loop resulted in undamped oscillations as shown in Fig. 4-11. At point (1) the control loop was switched into operation and at point (2) it was switched out of the circuit. This oscillation was shown to be caused by the long time constant in the electrometer circuit and the response of the motor driven autotransformer in the arc supply. The solution to the oscillation problem was to replace the motor drive as the control element by silicon controlled rectifier circuits which provide very fast, linear control. Experimental operation of this version of the loop was quite satisfactory although there was room for further improvement of the time response. Figure 4-12 shows the time response of neutral efflux and beam current to step changes in the bias signal which determines the equilibrium point of the system. The feedrate was kept constant during these tests.

A new arc voltage power supply was designed and constructed. The first supply worked adequately but was unnecessarily large and expensive. The new supply operates from single phase power, requiring fewer power controllers, transformers and diodes. Control is accomplished by means of silicon controlled rectifiers. Two current sensors are included; a relay which operates at an output current of about 20A to control operation of the cathode heater and a magnetic amplifier sensor which detects excessive arc currents and turns off the supply momentarily. The provisions for controlling the cathode heater power and excessive arc currents were incorporated as part of the start-up and transient control aspects of the complete control system.

4.4.2 Feed Control Loop Tests

The feed system control shown in Fig. 4-10 was also tested with the engine. This loop controlled power to the feed system
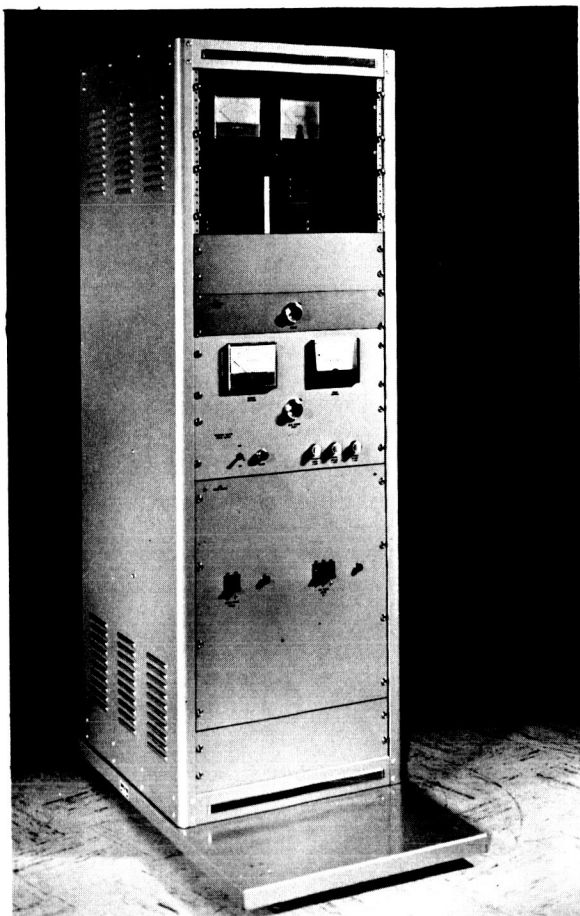
a   Front View   b   Rear View

FIG. 4-9   FEEDRATE AND ARC POWER CONTROLLER CONSOLE
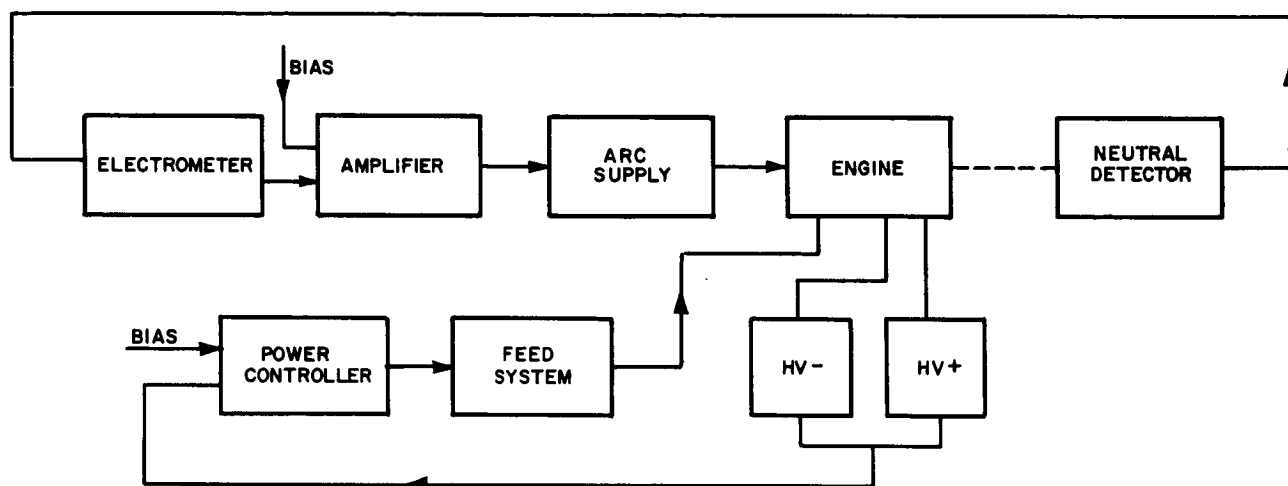
FIG. 4-10   EXPERIMENTAL CONTROL SYSTEM
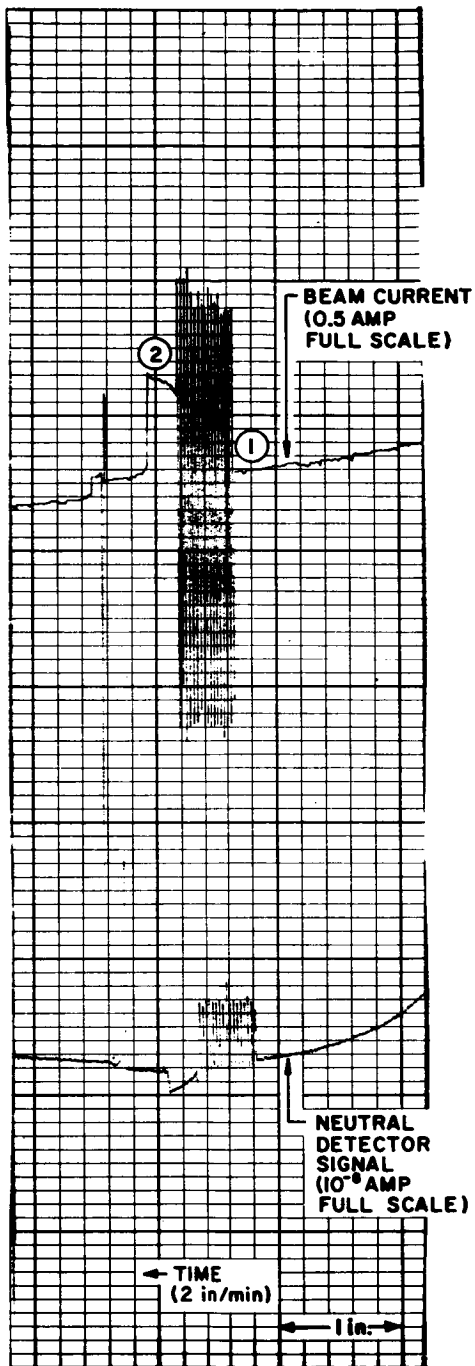
FIG. 4-11   RESPONSE OF ARC CONTROL
LOOP WITH MOTOR-DRIVEN
AUTOTRANSFORMER CONTROL
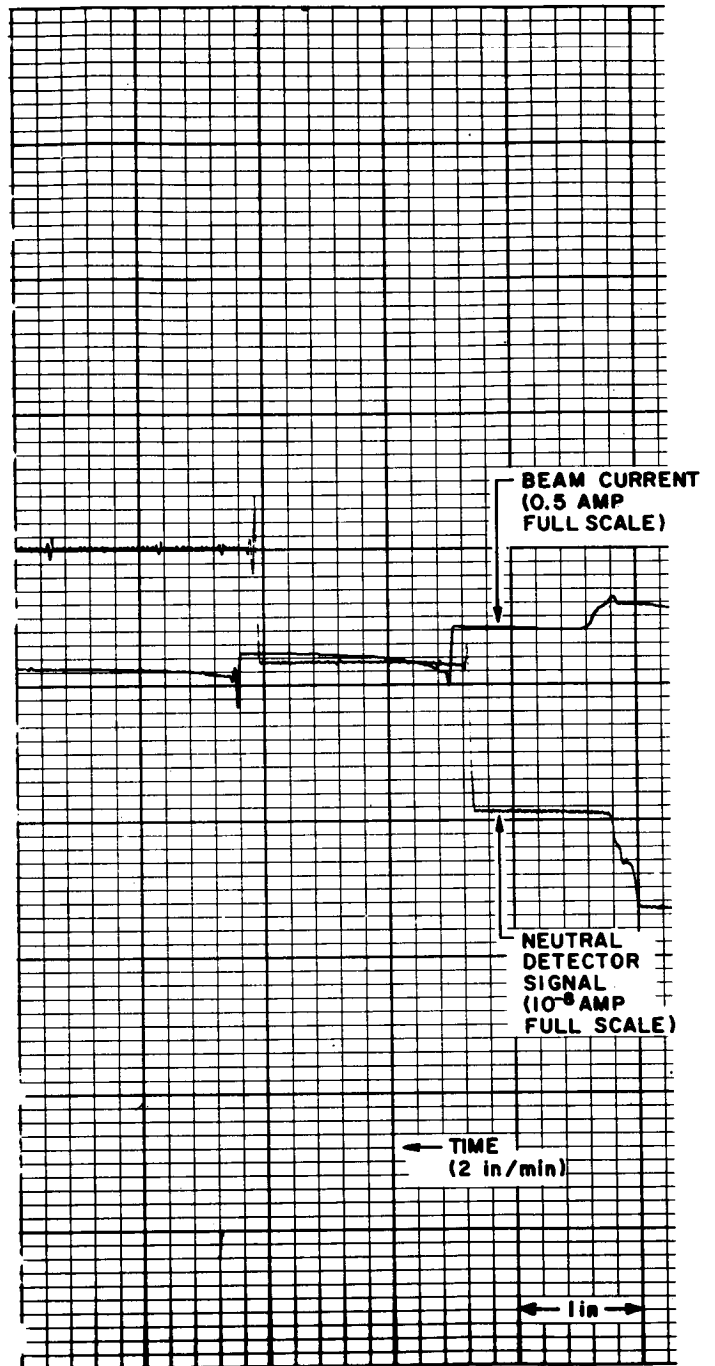
FIG. 4-12   RESPONSE OF ARC CONTROL LOOP
WITH SILICON CONTROLLED
RECTIFIER CONTROL

to produce a predetermined value of net current (beam current) from the engine. The first version of this loop used a motor driven control of the heater power to a laboratory feed system. As was found in the arc control loop, the combination of the motor drive response and a long time constant (in this case, the thermal time constant of the feed system) produced unstable behavior as shown in Fig. 4-13. The feed rate control bias was set to give a 250 ma beam. Operation at (1) was with a valve opening such that the oscillations produced by the control loop varied the reservoir temperature between 298.5^{o}C and 300°C. The valve opening was then reduced (giving the large drop) and operation at (2) was established. Although the period and amplitude are similar, the reservoir was fluctuating between 305.5 and 310.5^{o}C.

When the motor drive was replaced by a silicon controlled rectifier circuit the behavior of the loop was excellent as is shown in Fig. 4-14. Here the variations in feed rate indicated by (1), (2) and (3) were produced by changing the bias settings to the controller. As can be derived from the strip chart traces, for moderate changes, the feedrate can be increased at about 3 ma/sec. with a small overshoot and decreased at about 1.3 ma/sec. The time constants are characteristic of the laboratory reservoir at the power levels used.

4.4.3 Two-Loop Operation With Engine

Finally, both loops were operated simultaneously with the DD engine. A sample of the strip chart recording is shown in Fig. 4-15. At point (1) the valve opening was suddenly reduced and at point (2) it was suddenly increased. On the two channel recorder used, the pen for the neutral efflux channel leads the pen for the beam current channel by a little less than one small time division. The faster response of the arc control loop is demonstrated by the smaller deviation of the neutral detector signal. The deviations and recovery times of the beam - feedrate loop are in agreement with those of Fig. 4-14.

FIG. 4-14   RESPONSE OF FEED SYSTEM LOOP WITH
SCR CONTROL

FIG. 4-13   RESPONSE OF FEED SYSTEM LOOP WITH MOTOR-
DRIVEN AUTOTRANSFORMER CONTROL

3670-Final

128
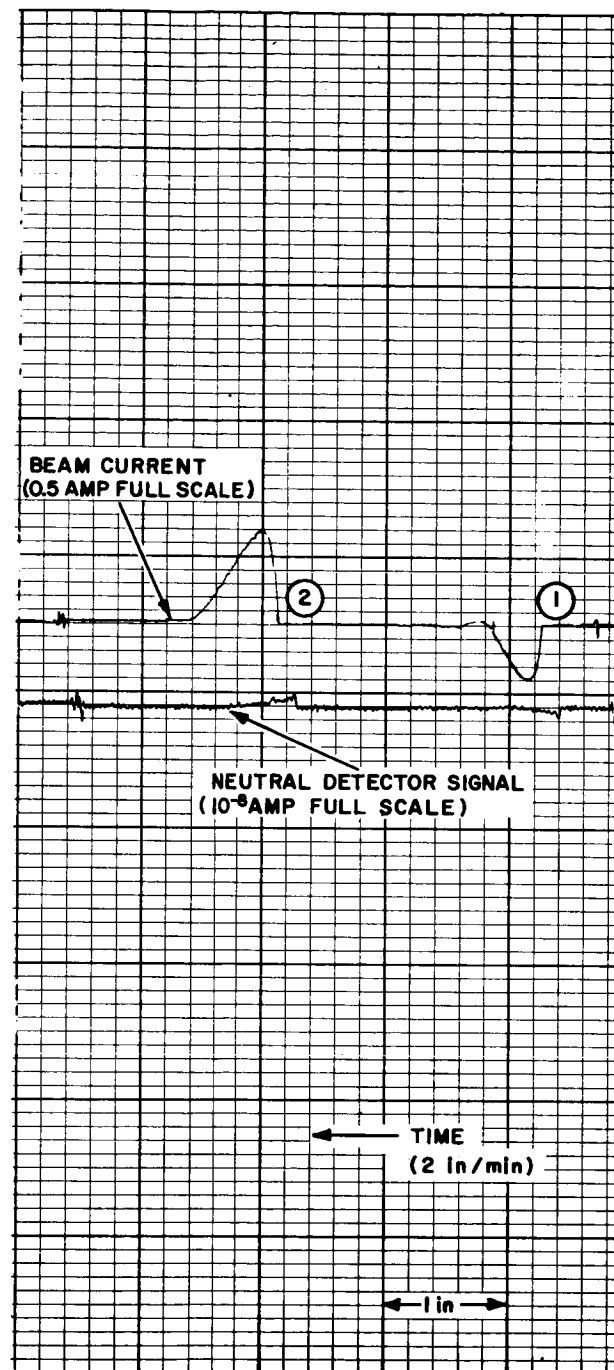
FIG. 4-15   RESPONSE OF TWO-LOOP SYSTEM
WITH SCR CONTROL

The results of these control loop tests conducted
with operating engines were very encouraging and operation with the
zero-g feed system was undertaken.

4.4.4 Zero-G Feed System Tests

The two-loop control system was operated with the
engine and zero-g feed system. The laboratory valve was used in
this test because the solenoid valve was not yet available. The
principal difference between this test and previous tests lay in the
response characteristics of the zero-g feed system. This difference
was first suspected from the response of the feed system control loop.
Figure 4-16 shows the response to step changes in the cesium vapor
valve setting. This response was attributed to the zero-g feed system
since runs using laboratory feed systems have exhibited nearly ideal
performance as reported above. Operation of the arc control feedback
loop was, as might be expected, the same as in the previous tests.

In order to improve the response of the feed system
control loop it was necessary to determine the response characteristics
of the zero-g feed system. This was done with the experimental
arrangement shown in Fig. 4-17. A low frequency sinusoidal signal
generator is used to drive the open loop system; beam current amplitude
and phase relative to the input signal are determined from the recorder
chart and are plotted against frequency to give the "Bode plot" shown
in Fig. 4-18. This representation of system response is commonly used
in stability analysis. The criterion for system stability is that the
loop gain decrease to unity at a frequency lower than that at which
the phase reaches 180°. As can be seen from the plot, the feed system
control loop is stable in agreement with observation. However, the
phase margin, the difference between 180° and the phase at unity gain,
is small. To provide smoother system response, it was decided to
increase the phase margin by the addition of a compensating network.
This network, with its response, is shown in Fig. 4-19. When it is
added to the system the phase margin is increased to approximately 45°,
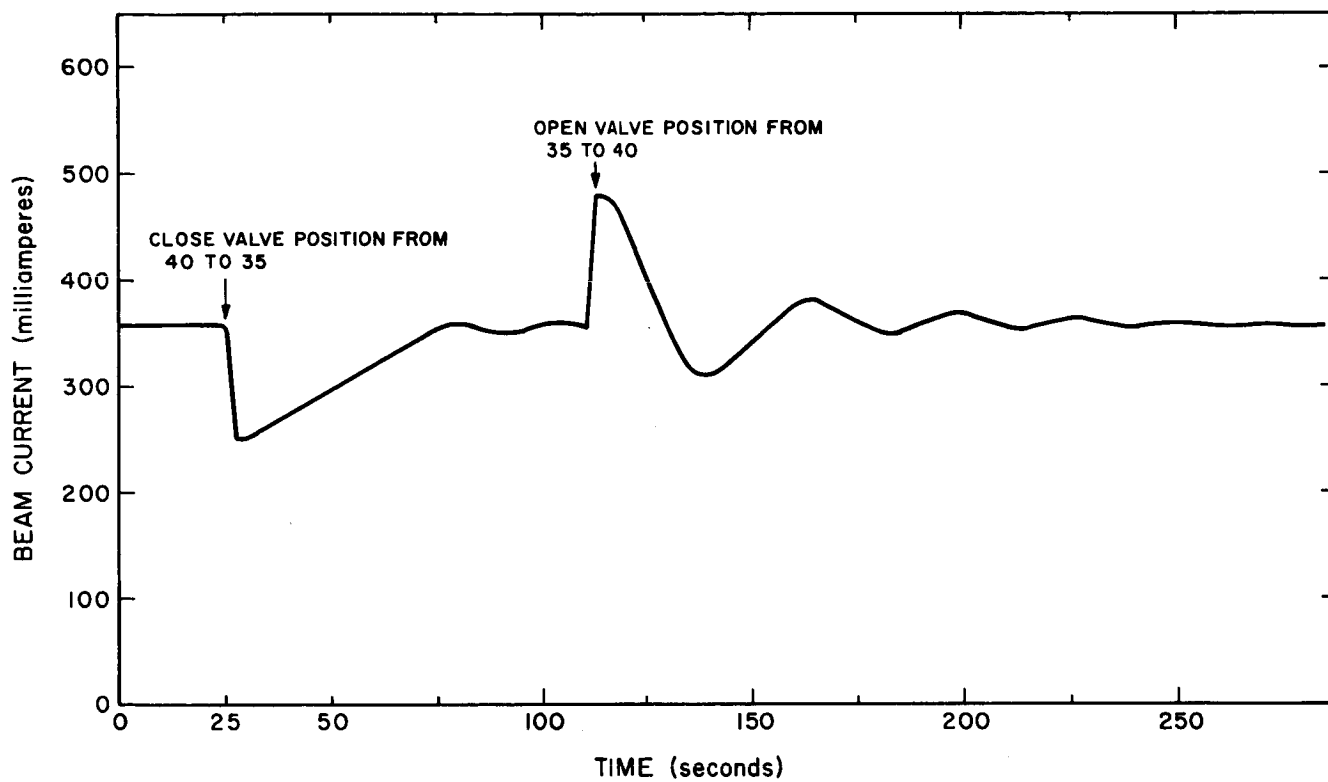
FIG. 4-16   ZERO-G FEED SYSTEM LOOP RESPONSE TO FLOW TRANSIENTS
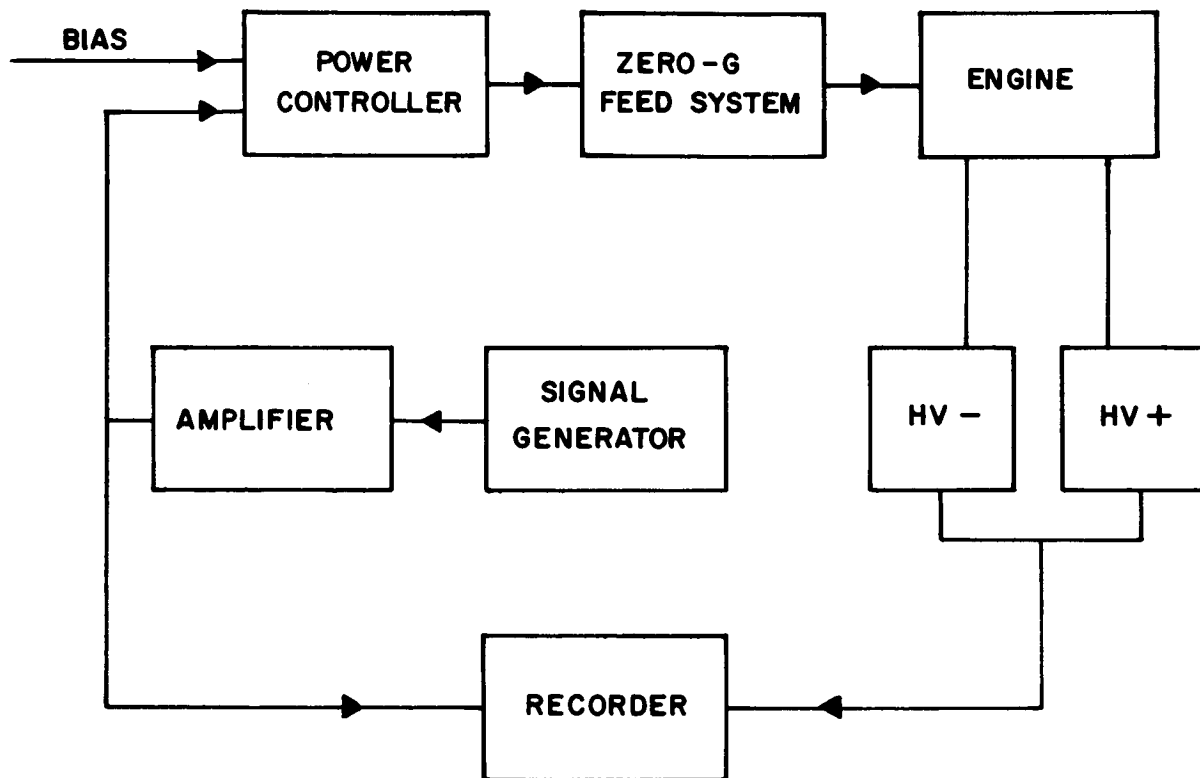
FIG. 4-17   EXPERIMENTAL ARRANGEMENT FOR DETERMINING FEED SYSTEM
LOOP RESPONSE
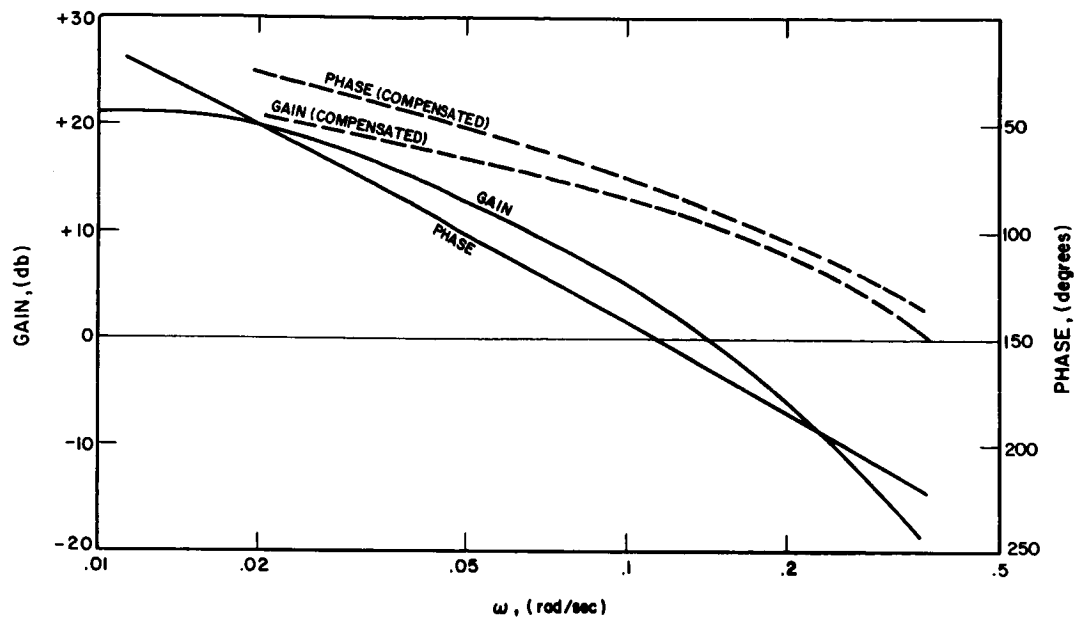
FIG. 4-18   BODE PLOT FOR ZERO-G SYSTEM
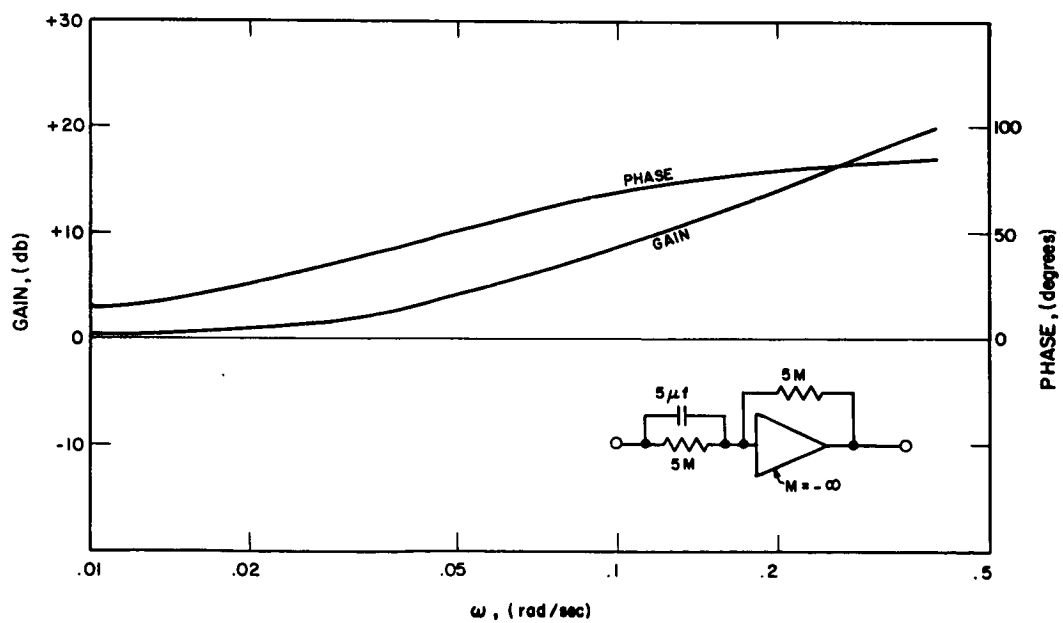
FIG. 4-19   COMPENSATION NETWORK AND RESPONSE FUNCTIONS

a value sufficiently large to produce satisfactory response. The
modified gain and phase curves are indicated by the dashed lines in
Fig. 4-18.

The feed system control loop thus compensated was
tested with the zero-g feed system. System operation is graphically
shown in Fig. 4-20. Curve A is the plot of beam current versus time
when the compensation network includes a 5 microfarad capacitor as
originally computed. The beam variations shown are responses to
changes in a control system setting.

Response was considered satisfactory but unnecessarily
slow since about 1.26 minutes were required for the beam current to
rise to 90 percent of its final value. The system was operated
without a capacitor in the following run with the results shown in
curve B of the same figure. As indicated in the plot, the system
was unstable and oscillated at 1.6 cycles per minute.

Performance of the final compensation network design
using a 1 microfarad capacitor is shown in curve C. For a decrease,
the beam current reaches its final value in 0.5 minutes with only one
major undershoot of 15 percent. When the current is caused to rise
an amount equal to the previous decrease, it reaches its final value
in 0.75 minutes with an overshoot of less than 5 percent. This
response was considered satisfactory and there appeared to be no
problem in adjusting the control loop to handle a wide range of
variations in feed systems and their thermal response characteristics.

4.4.5 Engine Mounted Neutral Detector Tests

For obtaining engine data and performing control
system loop tests a neutral detector independently mounted in the
vacuum facility was first used. This detector had a shutter which
allowed background readings to be taken (background and drift were
found to be negligible.) The detector was mounted so that its
entrance aperture was 20-1/2 inches from the center of the screen
electrode and is oriented at an angle of 24-1/2° to the beam axis.
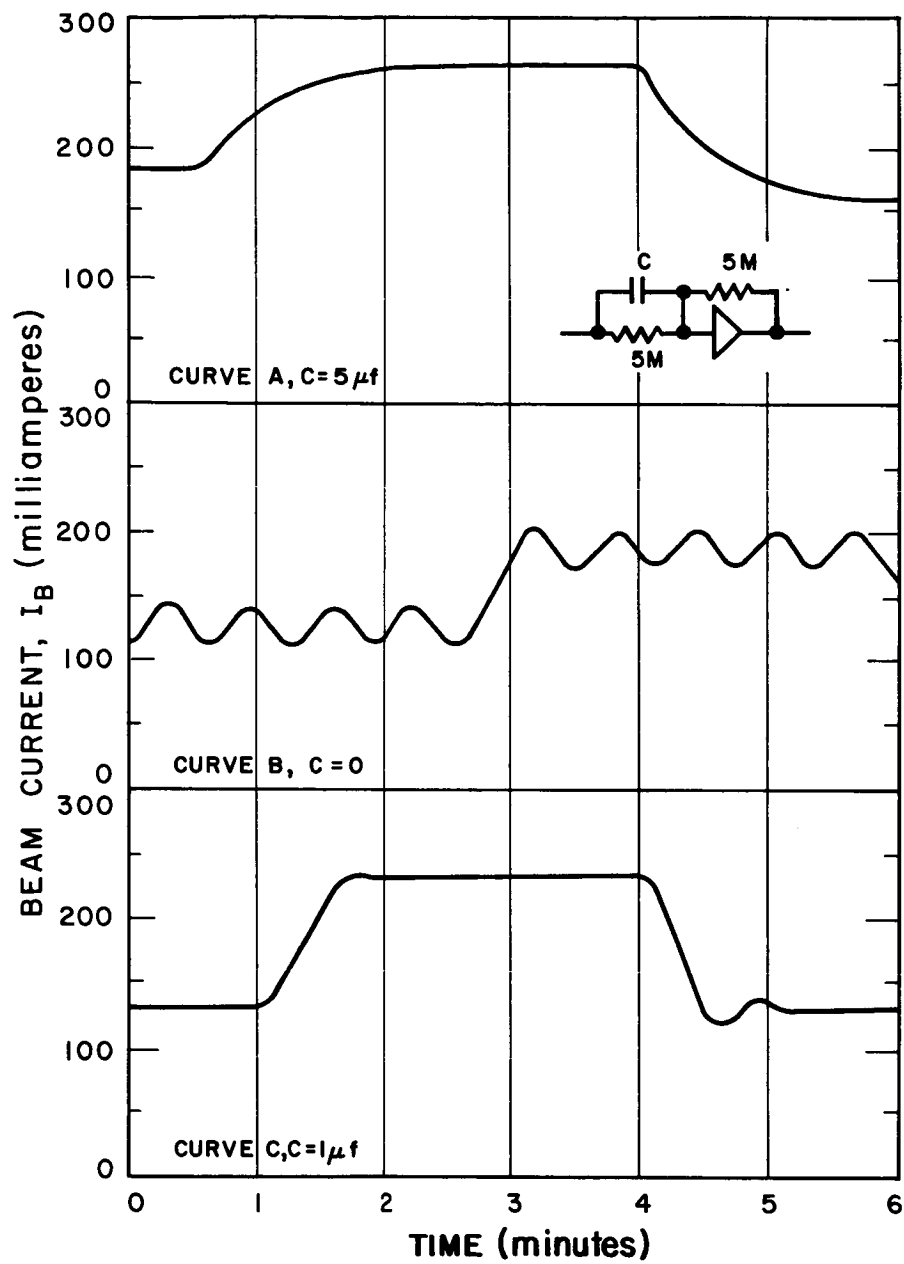
FIG. 4-20   FEED SYSTEM LOOP RESPONSE CHARACTERISTICS

Since the final engine system was to include a neutral detector, tests with a detector mounted on the engine were also conducted. The engine mounted detector was first attached so that its entrance aperture was 5 inches from the center of the screen electrode and it was oriented at an angle of 54° with respect to the beam axis. Figure 4-21 presents a comparison of signals from the engine mounted detector with those from the tank mounted detector. Except for the large zero drift, the results were reassuring since the curves are quite linear and the slopes are fairly uniform. In the case of the data represented by circles, a zero point was taken, by removing the filament bias, a short time before the data were taken. The zero reading was about -14 nanoamps and was in good agreement with the curve.

The zero drift was characterized by a large detector output signal remaining when the filament bias was removed. The time dependence at the drift suggested that thermoelectric phenomena might be responsible. Operating, as it does, in close proximity to the engine, the detector and its leads reach higher temperatures than does the tank-mounted detector.

Further testing indicated that the large signal drift was due to a combination of thermoelectric effects and leakage impedances which caused zero errors. It was concluded that the leakage was at the surface of the glass feed-through insulator which insulates the collector from the body of the detector. It was also concluded that the thermoelectric junction was at the connection of the external lead to the central conductor of this feed-through. To eliminate the zero drift, a filament-collector section was designed which replaced the glass insulator with a tantalum-clad tantalum coax with magnesium oxide insulation. The outer sheath was brazed into the housing with the end inside the detector carefully shadow-shielded to maintain high leakage impedance. The tantalum coax was carried to about a foot away from the detector before being joined to a copper coaxial cable. Since both the inner conductor and sheath junctions are similar
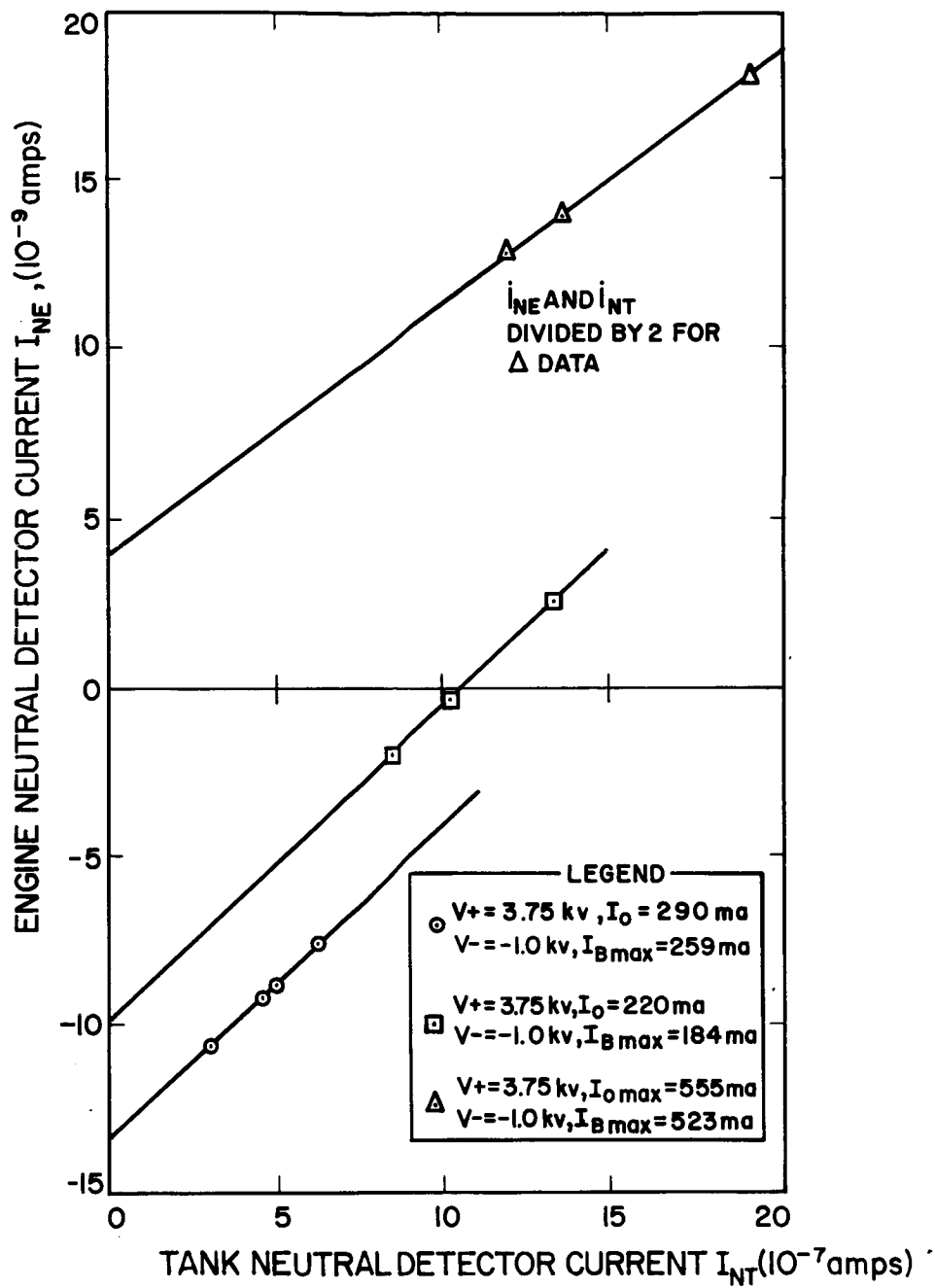
FIG. 4-21   COMPARISON OF ENGINE MOUNTED NEUTRAL
DETECTOR WITH TANK DETECTOR

and at the same temperature; the zero error due to the thermoelectric effect should have been eliminated.

To evaluate this system, a neutral detector of the old configuration was first run with an engine. When the engine was first started, the zero level, measured by removing the filament bias, became positive and then decreased toward zero. After operation of the engine for about an hour, thermal equilibrium was reached and data were taken. Flow rates determined by the engine mounted detector were within 3 percent of those determined by the tank detector and always lower.

Over the following few hours of engine operation correlation data were taken. The zero reading of the engine mounted detector was not subtracted. The engine was operated over a wide range of beam currents and neutral efflux during this test. The test indicated that the major source of the discrepance in the flow rate determinations is the failure of the two detectors to agree at zero, the correlation being otherwise adequate.

For the second test, the all tantalum feed-through section was used with the detector. When the engine was started, no initial zero drift was observed. Flow rate determinations made with the engine detector agreed to within 1 percent with those made with the tank mounted detector.

4.5 Start-Stop Tests

Experimental engine and control subsystem operation led to the adoption of a two-loop control system as had been anticipated since the early months of the development program. A feed system loop operates the power input to the controlling element of the feed system to maintain engine operation at pre-programmed values of beam currents. The only problem encountered with this feedback involved the response of the zero-g feed system. This problem had been handled satisfactorily by the addition of a compensation element.

The second loop operates on the power input to the arc power supply to maintain engine operation at pre-programmed values of neutral efflux.

The engine had been found capable of efficient operation with a constant value of magnetic field. Since the primary purpose of this field is to restrain primary electrons until they become thermalized, this was not surprising.

A third major part of the control system is the programmer responsible for the start up and shutdown phases of engine operation. This aspect of system development received considerable attention.

4.5.1   Sequence Tests With DD Engine

The initial approach to the automatic starting sequence was to heat the feed system to temperature, start the engine with high voltage, arc voltage, etc. on, close the control loops, and step the beam and neutral efflux references to the desired level in preselected increments.

The first DD engine system start-up tests were conducted with a zero-g feed system. An early sequence is depicted on the temperature-time profile of Fig. 4-22. At the start, 65 watts of power was applied to the valve heater and 100 watts to the cathode heater. At 18 minutes the valve body was warm enough to prevent cesium condensation. At this time the valve heater power was reduced to its steady state value of 32 watts and 32 watts was applied to the vaporizer heater. At about 23 minutes the arc current was up to 20 amperes and the cathode heater was switched off. However, stable high voltage operation could not be maintained until about 33 minutes after which the system was well behaved. The beam came on at about 100 ma.

Figure 4-23 is a transcription of the recording of beam current and neutral efflux during shut-off. At t = -1 minute the engine was cut from 500 ma beam to 435 ma and at the time noted, the valve was closed. It appeared that with the flow shut off and with
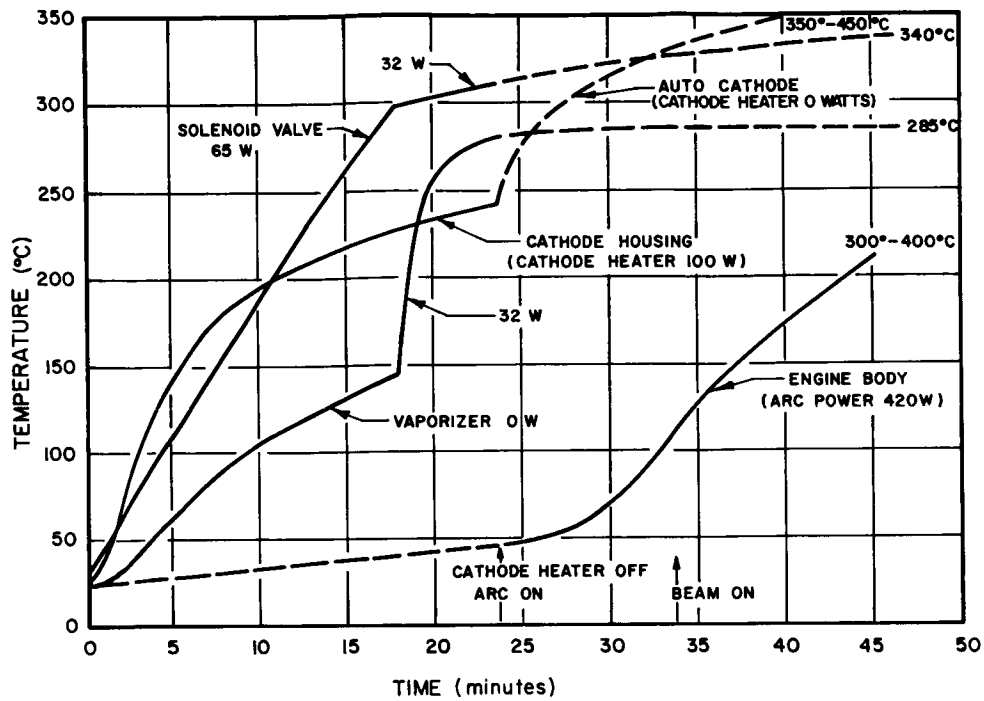
FIG. 4-22   DD ENGINE WARM-UP
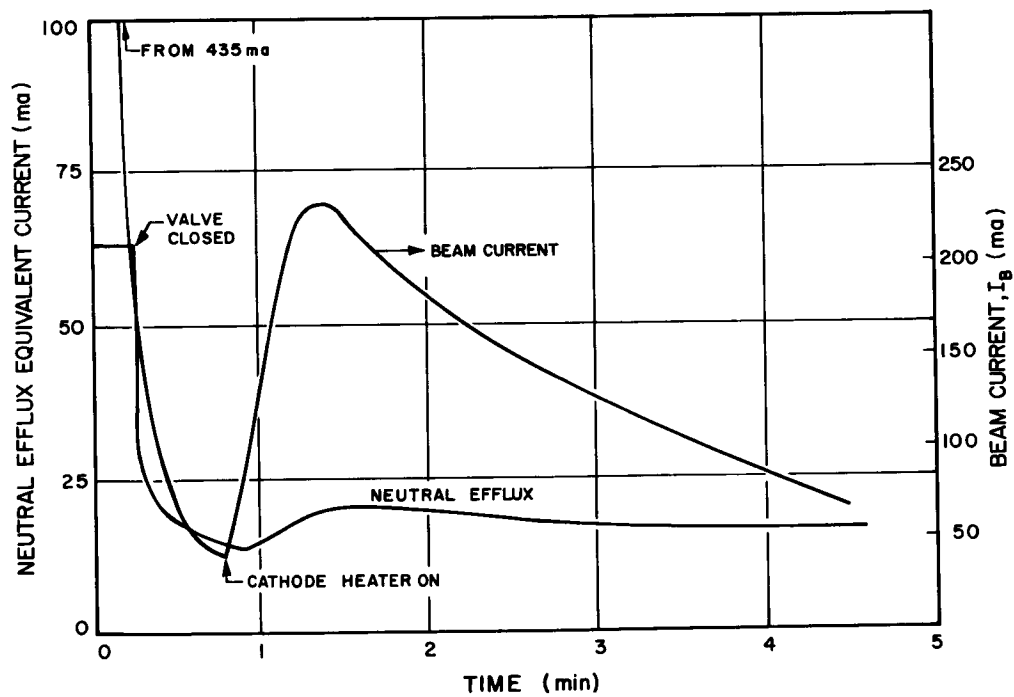
FIG. 4-23   DD ENGINE TURN-OFF CHARACTERISTICS

the cathode heat and arc power on full, the engine could simply be shut off (all voltages) after a period of approximately 5 minutes. Later tests were made with a laboratory reservoir which had slower feed response than the zero-g feed system but which did not alter the engine body temperature profile.

The first part of the turn-on cycle was quite straightforward, requiring from 10 to 15 minutes to heat the feed system. Establishing the arc was not a problem with the exception that a certain amount of cesium condensed in the engine before the arc started. This was held to a minimum by applying the feed to the engine with a fast rate of rise.

After starting the arc it was found advantageous to apply maximum arc power, limiting the arc current to about 30 amps by controlling the feed. This allows the engine to warm up and reduced the cesium loss to a minimum by reducing cesium adsorption on the engine walls.

After a warmup period of about ten minutes it was possible to switch on preset high voltages to establish a beam at an initial level of approximately 150 ma. Within another five to ten minutes, the beam level could be increased to 400 ma. The time required to establish a full 500 ma beam depended on the rate of rise of the engine body temperature.

4.5.2 Sequence Tests With DE Engine

It had been observed that the DD engine was subject to breakdowns until a body temperature of about $100^{o}C$ was reached. A solution found for this problem was to initiate an arc of about 30 amperes and allow arc power to heat the body prior to extracting a beam. Figure 4-24 shows a composite recording of neutral efflux during a typical start-up sequence. It was found that a maximum efflux level was reached, after which the efflux dropped to approximately 150 ma equivalent ion flow. This indicated that some particular part of the engine must condense and re-evaporate a large amount of cesium before equilibrium can be obtained.

Two start-ups were made holding the arc current at 50 amperes for 10 minutes prior to applying high voltage. Neutral efflux recordings were slightly higher than shown in Fig. 4-24 but very similar in nature (slow rise to peak, then a drop to a steady value). The beam came on smoothly at a level of about 250 ma when high voltage was applied.

The temperature of the body immediately after the neutral efflux peak was about 70° to 80°C. As a check on the necessity of preheating, another attempt at a cold start was made. The engine operated very well for the first five minutes. During the second five minutes, however, numerous breakdowns occurred. After this period, smooth operation returned. The body temperature was again on the order of 80° to 100°C at recovery.

As a final check, the feed system and cathode were heated until the body temperature reached 83°C. At this point the high voltage, magnet, and arc power were turned on. When the valve was opened, the arc struck, a beam was established at 100 ma, and no breakdown problems were encountered. The feed was increased slowly to 250 ma in two minutes.

Having established the requirement for heating the engine in a second preheating cycle, a modified feed loop mode was designed to automatically hold the arc current constant. Operation of this loop is indicated by the curve of Fig. 4-25. In this curve, the arc current "demand" is a reference dial setting. Gain is not extremely high as indicated by the offset zero, but is adequate for operation during the "preheat 2" cycle.

Data from a start-up sequence using a programmed arc heating phase (preheat 2) is shown in Fig. 4-26. The cesium efflux from the engine during preheat 2 rose continuously to a peak at about 30 minutes. (Three bursts of cesium were due to bursts from the feed system and may be neglected.) The last peak was not accompanied by large arc current transients and is interpreted as cesium evaporation from the vicinity of the electrodes.
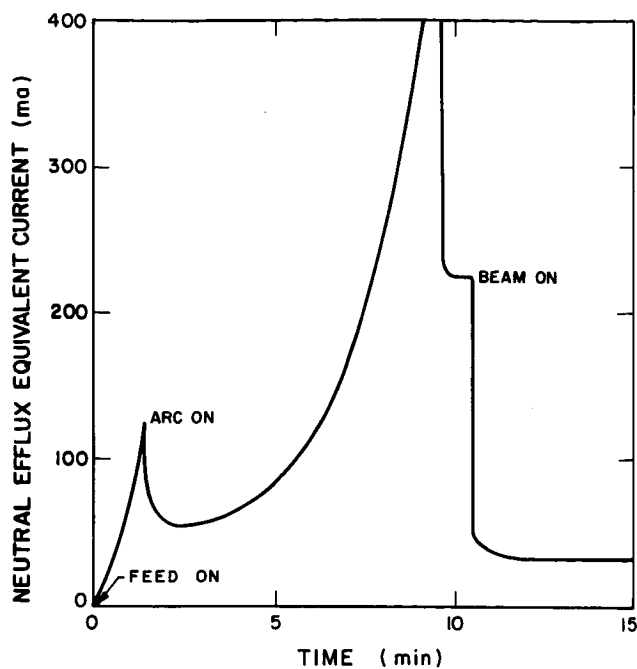
FIG. 4-24

NEUTRAL EFFLUX DURING
ENGINE START-UP

FIG. 4-25

FEED LOOP OPERATION IN ARC
CURRENT REGULATING MODE
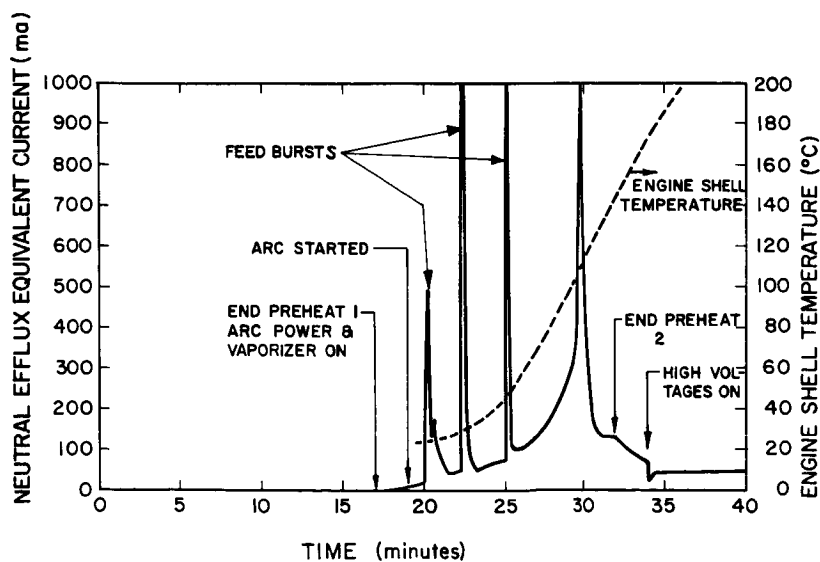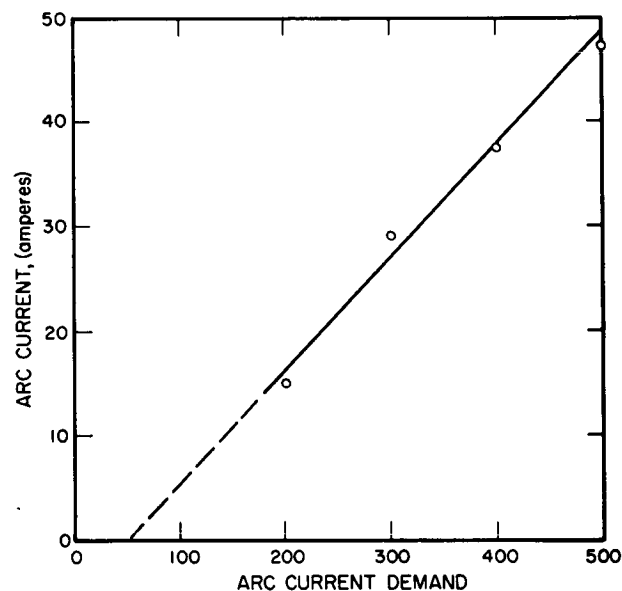
FIG. 4-26

NEUTRAL EFFLUX AND ENGINE
TEMPERATURE DURING PRE-
HEAT 2

3670-Final   143

During testing with the DE engine it was decided to introduce a clean-up period following preheat 2 and prior to applying high voltage. For the duration of the first step on the interval timer, feed is shut off and the arc voltage is maintained. At the end of this interval, high voltage is switched on and a demand for one-half the preset full beam is established. In most cases this clean-up allowed the application of high voltage without any arcing.

4.5.3 Final Configuration

The final sequence determined for automatic starting of the DE engine was as follows:

Preheat 1

at $t = 0$ (when start command is given) Open solenoid valve
and turn on:

      neutral cesium detector

      neutralizer

      magnet

      cathode heater

      valve heater (to high heat)

      flange heater (between vaporizer and valve)

Preheat 2

at $t = t_1$ (timed from 0 to 30 minutes after $t = 0$) turn on:

      vaporizer

      arc power (to preset level)

      valve power (to normal heat)

      automatic regulation of feed to maintain
       a 30 ampere arc

Clean-Up

at $t = t_2$ (timed from 0 to 30 minutes after t_1):

      close feed loop (demand zero beam)

      close arc loop

Stepping

at $t = t_2 + 2$ minutes - turn on high voltages and demand one-
half of full beam. Increase beam demand in 9 steps
at 2 minute intervals to full beam.
(During the start sequence and all automatic operation, the cathode
heater is turned off when the arc current exceeds 20 amperes and back
on when the arc current falls below 10 amperes.)

The turn-off sequence was modified to perform as
follows:

at $t = 0$ (when stop command is given) shut off vaporizer allowing
the beam to drop to about 20 percent.

at $t = 2$ minutes - turn arc power on full to extract most all of the
remaining cesium as beam ions.

at $t = t_2$ (when arc current falls below 10 amps) turn on cathode
heater.

at $t = 6$ minutes remove all power from the engine.

This sequence leaves the engine quite dry of cesium
which makes subsequent starts smoother and prevents buildup of cesium
hydroxide on the engine when it is removed from the vacuum system.

4.6 System Integration

Up to this point, the effort had been to determine performance
of the individual subsystems and engine components. It was now
necessary to test, and modify as required, the entire system. This
led to the modification of the arc control loop, the addition of
certain transient handling capabilities, and many minor adjustments in
the system.

4.6.1 Feed System

An external vaporizer was tested with the DE engine
feed system. The detail of the construction of the external-heater
vaporizer is shown in Fig. 4-27a along with a plot of the feed control
loop response using no compensation. The delay characteristic of the
external vaporizer heater system was considerably reduced and was

about one-third that of the internal vaporizer heater system.

Figure 4-27b shows the response obtained using the compensation network used with external heater feed system. This was obviously too much compensation for the external vaporizer heater system, causing oscillations at a frequency of about 0.3 cycles per second.

To determine the compensation required to increase the damping of this vaporizer, data were taken for a Bode plot. Correct compensation was then used yielding slightly less than critically damped response.

4.6.2 Arc Control Loop

Considerable effort had been made to improve the operating characteristics of the neutral cesium detector used to sense the neutral efflux from the engine. The zero-level drifts previously discussed were reduced to acceptable levels by reducing the number of dissimilar metal junctions in that portion of the collector circuit which is in close proximity to the hot engine. More extended testing of the engine system showed that long-term drifts due to accumulation of cesium within the detector caused operation of the arc control loop to deteriorate after a period of about 5 to 10 hours.

Since it was not feasible to do the extensive work required to eliminate this problem, another approach to the arc control loop was taken. Figure 4-28 shows plots of beam current versus arc current for the DD engine at two different flowrates. The data points are labeled with the mass utilization efficiency. As can be seen, the points of constant mass efficiency lie along nearly parallel straight lines.

The fundamental design of the new arc control loop then was to place the engine operation along one of these constant mass-efficiency lines by regulating the arc current from the measured beam current. A feedback system was constructed to regulate the arc current along a similar curve determined for the DE engine.
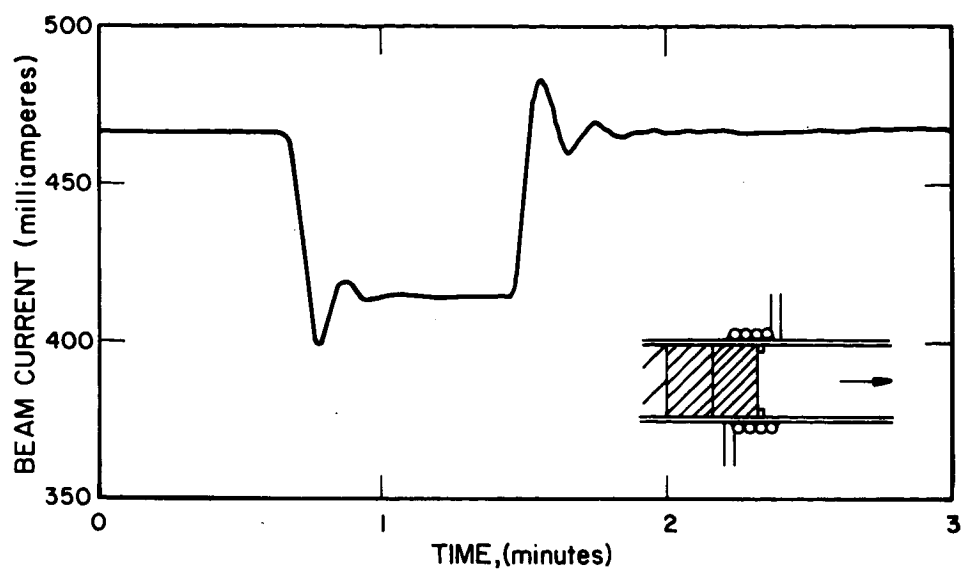
FIG. 4-27a   FEED SYSTEM RESPONSE WITH EXTERNAL VAPORIZER
HEATER (Uncompensated)
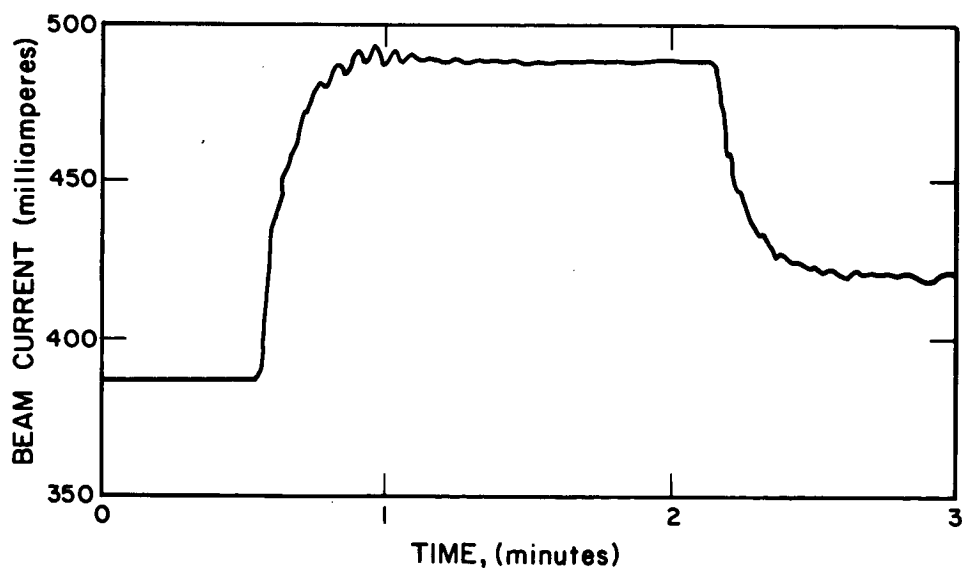
FIG. 4-27b   FEED SYSTEM RESPONSE WITH EXTERNAL VAPORIZER
HEATER (Compensated)
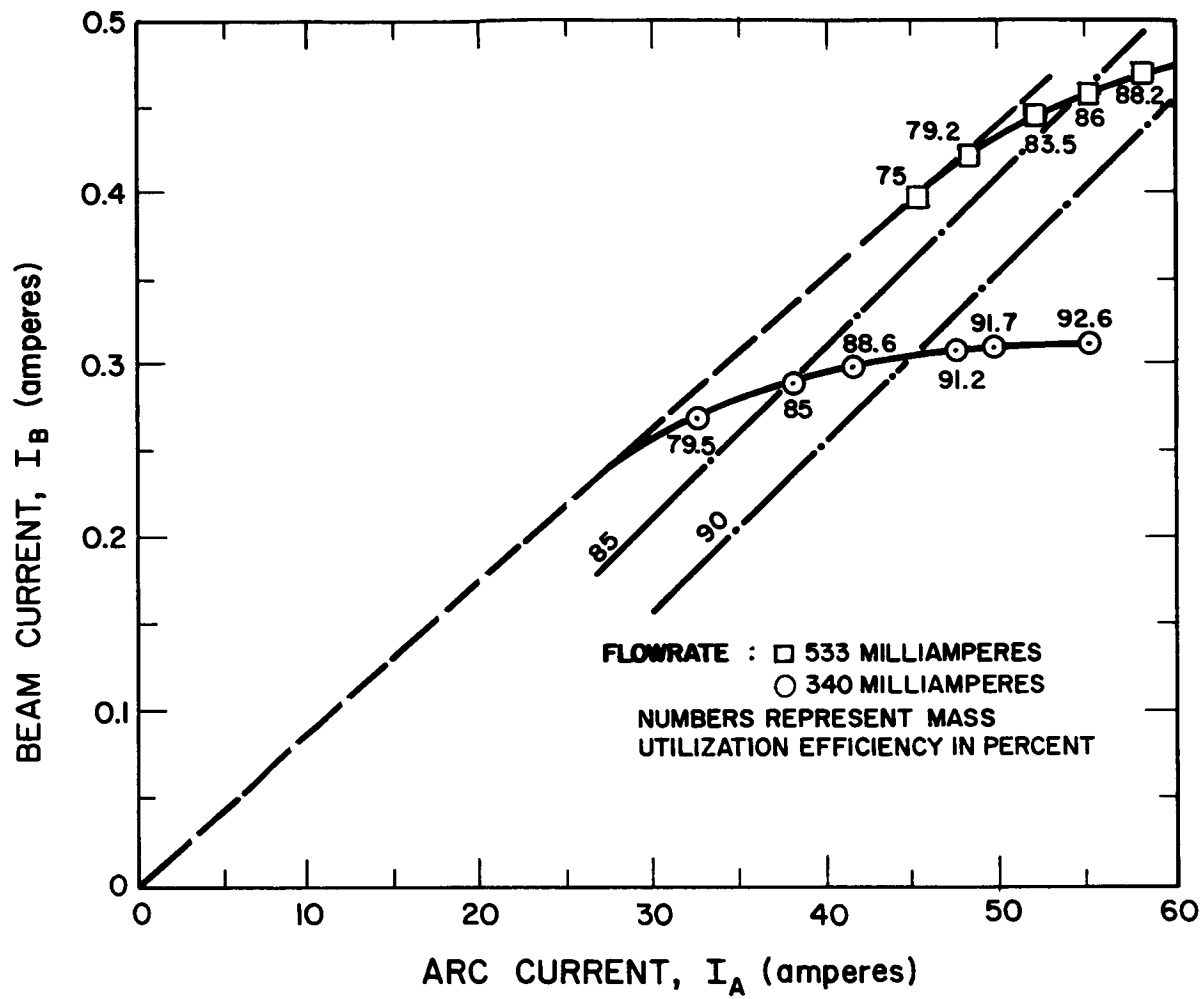
FIG. 4-28   DD ENGINE CHARACTERISTICS

Data taken using the DE engine and this control loop are shown in Figs. 4-29, 4-30, and 4-31. While for higher beam currents the system operates at nearly constant mass utilization efficiency, the source power efficiency is poor at beam levels below two-thirds of the maximum beam.

As a compromise, the control circuit was changed to obtain the operation shown by the square data points in Figs. 4-29, 4-30, and 4-31. In this way, the power efficiency of the engine is maintained down to less than 1/3 of full beam with a nearly constant mass efficiency at the upper range of operation.

Figure 4-32 shows a block diagram of the closed loop portion of the control systems in its final design.

4.6.3 Transient Handling Capabilities

The high voltage supply overload circuits were modified to cause both the positive and negative voltages to be removed from the engine when either supply is overloaded. This eliminates sustained arcs between the electrodes which can occur when the arcing current is too low to trip the positive supply. The two high voltages are also reapplied to the engine at the same time. Tests with the DE engine indicated that unless both supplies were turned on together, either extrusion and electron backstreaming or high interception occurred causing the first supply to cycle off before the second was on.

A third addition to the high voltage supplies was made to prevent flooding and complete failure of the engine when continuous arcing suppressed the beam current feedback and increased the feed rate. A capacitor charging circuit is used to detect continuous arcing. When such a condition is detected, the high voltages and vaporizer power are cycled off for approximately thirty seconds, then returned to normal.

4.7 System Stability Evaluation

The performance of the control system required by contract is discussed in Section 6 of this report. From the control system
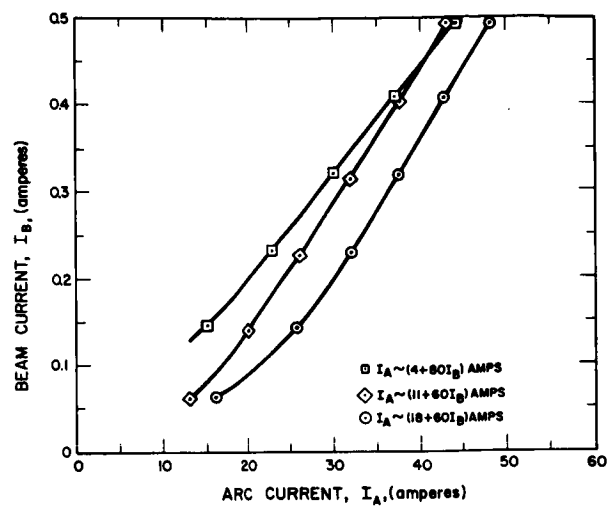
FIG. 4-29

ARC CONTROL CHARACTERISTICS FOR
THE BEAM-ARC CONTROL MODE
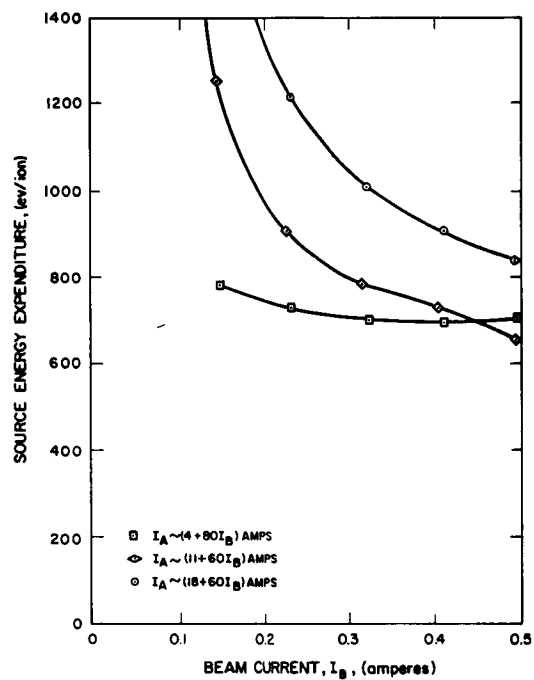
FIG. 4-30

IONIZATION ENERGY FOR THE BEAM-
ARC CONTROL MODE
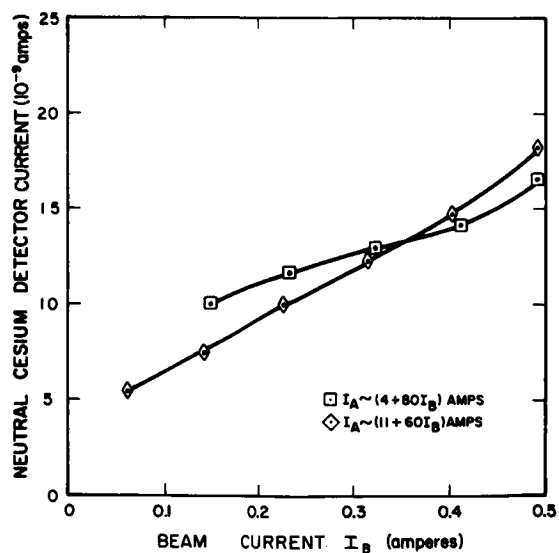
FIG. 4-31

NEUTRAL EFFLUX VS BEAM CURRENT
FOR THE BEAM-ARC CONTROL MODE
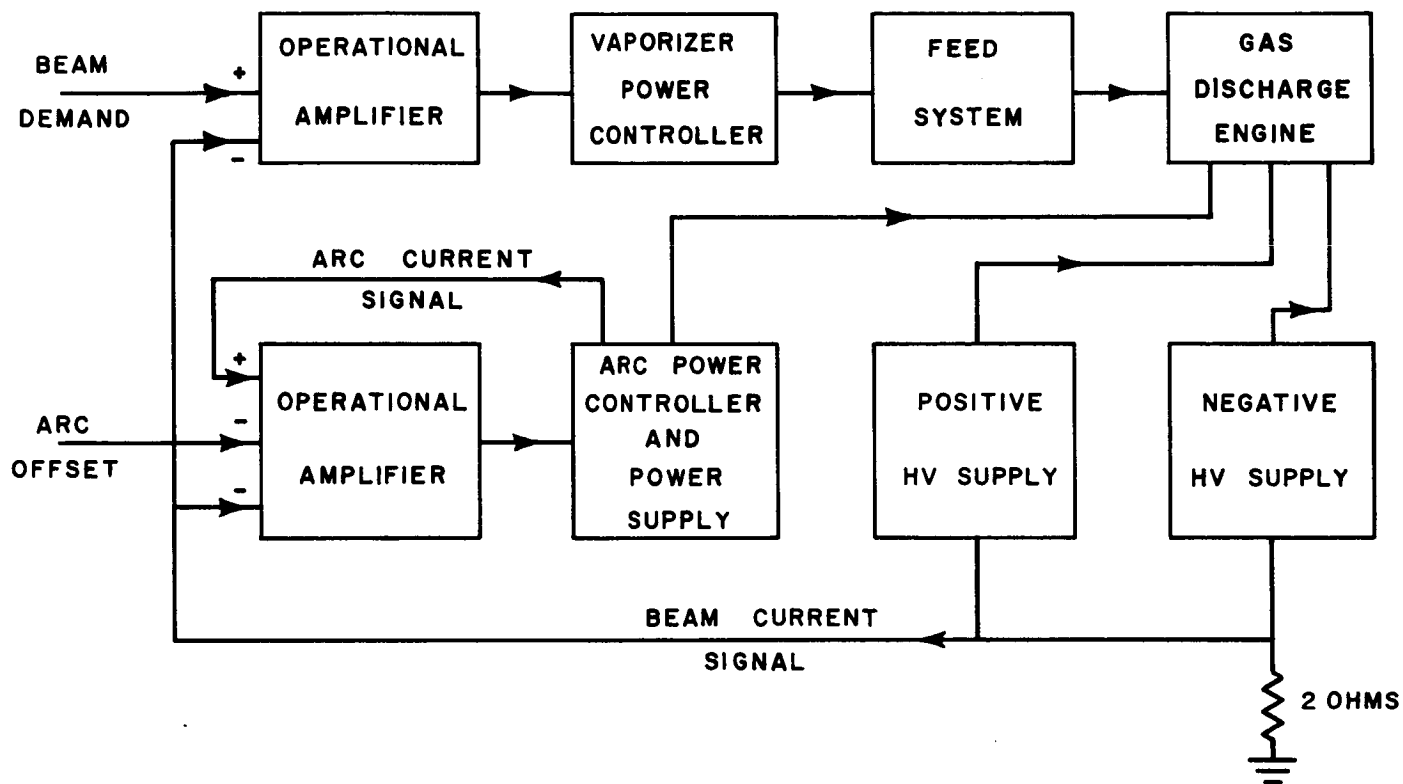
FIG. 4-32   DE ENGINE CONTROL SYSTEM

standpoint, however, stability, both long-term and transient, are of the utmost importance.

The long term stability of the system is indicated by the fact that less than one percent drift in engine parameters could be observed during the 77 hours of operation. Although three control system breakdowns occurred, the cause for all three was determined and eliminated.

To determine transient stability, the engine was operated with the 750-hour feed system and various perturbations were made. Figure 4-33a shows the beam current and neutral efflux recordings made with no feed system compensation. During the interval shown, the beam reference was suddenly reduced and later increased. There was very slight overshoot with this system. Figure 4-33b shows the response with proper compensation. Again, the response has improved over the previous feed system.

Figure 4-34 shows more perturbations of the same system. The changes made in the system were rather drastic but no difficulty was encountered. The third set of perturbations involved the addition of an external impedance in series with the arc. This added impedance was equivalent to 20 percent of the initial arc impedance. With the added impedance in the system, the arc current was reduced by two percent, the neutral efflux was increased by 4 percent, the beam current was unchanged, and the mass efficiency of the engine was reduced by 0.5 percent. When the resistance was switched out of the system, all parameters returned to their original condition.

4.8 Delivered System

4.8.1 Physical Description

The control system consists of three units; a main control unit, an auxiliary power rack, and a high voltage power supply unit. Figure 4-35 is a photograph of the complete control system with the power supplies.
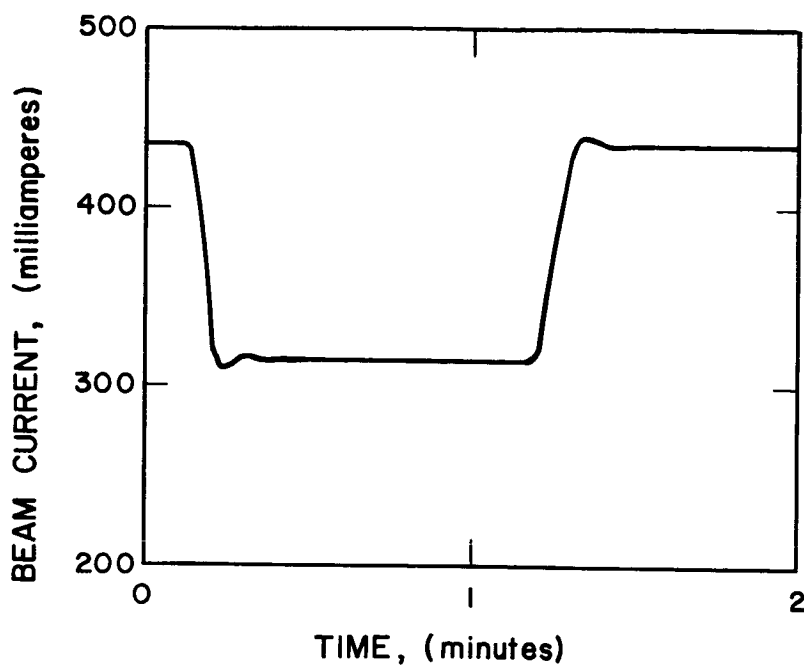
FIG. 4-33 a

750-HOUR FEED SYSTEM
RESPONSE (uncompensated)
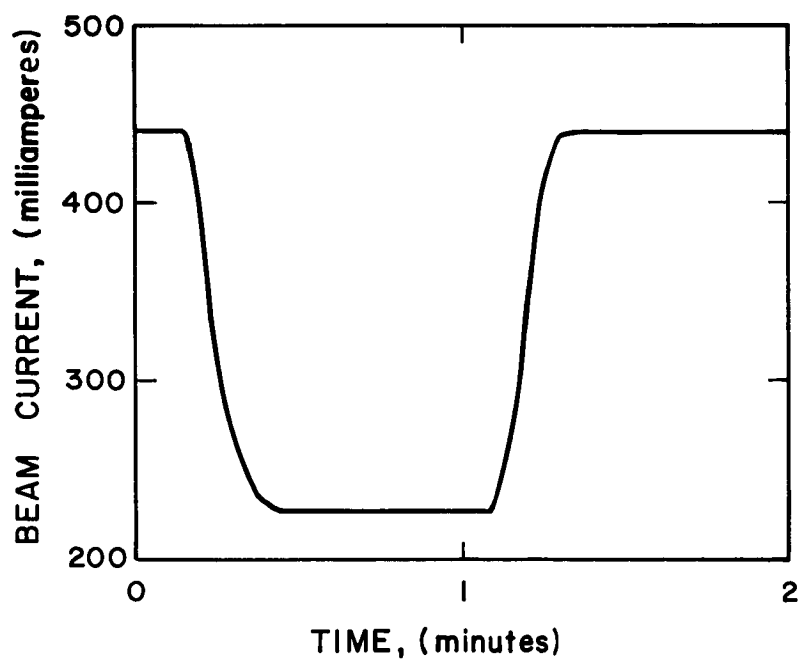
FIG. 4-33 b

750-HOUR FEED SYSTEM
RESPONSE (Compensated)
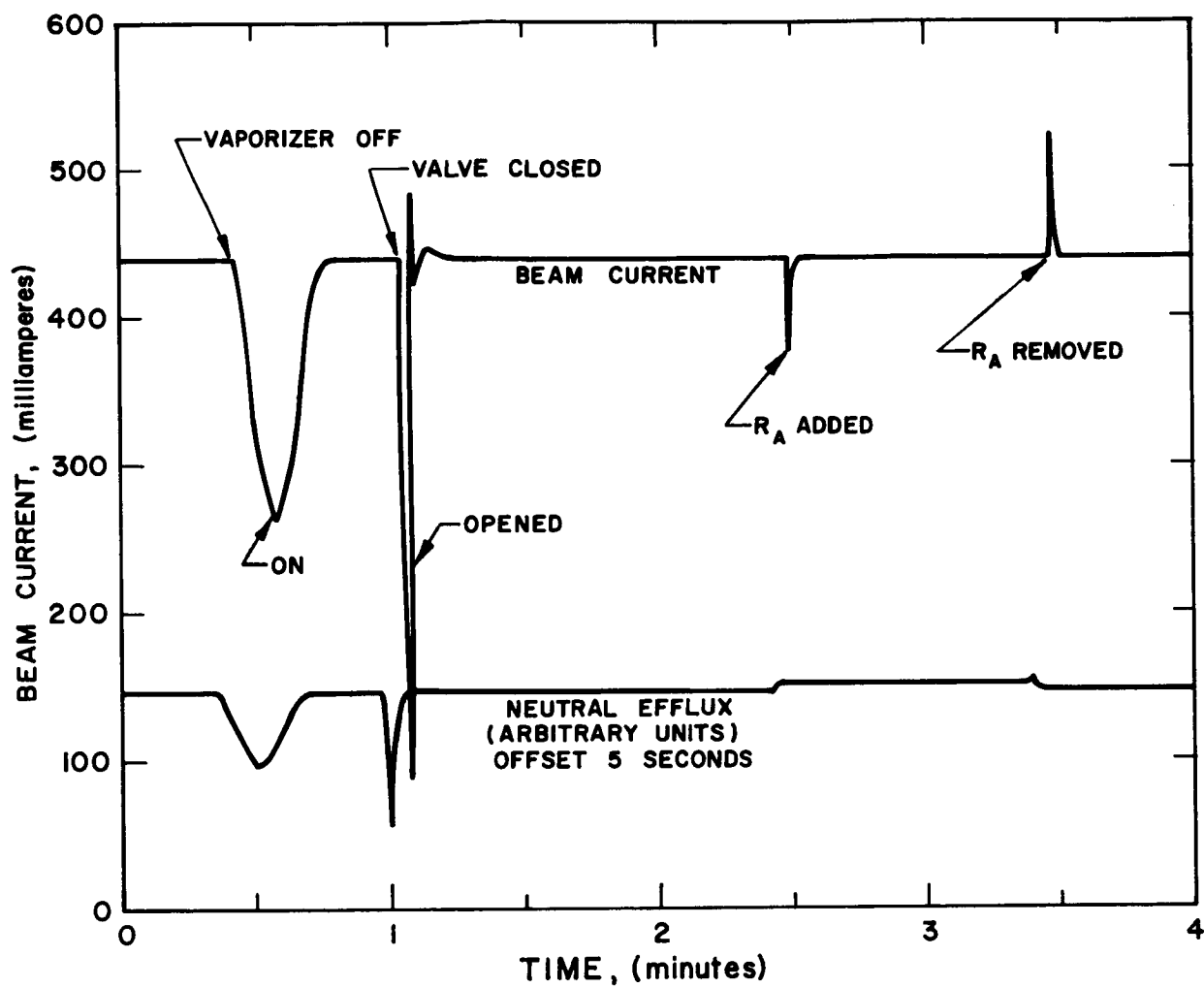
FIG. 4-34   EFFECTIVE PERTURBATIONS ON SYSTEM OPERATIONS

The double relay rack cabinet on the right (the control console) contains the programmer, all of the control elements, and those meters which operate near ground potential. The short relay rack in the center houses the heater step-down transformers, magnet power supply, valve control circuit, arc power supply and those meters which operate at high voltage. This unit is intended to be placed in a safety enclosure next to the power feed-through flange of the vacuum tank. The relay rack on the left is the high voltage supply cabinet which contains the positive 6KV and negative 3KV high voltage supplies. The programmer with its timers and manual override switches is at the top of the left side of the control console. Below it, in order, are the positive high voltage control panel, the feedrate (beam) control, and a unit containing the neutral cesium detector filament control and the neutralizer power control. At the top of the right side of the twin rack is the neutral efflux meter. Below this, in order, are the negative high voltage control panel, the arc controller, and controls for the cathode heater, the valve heater, and flange heater.

The units listed above are those containing operating controls and therefore are mounted above the desk-high writing table. On the right side just below the table is the power amplifier chassis containing the arc and vaporizer linear power controllers.

The junction box is the lower chassis on the right side. An equipment drawer for storing cables, tools or reference material is located on the bottom at the left side. The 300 VDC power supply is mounted in the rear left side above the equipment drawer. Controls normally used for adjusting parameters during operator cont-rolled engine experiments are mounted on the front panel. Controls used for setting bias levels or calibration of automatically sequenced parameters are located inside the chassis or on the rear panels. Test jacks located either on the front or rear panels are provided as an aid in setting and checking circuits.
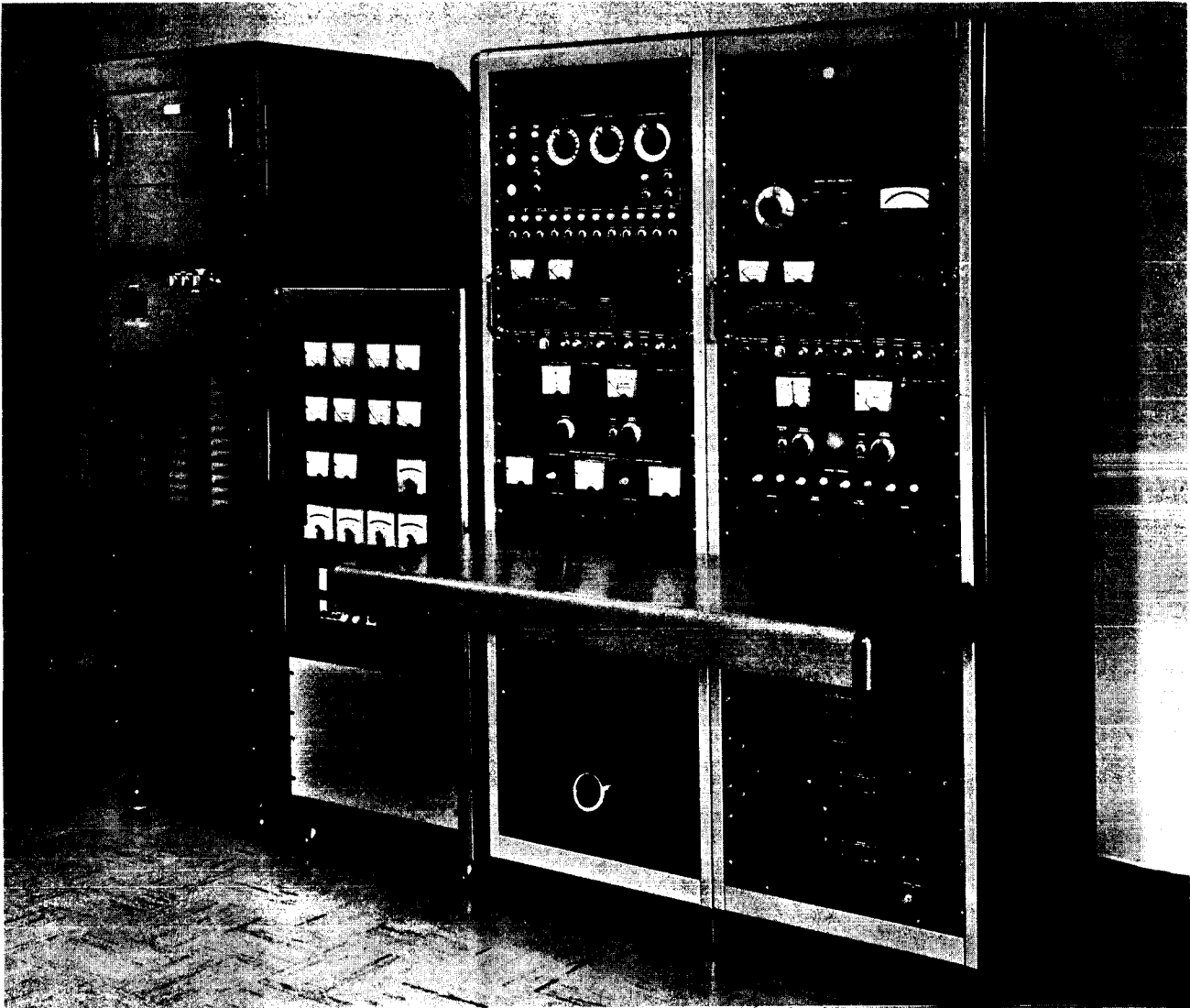
FIG. 4-35   DE CONTROL SYSTEM AND POWER SUPPLIES

In the inter-chassis cables all connector pins including the spare pins are wired. The control console is designed so that 95 percent of all inter-chassis connections pass through the junction box, providing a central location for making circuit alterations or checking passage of signals from chassis to chassis. The junction box also includes the 50 ampere main circuit breaker, the 30 ampere auxiliary circuit breaker, and the bias supplies.

The auxiliary rack is a 4 foot high cabinet which houses four main components. The arc power output chassis is located on the bottom of the rack. The magnet power supply and the valve solenoid supply are located in the middle chassis. The magnet voltmeter and ammeter as well as the valve solenoid ammeter are located on the front panel of this chassis. The transformer chassis, in the upper level, includes the heater transformers for the valve, vaporizer, flange, cathode, neutral detector filament, and neutralizer. All system and interchassis connections are made via plugs and receptacles at the transformer chassis. The meter panel constitutes the fourth major component of the auxiliary power rack. The meter panel is constructed of plastic board to insulate the meters from the steel cabinet, since all the voltmeters, ammeters and the thermocouple meters operate at ion source (high positive) potential. Voltmeters and ammeters are provided for the vaporizer, cathode heater, arc power, valve heater and flange heater. Panel meters are provided for thermocouples located at the vaporizer, engine shell, valve body, reservoir and cathode housing. Since high voltage components are exposed, this cabinet must be operated inside a safety enclosure.

A single cabinet contains the positive and negative high voltage supplies. The latter supply is located in the upper section of the rack and the positive supply occupies the lower two thirds of the rack. Controls and meters for each supply are located in the respective control panels installed in the control console.

4.8.2 Functional Details

Primary Power

The control system utilizes three wire 240/120 volt 60 cps power. During normal operation of the DE engine live current is about 21 amperes. Primary power is controlled by two magnetic circuit breakers with thermal overload relays. The main or input circuit breaker is set to open at 50 amperes. This rating is chosen to assure that the breaker will not open under high voltage surge conditions. The main breaker opens the two line wires and the neutral when it is de-energized. Thus, only the power ON button circuit is protected by a 5 ampere control power fuse located on the front panel of the junction box. An auxiliary circuit breaker with thermal overload relay set to open at 30 amperes controls and protects lines going to the control and amplifier circuits in the control console, auxiliary power rack, and negative high voltage supply. Manual reset buttons to reset the circuit breakers are located on the front panel of the junction box. Both circuit breakers operate simultaneously when the system power ON and OFF buttons are pressed.

6 V.D.C Bias Power

Two identical semiconductor regulated power supplies furnish positive and negative 6 VDC bias power. Each supply is rated at 0.75 amperes and is electronically protected against short circuits.

300 VDC Supply

A dual regulated power supply provides both positive and negative 300 VDC power for the operational amplifiers. The positive voltage output is also used for the neutral efflux detector. Each 300 VDC supply is capable of furnishing 100 milliamperes.

Neutral Detector Supply

Sweep and bias voltages are developed in a circuit box which is in the rear of the Neutralizer and Neutral Detector Panel. The 0 to 300 VDC sweep voltage and 0 to 60 VDC bias voltage are set by adjustable potentiometers. Test jacks for each voltage and common are provided to aid in making adjustments.

High Voltage Power Supplies

The high voltage supplies constitute a major subsystem of the control system. The positive supply is capable of supplying up to 6000 VDC at 1000 milliamperes. The negative supply is rated to furnish up to 3000 VDC at 200 milliamperes. Aside from some interrelated control functions and the sharing of a common high voltage cabinet rack, each supply is independent. A separate control panel with a voltmeter and milliameter is provided for each. The control panels are located on the control console. Each control panel is connected to its respective control terminal board on the high voltage rack by a 25 foot length of ten conductor cable. A 25 foot power cable transmits primary AC power from the junction box to the high voltage rack. Within the control console a cable connects the two high voltage control panels with each other and the junction box.

The positive supply requires 120 VAC for the control circuits and 240 VAC for the power supply input. The control circuit is protected by a fuse. The 240 VAC circuit is protected by an input circuit breaker. The supply incorporates a motor-driven variable transformer for voltage control, a step-up transformer, four mercury vapor rectifiers in a bridge circuit, and an L-C filter. The only control component in the high voltage rack is the line contactor. All other control components such as switches, indicator lamps, over-voltage control, over-current control and external interlock connection are located in the control panel. A time delay relay is provided to delay application of high voltage until the mercury vapor rectifiers reach normal operating temperature. The positive high voltage supply has two modes of operation. In the normal mode, when the over-current relay operates, the supply will remain off until the operator presses the reset button. In the cycling mode the high voltage is automatically reapplied after a few tenths of a second delay. A surge cycling control circuit limits the cycling; repeated current overloads

(typically 5) cause the power supply to be shut down for 30 seconds, then restarted. At the same time the feed system vaporizer heater is shut down to facilitate recovery of the system at the end of the 30 second period. Negative and positive high voltage over-current circuits are interlocked so that both supplies cycle together. The ground return connections for both the negative and positive supplies are made through a common 2 ohm resistor in series with the ground. The voltage across this resistor is an analog of the ion beam current. This voltage is used in the feed and arc control loops.

The negative high voltage supply operates with 120 VAC power. The negative control panel is almost identical in appearance and circuit design to the positive control, except for the lack of the surge cycle circuit. The power supply circuit consists of a motor driven autotransformer for voltage control, a step-up transformer, a semiconductor rectifier bridge and an R-C filter.

Programming and Switching

Overall system control is provided by the Programmer which includes switches, timers, relays and indicator lamps appropriate for the functions assigned. System and auxiliary power are applied simultaneously when the system power ON button in pressed. Closing of the main and auxiliary circuit breakers is indicated by the lighting of the SYSTEM POWER and AUXILIARY POWER lamps. Both circuit breakers immediately open and the system is completely de-energized when the power OFF button is pressed.

The eleven three-position toggle switches arrayed across the lower part of the Programmer panel are the function control switches. Each switch controls a particular function such as opening or closing of the valve, turning on of heaters or loop control. The upper and center position of each switch controls the function as indicated in the following tabulation. The down position of each switch is the AUTO position in which the functions are programmed.

SWITCH	FUNCTION CONTROLLED	
Name	Upper Position	Center Position
Valve	Valve open	Valve closed
Valve Heat	Heat normal	Heat high (for preheat)
Flange and Valve Heaters	Heaters on	Heaters off
Cathode	Heater on	Heater off
Neutral Detector	A.C. power on	A.C. power off
Magnet	Supply on	Supply off
Neutralizer	Heater on	Heater off
Arc	Power amplifier energized	Power amplifier off
Arc Control	Control loop closed	Arc power preset
Vaporizer	Power amplifier energized	Power amplifier off
Feed Loop Control	Beam Current control loop closed	Beam current controlled by arc intensity

The mode switches on the beam and arc control panels and the switches on the high voltage control panels are also used in manual control and setting up for automatic operation.

Automatic Operation

The prime purpose of the control system is to automatically start-up the engine, power it, and automatically go through the shut-down procedure. Programmed operation is initiated by momentarily pressing the program START button. The PROGRAM lamp lights to indicate that the program is in process, PREHEAT 1 timer starts and the appropriate function lamps light. Functions that operate during the first preheat cycle include the following:

Name	Remarks
Valve	open, lamp lit
Valve Heat	High (valve heat lamp not lit) valve PREHEAT lamp on heater control panel lit.
Flange and Valve Heaters	Lamp lit
Cathode	Lamp lit
Neutral Detector	Lamp Lit
Magnet	Lamp lit
Neutralizer	Lamp lit

Upon completion of the time set for preheat 1, preheat timer No. 2 starts. Also the arc power amplifier is energized as indicated by lighting of the ARC lamp; and the vaporizer heater is energized as indicated by lighting of the VAPORIZER lamp. During preheat No. 2 power input to the arc is preset and vaporizer heat is controlled by arc intensity. At the conclusion of preheat cycle No. 2, the feed loop shifts from arc current control to beam current feedback as indicated by lighting of Feed Loop Control lamp. The arc control loop shifts to closed loop operation as indicated by lighting of the ARC CONTROL lamp. During the first cycle of the programmed reference the arc and vaporizer are de-energized by withholding the reference voltages to the respective control circuits. Upon completion of the first programmed reference cycle the arc and the vaporizer are again energized and the high voltage supplies are turned on as indicated by lighting of the HIGH VOLTAGE lamp.

During the remaining eight steps of the programmed reference the beam current is brought up to normal operating level by smoothly graduated steps. The LAST STEP lamp lights when the programmed reference reaches the tenth step.

Shut-Down Programs

Momentarily pressing the System Power OFF button de-energizes the complete control system and engine instantaneously.

This method may be used during manual or programmed operation.

If the program STOP button is momentarily pressed before the programmed reference reaches step 10 (last step) the heater and high voltage supplies are immediately turned off, the timers are reset and the programmed reference is returned to its initial position. If the program STOP button is momentarily pressed after the programmed reference reaches step 10, the programmed reference moves on to step 11, the first of four steps in the automatic shutdown cycle. At step 14, all heater and high voltage supplies are de-energized, all timers recycled and the programmed reference returns to its initial position. The automatic shutdown procedure may be expedited by repeated pressing of the single STEP button after the program STOP button has been pressed.

Heater Power

Since all heaters require less than 25 volts RMS, they are energized by step-down transformers which are located in the auxiliary power rack. The input power to each transformer, except that for the vaporizer, is controlled by a variable autotransformer located in the control console. The vaporizer heater supply is discussed in a following paragraph on the feed control loop. The valve, flange and cathode heater autotransformers are located on the heater control panel. The latter includes a relay for energizing the valve and flange heater variacs. The function switch or program relay, both in the programmer, energize the heater power relay. Two valve heat variacs are used. The PREHEAT control sets the power for the preheat No. 1 period. The NORMAL control sets the valve heater power applied during remaining run sequence. Selection of the proper valve heater variac is accomplished by means of a relay which when de-energized connects the preheat variac into the circuit. This is indicated by the lighting of the appropriate indicator lamp on the heater control panel. When normal valve heat is called for, the heat selector relay is energized thus switching the normal heat

variac into the circuit and lighting the associated indicator lamp.

When the arc current exceeds 20 amperes, the cathode heater is de-energized and the cathode indicator lamps on both the programmer and heater control panel are extinguished. When the arc current falls below approximately 10 amperes, the cathode heater is re-energized.

The neutralizer heater and the neutral detector filament variacs are located on the neutralizer and neutral detector control panel. Neutralizer heater voltage and current are indicated by panel meters adjacent to the variac. An ammeter is provided for indication of neutral detector filament current.

Feed Control Loop

The feed control loop is shown in the system block diagram, Fig. 4-36. The essential components of the feed control loop are the operational amplifier, vaporizer power amplifier, step down transformer and the vaporizer heater. The beam current feedback signal is the voltage developed by the beam current in passing through the 2 ohm resistor in series with the high voltage power supply ground return. The analog voltage of arc current is developed in the arc current transductor. The feed loop transfer relay, K402, switches the appropriate signal and reference inputs to the UPA-2 operational amplifier. During the preheat cycles of the program, relay K402 is de-energized, the amplifier input feedback signal is the analog of arc current and the operating level is set by the arc reference potentiometer R405. At the end of the preheat cycles, feed loop transfer relay K402 is energized. In this condition the voltage analog of beam current is the operational amplifier input feedback signal and the voltage reference input is provided by the programmed reference. The voltage source for the latter is the REFERENCE control, R402, located on the front panel of the beam control chassis. The 47K and 100K resistors in combination with the one microfarad capacitor at the signal input of the operational amplifier
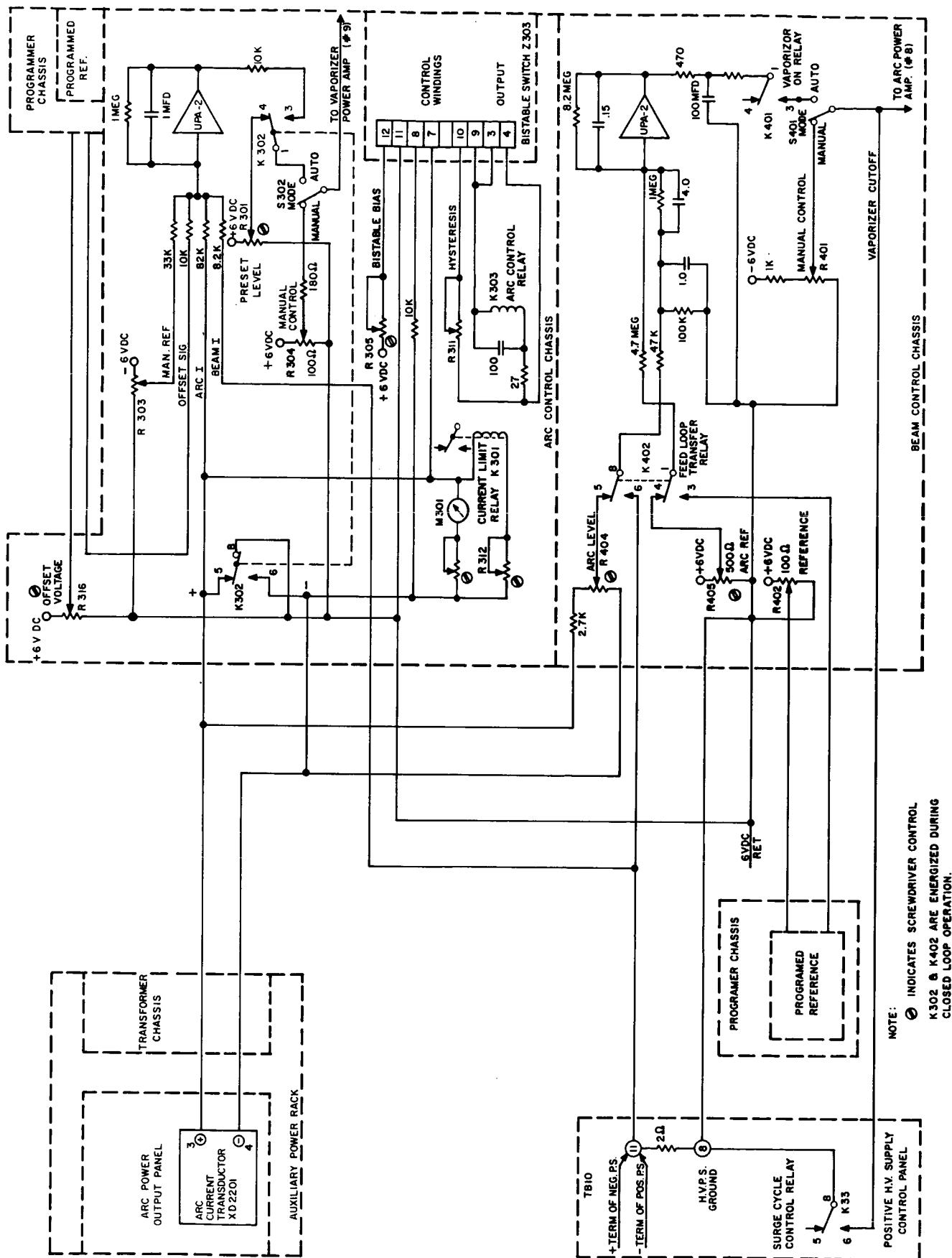
FIG. 4-36 BLOCK DIAGRAM ARC AND BEAM CONTROL FUNCTIONS

165

form an R-C filter which prevents high frequency noise from reaching the amplifier. The signal is applied to the summing point via a 1 megohm resistor shunted by a 4 mfd capacitor to assure proper response to changes in the signal while providing the desired gain under steady state conditions. The amplifier feedback resistor is 8.2 megohms. The shunting 0.15 mfd capacitor controls high frequency response. Output of the operational amplifier is filtered by the 470 ohm resistors in conjunction with the 100 mfd capacitor. The signal is then routed through the vaporizer-on relay K401, which prevents turn-on transients from reaching the power amplifier, and then to the front panel MODE switch S401. In the MANUAL setting the mode switch applies the output of MANUAL CONTROL potentiometer R401 to the input of the power amplifier; in the AUTO position the operational amplifier output signal is applied.

The vaporizer cutoff line is controlled by a pair of normally open contacts on the surge cycle control relay K33 which is located in the positive high voltage control panel. The control relay closes during the 30 second waiting period following repetitive overloads and grounds the cutoff line, thus short-circuiting the signal normally applied to the vaporizer power amplifier. The latter consists of a magnetic-amplifier-triggered silicon controlled rectifier which provides control of the power applied to the vaporizer step-down transformer. The step-down transformer has a 115 VAC primary and a high voltage insulated secondary rated at 10 volts, 20 amperes.

Arc Control

Operation of the arc control loop can be understood by refering to the system block diagram shown in Fig. 4-36. The arc control utilizes the same voltage analogs of beam current and arc current as the beam control loop The major arc control components are the arc control chassis and the power amplifier located in the

control console; and the arc power output panel which is a unit of the auxiliary power rack. Arc circuit operation commences when the first preheat cycle is complete and the arc power relay in the power amplifier chassis closes, thereby applying 120 vac power to the input of the arc power amplifier. At this time arc-loop transfer relay K302 is in the de-energized condition, and the output of preset level control R301 is applied to the signal control winding of the power amplifier. Thus, during preheat cycle no. 2 the arc operates at a preset level (open loop).

At completion of preheat cycle no. 2 the arc loop transfer relay K302 is energized, closing the arc control loop. Power amplifier control is transferred from the preset control to the output of the operational amplifier. A second set of contacts on K302 transfers the grounded line of the arc current transductor from the positive side to the negative side so that its output signal is now positive with respect to ground. Three reference voltages and one feedback signal are applied to the input of the operational amplifier. The first reference voltage is the manual reference which is derived from the front panel control R303. The second reference input is the offset signal which originates as the output of offset voltage potentiometer R316, a screwdriver adjustment, and becomes the offset signal after passing through the stepping switch of the programmed reference. The arc current analog acts as a negative feedback signal while the beam current analog is a reference signal which serves to call for increased arc current with increased beam current. The result is the beam current arc current characteristic shown in Fig. 4-29.

The power amplifier utilizes a pair of magnetic-amplifier-triggered silicon controlled rectifiers to control the power applied to the primary of the arc power supply step-down transformer. Power amplifier output is proportional to the current applied to the control winding by either the output of the operational

amplifier (closed loop), the setting of preset potentiometer (open loop) or setting of MANUAL CONTROL (manual mode).

The arc power supply consists of the step-down transformer, a silicon bridge-type rectifier and L-C filter all located in the arc power output panel. Also located here is the arc current transductor, a magnetic amplifier controlled rectifier which produces a signal proportional to the arc current. Both the power transformer and transductor provide high voltage insulation required to isolate primary lines and signal output lines from high engine potentials.

The arc control chassis also performs auxiliary functions. A front panel milliammeter with a calibrating multiplier resistance connected across the transductor circuit provides indication of arc current. A sensitive relay K301 and calibrating resistance connected across the transductor circuit provides indication of arc current. A sensitive relay K301 and calibrating resistance also connected across the transductor circuit are used for limiting the current. This circuit is set so that when arc current exceeds 60 amperes, the relay closes and its contacts energize an auxiliary control winding of the power amplifier which cuts off the output, momentarily extinguishing the arc. The third auxiliary function is performed by the arc interlock circuit which also uses the transductor signal. This circuit opens the cathode heater circuit when arc current reaches 20 amperes and closes the heater circuit if arc current is 10 amperes or less. The arc interlock circuit incorporates a magnetic bistable switch that normally has zero output but when activated puts out about 24 VDC. The transductor signal is applied to one control winding of the bistable switch. The bistable bias control R305 establishes the value of the transductor signal which switches the bistable. The setting of a second control, the hysteresis control, R311, determines what proportion of the output signal is returned to a second control winding of the bistable. Application

of feedback in this manner produces hysteresis which prevents rapid cycling at the cathode heater. The bistable amplifier output is applied to the coil of arc control relay K303 which completes the circuit for a repeater relay solenoid in the programmer, which in turn opens the cathode heater A.C. line.

5. ENGINE SYSTEM PERFORMANCE AND EVALUATION

5.1 Engine Performance

The performance of the DE engine systems was measured over a wide range of operating parameters. Thrust levels of from 3 to 15.3 millipounds and power to thrust ratios of 153 to 205 kilowatts per pound were obtained at specific impulses from 4100 to 7050 seconds. Ion source mass utilization efficiencies from 81 to 95 percent were achieved at energy expenditures of 500 to 850 electron volts per ion.

Figure 5-1 shows some of the data taken with the DD, DE 1, and DE 2 engines. Table 5-I is a compilation of data obtained with the DE engine systems. Points 4, 12, 13, 14, 21, and 25 were taken with the DE-1 system. Point 18 was taken with the DE-2 engine and the 750-hour feed system. All remaining points were taken with DE-2 engine using the 50-hour feed system. Points 6, 8, 9, 16, 20, and 22 were taken in a 5 foot by 12 foot vacuum chamber. All other points were taken with the engines operated in a 2 foot x 6 foot vacuum chamber. In addition, all DE-2 points were taken after a minimum of 10 minutes steady operation and at pressures below 5×10^{-6} millimeters of mercury.

As the data shows, the engine source efficiency (ev/ion vs mass efficiency) improves at higher beam levels. Overall engine efficiency depends on the tradeoff between arc power and mass efficiency, a higher mass efficiency being desired at higher specific impulses. All the data presented in Table 5-I are not at optimum levels but rather are intended to show the wide range over which the engine may be operated with reasonable efficiency. High beam levels
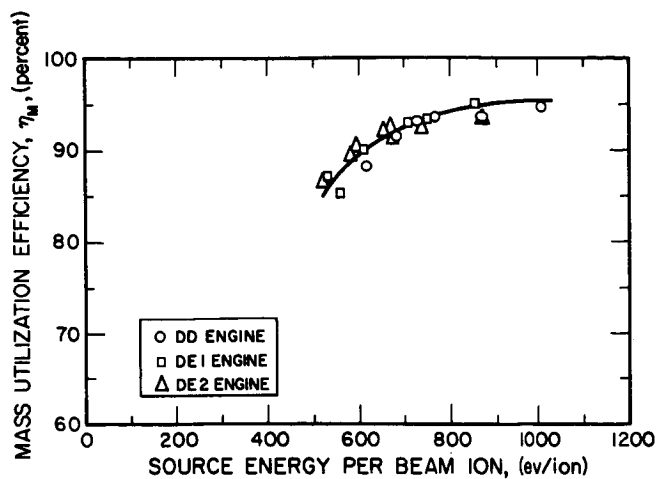
FIG. 5-1a

COMPARISON OF MASS UTILIZATION
DATA, DD AND DE ENGINES
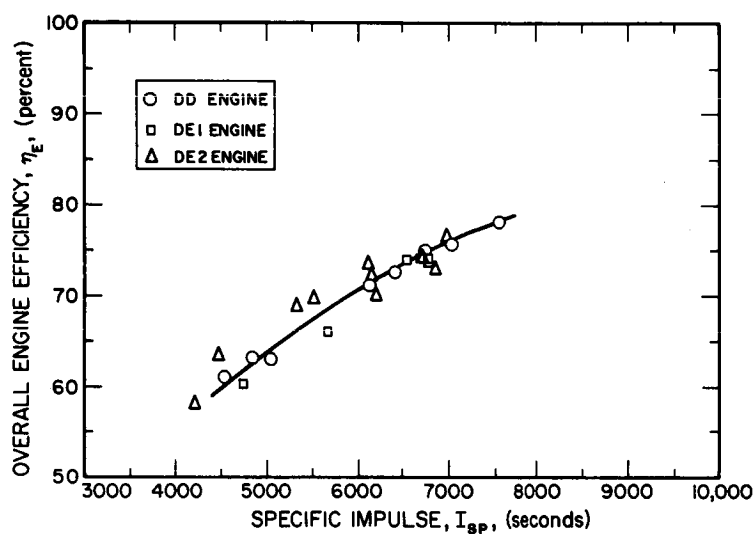
FIG. 5-1b

COMPARISON OF ENGINE
EFFICIENCIES, DD AND DE
ENGINES
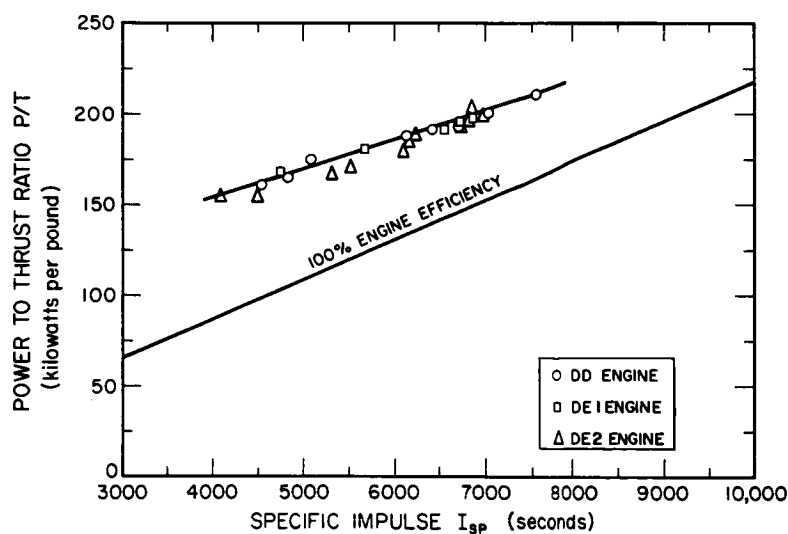
FIG. 5-1c

COMPARISON OF ENGINE
PERFORMANCE, DD AND
DE ENGINES

TABLE 5-I   DE ENGINE SYSTEM DATA

Run	1	2	3	4
Positive High Voltage, V_+ (kv)	1.6	2.0	2.5	2.5
Negative High Voltage, V_- (kv)	1.4	1.6	1.6	1.75
Negative HV Current, I_- (amp)	0.003	0.006	0.010	0.011
Beam Current, I_B (amp)	0.200	0.325	0.450	0.529
Arc Voltage, V_A (volt)	6.4	6.2	6.1	6.9
Arc Current, I_A (amp)	19.5	28.0	38.0	43.0
Beam Power, P_B (kw)	0.320	0.650	1.125	1.320
Drain Power, P_D (kw)	0.009	0.022	0.041	0.047
Magnet Power, P_M (kw)	0.007	0.007	0.008	0.006
Arc Power, P_A (kw)	0.125	0.174	0.232	0.297
Total Power, P_T (kw)	0.461	0.835	1.406	1.670
Thrust, T (mlb)	3.01	5.47	8.46	10.0
Power to Thrust, P/T (kw/lb)	153.0	153.0	166.0	167.0
Power Efficiency, η_P (percent)	69.5	78.0	80.0	79.0
Mass Efficiency, η_M (percent)	83.5	81.5	86.5	85.0
Overall Engine Efficiency, η_E (percent)	58.0	63.5	69.0	67.0
Specific Impulse, I_{sp} (sec)	4100	4480	5310	5220
Ratio of Drain Current to Beam Current, I_-/I_B (percent)	1.5	1.85	2.2	2.1
Source Energy per Ion, P_A/I_B (kev/ion)	0.625	0.535	0.516	0.562

TABLE 5-I   DE ENGINE SYSTEM DATA (contd)

Run	5	6	7	8	9	10	11
V_+ (kv)	2.5	2.5	3.0	3.0	3.0	3.0	3.0
V_- (kv)	1.6	1.55	0.9	1.3	1.15	1.35	1.35
I_- (amp)	0.010	0.0075	0.008	0.007	0.008	0.0095	0.009
I_B (amp)	0.450	0.400	0.450	0.450	0.442	0.450	0.450
V_A (volt)	6.7	7.2	6.8	7.3	7.5	7.3	8.0
I_A (amp)	39.0	34.0	39.0	38.0	38.5	41.0	46.0
P_B (kw)	1.125	1.000	1.350	1.350	1.326	1.350	1.350
P_D (kw)	0.041	0.030	0.031	0.030	0.033	0.041	0.039
P_M (kw)	0.008	0.008	0.008	0.008	0.008	0.008	0.009
P_A (kw)	0.261	0.245	0.265	0.270	0.289	0.299	0.368
P_T (kw)	1.435	1.283	1.654	1.658	1.656	1.698	1.766
T (mlb)	8.46	7.52	9.27	9.28	9.11	9.27	9.27
P/T (kw/lb)	170.0	171.0	178.0	179.0	182.0	183.0	190.0
η_P (percent)	78.5	78.0	81.5	81.5	80.0	79.5	76.5
η_M (percent)	89.5	89.0	90.0	88.5	89.0	91.0	91.5
η_E (percent)	70.0	69.5	73.0	72.0	71.0	72.0	70.0
I_{sp} (sec)	5500	5450	6070	5940	5970	6140	6180
I_-/I_B (percent)	2.2	1.9	1.8	1.6	1.8	2.1	2.0
P_A/I_B (kev/ion)	0.580	0.612	0.589	0.600	0.654	0.664	0.818

TABLE 5-I   DE ENGINE SYSTEM DATA (contd)

Run	12	13	14	15	16	17	18
V_+ (kv)	3.2	3.2	3.5	3.6	3.6	3.6	3.6
V_- (kv)	0.9	0.9	1.0	0.8	0.9	0.8	0.75
I_- (amp)	0.012	0.016	0.010	0.0065	0.007	0.0075	0.0065
I_B (amp)	0.468	0.509	0.565	0.425	0.432	0.433	0.429
V_A (volt)	7.7	8.0	7.4	7.25	7.9	7.6	8.1
I_A (amp)	52.0	47.5	47.0	38.0	39.5	42.0	41.5
P_B (kw)	1.561	1.630	1.980	1.530	1.555	1.559	1.543
P_D (kw)	0.051	0.066	0.043	0.029	0.032	0.033	0.033
P_M (kw)	0.003	0.004	0.006	0.008	0.008	0.008	0.008
P_A (kw)	0.400	0.380	0.348	0.276	0.312	0.319	0.336
P_T (kw)	2.015	2.080	2.377	1.843	1.907	1.919	1.920
T (mlb)	10.0	10.85	12.6	9.59	9.76	9.77	9.68
P/T (kw/lb)	202.0	192.0	189.0	192.0	195.0	196.0	198.0
η_p (percent)	78.0	78.0	83.0	83.0	81.5	81.0	80.5
η_M (percent)	95.0	94.0	90.0	91.0	91.5	92.0	91.5
η_E (percent)	74.0	73.0	75.0	75.5	74.5	74.5	73.5
I_{sp} (sec)	6600	6500	6550	6700	6745	6780	6720
I_-/I_B (percent)	2.6	3.1	1.7	1.5	1.6	1.7	1.5
P_A/I_B (kev/ion)	.855	0.745	0.614	0.649	0.723	0.737	0.784

TABLE 5-I DE ENGINE SYSTEM DATA (contd)

Run	19	20	21	22	23	24	25
V_+ (kv)	3.6	3.7	3.8	3.8	3.8	3.8	4.0
V_- (kv)	0.8	0.9	0.9	0.8	0.8	0.9	1.0
I_- (amp)	0.010	0.0055	0.028	0.007	0.0095	0.026	0.022
I_B (amp)	0.430	0.355	0.482	0.500	0.500	0.506	0.643
V_A (volt)	8.2	7.8	6.4	7.5	7.5	7.9	6.7
I_A (amp)	45.5	34.5	35.0	43.5	44.0	45.5	51.5
P_B (kw)	1.548	1.314	1.830	1.900	1.900	1.922	2.570
P_D (kw)	0.044	0.025	0.134	0.032	0.044	0.122	0.110
P_M (kw)	0.009	0.008	0.004	0.008	0.009	0.004	0.006
P_A (kw)	0.373	0.269	0.224	0.326	0.330	0.360	0.345
P_T (kw)	1.974	1.616	2.192	2.266	2.283	2.408	3.031
T (mlb)	9.71	8.13	11.2	11.6	11.60	11.75	15.3
P/T (kw/lb)	203.0	199.0	196.0	195.0	197.0	205.0	198.0
η_p (percent)	78.5	81.5	84.0	84.0	83.0	80.0	85.0
η_M (percent)	93.0	90.5	88.0	91.0	92.0	93.0	87.0
η_E (percent)	73.0	73.5	74.0	76.5	76.5	74.0	74.0
I_{sp} (sec)	6850	6750	6700	6860	6970	7050	6780
I_-/I_B (percent)	2.3	1.6	5.8	1.4	1.9	5.2	3.4
P_A/I_B (kev/ion)	0.867	0.758	0.465	0.653	0.660	0.710	0.536

required for a given thrust at low specific impulses are not compatible with the resultant low voltages. Therefore, electrodes with more apertures of small diameter and gap would be required to increase the obtainable thrust at lower impulses.

DE 1 engine performance in Fig. 5-1 was extracted from data taken in the course of system integration tests and no optimization was attempted for those points. The DE 2 engine performance data were taken with a moderate attempt at optimization and as indicated in Figs. 5-1b and 5-1c, higher engine efficiencies and lower power-to-thrust ratios were obtained.

5.2 DE 1 Engine System Tests

During January 1964, the DE 1 system underwent qualification tests consisting of 10 automatic start-ups and shut-downs and a 77-hour run.

5.2.1 Start-Stop Tests

The automatic start-stop tests were spaced to allow cooling of the system between operating periods. The following schedule was used:

TABLE 5-II

START-STOP TEST SCHEDULE

Test	Date	Start Time	Stop Time
1	7 Jan.	1230	1350
2	7 Jan.	1700	1802
3	7 Jan.	2100	2205
4	8 Jan.	0450	0556
5	8 Jan.	0900	1003
6	8 Jan.	1300	1404
7	8 Jan.	2200	2308
8	9 Jan.	0200	0308
9	9 Jan.	0600	0708
10	9 Jan.	1000	1113

In runs 1 and 10, the system was taken out of automatic operation, after 10 minutes steady state operation, long enough to take mass utilization measurements. The measurement for test 1 was 92.4 percent; the measurement for test 10 was 91.5 percent. Typical operating characteristics at full beam during the test were: (Data of test 3)

TABLE 5-III

TYPICAL FULL BEAM OPERATION FOR START-UP TESTS

Positive High Voltage, V_+ (kv)	3.55
Negative High Voltage, V_- (kv)	0.93
Negative HV Current, I_- (amp)	0.0073
Beam Current, I_B (amp)	0.478
Arc Voltage, V_A (volt)	8.05
Arc Current, I_A (amp)	44.5
Beam Power, P_B (kw)	1.697
Drain Power, P_D (kw)	0.033
Magnet Power, P_M (kw)	0.009
Arc Power, P_A (kw)	0.358
Total Power, P_T (kw)	2.097
Thrust, T (mlb)	10.7
Power to Thrust, P/T (kw/lb)	196
Power Efficiency, η_P (percent)	81 percent
Mass Efficiency, η_M (percent)	~91.5 percent
Overall Engine Efficiency, η_E (percent)	~74 percent
Specific Impulse, I_{sp} (sec)	6700
Ratio of Drain Current to Beam Current, I_-/I_B (percent)	1.5 percent
Source Energy per Ion , P_A/I_B (kev/ion)	0.750

A typical run sequence is depicted in Fig. 5-2. In this figure the beam current and neutral efflux (in equivalent milliamperes) are shown plotted versus time. The test is initiated by pushing a single start button. During the "Preheat 1" phase the cathode heater,
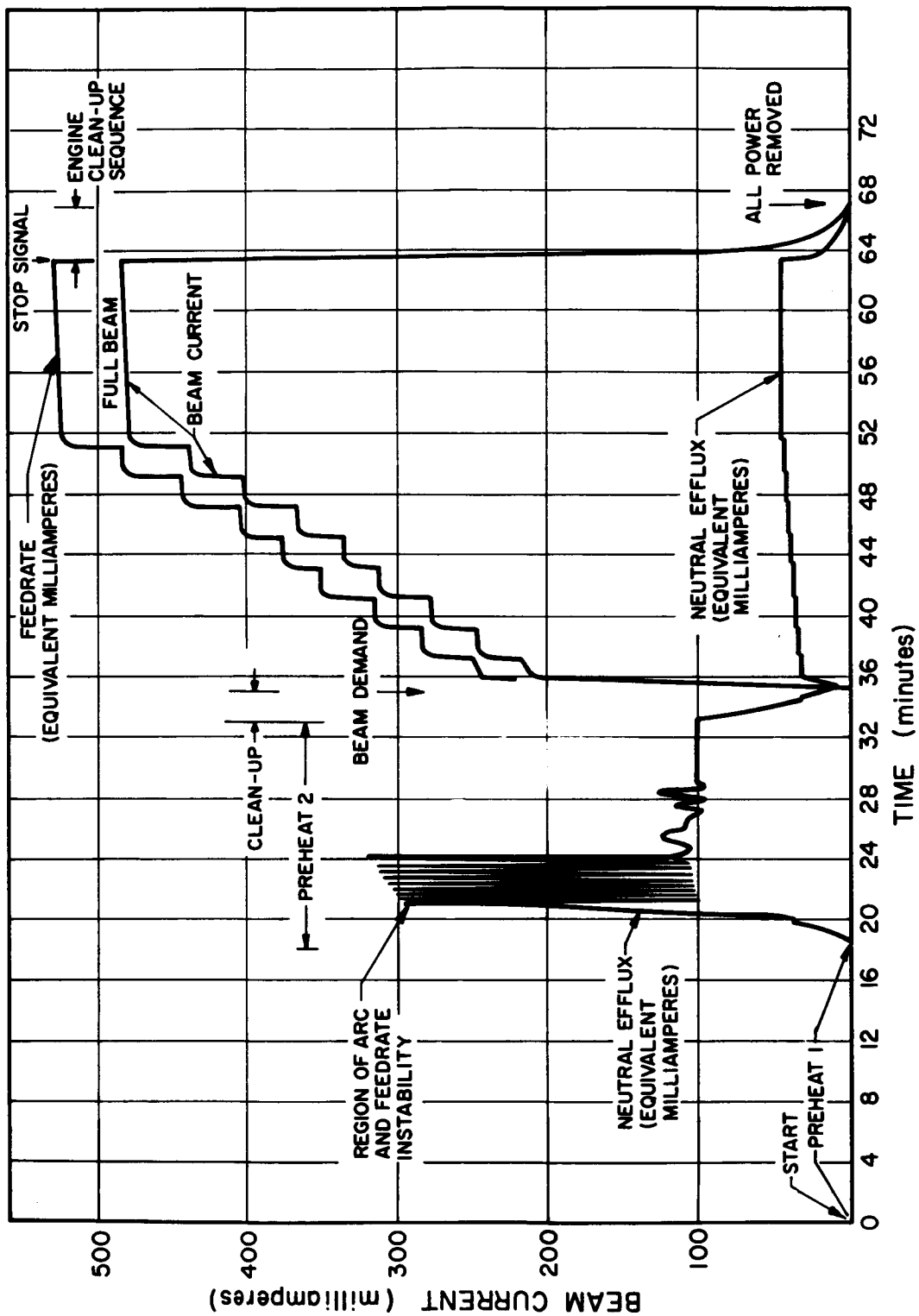
FIG. 5-2 TYPICAL START-STOP TEST

magnet, neutralizer, and valve heater are turned on, the valve heater power being set to a high value. The purpose of this phase is to heat the valve to a high enough temperature (~ 350°C) so that when cesium flow is established condensation in the valve will not ruin feedrate control. This phase was set at 18 minutes with about 150 watts into the valve heater.

In the "Preheat 2" phase the arc is used to heat the body of the engine, again to prevent condensation and feed control problems. At switchover from "Preheat 1" to "Preheat 2" the valve heater power is dropped to its normal value of 65 watts, the arc voltage is turned on, and the vaporizer heater is energized. In this phase, the feed system is controlled to give an arc current of about 30 amperes. The large excursions shown for the neutral efflux for the start of "Preheat 2" in Fig. 5-2 are due to the valve ball not being above the cesium condensation temperature. That is, "Preheat 1" was not quite long enough. Toward the end of "Preheat 2" all components have reached operating temperature and the neutral efflux is steady. The "Preheat 2" timer was set for 15 minutes.

At the end of "Preheat 2" a 2 minute cleanup phase, in which the vaporizer power is removed, takes place. During "Preheat 2" and subsequently the cathode heater is keyed to the arc current so that cathode heater power is removed when the arc current goes above 20 amperes and is not turned back on until the arc current falls to below 10 amperes. The cathode heater is therefore off during "Preheat 2" and during following operation with a beam current over about 80 milliamperes.

After the cleanup period, the system turns on the high voltage supplies and the vaporizer heater with a beam demand of about half the full beam. The normal feedrate and arc control loops are now in operation. The system was set to step the beam demand to full beam in 9 steps at 2 minutes intervals. The steps and intervals are both programmable. Performance at full beam is listed in Table 5-III.

After a minimum of 10 minutes in full operation, the system stop button was pushed to initiate the automatic stop sequence. This sequence takes place with three 2 minute intervals. In the first interval the beam demand is set to zero with the arc control loop still in normal operation. In the next two intervals the arc is turned on full to clean out any remaining cesium in the chamber. At the end of the 6 minute stop sequence all power is removed from the engine system. The engine is clean and after cooling a suitable time the next test is initiated by pushing the start button.

5.2.2 77-Hour Run

The feed system had been loaded with about 250 gms cesium prior to the start-stop tests. After some preliminary operation on 5 January and the 10 start-stop tests, it was estimated that about 220 gms cesium remained in the reservoir. Since previous experience had indicated that it was difficult to extract the last 30 to 40 gms of cesium from a DE reservoir, it was estimated that 185 gms of cesium were available for the continuous run.

The choice was made to go for a 75-hour run at lower thrust rather than a 50-to 60-hour run at very high thrust. Engine operating conditions were chosen to give approximately 75 hours operation with 180 gms of cesium. The run was started on 9 January with full thrust from 1530 on. During the test, which actually lasted about 80 hours, there were five interruptions of full thrust. At 9 hours an SCR in the magnet power supply went out and the supply was replaced. At 20 hours and at 48 hours there were brief interruptions due to failure of relays.

At 58 hours there was a period of instability during which the engine was below specified thrust for about 1/2 hour. This appeared to be caused by a large burst of cesium from the feed system which flooded the engine and got cesium on the electrode insulators. It was cleaned up by "idling" the engine for a while. At 72 hours a fall in beam current and rise in vaporizer temperature was encountered.

This was a typical "breakaway" of the liquid-cesium interface from the front of the vaporizer and usually signifies that the cesium supply is getting low. In this case the system was taken back to full thrust and ran for several more hours. At about 79.5 hours another "breakaway" occurred. To continue the run, the vaporizer heater power would have had to be maintained above a safe limit so the test was terminated at that point.

The time history of the vaporizer temperature and the vaporizer heater power is presented in Fig. 5-3. The events discussed above and the periods for which the system was at lower-than-acceptable thrust are indicated on the figure.

The run was made at the following performance level: (Data of 11 January - 1000 am).

TABLE 5-IV

OPERATING LEVEL DURING 77 HOUR TEST

Positive High Voltage, V_+ (kv)	3.55
Negative High Voltage, V_- (kv)	0.89
Negative HV Current, I_- (amp)	0.0076
Beam Current, I_B (amp)	0.430
Arc Voltage, V_A (volt)	7.95
Arc Current, I_A (amp)	40.5
Beam Power, P_B (kw)	1.527
Drain Power, P_D (kw)	0.034
Magnet Power, P_M (kw)	0.010
Arc Power, P_A (kw)	0.322
Total Power, P_T (kw)	1.893
Thrust, T (mlb)	9.63
Power to Thrust, P/T (kw/lb)	196.0
Power Efficiency, η_p (percent)	80.5 percent
Mass Efficiency, η_M (percent)	91.0 percent
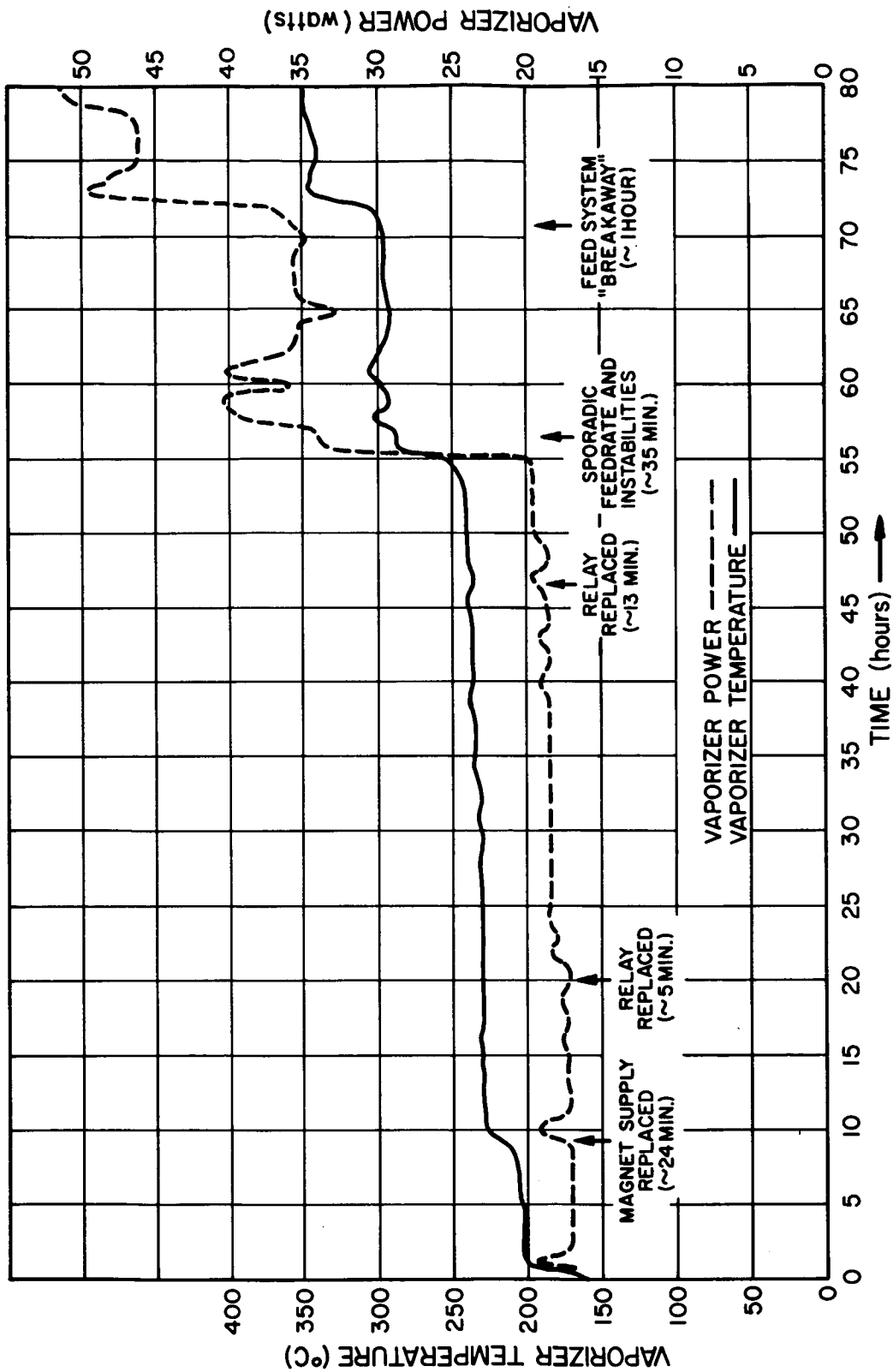
FIG. 5-3   VAPORIZER TEMPERATURE AND POWER DURING 77-HOUR RUN

TABLE 5-IV (contd)

Overall Engine Efficiency, η_E (percent)	73.5 percent
Specific Impulse, I_{sp} (sec)	6650
Ratio of Drain Current to Beam Current, I_-/I_B (percent)	1.8 percent
Source Energy per Ion, P_A/I_B (kev/ion)	0.750

In addition, at the time this data was taken, neutralizer power was 129 watts and the vaporizer heater power was 19 watts.

5.2.3 Condition of System After Test

A photographic record of the engine components was made after the tests. Figure 5-4 is two views of the system upon its removal from the vacuum tank. Except for copper, sputtered from the collector, coating on areas facing the collector, the system appeared to be very clean. The portion of the neutralizer facing the collector was also coated with copper despite its elevated temperature during system operation. Figure 5-5 is a view of the arc chamber with the electrodes removed. A pattern due to sputtered copper from the collector passing through the electrode aperture array is evident on the anode.

Figure 5-6 shows the autocathode used in the DE 1 tests on the right and a new cathode (DE 2) on the left for comparison. The DE 1 cathode did not appear different from a cathode run only a few hours. Most of the differences in finish are due to the fact that the DE 1 cathode had been used before the reported tests and had been liquid-honed a few times.

The accelerating electrode is shown in Fig. 5-7. The only measurable erosion was on the downstream side shown in Fig. 5-7a. The copper deposit on the downstream side was about 0.0005 inch thick (measured at the periphery where there is no erosion) and peeled off easily. The erosion, which was apparently due to charge exchange was measureable only at "pits" between apertures. The measured depths corresponding to the indicated positions (arrows) on Fig. 5-7a were:
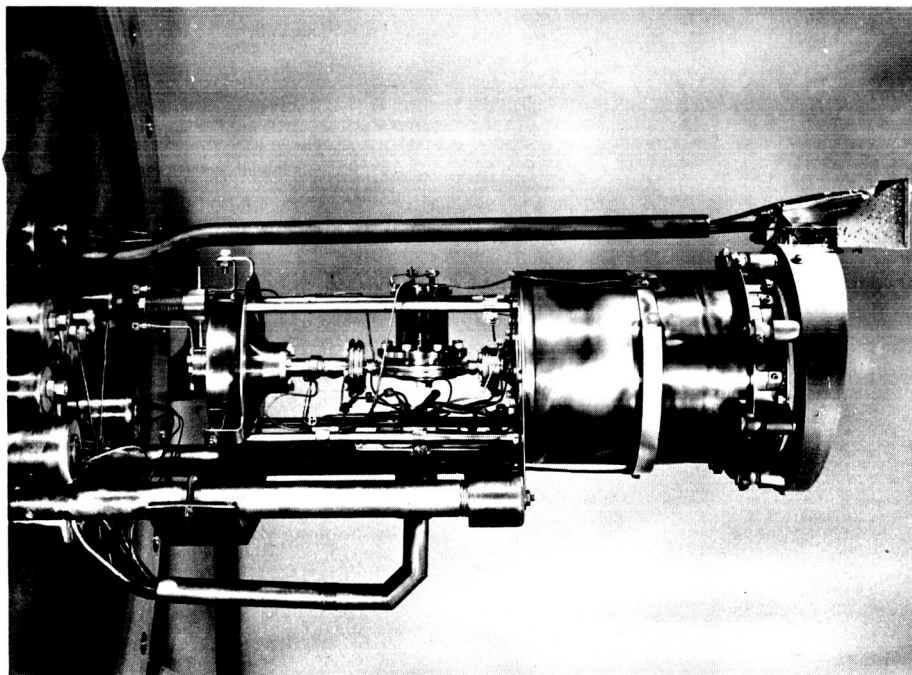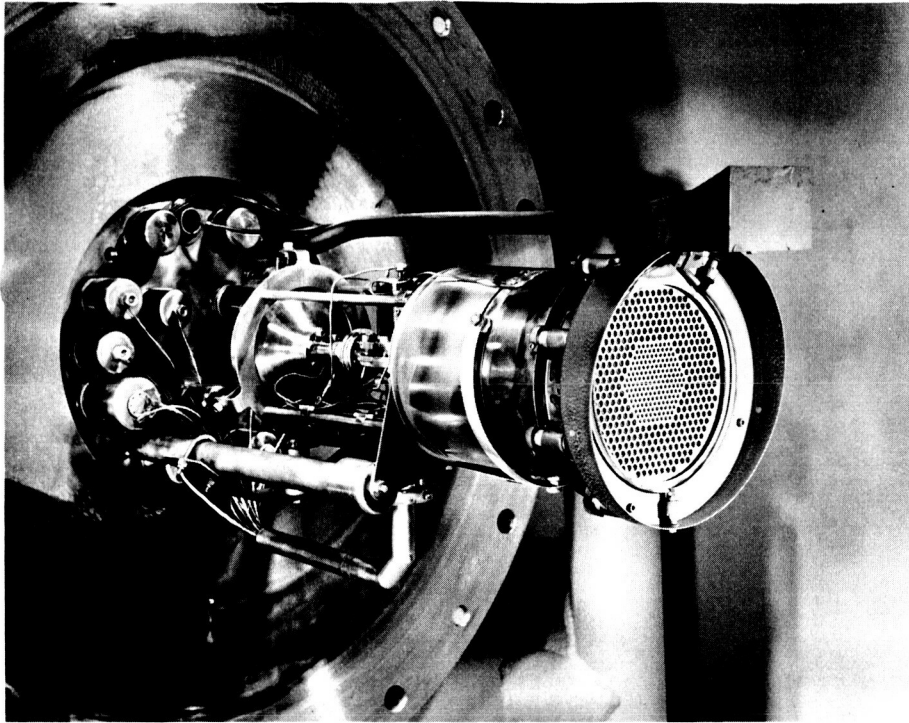
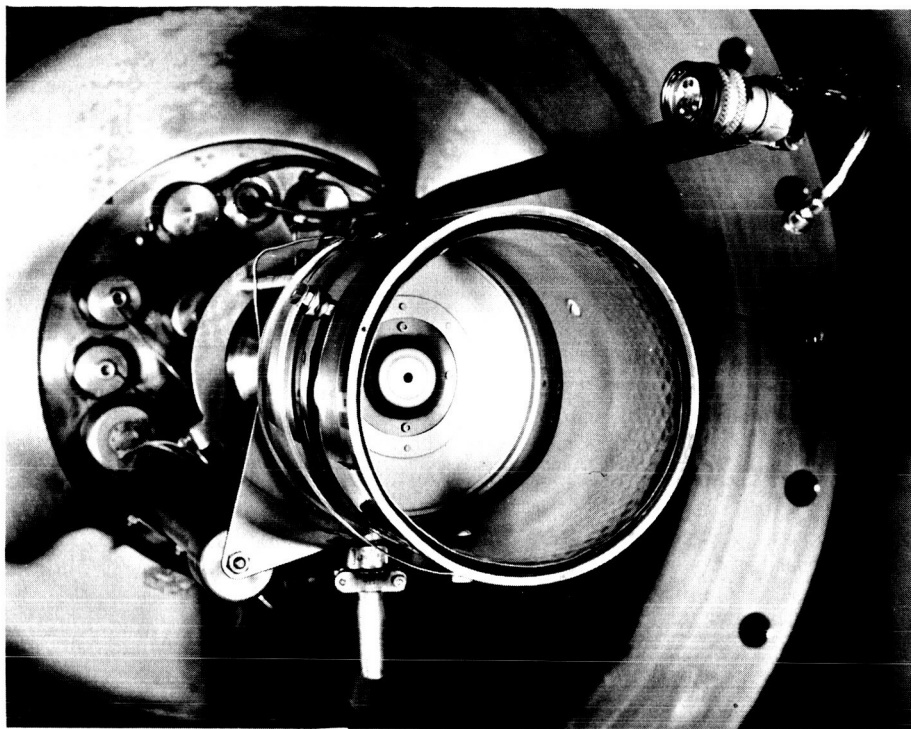FIG. 5-4   DE ENGINE SYSTEM AFTER QUALIFICATION TEST
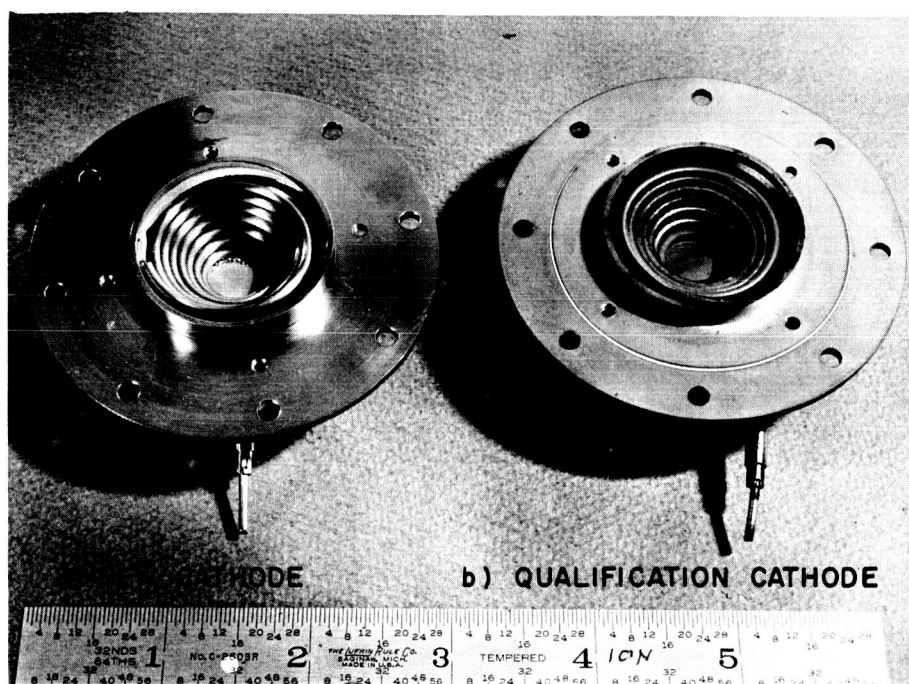
184

FIG. 5-5   DISCHARGE CHAMBER

FIG. 5-6   AUTOCATHODE

1. 0.004 inch deep pits (12 places - 2 on each side as shown).

2. 0.001 inch deep pits (typical at other places in region between different size holes).

3. 0.0005 inch deep pits (typical between small holes in central portion of electrode).

4. Pits visible but not measurable - less than 0.0002 inch deep (typical of pits between large holes).

The deep pits occur only in the region between the two sizes of apertures where there is a large (web) area and deeper pits should not affect structural or ion-optical performance of the accelerator. It appears that the accelerating electrode should have a lifetime of several thousand hours under the operating conditions of the test. The upstream side of the accelerating electrode, Fig. 5-7b, showed some discoloration but no measurable erosion.

The screen electrode is shown in Fig. 5-8. Some discoloration is evident but no erosion. The insulators, as shown in Fig. 5-8a, got a little dirty where they were not shielded but generally stayed quite clean. The screen electrode picked up an additional .005 inch bow toward the accelerating electrode but this has no significant affect on engine operation at the design level.

Figure 5-9 shows the valve disassembled in the dry box. It appeared to be quite clean but there was a coating built up on the ball. An analysis of the coating disclosed less than 0.05 percent impurities besides the base iron present. Figure 5-10 shows the vaporizer section separated from the reservoir. The porous inserts of both components appeared to be well wetted with cesium. Some of the cesium was sent out for analysis and the only impurity found was an immeasurably small trace of silver. This must have been present in the original cesium or in the porous nickel inserts since no silver-based brazes or materials are used in fabrication or assembly of the feed system.
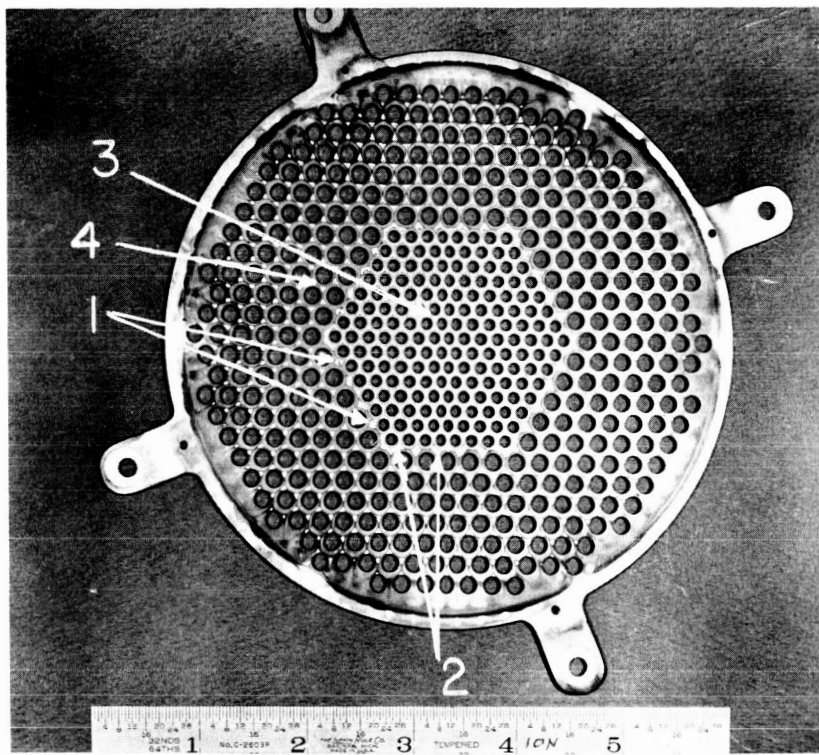
a   ACCELERATING ELECTRODE - DOWNSTREAM SIDE
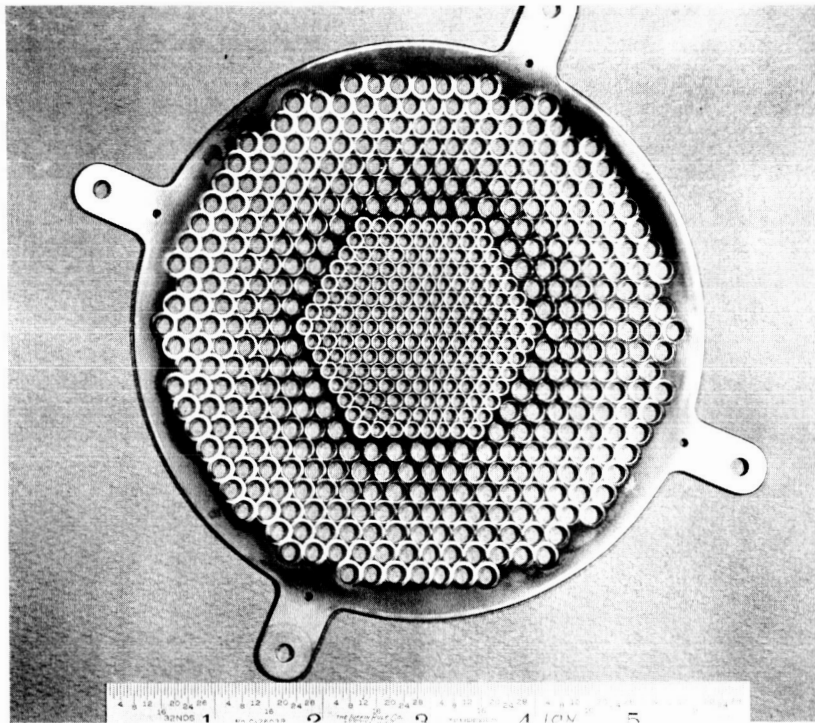
b   ACCELERATING ELECTRODE - UPSTREAM SIDE
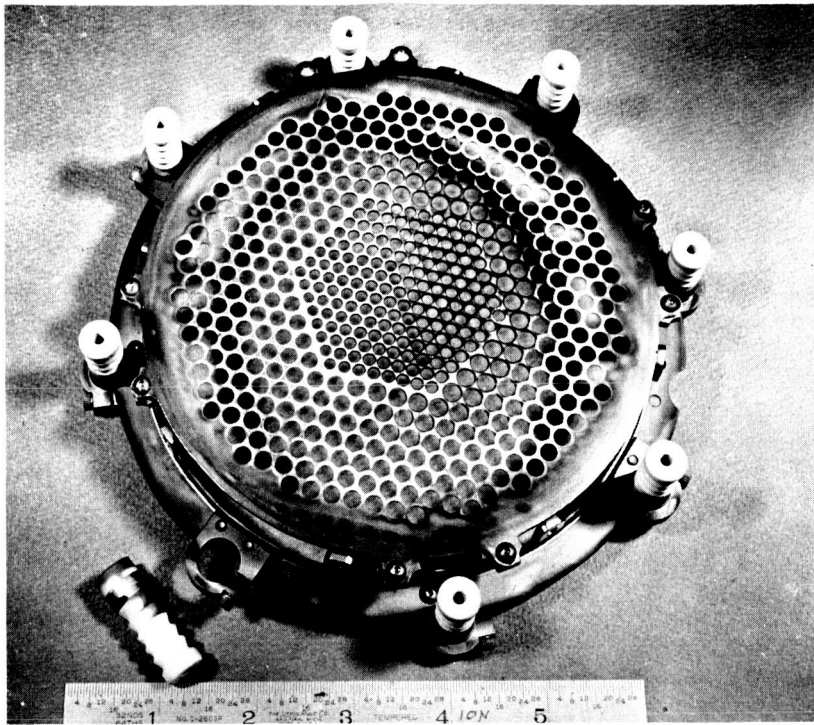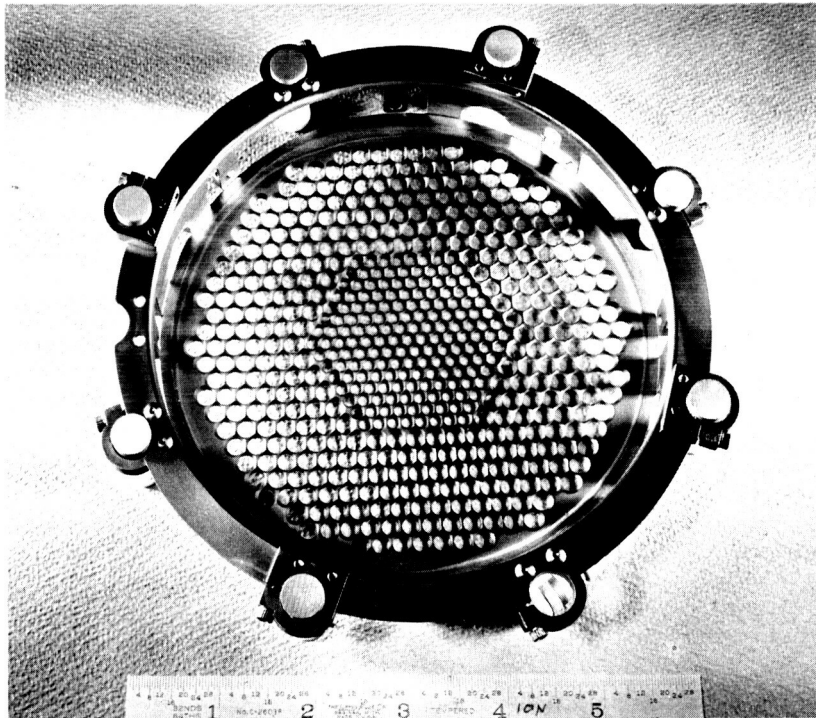
FIG. 5-7   ACCELERATING ELECTRODE

a   SCREEN ELECTRODE - DOWNSTREAM SIDE

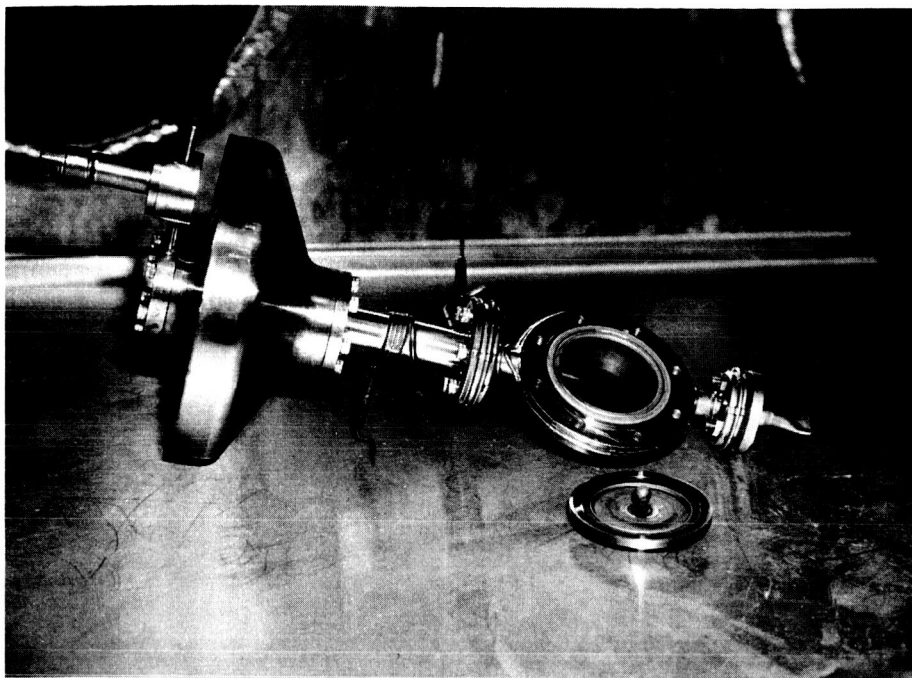b   SCREEN ELECTRODE - PLASMA SIDE

FIG. 5-8   SCREEN ELECTRODE

FIG. 5-9   SOLENOID VALVE PARTS
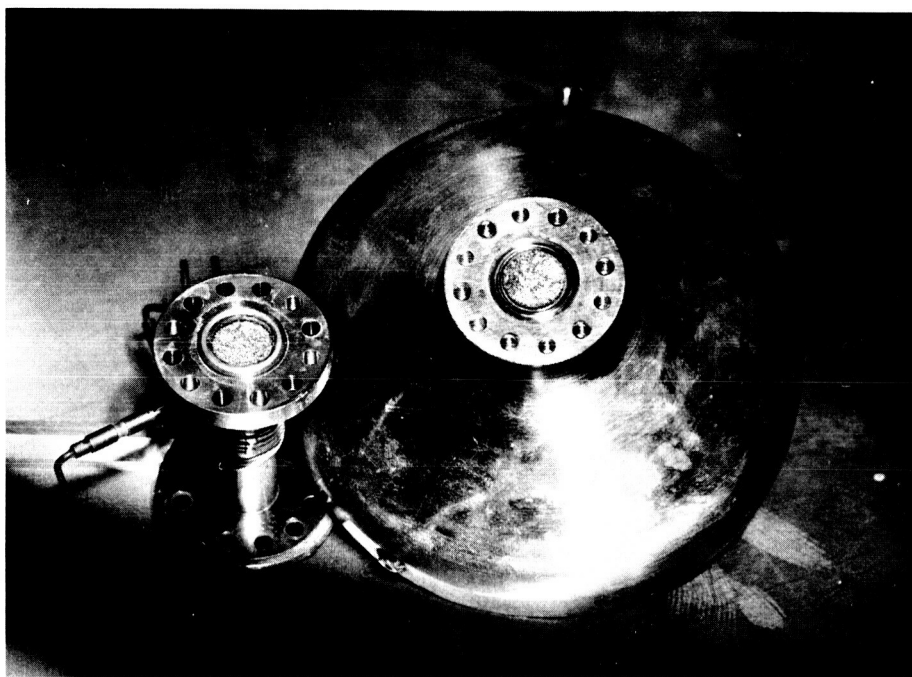
FIG. 5-10   FEED SYSTEM PARTS

5.3 DE 2 System Tests

The DE 2 engine and feed system were first operated with the DE 1 control system and operation was found to be quite similar. The same performance and efficiency of operation to within 1 percent were attained with a slightly lower magnetic field, slightly lower arc voltage, and slightly higher arc current than for the DE 1 engine. The differences were on the order of 5 percent and are attributed to a measured 7 percent higher magnetic field (per ampere magnet current) at the screen electrode for the DE 2 engine and 12 percent higher field at the cathode for DE 1 engine. The fabrication and assembly of the auto-cathode is rather complex, causing some variation between cathodes which might also be a factor. The efficiencies of the two engines for a given operating point were quite close.

The DE 2 engine and feed system were then operated with the DE 2 control system and power supplies. DE 1 performance data was extracted from data taken in the course of system integration tests and no optimization was attempted. The DE 2 engine performance data was taken with a moderate attempt at optimization and higher engine efficiencies and lower power-to-thrust ratios were obtained in this case.

Figure 5-11 is a reproduction (65 percent scale) of a strip chart record of beam current and neutral efflux signals during an automatic start with the DE-2 system. The pens are spaced "1 minute" apart with the neutral efflux signal pen leading. Start marks for the pens are shown at the right and the time scale is indexed for both pens. In this case the "preheat 1" timer was set for 20 minutes and the preheat 2 timer for 15 minutes. The turn-on was made from a system at about 10°C and was quite smooth. The slightly longer "preheat 1" period appears to reduce the feed instabilities in the "preheat 2" phase considerably.

FIG. 5-11   DE2 SYSTEM START-STOP TEST

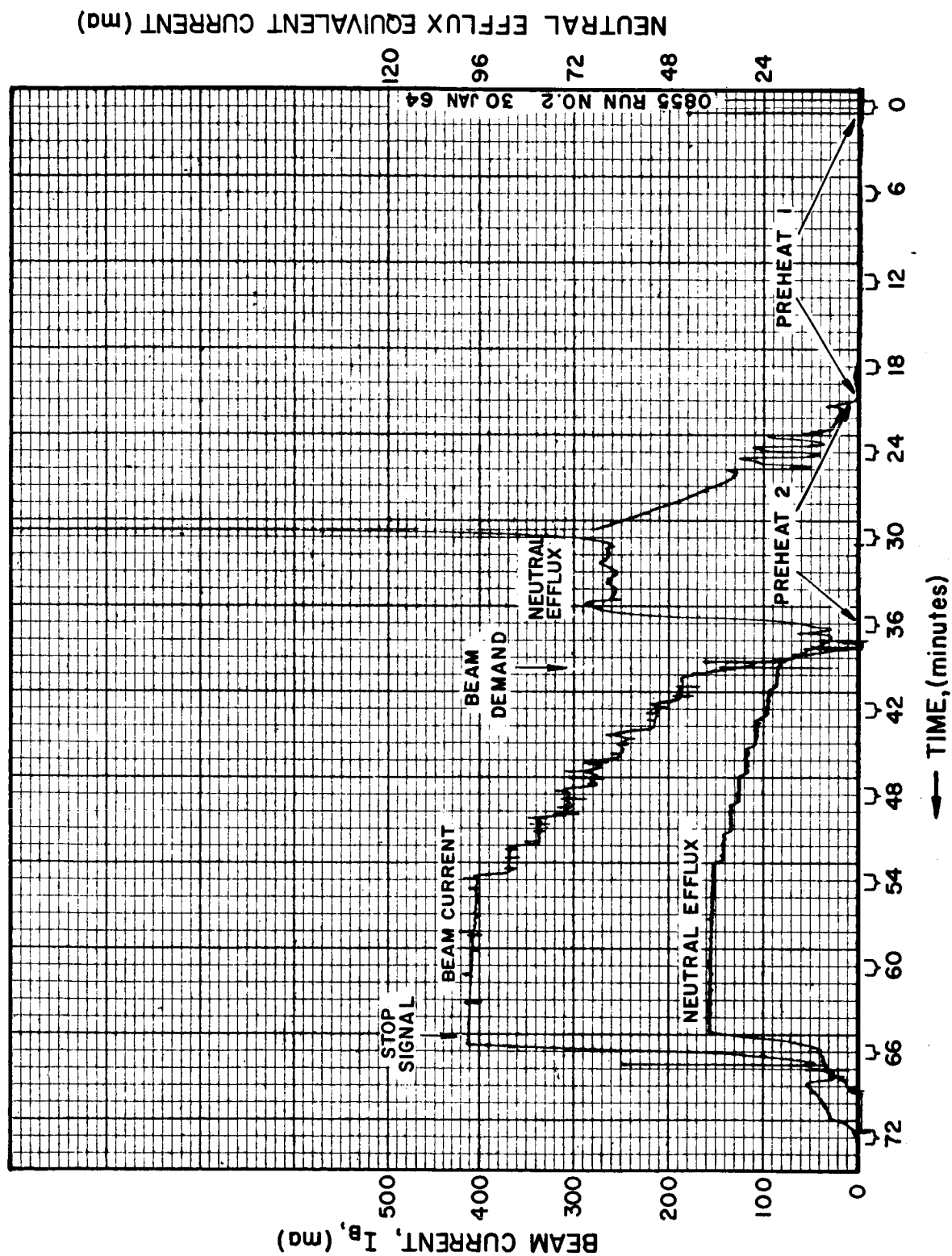Following these tests, the DE 2 engine system was run in a 5 foot x 12 foot vacuum tank to determine whether there was any difference in operation as compared with previous runs made in a 2 foot x 6 foot chamber. A successful start-stop test plus about six hours of continuous operation at varied operating levels revealed no difference in operation; operating levels agreed to within one percent.

5.4 Tests with 750-Hour Feed System

The DE 2 engine was cleaned and reassembled with the 750-hour feed system. The complete system is shown in Fig. 5-12. An automatic start revealed that the feed system response was considerably faster than that of the 50-hour feed system. This response caused some oscillation during the "Preheat 2" phase and later in full beam operation. The compensation in the feedrate control loop was changed and a second start-stop test was performed. No difficulty was encountered. When the system was at full beam, operation was switched to manual and the performance of the engine was evaluated. Again, no significant differences were measured.

5.5 Lifetime Expectations

As mentioned in Section 5.2, the only degradation of the engine system which could be observed after the 77 hours of operation was erosion of the accelerating electrode. Pits between apertures in the transition area between the smaller and larger aperture sizes measured 0.004 inches deep. If this erosion were to continue at such a rate and if failure were to occur when these 12 pits pierced the accelerating electrode, a lifetime of only 900 to 1000 hours would be expected. That the engine would fail when these pits became as deep as the original electrode is extremely unlikely because of the large mass areas in those regions. It is also not expected that pits would deepen at a constant rate and the 1000 hour estimate is extremely pessimistic. Other considerations might indicate a lifetime expectation of several thousand hours but it is not valid to extrapolate the test period beyond an order of magnitude.
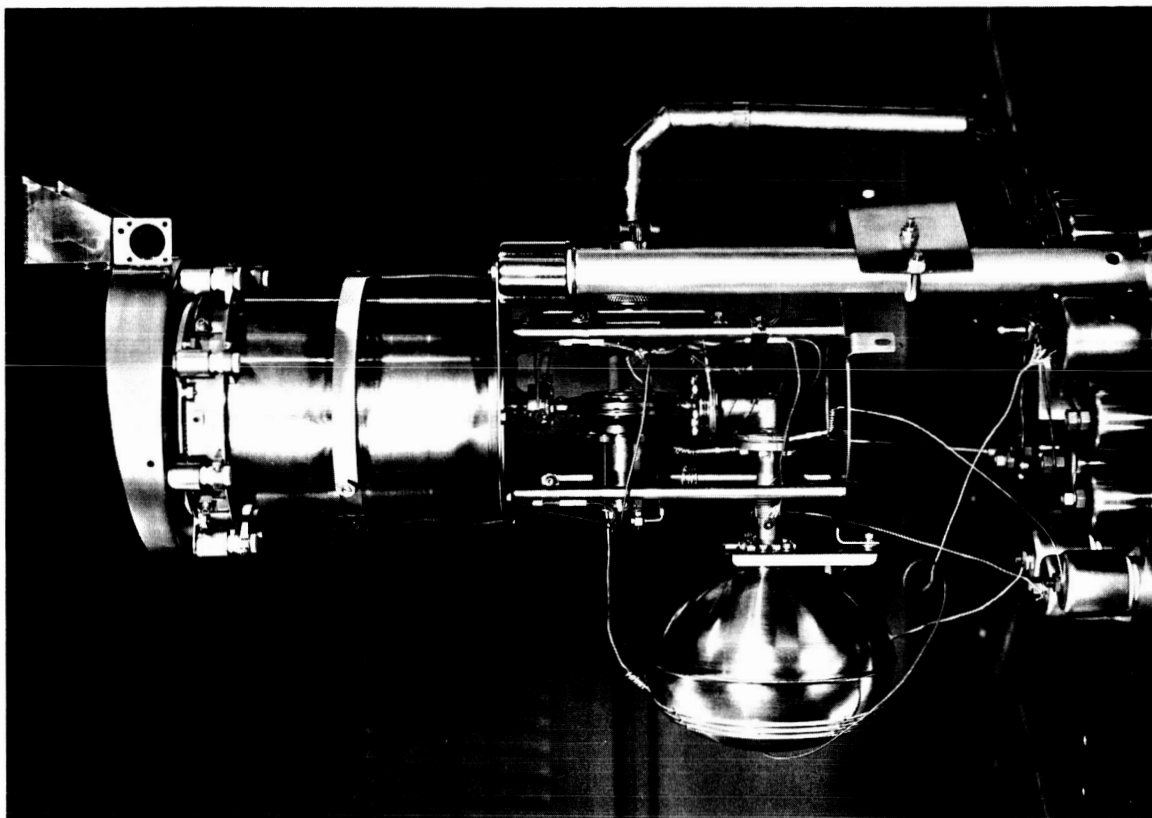
FIG. 5-12   DE2 ENGINE AND 750-HOUR FEED SYSTEM

5.6 Conclusions

The cesium gas discharge ion source has been developed into an ion rocket engine system of demonstrated performance, high reliability, and lifetime potential. The engine readily exceeds the specified goals as given in the Introduction, Section 1; and the capillary feed concept has resulted in simple, efficient, and inherently reliable zero-g feed systems. The engine system control characteristics have been shown to provide for a high degree of regulation of thrust, power, and specific impulse as well as automatic start and stop procedures.

The lifetimes of the DE engine and 750-hour zero-g feed system need to be determined by longer test periods and subsequent analyses. The control and power system characteristics have been sufficiently determined to make feasible a flight-type system design.

The zero-g feed system is clearly scalable to much larger sizes. The capillary feed porous vaporizer system can also be used to feed several engines from a single cesium storage reservoir with separately regulated or controlled feedrates. It is anticipated that the electron-bombardment cesium ion engine can be scaled to much higher thrust levels without sacrifice of any of its high performance characteristics.

REFERENCES

1. R. C. Speiser, et al., "30 Kilowatt Ion Norbset Engine System Study," NASA CR-54068, Jun 1964

2. R. C. Speiser, et al., "Study of a Gas Discharge Cesium Ion Source," EOS Report No. 2120-Final, Jan 1963

3. S. L. Eilenberg, et al., "Applied Research on Contact Ionization Thrustor," Final Report under Contract AF 33(657)-10980, EOS Report No. 3830-Final, May 1964 (Classified)

4. "Quality Assurance Program Provisions for Research, Test, and Development Projects," NASA-Lewis Document QA-1a, Jul 1962

5. "Quality Assurance Plan, Revised," EOS Report 3670-QAP-2, Jan 1963

APPENDIX A
QUALITY ASSURANCE

APPENDIX A

QUALITY ASSURANCE

The quality assurance system employed was evolved during the early phases of the contract effort. Close cooperation between technical and product assurance personnel resulted in a flexible, efficient system for providing program support.

The basic system may be described as a shop traveler scheme. Quality information pertaining to fabricated articles and assemblies is entered on the traveler while work is in process. The traveler is ultimately placed in a permanent file as a record of actual detail and past history. Supplementing shop traveler information are laboratory logbooks containing test data, logbooks containing calibration records, and material certification files at receiving inspection. The shop travelers are instrumental in establishing quality criteria. Engineering drawings, test procedures, material and process specifications, and their respective revisions are prepared with the aid of the quality information on hand.

A.1 QUALITY ASSURANCE PROGRAM REQUIREMENTS

Detailed quality assurance program requirements are specified in Ref. 4. A detailed quality program plan meeting these provisions was generated at the beginning of the program and a Quality Control Manual (Ref. 5 was prepared.

A.2 QUALITY ASSURANCE PROGRAM FUNCTIONS

Quality assurance program functions pertain to the overall project activity and are not intended to be accomplished by any one department or group. Specific quality obligations are imposed on organizational elements other than the EOS Product Assurance Group which retains responsibility for the execution of product assurance policies and programs. A representative from Product Assurance is assigned to the project to work together with these other organizational elements. The representative assists these groups in performing their quality assurance assignments. In this manner project and quality activity are continuously integrated.

(a) Documentation

Essential material and process specifications are prepared by the Project Design Section. After preparation and review, approval of the specification by the cognizant scientist or engineer is obtained. This approval signifies that the specification is sufficiently complete and accurate to ensure material and article verification and reproducibility.

Test procedures are prepared by the appropriate Project Engineering Section where test information supplemental to existing drawings and specifications is desirable to ensure test repeatability and uniformity of results. Each procedure also provides for acquisition and preservation of essential test data. After preparation and review, approval by the cognizant scientist or engineer is obtained.

Inspection policies and procedures are supplemented with special inspection instructions provided where necessary to ensure material and article quality verification and reproducibility (Ref. 5).

Test and laboratory data are recorded in bound laboratory logbooks which are identified with the project and the cognizant

scientist or engineer involved.

Engineering drawings are prepared by the Project Design Section. Approval by the cognizant scientist or engineer is obtained after drawing preparation and engineering review.

Fabricated article records are filed at the Project Design Section. These records consist of completed shop travelers. In process, the shop traveler provides continuous material and article identification in all phases of fabrication.

Material certification records are filed at receiving inspection. The certifications are extracted upon receipt and filed upon acceptance of incoming materials.

The Electrical Laboratory Section maintains an up-to-date schedule for data acquisition equipment calibrations. Calibration data are recorded in bound laboratory logbooks which are identified with the project.

(b) Drawing and Specification Review and Control

Engineering reviews of the expected product performance and life, as well as the associated developmental product design documents, are held as frequently as necessary to ensure proper specification of the physical and material characteristics which determine product quality and reliability. Such reviews are conducted by a review board composed of at least one representative each from Project Engineering, Design, and Quality Assurance. In each case, a Board Chairman, appointed by the Project Supervisor, conducts the review and is responsible for documenting the recommended action resulting from the review. A copy of each such document is filed by the Project Engineering Section.

Control of drawings and specifications is maintained by the Project Design Section. The material planner affixes a copy of the applicable drawing and/or specifications to each work authorization.

Upon completion of the job the work authorization, drawing, and/or specifications are returned to the Project Design Section for permanent filing. This combination of work authorization, drawing, and/or specification constitutes the shop traveler.

The work authorization is a standard work request or purchase request form. Any special requirements are enumerated on the work authorization. Approval by the cognizant scientist or engineer is required before work is performed or purchases are made.

All shop travelers are reviewed by the Quality Assurance Engineer assigned to the project. It is his responsibility to verify that all necessary information is properly documented on the travelers.

(c) Receiving Inspection

Receiving inspection is performed on incoming material including parts and assemblies. Material is inspected to the standards and information contained on the shop traveler. After acceptance by receiving inspection, material certifications are filed by the inspector and the properly identified goods are forwarded to the project storage area. Shop travelers are forwarded to the originator for approval. After approval, the shop traveler becomes a permanent record in the Project Design Section file.

(d) Fabricated Article Controls

In-process inspections are performed on fabricated articles and assemblies. Detailed quality criteria are contained on the shop traveler. Inspections and/or tests are performed at or before the last point at which acceptability may be verified (Ref. 5). Control during processing and fabrication is verified by the Quality Assurance Engineer who reviews the shop travelers to ensure that all necessary information is properly recorded.

(e) Final Inspection

All EOS produced goods undergo a final inspection subsequent to processing and testing but prior to shipment to the customer. Final

inspection, in general, assures conformance with all applicable customer specifications. Quality control program records generated during the production of each end item are reviewed and test results are evaluated with respect to customer requirements. A final test and inspection report is submitted to NASA-Lewis. Any modification after final test and inspection requires retest and reinspection to the extent determined necessary by NASA-Lewis, including submission of new data.

(f) Nonconforming Materials and Articles

When an inspector finds incoming or in-process goods which depart from specifications or drawings, he rejects the goods, noting the discrepancies on the shop traveler. The material, article, or assembly is positively identified as being discrepant and is either reworked or physically separated from other materials until proper disposition has been accomplished. Such disposition results from a materials review, either summary or formal, under the cognizance of Quality Assurance.

Summary review consists of an acceptance by the Quality Assurance representative of the cognizant engineer's written recommendation for disposition of discrepant material. Use of discrepant material may only be authorized by signature of a responsible engineering representative and the Quality Assurance representative involved.

Formal review consists of a meeting of the Materials Review Board at which discrepant material disposition is determined, and the action is documented and reported.

The Materials Review Board consists of responsible representatives from:

(1)   Quality Assurance - Chairman

(2)   Project Engineering

(3)   NASA-Lewis

Use of discrepant material intended for delivery to NASA-Lewis may only be authorized by unanimous approval of the Materials Review Board. Action of the Materials Review Board is entered on the shop traveler. Signatures of the Review Board members constitute authorization.

3670-Final

Should discrepant material be authorized for use, a sketch
number is obtained from the material planner. The sketch number is
entered on the shop traveler in place of the drawing number. Article
disposition is noted on the shop traveler.

(g) Parts Identification

All parts and assemblies destined for inclusion into customer
goods are identified by part number and serial number, where applicable.
Identification of any part (or assembly) is done in such a manner as to
obviate the possibility of damage to the part.

Part number identification includes the EOS drawing number,
revision letter, and dash number, where applicable. Part number
identification for authorized nonconforming articles is the sketch
number which is assigned by the material planner for the particular
article involved. Raw materials are identified by P.R. (purchase
requisition) or P.O. (purchase order) number.

Quality Assurance personnel are responsible for marking or
tagging fabricated articles with the part number identification.
Serial numbers are assigned by the project stock room to all fabricated
articles. The serial number is marked or entered on the tag next to
the part number. Those parts which are not originally identified with
an EOS drawing number do not require part number identification.
Such parts are placed in general storage. These parts are described
by their commercial designation.

(h) Data Acquisition Equipment Calibration

Equipment used in the acquisition of data is calibrated,
evaluated, controlled, and maintained to ensure reliability and accuracy.
Quality Assurance is responsible for ensuring that all equipment used
in acquisition of data undergoes proper periodic, or otherwise scheduled,
calibrations which are traceable to the National Bureau of Standards.
The equipment maintenance requirements are met prior to completion of
calibration.

An up-to-date schedule for equipment calibrations is maintained by the Ion Physics Electrical Laboratory Section. Procured calibration services employ instruments which have calibrations traceable to national standards. Certifications of these calibrations are filed in appropriate laboratory logbooks. In-house calibrations are traceable to procured calibrations. Calibration data are maintained in laboratory logbooks by Ion Physics Electrical Laboratory personnel.

All data acquisition equipment used bears identification which clearly establishes calibration status. Written procedures are used for the calibration, maintenance, and control of data acquisition equipment. Calibration records are used to determine deterioration trends from which calibration periods or schedules are optimized.

Special equipment, designed to provide specific measurements, is evaluated prior to data acquisition usage. Project engineering personnel evaluate such equipment for accuracy and document the results in laboratory logbooks. In addition, the equipment is operated using actual test procedures and conditions to verify correctness of the procedure, ease of operation, and accuracy.

A.3 QUALITY ASSURANCE PROGRAM INFORMATION

DE-1 and DE-2 final inspection reports were prepared for the two delivered systems. These systems included flight prototype engines, flight prototype "zero-gravity" propellant feed systems and rack-mounted laboratory power supplies and controls. Test and calibration data gathered during development and qualification testing were recorded in bound laboratory logbooks.

Over five hundred shop travelers were processed during the contract period. Quality information contained on completed travelers was reviewed. Engine and feed system vellums were revised in accordance with pertinent red-marks contained on the travelers.

Special processing instructions were issued for the following:

1) X-ray of ceramic insulators.

2) Vacuum brazing of tantalum to tantalum with molybdenum-cobalt filler material.

3) Vacuum brazing of tantalum to titanium with nickel-gold filler material.

4) Torch brazing of copper to copper with silver-copper-nickel filler material.

5) Torch brazing of copper to stainless steel with silver-copper nickel filler material.

6) Torch brazing of glass hermetic sealed electrical receptacles with indium-copper-silver filler materials.

7) Torch brazing with indium-copper-silver filler material.

8) Vacuum brazing of tantalum to kovar with nickel-gold filler material.

9) Vacuum brazing of stainless steel sheathed heater wire to stainless steel with nickel-gold filler material.

The following test procedures were released:

3670-1) Feed system leak check, electrical test

3670-2) Cathode check

3670-3) Magnet coil check

3670-4) Electrode system check

3670-5) Engine check

3670-6) Positive high voltage power supply test

3670-7) Negative high voltage power supply test

3670-8) Air electrical check, feed system-engine-neutral detector installation

3670-9) Neutral cesium detector check

3670-10) Neutral cesium detector calibration

3670-11) Programmer test

3670-12) Control system start-stop test

3670-13) Power amplifier chassis test

3670-14) Junction box test

3670-15) 300 volt supply test

3670-16) Transformer chassis test

3670-17) Beam control chassis test

3670-18) Arc control chassis test

3670-19) Neutralizer and neutral detector control panel test

3670-20) Heater control panel test

3670-21) Arc power output panel test

3670-22) Meter panel test

3670-23) Valve solenoid and magnet supply chassis test

3670-24) Neutral efflux indicator test

The following calibration procedures were released:

QA-14)   Instrument Maintenance and Calibration

CP 3670) Ion Physics Electrical Laboratory calibration procedures.

A.4 FAILURE REPORTS

Eight failure modes were reported during the DE phase of the contract period. These are summarized below.

Number of failure modes reported   8

Corrective action taken   6

Corrective action not required   2

(a) Valve

The valve was stuck closed and would not re-open during vacuum test with DE-1 on 12 November. 1.3 amps were applied to the valve which then functioned normally. It is suspected that the spring rubbing against the solenoid housing created this difficulty.

Print revision 703357A was released adding note 10 which requires a 0.0005-0.0010 inch coating of molybdenum disulfide on the spring for lubrication purposes.

(b) Terminal Board

Serious arcs were observed between DE-1 engine and a teflon terminal board during testing on 18 November. The teflon board was replaced with an alumina ceramic terminal board.

(c) V- Power Supply

Capacitor C5 in the V- power supply failed after continuous cycling (arcs in vacuum chamber) for about one minute with DE-1 on 8 December. The capacitor which failed was rated at 250V. It was replaced with a 450V capacitor.

The control system has functioned normally since the capacitor was replaced. Further corrective action was not required.

(d) Feed System

On 11 December the feed system functioned for ten minutes with DE-1 after which time it appeared to be dry. Failure analysis showed that a gap existed between inserts in the vaporizer and reservoir sections. This gap was a consequence of improper assembly.

The feed system loading procedure was released as part of the "Assembly, Cleaning, and Operating Procedures for DE Engine System". The procedure for avoiding a gap between inserts is included.

(e) Electrode System

High drain currents between V+ and V- terminated vacuum testing on 23 December. Inspection after testing showed the engine and test setup to be in good condition. The electrode gap was 0.070 inches.

On 26 December the engine was tested with a 0.079-inch gap. Drains were consistently between 1.2 and 1.5 percent. This substantiates the belief that the drains were due to too high a gap field and perhaps accelerating electrode surface roughness.

Print revision 703705A was released specifying an 0.074-inch minimum electrode gap.

(f) Neutral Cesium Detector

Neutral cesium detector background readings were observed to increase with time. As a consequence, the engine control loop diverted additional power to the arc.

The neutral detector was removed from the arc current control loop. It is used only as a diagnostic measuring device and is not part of the primary thrust-producing components. Corrective action regarding background readings was therefore not specifically required.

(g) Magnet Power Supply

On 10 January 1964, the magnet power supply overheated after 8-3/4 hours of continuous operation. The TR 346 silicon rectifier had overheated and failed. Print 705046, valve solenoid and magnet supply chassis, was released incorporating a 100 cfm Rotron fan for forced air cooling in the magnet supply console.

(h) Programmer

On 10 January 1964, KRP11A relay in the programmer overheated after 19 hours of continuous operation. On 11 January 1964, KRP14A relay in the programmer overheated after 45-1/2 hours of continuous operation. Circuit analysis shows that 160 V were applied to the relays which are rated 115 V. Print 705043, programmer schematic, was released with dropping resistors in series with these relays.

3670-Final